# MODIFYING DESIGN OF FOUR-PORT COUPLERS FOR ENHANCED SIX-PORT REFLECTOMETER PERFORMANCE

YAO JIJUN

NATIONAL UNIVERSITY OF SINGAPORE

2008

# MODIFYING DESIGN OF FOUR-PORT COUPLERS FOR ENHANCED SIX-PORT REFLECTOMETER PERFORMANCE

**YAO JIJUN**

(*M.Eng., Huazhong University of Science & Technology*)

A THESIS SUBMITTED
FOR THE DEGREE OF DOCTOR OF PHILOPHY
DEPARTMENT OF ELECTRICAL & COMPUTER ENGINEERING
NATIONAL UNIVERSITY OF SINGAPORE

2008

# ACKNOWLEDGEMENT

During my Ph.D. candidature at NUS ECE Dept, I learned a lot from my supervisor, Prof. Yeo Swee Ping – his hard-working attitude, his patience, his ideas on doing research, … many, many things. It is an honor to be one of his students.

I also need to thank my wife, Ms. Su Yingrong. She is the one who encouraged me through these years. Without her unflagging support on family matters, I could not carry out my research so smoothly.

I would also like to extend my appreciation to Mr. Sing Cheng Hiong and Ms. Lee Siew Choo for their kind assistance during fabrication and measurements. I would like to thank my fellow course-mates and postgraduate students in NUS ECE Dept's Microwave Laboratory for their friendship and knowledge sharing.

# TABLE OF CONTENTS

Chapter 5....

Chapter 6....

Chapter 7....

# Abstract

Six-port reflectometers based on standard four-port couplers are inexpensive but the designs reported thus far in the literature are either for narrow-band operation or do not meet the optimum design specifications. The analysis, design and tests conducted on three modified four-port structures have resulted in three prototype couplers for use as the building blocks of three prototype six-port reflectometers that are capable of meeting the optimum performance requirements. The measured bandwidths of the two microstrip-implemented reflectometers based on the modified designs for branch-line and rat-race couplers are 29% and 33% respectively. Other planar implementations have subsequently been explored in an attempt to widen the operating bandwidth, and laboratory tests on the third prototype reflectometer (implemented in coplanar waveguide) have confirmed optimum measurement performance over an extended bandwidth of 80% (from 1.2GHz to 2.8GHz). A comparison of the measurements taken by all three prototype reflectometers with the corresponding readings obtained by a commercially-available vector network analyzer has demonstrated that measurement accuracies of ±0.02 and $\pm 2^{\circ}$ can be readily achieved for the magnitude and phase, respectively, of the reflection coefficient for the one-port device under test.

# LIST OF TABLES

# LIST OF FIGURES

# List of Symbols

$\vec{\bullet}$ : complex values, vectors

$\angle\vec{\bullet}$ : arguments of complex values

$|\vec{\bullet}|$ : magnitudes of complex values

$\vec{S}$ : scattering matrix

$\vec{I}$ : unitary matrix

$\vec{q_i}$ : reflectometer phasors, i = 1,2,3,…, N-3

$k_i$ : reflectometer constants, i = 1,2,3,…, N-3

$\vec{A_i}$ : reflectometer constants, i = 0,1,2,3,…, N-3

$\vec{\Gamma}$ : reflection coefficient of loads

$\Gamma_R$ : real part of $\vec{\Gamma}$

$\Gamma_I$ : imaginary part of $\vec{\Gamma}$

$p_i$ : readings of power meter number i, (i = 0,1,2,3,…, N-3)

EVMS: error magnitude mean square, defined in (2.18)

DUT: device under test

U,V,Z,Y four-port coupler representative symbols

$\vec{\gamma}$ : transmission coefficient of four-port couplers $\vec{S}_{23}$

$\vec{\alpha}$ : transmission coefficient of four-port couplers $\vec{S}_{12}$

$\vec{\beta}$ : transmission coefficient of four-port couplers $\vec{S}_{14}$

$\vec{\tau_i}$ : reflection coefficients $\vec{S}_{ii}$, (i = 1,2,3,4)

$\vec{\xi_i}$ : reflection coefficients $\vec{S}_{13}, \vec{S}_{24}$

$Y$ : characteristic admittance of line

$Z$ : characteristic impedance of line

$\theta$ : electrical angle of line

o/c : open circuit

s/c : short circuit

$\beta$ : propagation constant of transmission line

$\varepsilon$ : dielectric constant of substrates

$F_{error}$ : error cost function

$W_i$ : weights of error cost function

$b_k$ : input wave at port $k$

$a_k$ : outgoing wave at port $k$

# Chapter 1

# INTRODUCTION

## 1.1 General Background

The six-port reflectometer (Figure 1.1) has attracted much interest after its introduction in the 1970s. The inherent advantage of this instrument is that it is able to determine the complex reflection coefficient $\Gamma$ of the device under test (DUT) simply from four scalar power readings $P_k$ (where the subscript k refers to the reflectometer port to which each power sensor is attached). The underlying principle is simple but elegant**:** associated with each $P_k / P_{reference}$ power ratio is a circle in the $\Gamma$ plane, and the solution is given by the common intersection of the three circles associated with the three power-ratio readings. Such a principle is thus useful for microwave-impedance measurements [1.1-1.4] which have usually been performed by the more expensive instruments based on the heterodyne technique. Besides metrology, the six port concept has found application in other areas such as non-linear large-signal component modeling [1.5], digital receiver design [1.6] and microwave diversity imaging [1.7].

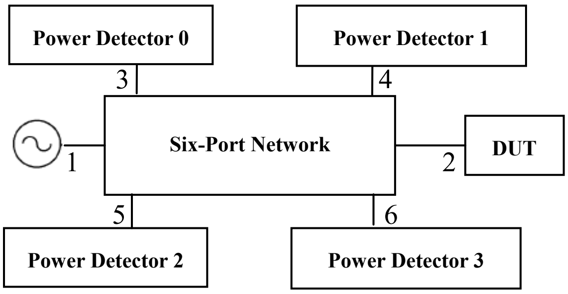

Figure 1.1 Schematic diagram of 6-port reflectometer

As illustrated in Figure 1.1, the six-port concept can be applied to any ‘black box’ with six ports that are to be connected to the DUT, four power sensors and some external source. Hence, the six-port reflectometer (when described in generic form) actually allows for a diversity of hardware implementations. The wide range of implementation possibilities has led to the need for optimum performance criteria to be spelt out. Engen [1.2] offered the following design guidelines for the generic six-port reflectometer:

> “… The design for the six-port network revolves primarily around the choice of positions for the circle centers. From symmetry, these should be equidistant from the origin and spaced at 120°. The optimal distance from the origin is problematic, but a value of 1.5 is satisfactory in most applications …”

The practical utility of the six port concept has prompted researchers to propose many different hardware systems. Initially, Engen [1.8] and Hoer [1.15] suggested the use of four-port couplers as the basic building blocks of six port reflectometers. Since then, millimeter-wave versions of six-port reflectometers have also been reported using magic-T junctions [1.14] and other available components [1.16]. MMIC implementations have additionally been attempted [1.17-1.18]. However, most of the systems reported thus far in the literature do not comply with the optimum design criteria expounded by Engen [1.2].

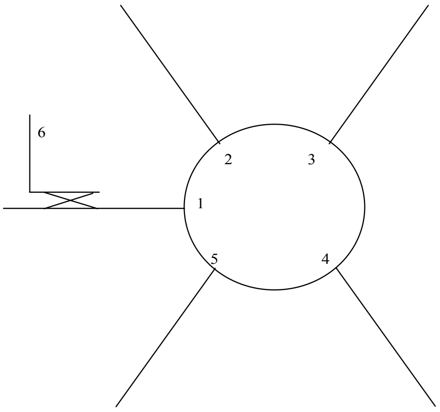

Figure 1.2 Schematic representation of 6-port reflectometer based on symmetrical 5 port junction

For this reason, a number of researchers explored the use of novel components such as the symmetrical five-port and six-port couplers [1.9-1.13] to develop new six-port reflectometers that are capable of complying with Engen's optimum design criteria. Depicted in Figure 1.2 is one such example which employs the symmetrical five port coupler in conjunction with a directional coupler to provide the additional sixth port. This novel component has five arms attached (with angular separations of $72^{o}$) to a central junction which may take on different physical forms (such as disc or ring). Extrapolating from this, Yeo [1.10] has additionally attempted to use the symmetrical six-port coupler to develop yet another new six-port reflectometer that is similarly capable of meeting the optimum design criteria. However, it is not easy to design symmetrical five-port or six-port couplers. Neither can these novel components be readily purchased because they are at present not available commercially. Hence, we will revert to investigate how the more familiar four-port couplers may be re-designed so that they can be more effectively utilized as the core components of the six-port reflectometer which, when appropriately re-configured, is now able to meet the optimum performance specifications.

## 1.2 Project Objectives

Although hybrid and quadrature couplers are widely available, it is known that the six-port reflectometers based on such four-port couplers do not meet the optimum design specifications. The question that thus arises is whether it is possible to modify the design of the four-port couplers for use as the basic building blocks of six-port reflectometers. One possible approach is to simply choose the magic-T junction as replacement. The waveguide version of the magic-T junction helps to illustrate, as depicted in Figure 1.3, how four of these components may be inter-connected in order to function as a six-port reflectometer. However, it will be difficult for us to extend the operating bandwidth of such an instrument beyond 5% if we merely resort to the standard magic-T junction.

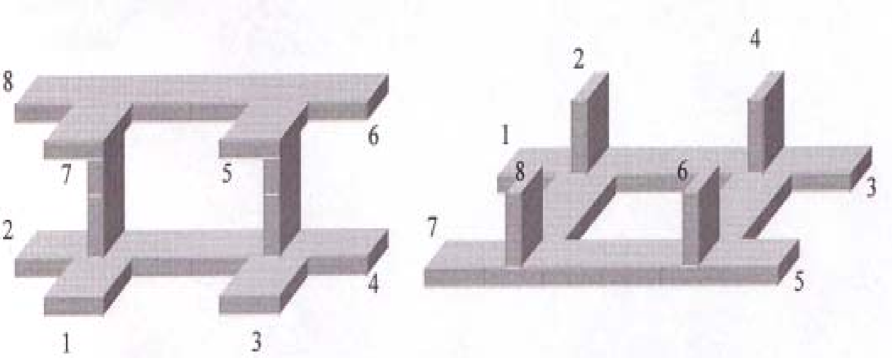

Figure 1.3 Six-port reflectometer based on four magic-Ts

In addition to the task of re-designing the four-port couplers (so as to obtain suitable equivalents of the magic-T junction), there is the need to address the underlying requirements for six-port reflectometers to yield optimum performance. The research tasks may be summarized in the following manner**:**

(a) determine from network analysis how the six-port reflectometer (as a generic ‘black box' with six ports) should be configured in order to yield system characteristics that allow for optimum performance (taking also into consideration how much hardware imperfections may be tolerated during practical implementation and routine operations)

(b) re-design the four-port couplers (in planar form) for the purpose of using them as the building blocks of six-port reflectometers that are capable of yielding optimum performance over the requisite bandwidth

(c) inter-connect four of these modified four-port couplers so as to construct and test prototype six-port reflectometers that meet the optimum design specifications over the requisite bandwidth.

The analysis and results have already been reported in the following papers:

(a) J.J. Yao and S.P. Yeo, "Six-port reflectometer based on modified hybrid couplers," IEEE Transactions on Microwave Theory & Techniques, vol. 56, pp. 493-498, 2008

(b) J.J. Yao, Y. Chen and S.P. Yeo, "Modifying hybrid coupler design to enhance six-port reflectometer performance," European Microwave Conference Digest, 2005, pp. 256-259

(c) Y. Chen, J. Yao and S.P. Yeo, "Matched symmetrical six-port microstrip coupler," IEEE International Microwave Symposium Digest, 2005, pp. 1223-1226.

(d) Y. Chen, J.J. Yao, and S.P. Yeo, "Improving design of symmetrical six-port microstrip coupler", Progress in Electromagnetics Research Symposium Digest, 2005, pp. 598-601.

## 1.3 Organization of Thesis

After the introductory overview in Chapter 1, we begin our generic analysis in Chapter 2 by considering the N-port reflectometer instead of dwelling entirely on the six-port reflectometer. The general insights we thus gained for the N-port reflectometer are naturally helpful when we subsequently return to our primary focus on the six-port reflectometer. Of particular interest too are the queries that need to be addressed in the design guidelines proffered by Engen and other researchers. We have additionally resorted to Monte Carlo simulations to supplement the findings accrued from network analysis. A pilot design of a prototype eight-port reflectometer is also performed in order to reinforce our understanding of the general fundamentals.

The overall objective of Chapters 3-6 is the development of six-port reflectometers based on modified four-port couplers. In the ideal case (where hardware imperfections are assumed to be negligible), our analysis shows that such six-port reflectometers should be able to meet the optimum design considerations discussed in Chapter 2. In practice, however, hardware imperfections will deteriorate the system performance of the resultant instrument. Before we can proceed with the detailed designs, we will thus have to investigate in Chapter 3 the effects of hardware imperfections (in the four-port couplers, inter-connecting links, power detectors and spurious parasitics) on the system behavior of the six-port reflectometer and thereafter suggest various re-configuration possibilities to address these problems.

Prior to the designs and tests reported in Chapter 5 for our three prototype four-port couplers (*viz* two microstrip-based couplers with measured bandwidths of 26% and 32% in Sections 5.1 and 5.2 respectively and another CPW-based coupler with measured bandwidth of 80% in Section 5.3), we also need to consider in Chapter 4 the detailed analysis underlying the models of the different coupler structures, parasitic elements and compensation techniques. Further refinement is subsequently required when inter-connecting such re-designed four-port couplers to construct our prototype six-port reflectometers.

In Chapter 6, we have additionally incorporated adjustable elements that allow us to fine-tune the behavior of our six-port reflectometer circuits. The calibration procedure selected in Section 6.1 also helps to correct for hardware imperfections. The laboratory tests conducted in Chapter 6 provide confirmation of the performance results meeting the optimum design specifications for our three prototype six-port reflectometers (with measured bandwidths of 29% and 33% for our two microstrip-implemented reflectometers in Sections 6.2 and 6.3 respectively, and measured bandwidth of 80% for our CPW-implemented reflectometer in Section 6.4).

We finally conclude in Chapter 7 with a summary of our principal findings and suggestions for possible future work.

## REFERENCES

[1.1] G.F. Engen, “The six-port reflectometer: an alternative network analyzer”, IEEE Trans. Microwave Theory Tech, vol. 25, no.12, pp. 1075-1080, Dec. 1977

[1.2] G.F. Engen, “A historical review of the six port measurement technique”, IEEE Trans. Microwave Theory Tech, vol. 45, no.12, pp. 2414-2417, Dec. 1997

[1.3] H. Cronson, “A dual six-port automatic network analyzer”, IEEE Trans. Microwave Theory Tech, vol. 29, no. 4, pp. 372-378, Apr. 1981

[1.4] C. Hoer , “A network analyzer incorporating two six-port reflectometers”, IEEE Trans. Microwave Theory Tech., vol. 25, no. 12, pp. 1070-1074, Dec. 1977

[1.5] G. Berghoff, “Automated characterization of HF power transistors by source-pull and multi-harmonic load-pull measurements based on six-port techniques”, IEEE Trans. Microwave Theory Tech., vol. 46, no. 12, pp. 2068-2073, Dec. 1998

[1.6] J. Li, “Computer and measurement simulation of a new digital receiver operating directly at millimeter-wave frequencies”, IEEE Trans. Microwave Theory Tech., vol. 43, no. 12, pp. 2766-2773, Dec. 1995

[1.7] H.C. Lu, “Microwave diversity imaging using six-port reflectometer”, IEEE Trans. Microwave Theory Tech., vol. 47, no. 1, pp. 84-87, Jan. 1999

[1.8] G.F. Engen, “An improved circuit for implementing the six-port technique of microwave measurements’, IEEE Trans. Microwave Theory Tech., vol. 25, no. 12, pp. 1080-1083, Jan. 1999

[1.9] S.P. Yeo, “First-order model of symmetrical six-port microstrip ring coupler”, IEEE Trans. Microwave Theory Tech., vol. 39, no. 9, pp. 1666-1669, Sept. 1991

[1.10] S.P. Yeo, “Analysis of symmetrical six-port junction when configured as a six-port reflectometer”, IEEE Trans. Instrum. Meas., vol. 41, no. 2, pp. 193-197, Apr. 1992

[1.11] E.R.B. Hansson and G.P. Riblet, “An ideal six-port network consisting of a matched reciprocal lossless five-port and a perfect directional coupler”, IEEE Trans. Microwave Theory Tech., vol. 31, no. 3, pp. 284-288, Mar. 1991

[1.12] S.P. Yeo, “Improved design for symmetrical six-port microstrip coupler”, IEEE Trans. Microwave Theory Tech., vol. 48, no. 6, pp. 1074-1077, Jun. 1992

[1.13] S.P. Yeo, “Improvements in design of six-port reflectometer comprising symmetrical five-port waveguide junction and directional coupler”, IEEE Trans. Instrum. Meas., vol. 39, no. 1, pp. 184-188, Jan. 1992

[1.14] J. Bellantoni, “Millimeter-wave components for use in a variable state four-port network analyzer”, IEEE Trans. Microwave Theory Tech., vol. 36, no.12, pp. 1880-1885, Dec. 1988

[1.15] C. Hoer , “Using an arbitrary six-port junction to measure complex voltage ratios”, IEEE Trans. Microwave Theory Tech., vol. 23, no.12, pp. 978-984, Dec. 1975

[1.16] M. Weidman, “A semi-automated six-port for measuring millimeter-wave power and complex reflection coefficient”, IEEE Trans. Microwave Theory Tech., vol. 25, no.12, pp. 1083-1085, Dec. 1977

[1.17] F. Wiedmann, “new structure for a six-port reflectometer in monolithic microwave integrated circuit technology”, IEEE Trans. On Instrument. & Measurement., vol. 46, No. 2, pp. 527-530, Apr. 1997

[1.18] J. Hesselbarth, “Two new six-port reflectometers covering very large bandwidths”, IEEE Trans. Instrum. Meas., vol. 46, no. 4, pp. 966-969, Aug. 1997

# Chapter 2

# SIX-PORT REFLECTOMER DESIGN CONSIDERATIONS

Although we shall eventually focus our efforts on the six-port network, our discussion in Chapter 2 shall initially embrace the generic N-port network (where N = 5, 6, 7, …). As pointed out by Engen [2.1], the key design consideration "… revolves primarily around the choice of positions for the circle centers." Probert and Carroll [2.2] showed that these circle centers (which Engen referred to as q-points) should lie on a circle or ellipse with equal angular separations in order to minimize the system uncertainties in measuring $\vec{\Gamma}$ of the one-port device under test (DUT). As for the N = 6 case (representing the six-port reflectometer network), Engen [2.1] already stated that the magnitudes and angular separations of all three q-points should be equal**;** although it is obvious from symmetry consideration that the common angular separation must be $120^o$, what the common magnitude ought to be is not immediately apparent and Engen suggested that 1.5 may be good enough for most applications. Nevertheless, we should still address this ambiguity and seek to ascertain the optimum magnitude of the q-points. This is important because designing a network with q-points having optimum magnitudes (in addition to $120^o$ angular separations) will help to reduce the measurement uncertainty of the reflectometer arising from, for example, power-detector reading errors.

Another consideration when attempting to design wide-band reflectometers (or receivers) is that it is very difficult to implement the hardware for an N-port network with q-points having near-optimum magnitudes and angular separations over the entire bandwidth. Consider, by way of example, the wide-band reflectometer structure proposed by Hesselbarth [2.8]**;** his experimental results showed the q-points deviating from their optimum positions at various frequencies in the specified bandwidth. Instead of looking only for the optimum magnitude of the q-points, we ought to provide some allowance and additionally look for the range of acceptable magnitudes for the q-points of the N-port networks.

## 2.1 Generic Analysis

Probert and Carroll [2.2] showed that the q-points of the N-port networks should lie on a circle or ellipse and have equal angular separations in order to minimize the MSE (mean squares error) for the reflectometer's measurement accuracy. However, we need to re-visit certain details in their analysis and will start by briefly tracing their derivation.

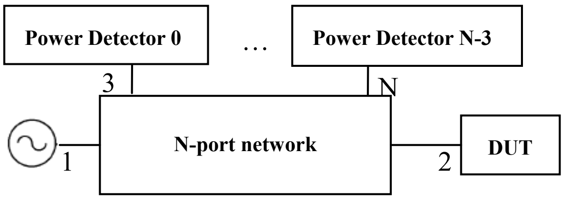

Figure 2.1 Schematic diagram of N-port reflectometer

Depicted in Figure 2.1 is the general N-port reflectometer under study. The scattering analysis of such a network will yield the following set of system equations for the power ratios $p_i$ (which are obtained by using the power-detector reading $P_0$ as the reference to normalize all of the other N-3 power-detector readings $P_i$):

$$p_i = k_i \left| \frac{1+\overrightarrow{A_i}\,\overline{\Gamma}_{DUT}}{1+\overrightarrow{A_0}\,\overline{\Gamma}_{DUT}} \right| \qquad i = 1, 2, 3\ldots\ldots, \text{N-3} \qquad (2.1)$$

where $k_i$ are real constants and $\overrightarrow{\mathrm{A}_i}$ are complex constants of the N-port network.

For the ideal case, the six-port coupler and all power detectors should be reasonably well-matched. Another condition for ideal-case operation is that the reference power-detector reading $P_0$ should measure only the incident power. Under such circumstances, the constant $\overrightarrow{A_0}$ $A_0$ reduces to 0 and Equation 2.1 will then be simplified to**:**

$$|\,\overline{\Gamma}_{DUT} - \overrightarrow{q_i}\,|^2 = p_i / K_i\,, \quad i = 1, 2, 3\ldots\ldots, \text{N-3}; \qquad (2.2)$$

where $K_i = k_i \;/\; |\overrightarrow{A_i}|$ .

Expanding Equation 2.2 will yield**:**

$$\Gamma_R{}^2 + \Gamma_I{}^2 - 2x_i\Gamma_R - 2y_i\Gamma_I + x_i^2 + y_i^2 = P_i/(P_0K_i) \qquad i = 1, 2, 3\ldots\ldots, \text{N-3}; \qquad (2.3)$$

where $\overline{\Gamma}_{DUT} = \Gamma_R + j * \Gamma_I$

and $\overrightarrow{q_i} = x_i + j * y_i$ .

Equations 2.3 may then be re-written in more compact form by employing vector notation in the following manner:

$$\Gamma_R{}^2 + \Gamma_I{}^2 - 2\overline{x}\Gamma_R - 2\overline{y}\Gamma_I + \overline{R}^2 = \overline{\chi} \tag{2.4}$$

where $\overline{x} = [x_1, x_2 ......, x_{N-3}]^T \qquad \overline{y} = [y_1, y_2 ......, y_{N-3}]^T$

$\chi_i = P_i / (P_0 K_i) \qquad \overline{\chi} = [\chi_1, \chi_2 ......, \chi_{N-3}]^T$

$\overline{R}^2 = [x_1^2 + y_1^2, x_2^2 + y_2^2 ......, x_{N-3}^2 + y_{N-3}^2]^T$

### 2.1.1 Optimum angular separations of q-points

In their analysis, Probert and Carroll [2.2] defined vectors $\overline{a}$ and $\overline{b}$ such that

$$\Gamma_R = \frac{\overline{a} \bullet \overline{\chi}}{2(\overline{a} \bullet \overline{x})} \qquad \Gamma_I = \frac{\overline{b} \bullet \overline{\chi}}{2(\overline{b} \bullet \overline{y})} \tag{2.5}$$

The errors in the power-detector measurements lead to an error $\delta\overline{\chi}$ where

$$\delta\Gamma_R = \frac{\overline{a} \cdot \delta\overline{\chi}}{2(\overline{a} \cdot \overline{x})} \qquad \delta\Gamma_I = \frac{\overline{b} \cdot \delta\overline{\chi}}{2(\overline{b} \cdot \overline{y})} \tag{2.6}$$

For Equation 2.5 to hold, the following should be noted from Equation 2.3:

$$\overline{b} \cdot \overline{x} = \overline{a} \cdot \overline{y} = 0 \tag{2.7}$$

$$\overline{b} \cdot \overline{R}^2 = \overline{a} \cdot \overline{R}^2 = 0 \tag{2.8}$$

$$\sum a_i = 0; \qquad \sum b_i = 0 \tag{2.9}$$

In addition, Probert and Carroll defined vectors $\overline{c}$ and $\overline{d}$ to be orthogonal to one another as well as to **x**.

$$\overline{y} = \overline{c} + \alpha \overline{x} \tag{2.10}$$

$$\overline{R}^2 = \overline{d} + \beta \overline{c} + \gamma \overline{x} \tag{2.11}$$

Assuming that $|\delta\chi_i| = \varepsilon$ for all i then yields

$$|\delta\rho_R|^2 = \frac{(\overline{a}\cdot\overline{a})\varepsilon^2}{4(\overline{a}\cdot\overline{x})^2} \qquad |\delta\rho_I|^2 = \frac{(\overline{b}\cdot\overline{b})\varepsilon^2}{4(\overline{b}\cdot\overline{y})^2} \tag{2.12}$$

and so minimizing $|\delta\rho_R|^2$ and $|\delta\rho_I|^2$ will require

$$\alpha = \beta = \gamma = 0 \tag{2.13}$$

Hence, the following conditions hold in $\overline{x}$, $\overline{y}$, $\overline{a}$ and $\overline{b}$ to establish the design criteria:

(a) $\overline{x}$ and $\overline{y}$ are orthogonal (2.14a)

(b) $\overline{a} = A\overline{x}$ and $\overline{b} = B\overline{y}$ where A and B are scalars (2.14b)

(c) $\sum x_i = 0 \qquad \sum y_i = 0$ (2.14c)

In the derivation outlined by Probert and Carroll, we notice that the assumption required for deriving Equation 2.12 is crucial for their analysis to be valid. To ascertain whether such an assumption is reasonable in practice, we need to refer to the manufacturer data-sheets of any commercially-available power detector where we usually find the accuracy data expressed in percentage or dB format**:** for example, we infer from the 0.5% or -0.02dB specifications that the power-detector readings $P_i$ have mesurement uncertainties with standard deviation of 0.005 $P_{i\_true}$. If the relative measurement error of the power meter is denoted by $\varepsilon$, we then obtain

$$|\delta\chi_i| = \frac{|\delta P_i|}{P_0 K_i} = \frac{\varepsilon P_i}{P_0 K_i} \tag{2.15}$$

To make all $|\delta\chi_i| = \varepsilon$ or $k\varepsilon$, we will have to impose

$$P_i / (P_0 K_i) = 1 \quad \text{or} \quad k \ (k \text{ is a constant}) \tag{2.16}$$

This additional assumption should be applied to Probert and Carroll's analysis in order to support their findings in [2.2]. However, there is some uncertainty regarding the availability of Equation 2.16 and we need to assume that we can design such a reflectometer with constant $P_i / (P_0 K_i)$ for a particular DUT.

### 2.1.2 Optimum magnitudes of q-points

As already demonstrated in Sub-Section 2.1.1, one possible solution for the conditions listed in Equation 2.14 is that the q-points should be distributed evenly on a circle. We assume the following distribution for $q_i$ :

$$x_i = r_c \cdot COS(\frac{i \cdot 2\pi}{n}) \qquad y_i = r_c \cdot SIN(\frac{i \cdot 2\pi}{n}) \tag{2.17}$$

where i = 0, 1, …, N-4, and n = N-3

and $r_c$ is the magnitude of the q point.

In Sub-Section 2.1.1, we denoted the relative measurement accuracy of the power detectors as ε; on extrapolation, we will now let $|\delta\chi_i| = \varepsilon\chi_i$. Since we assume all q-points to be distributed evenly on a circle, Equations 2.14(a) and 2.14(c) are naturally valid. In addition, Equation 2.14(b) is a possible solution for Equations 2.5 and 2.3**;** by extension, we may presume that Equation 2.14(b) holds for our situation. By substituting Equations 2.14, 2.17 and 2.18 into Equation 2.12, we then obtain the following magnitude-squared expression of the error vector**:**

$$\begin{aligned} &|\delta\Gamma_R|^2 + |\delta\Gamma_I|^2 \\ &= \frac{(\sum x_i \delta\chi_i)^2}{4(\sum x_i^2)^2} + \frac{(\sum y_i \delta\chi_i)^2}{4(\sum y_i^2)^2} \\ &= \frac{(\sum x_i \delta\chi_i)^2 + (\sum y_i \delta\chi_i)^2}{r_c^4 n} \end{aligned} \qquad (2.18)$$

The real and imaginary parts of the error vector (which are denoted as $\Gamma_R$ and $\Gamma_I$ respectively) have normal distributions in accordance with Equation 2.5. However, these two constituent parts are not independent of each other and so the magnitude of the error vector will not follow the chi-distribution. In fact, it is difficult to catalog it under any known distribution.

To help us choose a suitable figure of merit for the reflectometer's performance, we take a look at communication theory [2.18-2.22] where the concept of EVM (error magnitude error) is defined as:

$$EVM = \frac{\sqrt{|error\_vector|^2}}{\sqrt{|true\_vector|^2}} = \frac{\sqrt{|\delta\Gamma_R|^2 + |\delta\Gamma_I|^2}}{\sqrt{|\Gamma_R|^2 + |\Gamma_I|^2}} \qquad (2.19a)$$

However, the definition in Equation 2.19(a) suggests that the magnitude of the error vector will increase with the magnitude of the true vector while the value of EVM remains unchanged. This is clearly unacceptable for use in reflectometer design. We have opted, instead, to define the error vector's magnitude square (EVMS) in our effort to evaluate the reflectometer's performance.

$$
\begin{aligned}
EVMS &= E(|\delta\Gamma_R|^2 + |\delta\Gamma_I|^2) \\
&= \varepsilon^2 \frac{\sum |\chi_i|^2}{r_c^2 n} = \varepsilon^2 \frac{r_c^4 + |\Gamma_{DUT}|^4 + 4|\Gamma_{DUT}|^2 r_c^2}{r_c^2 n}
\end{aligned}
\qquad (2.19b)
$$

The following may be inferred from Equation 2.19(b):

- The performance of the reflectometer may be improved by increasing the number of ports. The measurement error EVMS due to power-detector uncertainty ε should decrease as N increases.

- The EVMS of measurement results increases with the DUT's reflection-coefficient magnitude**;** for our study, we have chosen $|\Gamma_{DUT}| = 1$ (which is the maximum reflection-coefficient magnitude for passive DUTs) to evaluate the total performance of the reflectometer. The relationship between the normalized EVMS and the corresponding q-point magnitudes is depicted in Figure 2.2 where we note that $EVMS \cdot n / \varepsilon^2$ has a minimum value at $r_c = 1$. We shall denote this as $\text{EVMS}_{\min}$ during our ensuing discussion in Section 2.2.

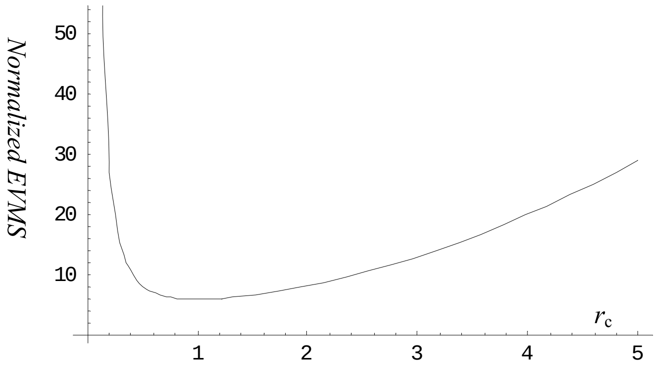

Figure 2.2 Variation of normalized EVMS ($EVMS \cdot n / \varepsilon^2$) with radius $r_c$ where $|\Gamma_{DUT}| = 1$

## 2.2 Range of Acceptable Design Settings

Before we proceed with our analysis to derive the range of magnitudes and range of angular separations that are permissible for q-points, we need to decide on the choice of benchmark. From Section 2.1 (regarding the optimum q-point positions and the corresponding EVMS estimation), we note that any deviation of the q-points from their optimum positions will lead to an increase in EVMS. By setting an estimation limit for EVMS, we can determine the range of acceptable values for the q-point magnitude and angular separation. There are other factors to be taken into consideration as well and we will look at each in turn under the ensuing sub-headings.

### 2.2.1 Range of acceptable values for magnitudes of q-points

Returning to Figure 2.2 (where $\text{EVMS}_{\text{min}}$ refers to the minimum in the plot of EVMS against q-point magnitude), we shall choose the upper limit for EVMS estimation as 2 $\text{EVMS}_{\text{min}}$ for the DUT with maximum reflection-coefficient magnitude of $|\vec{\Gamma}_{DUT}| = 1$. For such a choice of limit, Figure 2.2 indicates that the corresponding range of acceptable values for the q-point magnitude ought to be $0.36 < |\vec{q}_i| < 2.8$.

It is, however, uncommon to site the q-points within the unit circle and we should thus not include $0.36 < |\vec{q}_i| < 1$ for the design of six-port reflectometers (even though such a design had been reported in [2.8]). Attention should be drawn to the power-detector's dynamic-range requirement. For the case where $r_c > 1$, we may turn to the derivation provided by Somlo [2.10] for the dynamic-range requirement:

$$D_{dynamic\_range} = 20\log(\frac{r_c + 1}{r_c - 1}) \tag{2.20}$$

Hence, we note from Equation 2.20 that the power-detector's dynamic-range requirement ought to be 14dB if we adopt Engen's suggestion [2.1] of $r_c = 1.5$. In addition, it may be inferred from Equation 2.20 that the dynamic range will decrease with any increase of q-point magnitudes.

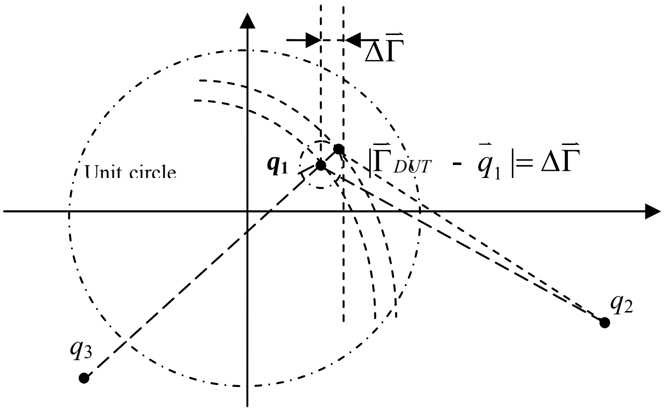

Figure 2.3 Illustration for dynamic-range requirement derivation

There is also the need to derive the dynamic-range requirement for the other case where $r_c \leq 1$. For the general N-port network, we shall assume that the q-points lie on a circle (with $r_c < 1$ and angular separations of $360^o/N$) and $\Delta\vec{\Gamma}$ denotes the minimum detectable reflection-coefficient magnitude that is required. Figure 2.3 depicts a possible scenario where $\vec{\Gamma}_{DUT}$ is in close proximity to (or even coincides with) the q-point denoted as $\vec{q}_1$; for such a scenario, we need to ensure that the reflectometer remains able to distinguish between the reflection coefficient $|\vec{\Gamma}_{DUT}| = |\vec{q}_1|$ (with minimum power reading at Port 1) and those reflection coefficients on the $|\vec{\Gamma}_{DUT} - \vec{q}_1| = |\Delta\vec{\Gamma}|$ circle as portrayed in Figure 2.3. We then note from Equation 2.3 that the minimum power reading should be at least $|\Delta\vec{\Gamma}|^2 K_i P_0$ and any reading smaller than this value will be rounded down to zero. It is not difficult to infer the maximum power reading to be $(1+r_c)^2 K_i P_0$ . Accordingly, the power-detector's dynamic-range requirement for $r_c \leq 1$ is given by

$$D_{dynamic\_range} = 20\log(\frac{1+r_c}{|\Delta\vec{\Gamma}|}) \tag{2.21}$$

Substituting the optimum $r_c = 1$ and minimum detectable reflection coefficient $|\Delta\vec{\Gamma}| = 0.01$ into Equation 2.21, we find that the power-detector's dynamic range should be 46dB. Comparing with Engen's suggestion of $r_c = 1.5$, we see that the power detector for the $r_c = 1$ case has a much larger dynamic-range requirement. Even though we may not have difficulty to realize a diode sensor with more than 46dB of dynamic range, it will be more cost effective to design a six-port reflectometer that requires a less demanding dynamic range for the power detectors. If, for example, the power-detector's dynamic range does not exceed 20dB, the q-points will then be sited in the $1.2 < |\vec{q}_i| < 2.8$ belt.

The power-detector's dynamic-range requirement is not the only factor that influences us to opt for a narrower range. Another consideration is the need for enhanced measurement accuracy which calls for a further reduction of the range of acceptable q-point magnitudes. Returning to consider the $r_c > 1$ case, Figure 2.4 depicts an extreme scenario for the measurement-accuracy requirement and we obtain the following expression (where the requisite minimum detectable reflection-coefficient magnitude is $|\Delta\bar{\Gamma}|$ and the power detector's measurement accuracy is $\varepsilon$ ):

$$(1+r_c)^2 = P_i/(K_i P_0) \tag{2.22a}$$

$$(1+r_c-|\Delta\bar{\Gamma}|)^2 = P_i^{'}/(K_i P_0) \tag{2.22b}$$

It then follows that

$$\varepsilon = \frac{\Delta P_i}{P_i} = \frac{2|\Delta\bar{\Gamma}|(1+r_c)-|\Delta\bar{\Gamma}|^2}{(1+r_c)^2} \approx \frac{2|\Delta\bar{\Gamma}|}{(1+r_c)} \tag{2.22c}$$

From Equation 2.22(c), we see that the range of q-point magnitudes is $r_c < (2|\Delta\bar{\Gamma}|/\varepsilon)-1$. For a typical power-detector with accuracy of 0.5% and minimum detectable reflection-coefficient magnitude of 0.01, the q-points will be sited within the $r_c < 3$ limit.

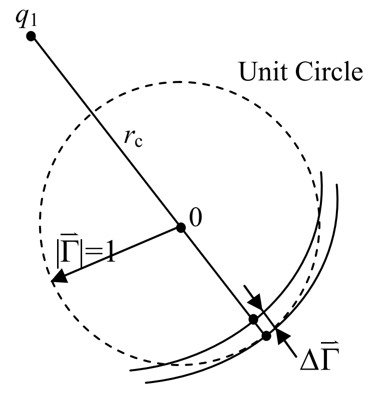

Figure 2.4 An extreme scenario for power-dectector's measurement-accuracy requirement

## 2.2.2 Range of acceptable values for angular separations of q-points

As for the range of permissible values for the angular separations of q-points, it is more complicated to attempt a similar line of analysis for even the simple case. By way of example, we shall consider a six-port reflectometer with $r_c$ = constant. The procedure is nearly the same as that employed in Sub-Section 2.1.2. We allow for two of the three q-points to depart around their ideal-case locations: $\vec{q}_2 = r_c\, e^{j\varphi}$ (with its original location denoted as $r_c\, e^{j2\pi/3}$) as well as $\vec{q}_1 = r_c\, e^{j\theta}$ (with its original location denoted as $r_c\, e^{j0}$). With the third q-point remaining at its ideal-case location (denoted as $\vec{q}_3 = r_c\, e^{-j2\pi/3}$), we then proceed to derive the EVMS($\varepsilon^2$,θ,φ, $\Gamma_{DUT}$) for such settings**:**

$$
\begin{aligned}
&\mathrm{EVMS}\left(\epsilon^2, r_c, \theta, \phi, \Gamma_{DUT}|\right) = \\
&\frac{\epsilon^2}{12\, r_c^2}\Bigg(\left(r_c^2 + |\Gamma_{DUT}|^2 + r_c\,|\Gamma_{DUT}|\,\mathrm{Cos}[\phi] - \sqrt{3}\, r_c\,|\Gamma_{DUT}|\,\mathrm{Sin}[\phi]\right)^2 + \\
&\quad\left(r_c^2 + (|\Gamma_{DUT}|)^2 + r_c\,|\Gamma_{DUT}|\,\mathrm{Cos}[\phi] + \sqrt{3}\, r_c\,|\Gamma_{DUT}|\,\mathrm{Sin}[\phi]\right)^2 + \\
&\quad\frac{1}{(1 + 2\,\mathrm{Cos}[\theta])^2} \\
&\quad\Bigg(12\Bigg(\left(r_c^2 + (|\Gamma_{DUT}|)^2 - 2\, r_c\,|\Gamma_{DUT}|\,\mathrm{Cos}[\theta-\phi]\right)^2 + \\
&\qquad\left(\frac{1}{2} + \frac{\mathrm{Sin}[\theta]}{\sqrt{3}}\right)^2\left(r_c^2 + (|\Gamma_{DUT}|)^2 + r_c\,|\Gamma_{DUT}|\,\mathrm{Cos}[\phi] - \sqrt{3}\, r_c\,|\Gamma_{DUT}|\,\mathrm{Sin}[\phi]\right)^2 + \\
&\qquad\left(-\frac{1}{2} + \frac{\mathrm{Sin}[\theta]}{\sqrt{3}}\right)^2\left(r_c^2 + (|\Gamma_{DUT}|)^2 + r_c\,|\Gamma_{DUT}|\,\mathrm{Cos}[\phi] + \sqrt{3}\, r_c\,|\Gamma_{DUT}|\,\mathrm{Sin}[\phi]\right)^2\Bigg)\Bigg)\Bigg)
\end{aligned}
\tag{2.23}
$$

The resultant EVMS expression we obtained in Equation 2.23 is complicated by the many permutations of possible variations. A simple example to consider is the case with fixed DUT and q-point magnitude $r_c$ ; depicted in Figure 2.5 is one such three-dimensional surface EVMS(θ,Φ) for the case where $|\vec{\Gamma}_{DUT}| = 1$ and $r_c = 2$.

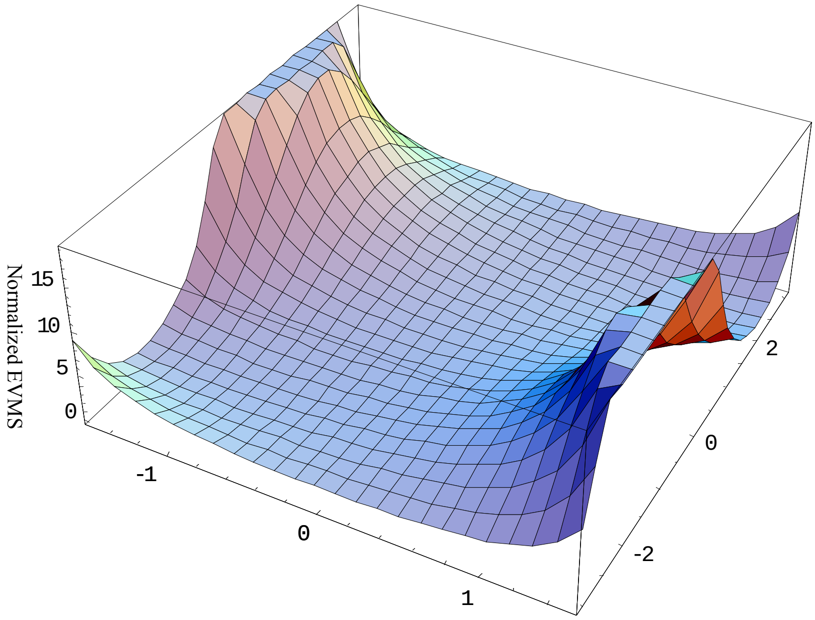

Figure 2.5 Three-dimensional surface depicting variation of EVMS(θ,Φ) where $|\overline{\Gamma}\ DUT| = 1$ and $r_c = 2$

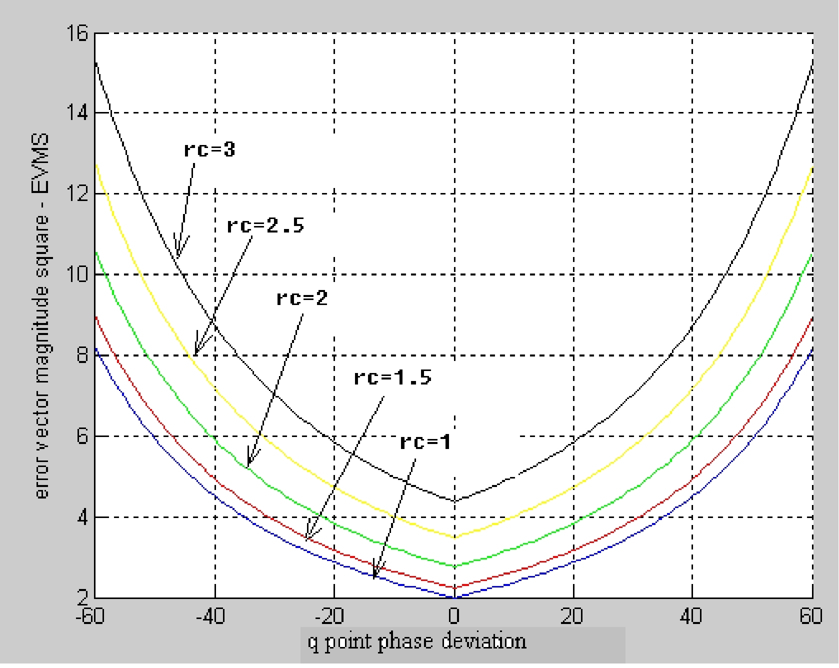

Figure 2.6 Variation of EF(θ) with q-point angular separation

For us to evaluate the overall performance of the six-port reflectometer system, we have to additionally define the following error function:

$$\mathrm{EF}(\theta,\mathrm{r_c}) = \max(\mathrm{EVMS}(\varepsilon^2,\theta,\phi,\mathrm{r_c},|\bar{\Gamma}_{\mathrm{DUT}}|)/\varepsilon^2,\ \{|\bar{\Gamma}_{\mathrm{DUT}}| \le 1, 0<\phi<2\pi\}) \qquad (2.24)$$

Plotted in Figure 2.6 are the results we obtained for the error function EF(θ) when we varied $r_c$ in steps of 0.5 from 1 to 3. As expected, the obvious conclusion from all five plots in Figure 2.6 is that the error function has a minimum value at $\theta = 0$ for any $\mathrm{r_c}$. In addition, an inspection of such plots allows us to address the question of how much departure of $q_1$ from its ideal-case location may be tolerated. Since Figure 2.6 shows the minimum-EVMS value increasing with $\mathrm{r_c}$, we have to set a new limit for all $\mathrm{r_c}$. We suggest that EF should not exceed 3 times the minimum value for all $\mathrm{r_c}$; based on this, we find the range of acceptable values for angular separation to be $|\theta| < 20^{\circ}$ for different $\mathrm{r_c}$. In practice, all three q-points will deviate from their respective ideal-case locations and it is not straightforward to attempt an analytical evaluation of these EVMS deviations when we move from our generic study to consider an actual implementation of a six-port reflectometer system (with hardware imperfections).

## 2.3 Monte Carlo Simulations

In Sections 2.1-2.2, we attempted to derive equations for the variations of EVMS due to the q-point departures from their ideal-case locations. Although we have obtained some useful results in the process, there is a limit to what can be achieved via such an approach. Hence, we shall proceed via computational simulations to obtain empirical results by using the Monte

Carlo procedure (which has already proven to be a very powerful tool for simulating a diversity of other phenomena).

### 2.3.1 Development of simulation software

To perform such computational simulations, we need to choose an appropriate six-port reflectometer set-up that is able to yield q-points known to be located in the regions of interest to our study. We have already reported in [2.12] one such six-port reflectometer set-up which comprises four modified hybrid couplers (which are symmetrical and lossless); details have also been provided in Sub-Section 3.2.1 explaining how scattering analysis has been employed to derive expressions for the three q-points of this six-port reflectometer system. Here we reproduce the expressions we had obtained for the two ratios of the three q-points:

$$\frac{\bar{q}_3}{\bar{q}_1} = \frac{\bar{\gamma}^2 \bar{\Gamma}_2}{\bar{\beta}^2 \bar{\Gamma}_1} \tag{2.25}$$

$$\frac{\bar{q}_2}{\bar{q}_1} = \frac{\bar{\gamma}^2 (\bar{\gamma}\bar{\Gamma}_2 + \bar{\beta}\bar{\Gamma}_1)}{\bar{\alpha}^2 (\bar{\beta} + \bar{\gamma})\bar{\Gamma}_1} = \frac{\bar{\gamma}^2 ((\bar{\beta}/\bar{\gamma})(\bar{q}_3/\bar{q}_1) + 1)}{\bar{\alpha}^2 (1 + \bar{\gamma}/\bar{\beta})} \tag{2.26}$$

For our Monte Carlo simulations, we also need the following expressions for the scattering coefficients of the constituent hybrid couplers:

$$|\bar{\beta}| = |\bar{\gamma}| \tag{2.27}$$

$$|\bar{\beta}|^2 + |\bar{\alpha}|^2 = 1 \tag{2.28}$$

$$2\arg(\bar{\alpha}) = \arg(\bar{\beta}) + \arg(\bar{\gamma}) \pm 180^o \tag{2.29}$$

The substitution of the hybrid coupler's scattering-coefficient expressions from Equations 2.27-2.9 into the six-port reflectometer's q-point ratio expressions of Equations 2.25-2.26 will then yield the following:

$$\frac{\vec{q}_3}{\vec{q}_1} = \frac{\bar{\Gamma}_2}{\bar{\Gamma}_1} e^{j2(\phi_\gamma - \phi_\beta)} \tag{2.30}$$

$$\frac{\vec{q}_2}{\vec{q}_1} = -\left|\frac{\vec{\gamma}}{\bar{\alpha}}\right|^2 \frac{(\vec{q}_3/\vec{q}_1) + e^{j(\phi_\gamma - \phi_\beta)}}{(1 + e^{j(\phi_\gamma - \phi_\beta)})} \tag{2.31}$$

To proceed, we need to choose some appropriate value for $e^{j2(\phi_\gamma - \phi_\beta)}$. After solving Equations 2.30-2.31 for the two q-point ratios, we can then obtain the scattering coefficients of the constituent hybrid couplers from Equations 2.27-2.31 for the design of the six-port reflectometer.

Summarized below are the settings required for our simulation:

(a) We shall presume the six-port reflectometer system to be well-matched and there will thus be zero entries along the diagonal of the overall system's scattering matrix: $S_{ii} = 0$ where $i$ = 1, 2, …, 6. If, in addition, the power detector $P_0$ shown in Figure 3.1 monitors only the input wave entering Port 1, the system equations are then simplified to $K_i\,|\vec{\Gamma} - \vec{q}_i|^2 = p_i$ for $i$ = 1, 2, 3 (where $p_i$ is the ratio of the power-detector reading $P_i$ to the reference power $P_0$).

(b) For the ideal-case six-port system, we note that $K_i = |\bar{S}_{1i}\bar{S}_{2i}|^2$ which thus leads us to presume that $K_i$ = constant for i = 1, 2, 3. This constant was chosen to be 0.07 for our simulations.

(c) We shall presume that $P_0$ = constant (which was chosen to be 1 mW for our simulations). This is not invalid in practice because the reference power-detector reading may be held constant by varying the power delivered from the source or by varying the coupling to the reference power-detector port.

(d) The characteristics of the power detectors may be obtained from the suppliers; for example, the HP4418B power detector is stated in the manufacturer's datasheets to have a relative accuracy of 0.01 (linear) and so the power-detector reading at Port i should be $P_i = P_{i}\_true$ + noise. We may presume the noise to be white Gaussian with standard deviation of $P_{i}\_true * 0.01$.

(e) We have found that 5,000 trials should be sufficient for our Monte Carlo simulations. For each set of q-points, we chose m*n DUT tests (where m is the number of DUT-magnitude variations and n is the number of DUT-phase variations) and the largest of the errors recorded during these m*n tests will be taken to represent the worst-case measurement uncertainties.

Depicted in Figure 2.7 is the flow-chart for our Monte Carlo simulations (based on the afore-mentioned settings) to obtain the worst-case EVMS for each DUT:

#1 define initial parameters: $P_0$, $K_i$ , ε (relative accuracy of power meter), N (trial number); input simulation parameters: $\overline{\Gamma}_{DUT}$, q-point locations

#2 calculate true values for $P_i$; then add white Gaussian noise to $P_0$ and $P_i$: $P_i^{'} = P_i + \Delta P_i$;

$$\sigma(P_i) = \varepsilon P_i$$

#3 treat noise-corrupted readings $P_i'$ as data which would have been obtained during an actual experiment and thus calculate the DUT's reflection coefficient $\vec{\Gamma}'_{DUT}$ and measurement error vector $\vec{\Gamma}_{DUT} - \vec{\Gamma}'_{DUT}$

#4 repeat step #2 and step #3 for N = 5,000 trials

#5 compute mean and standard deviation of error vector magnitude: $|\vec{\Gamma}_{DUT} - \vec{\Gamma}'_{DUT}|$

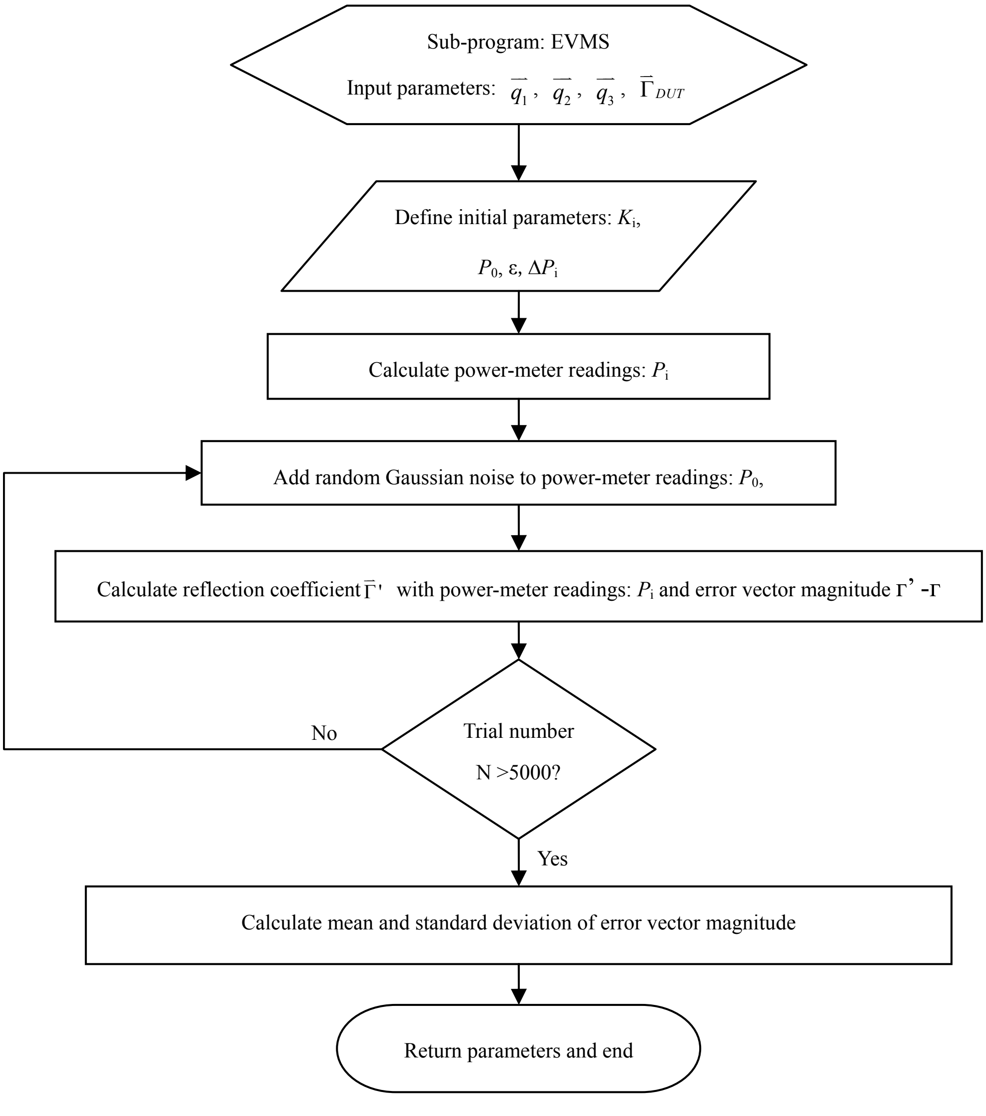

Figure 2.7 Flow-chart outlining Monte Carlo simulation process for specified DUT and q-point set

### 2.3.2 Variation of q-point magnitudes

To collect statistics on the q-point magnitude variations, we set the angular separations of the q-point locations to be $0^{o}$, $120^{o}$, $240^{o}$ while we vary the three q-point magnitudes (which are taken to be equal) over the range from 0.1 to 5 (in steps of 0.1). We also include a selection of DUTs in the simulations by varying $\vec{\Gamma}_{DUT}$ in the following manner:

- the magnitude of $\vec{\Gamma}_{DUT}$ has been systematically incremented (in steps of 0.1) from 0.1 to 1
- the phase of $\vec{\Gamma}_{DUT}$ has been systematically incremented (in steps of $\pi/6$) from 0 to $11\pi/6$.

The process outlined in Figure 2.7 allows us to compile statistics on the measurement inaccuracies that may be expected if 5,000 experiments had been performed repetitively in the laboratory for each choice of DUT. The flow-chart depicted in Figure 2.8 is then used to process the statistics to find the range of q-point magnitudes that may be regarded as acceptable given the maximum EVMS to be tolerated.

The Monte Carlo simulation results presented in Figure 2.9 show that the EVMS plot has a minimum at $|\vec{q}_i| \approx 1$. Since the EVMS plot does not have a sharp minimum point, we are allowed to choose a range of permissible values for the q-point magnitudes. Based on the tolerance criteria adopted earlier, we suggest $0.32 < |\vec{q}_i| < 3.2$ to be a suitable range. For comparison, we also plot in Figure 2.9 the results predicted by Equation 2.19 (with n = 3 and ε = 0.01). As expected, the recommendations offered by the two plots in Figure 2.9 are not dissimilar.

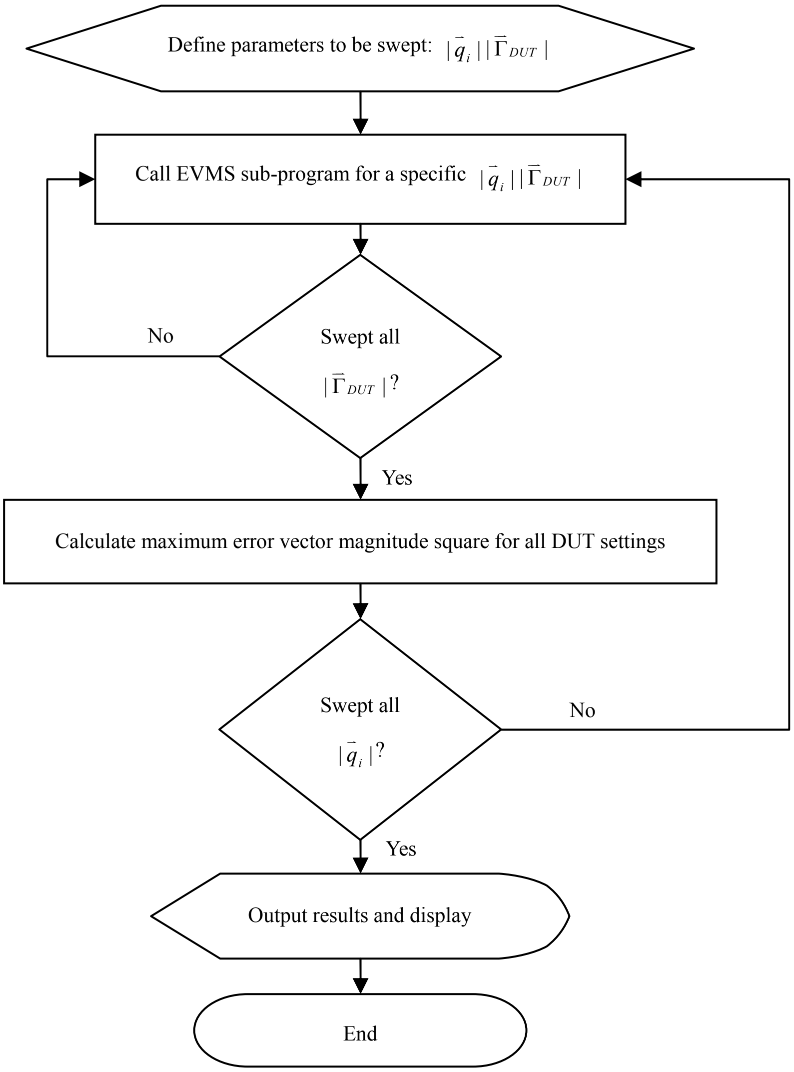

Figure 2.8 Flow-chart to search for acceptable range of q-point magnitudes

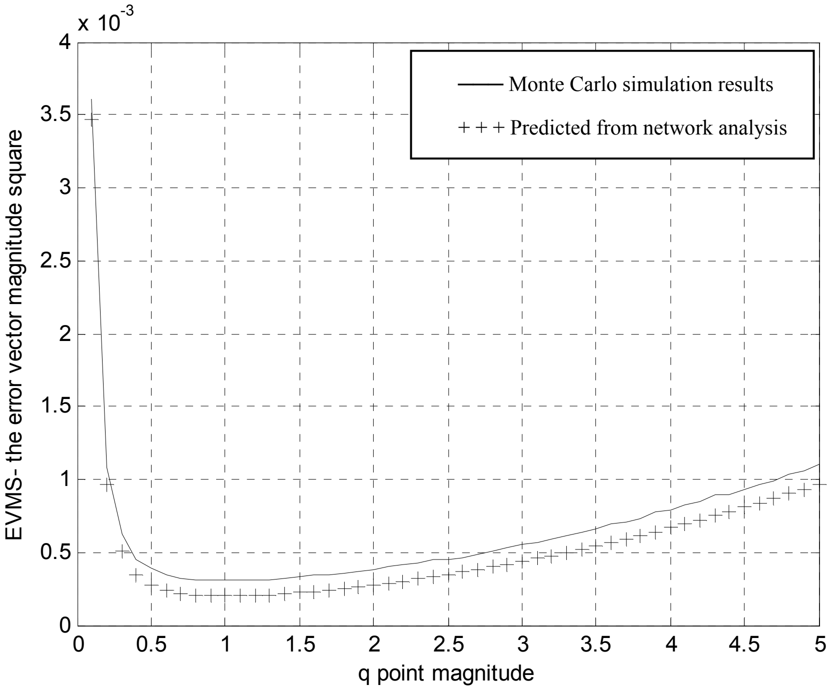

Figure 2.9 Monte Carlo simulation results depicting variation of EVMS with q-point magnitude

### 2.3.3 Variation of q-point angular separations

The same process is duplicated to search for the range of acceptable values for the angular separations of q-points. To collect statistics on the angular-separation variations, we set the three q-point magnitudes to be 1.5 while their angular coordinates are taken to be 0, $\theta$ and $\Phi$ where the latter two angles are swept over $\pi/3 < \theta < \pi$ and $\pi < \Phi < 5\pi/3$ respectively. The statistics compiled during the Monte Carlo simulations are then processed in accordance with the flow-chart depicted in Figure 2.10.

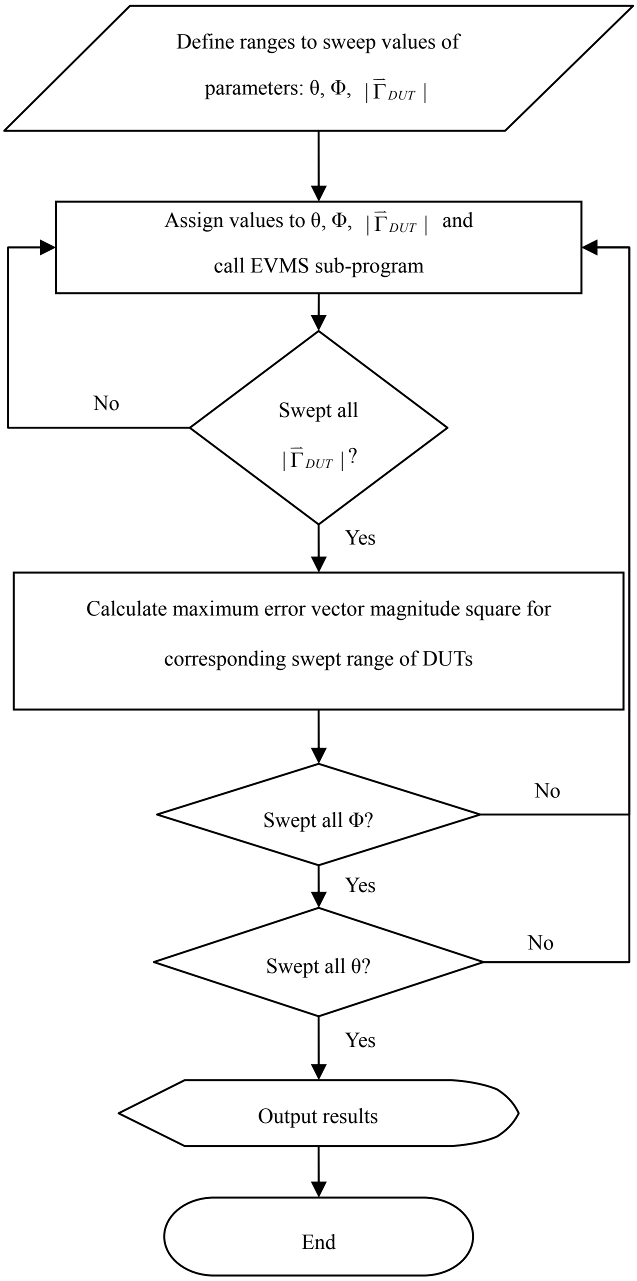

Figure 2.10 Flow-chart to search for acceptable range of q-point angular separations

The Monte Carlo results we thus obtained are presented as a two-dimensional surface in Figure 2.11(a) with the axes representing θ, Φ and EVMS. As expected, the minimum of the surface occurs at $\theta = \Phi = 120^{\circ}$. We shall set the EVMS limit as twice the minimum value. If two of the three q-points do not stray from their respective ideal-case locations, Figure 2.11(b) indicates that the angular coordinate of the remaining q-point may have a maximum range of approximately 40°. If only one q-point stays at its ideal-case location, Figure 2.11(c) shows each constant-EVMS locus as an approximate circle enclosing the ideal-case location and we recommend the following rough-and-ready limit to be imposed on the range of acceptable values for the angular separations of q-points:

$$(\arg(\vec{q}_2/\vec{q}_1))^2 + (\arg(\vec{q}_3/\vec{q}_2))^2 < C_{phase} \tag{2.32}$$

where we choose $C_{\text{phase}} \approx 0.7$ after an inspection of our Monte Carlo results.

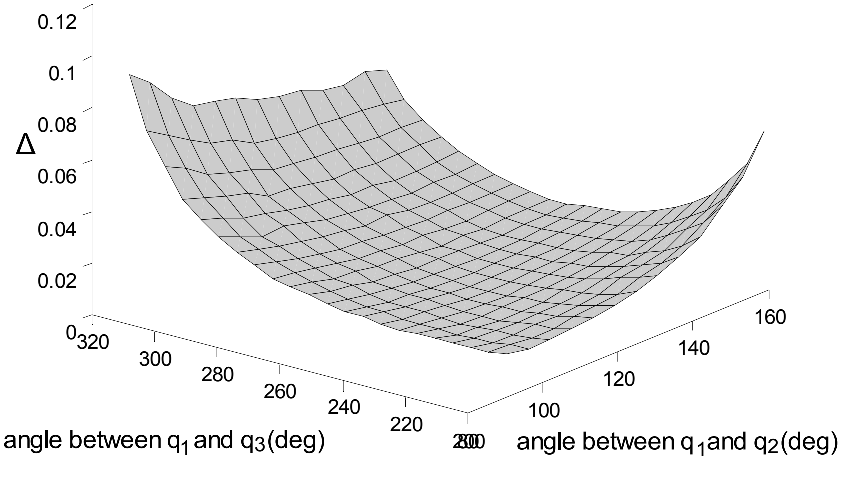

(a) Variation of EVMS with angular coordinates θ and Φ of two q-points where $r_c = 1.5$

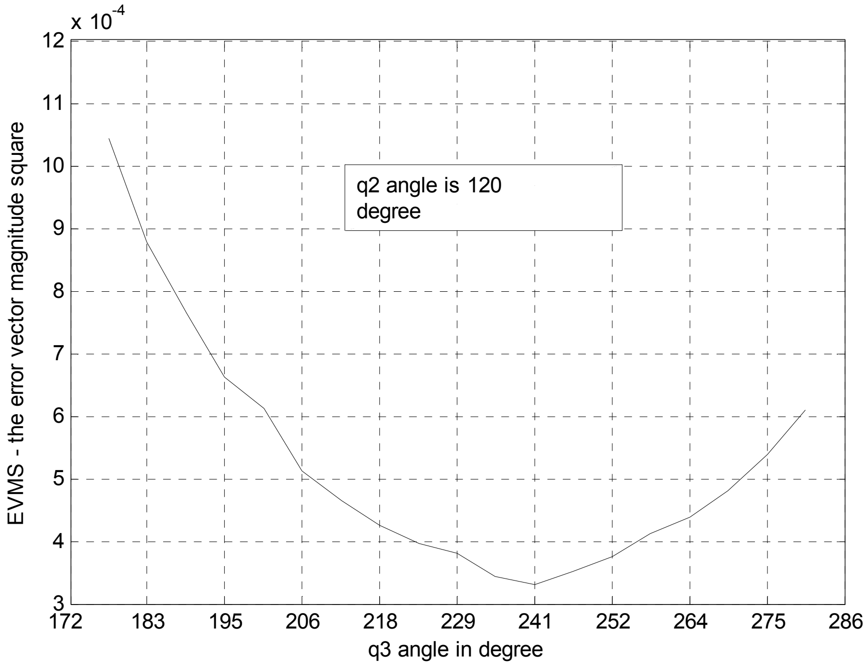

(b) Variation of EVMS with angular coordinate Φ of one q-point where $\theta = 120^{\circ}$ and $r_c = 1.5$

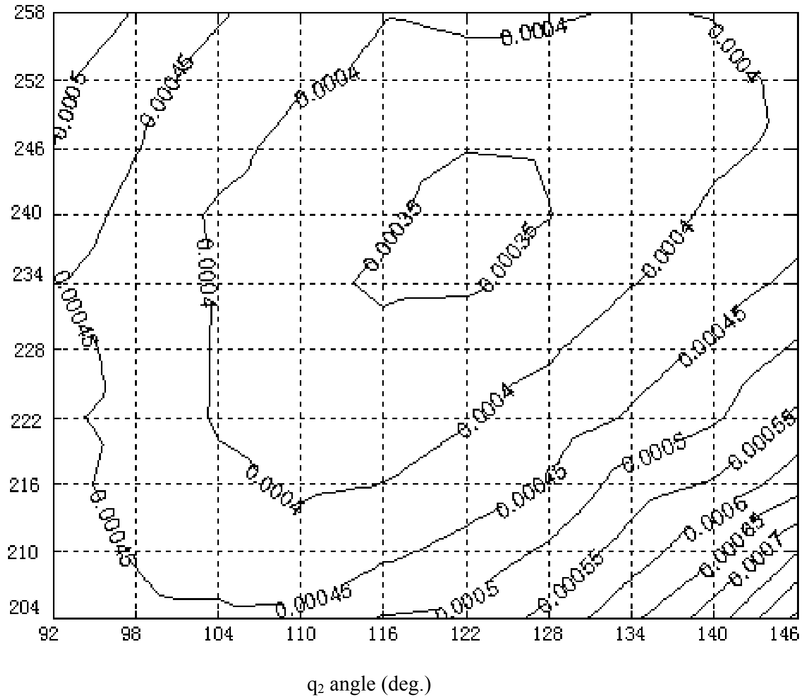

(c) Equi-EVMS contours for simulation results presented in (a) and (b)

Figure 2.11 Monte Carlo results for case study involving six-port reflectometer based on modified hybrid couplers

### 2.3.4 Other q-point variation scenarios

Another six-port reflectometer set-up we have chosen for inclusion in our Monte Carlo simulations comprises a symmetrical five-port junction together with a directional coupler to provide the additional sixth port. As explained by Cullen and Yeo [2.11], it is possible to study different q-point behavior patterns by simply changing the arrangement for connecting the symmetrical five-port junction with the directional coupler. Another useful feature is that we need to monitor only one scattering coefficient during the simulations because the analysis outlined in [2.11] has shown that the overall behavior of this six-port reflectometer system is essentially dependent on the residual mismatch of the symmetrical five-port junction. As an illustration, we reproduce in Figure 2.12(a) two of the configurations reported in [2.11] with their respective q-points depicted in Figure 2.12(b) as loci enclosing the ideal-case locations at $2\angle 0^{\circ}$, $2\angle 120^{\circ}$ and $2\angle 240^{\circ}$.

If the symmetrical five-port junction's scattering coefficients are denoted by $\eta$, $\mu$ and $\nu$ (where $\eta$ is the reflection coefficient looking into any port of the symmetrical five-port junction when the remaining four ports are terminated in matched loads and where $\mu$ and $\nu$ are the transmission coefficients between the adjacent and non-adjacent ports respectively) and the directional coupler's transmission coefficient is denoted by t, it has been shown [2.11] that the q-point expressions for the two six-port reflectometer configurations depicted in Figure 2.12(a) may be written in the following manner:

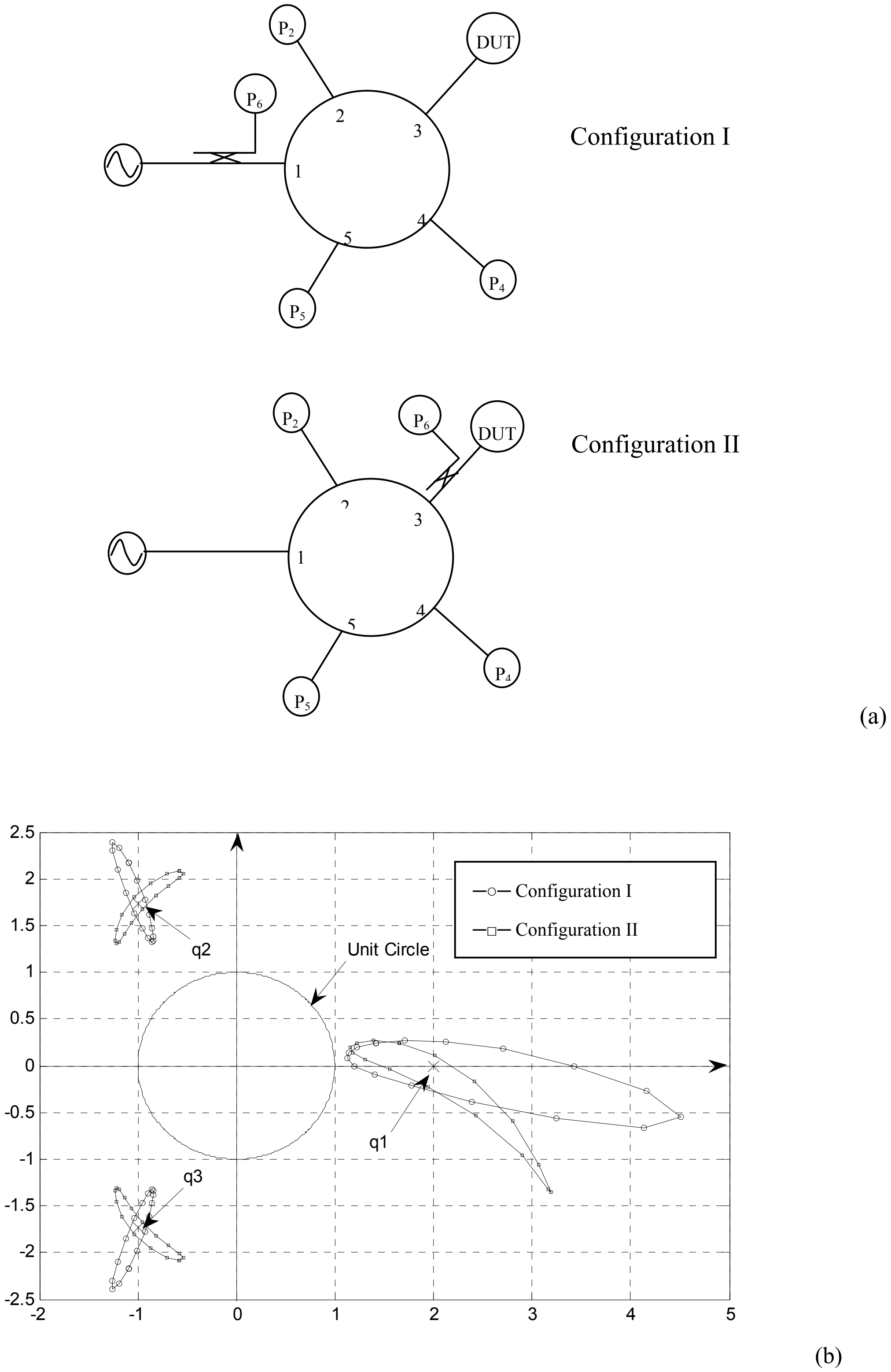

Figure 2.12 Plots reproduced from [2.11] for six-port reflectometer based on symmetrical five-port coupler with residual mismatch given by $\eta = 0.1 \exp(j\Phi_\eta)$

(a) two possible configurations

(b) locus tracing q-points for each configuration due to symmetrical five-port coupler's mismatch for Configuration I:

$$\vec{q}_1 = \frac{\bar{\rho}_1\eta^* - |\mu^2|(\eta - \nu^2/\mu)^*}{\bar{\rho}_1|\eta^2| - |\mu^2||(\eta - \nu^2/\mu)|^2} \tag{2.33a}$$

$$\vec{q}_2 = \frac{\bar{\rho}_2\eta^* - |\mu^2|(\eta - \nu)^*}{\bar{\rho}_2|\eta^2| - |\mu^2||(\eta - \nu)|^2} \tag{2.33b}$$

$$\vec{q}_3 = \frac{\bar{\rho}_3\eta^* - |\nu^2|(\eta - \mu)^*}{\bar{\rho}_3|\eta^2| - |\nu^2||(\eta - \mu)|^2} \tag{2.33c}$$

for Configuration II:

$$\vec{q}_1 = \frac{1}{t^2(\eta - \nu^2/\mu)} \tag{2.34a}$$

$$\vec{q}_2 = \frac{1}{t^2(\eta - \nu)} \tag{2.34b}$$

$$\vec{q}_3 = \frac{1}{t^2(\eta - \mu)} \tag{2.34c}$$

We infer from Equation 2.34 that the q-point magnitudes for Configuration II are related to the transmission coefficient t of the directional coupler. For a directional coupler with -20dB coupling, we need to substitute $1/t^2 = 1.01$ into Equation 2.34 and the three q-points of Configuration II will have ideal-case magnitudes of $|\vec{q}_i| = 2$. The EVMS results we compiled during the Monte Carlo simulations (where the process is based on the flow-chart shown in Figure 2.10) are presented as a two-dimensional surface in Figure 2.13(a).

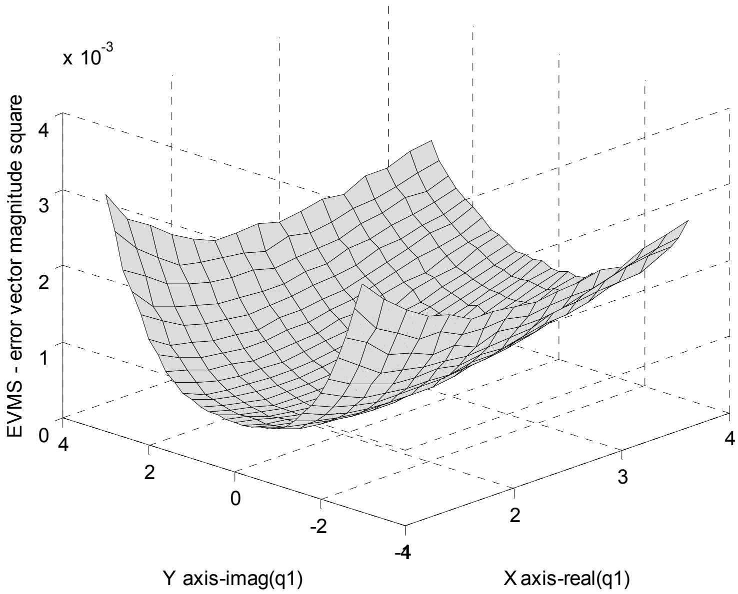

(a) Variation of EVMS with location of $q_1$

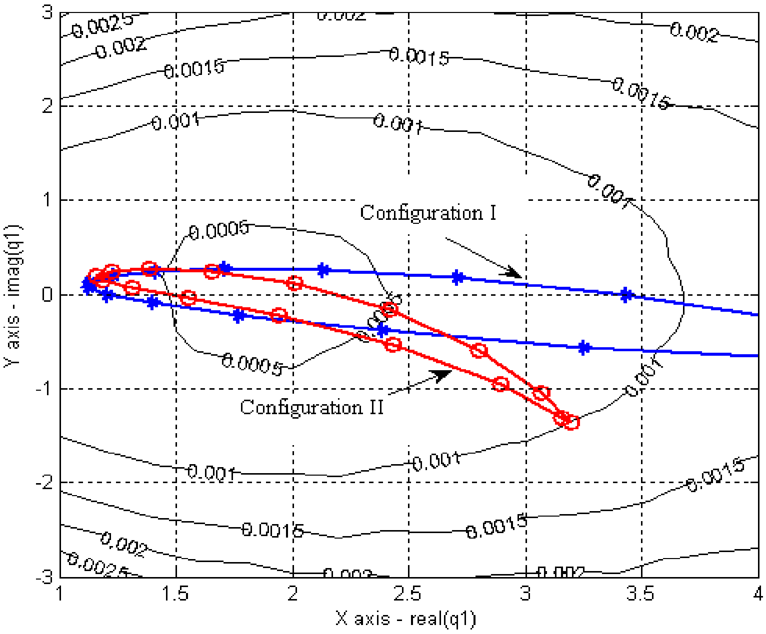

(b) Equi-EVMS contours together with q-point loci of Figure 2.12(b)

Figure 2.13 Monte Carlo results for case study involving six-port reflectometer based on symmetrical five-port coupler and directional coupler

We infer from the equi-EVMS contours and q-point loci presented together in Figure 2.13(b) that Configuration II (with worst-case EVMS of 0.001) is preferred to Configuration I (with worst-case EVMS of 0.0025) in terms of overall measurement accuracy. Our findings (based on the results we compiled from the Monte Carlo simulations) affirm what Cullen and Yeo reported in [2.11].

In addition, there are other six-port reflectometer set-ups (such as those reported in [2.13]-[2.14]) to be included in our simulation study. The q-point variations to be studied may be summarized thus**:**

#A Given that two of the q-points have equal magnitudes of, say, 1.5 ($|\vec{q}_2| = |\vec{q}_3| = 1.5$) and that the remaining q-point lies on the real axis ($\angle\vec{q}_1 = 0^{\circ}$), what will be the optimum angular separation for $\vec{q}_2$ and $\vec{q}_3$ if we vary the magnitude of $\vec{q}_1$? The scenario for Question #A is schematically portrayed in Figure 2.14(a).

#B Given that two of the q-points have equal angular displacements of, say, 45° from the real axis ($\angle\vec{q}_2 = -\angle\vec{q}_3 = 135^{\circ}$) and that the remaining q-point has a fixed location on the real axis ($\vec{q}_1 = 1.5\ \angle 0^{\circ}$), what will be the optimum magnitudes for $\vec{q}_2$ and $\vec{q}_3$? The scenario for Question #B is schematically portrayed in Figure 2.14(b).

#C Question #B is repeated except for a change of angular displacements: $\angle\vec{q}_2 = -\angle\vec{q}_3 = 90^{\circ}$ with $\angle\vec{q}_1 = 0^{\circ}$. The scenario for Question #C is schematically portrayed in Figure 2.14(c).

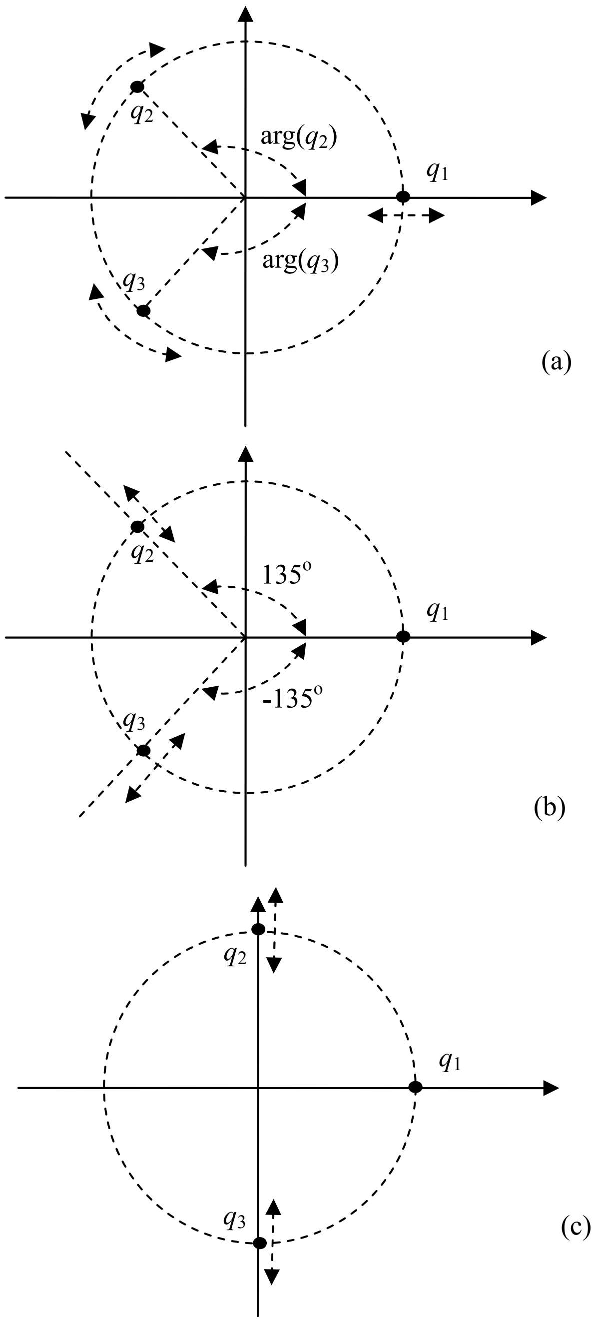

Figure 2.14 Schematic representations of q-point variation scenarios included in Monte Carlo simulation studies

(a) for $|\vec{q}_2| = |\vec{q}_3| = 1.5$, $\angle\vec{q}_1 = 0^{\circ}$, find optimum angular separation of $\vec{q}_2$ and $\vec{q}_3$ when varying magnitude of $\vec{q}_1$

(b) for $\angle\vec{q}_1 = 0^{\circ}$, $\angle\vec{q}_2 = 135^{\circ}$, $\angle\vec{q}_3 = -135^{\circ}$, $|\vec{q}_1| = 1.5$, find optimum magnitude of $\vec{q}_2$ and $\vec{q}_3$

(c) for $\angle\vec{q}_1 = 0^{\circ}$, $\angle\vec{q}_2 = 90^{\circ}$, $\angle\vec{q}_3 = -90^{\circ}$, $|\vec{q}_1| = 1.5$, find optimum magnitude of $\vec{q}_2$ and $\vec{q}_3$ ;

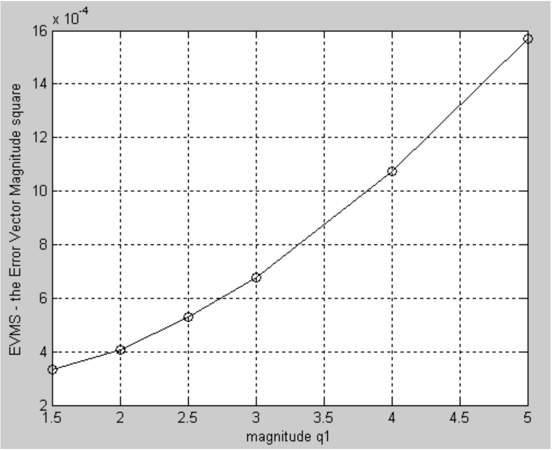

(a) Variation of minimum-EVMS value with $q_1$ magnitude

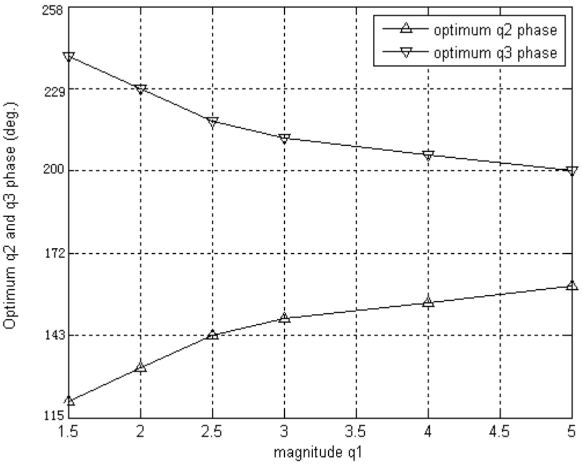

(b) Variations of $q_2$ and $q_3$ phases with $q_1$ magnitude

Figure 2.15 Monte Carlo simulation results for scenario depicted in Figure 2.14(a)

For Question #A, we need to determine where $\vec{q}_2$ and $\vec{q}_3$ ought to be located so as to minimize the EVMS for a particular location of $\vec{q}_1$ on the real axis. Figure 2.15 presents the results we obtained from Monte Carlo simulations for this particular scenario. From Figure 2.15(a) which depicts how the minimum-EVMS value will vary as we move $\vec{q}_1$ towards the right along the real axis, the obvious conclusion is that we should leave $\vec{q}_1$ at its original location because any shift will cause the minimum-EVMS value to increase. In Figure 2.15(b), we observe that the resulting angular separation of $\vec{q}_2$ and $\vec{q}_3$ decreases as we increase the magnitude of $\vec{q}_1$; in other words, $\vec{q}_2$ and $\vec{q}_3$ will move towards each other along the r = 1.5 circle circumference as we move $\vec{q}_1$ towards the right along the real axis. In fact, $\vec{q}_2$ and $\vec{q}_3$ will eventually come near to each other and we anticipate severe deterioration of measurement accuracies when $\vec{q}_2$ = $\vec{q}_3$ = -1.5 as may be inferred from Figure 2.15(a). If we choose the tolerance limit to be twice the lowest value, we may then conclude from the plot in Figure 2.15(a) that the magnitude of $\vec{q}_1$ should not be allowed to exceed 3.

The results obtained from the Monte Carlo simulations we performed to investigate the scenarios portrayed in Questions #B and #C are presented in Figures 2.16(a) and 2.16(b) respectively. For the scenario where $\angle\vec{q}_2 = -\angle\vec{q}_3$ = 135°, the plot in Figure 2.16(a) has a minimum when $|\vec{q}_2| = |\vec{q}_3| = 1$. After another round of simulations to consider the other scenario where $\angle\vec{q}_2 = -\angle\vec{q}_3$ = 90°, we observe that the plot in Figure 2.16(b) yields a minimum at $|\vec{q}_2| = |\vec{q}_3| = 1.45$ instead. Engen [2.1] inferred from symmetry considerations that the three q-points ought to have the same magnitude when they have the same angular separation of 120°. When their angular separations are not 120°, however, it is clear from the two scenarios we considered in Figure 2.16 that $\vec{q}_2$ and $\vec{q}_3$ need not have the same magnitude as $\vec{q}_1$.

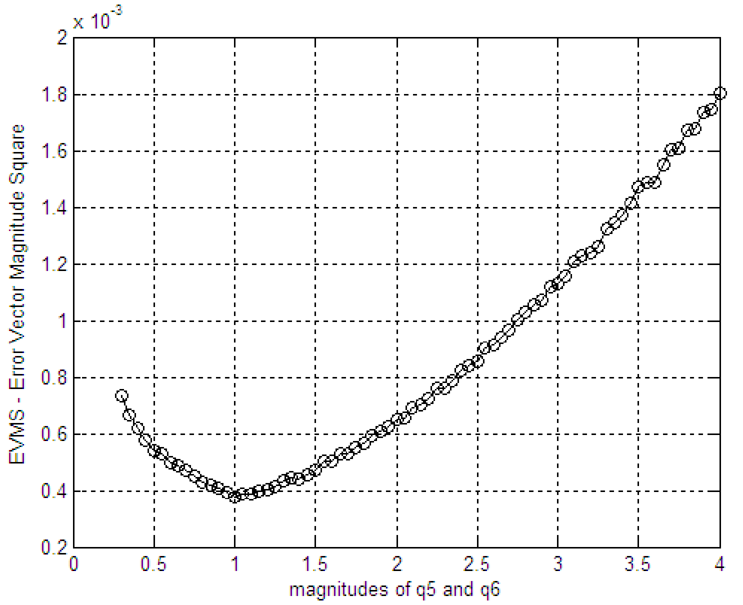

(a) Contour of EVMS ($|\vec{q}_2|, |\vec{q}_3|$) for $\angle\vec{q}_2 = -\angle\vec{q}_3 = -135^\circ$ and $\vec{q}_1 = 1.5 \angle 0^\circ$

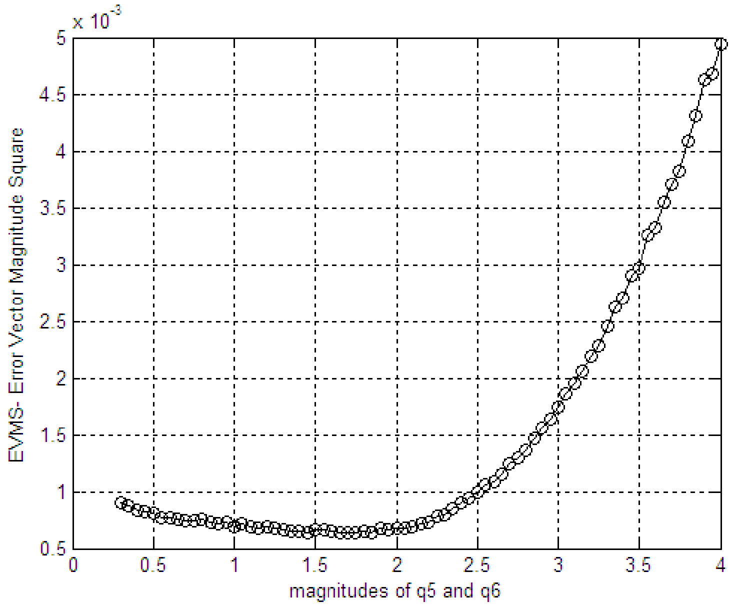

(b) Contour of EVMS ($|\vec{q}_2|, |\vec{q}_3|$) for $\angle\vec{q}_2 = -\angle\vec{q}_3 = 90^\circ$ and $\vec{q}_1 = 1.5 \angle 0^\circ$

Figure 2.16 Monte Carlo simulation results for scenarios depicted in Figures 2.14(b) and 2.14(c)

### 2.3.5 Actual q-point variations of prototype six-port reflectometer tested in Section 6.3

It should additionally be interesting to perform the Monte Carlo simulation tests based on the q-point variations of an actual six-port reflectometer. Of the three prototype six-port reflectometers we developed and tested in Chapter 6, we arbitrarily picked the one reported in Section 6.3 for these Monte Carlo computations. Having measured the system parameters of the microstrip-based six-port reflectometer depicted in Figure 6.12, we then calculated the $K_i$, $\bar{q}_i$ (for i = 1, 2, 3) and $\bar{B}_6$ at all of the test frequencies listed in Table 2.1.

TABLE 2.1

CALCULATED KEY PARAMETERS OF A REAL REFLECTOMETER BUILT IN CHAPTER 6

| Frequency | $q_1$ | | $q_2$ | | $q_3$ | | | | | |
|---|---|---|---|---|---|---|---|---|---|---|
| (GHz) | mag | arg | mag | arg | mag | arg | $k_1$ | $k_2$ | $k_3$ | $B_6$ |
| 2.0 | 1.06 | -63.1 | 1.20 | -102.1 | 1.24 | -68.3 | 0.41 | 0.13 | 1.50 | 1.12 |
| 2.1 | 1.03 | 5.5 | 4.04 | -59.8 | 1.21 | -22.7 | 0.47 | 0.02 | 1.43 | 1.22 |
| 2.2 | 1.72 | 92.62 | 3.04 | -85.77 | 0.99 | 35.20 | 0.18 | 0.03 | 0.32 | 2.59 |
| 2.3 | 2.32 | 159.71 | 3.39 | -53.40 | 1.12 | 59.79 | 0.09 | 0.03 | 0.13 | 4.99 |
| 2.4 | 2.01 | -140.22 | 2.77 | -33.64 | 1.98 | 96.03 | 0.10 | 0.06 | 0.12 | 12.61 |
| 2.5 | 1.93 | -86.24 | 2.18 | 11.29 | 2.39 | 144.54 | 0.10 | 0.09 | 0.12 | 27.80 |
| 2.6 | 2.06 | -45.41 | 2.13 | 63.04 | 2.22 | -170.76 | 0.07 | 0.07 | 0.12 | 41.64 |
| 2.7 | 2.09 | -12.11 | 2.26 | 108.64 | 1.94 | -136.98 | 0.06 | 0.06 | 0.13 | 38.26 |
| 2.8 | 2.06 | 20.01 | 2.31 | 150.55 | 1.91 | -102.72 | 0.06 | 0.06 | 0.15 | 21.99 |
| 2.9 | 1.93 | 52.09 | 2.53 | -169.82 | 2.01 | -58.37 | 0.06 | 0.05 | 0.17 | 11.97 |
| 3.0 | 1.75 | 93.62 | 2.72 | -138.10 | 2.09 | -10.91 | 0.07 | 0.05 | 0.17 | 10.35 |
| 3.1 | 1.83 | 145.98 | 2.39 | -103.57 | 2.17 | 31.67 | 0.08 | 0.07 | 0.15 | 21.00 |
| 3.2 | 2.28 | -160.54 | 2.06 | -55.18 | 2.28 | 67.99 | 0.05 | 0.08 | 0.12 | 25.81 |
| 3.3 | 2.65 | -113.74 | 2.09 | -4.35 | 2.39 | 105.71 | 0.04 | 0.07 | 0.10 | 13.08 |
| 3.4 | 2.43 | -66.17 | 2.22 | 40.23 | 2.42 | 151.17 | 0.05 | 0.06 | 0.09 | 18.25 |
| 3.5 | 2.34 | -18.55 | 2.35 | 91.25 | 2.45 | -158.11 | 0.06 | 0.05 | 0.09 | 35.72 |
| 3.6 | 2.22 | 10.06 | 3.85 | 161.72 | 2.74 | -93.55 | 0.05 | 0.02 | 0.15 | 8.75 |
| 3.7 | 1.50 | 52.39 | 17.47 | 157.82 | 2.60 | -26.37 | 0.07 | 0.00 | 0.54 | 4.18 |
| 3.8 | 1.63 | 143.32 | 2.41 | 167.81 | 2.92 | 15.78 | 0.09 | 0.04 | 0.73 | 74.35 |

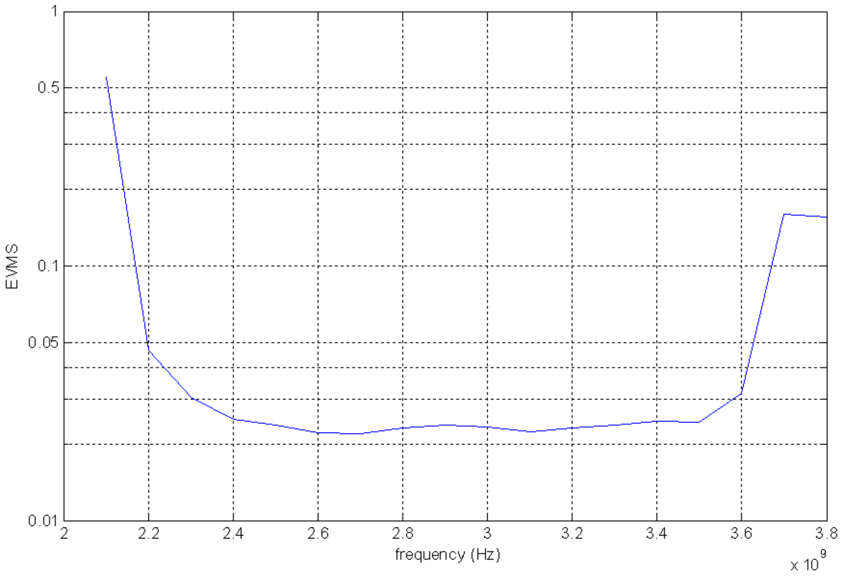

Figure 2.17 Monte Carlo simulation results depicting variation of EVMS with frequency for prototype six-port reflectometer developed and tested in Section 6.3

The variations of the q-points' magnitudes and angular separations for this prototype six-port reflectometer are also available from Figures 6.13-6.14 (in Section 6.3). We note from Table 2.1 that the magnitudes of $\vec{q}_1$, $\vec{q}_2$ and $\vec{q}_3$ lie in the range from 1 to 3 and their angular separations are in the range from 100° to 150° over the operating bandwidth from 2.4GHz to 3.5GHz. The Monte Carlo simulation results presented in Figure 2.9 confirm that there is a broad dip in EVMS over the 2.4-3.5GHz frequency range. However, we can expect the measurement accuracies to deteriorate outside the operating bandwidth in view of the EVMS plot rising sharply in the vicinity of 2.3GHz and 3.6GHz.

## 2.4 Pilot Design of N-Port Reflectometer

Although we started by considering the generic N-port network in Section 2.1, we subsequently studied the optimum design criteria specifically for the six-port network in Sections 2.2-2.3 because of the overriding focus in Chapters 3-6 on our objective of developing six-port reflectometers based on modified four-port couplers. As a brief digression before concluding Chapter 2, we should take the opportunity to extend beyond our six-port network analysis in Sections 2.2-2.3 to additionally explore the design of a prototype N-port reflectometer with the capability of yielding optimum measurement performance.

For the ideal-case N-port reflectometer discussed in Section 2.1, we may derive the following expression for each of the q-points:

$$\vec{q}_i = -\vec{S}_{i1} / (\vec{S}_{12} \vec{S}_{i2}) \tag{2.35}$$

with $S_{ii} = 0$ (for i = 1, 2, …, N) and $S_{DUT\_0} = 0$ (between the DUT port and the source-power monitoring port as shown in Figure 2.17). Inferring from Equation 2.29 that the behavior of such a q-point should be primarily dependent on $\vec{S}_{i1}$ and $\vec{S}_{i2}$, we may then propose the general circuit sketched in Figure 2.17 for the N-port reflectometer with optimum measurement performance.

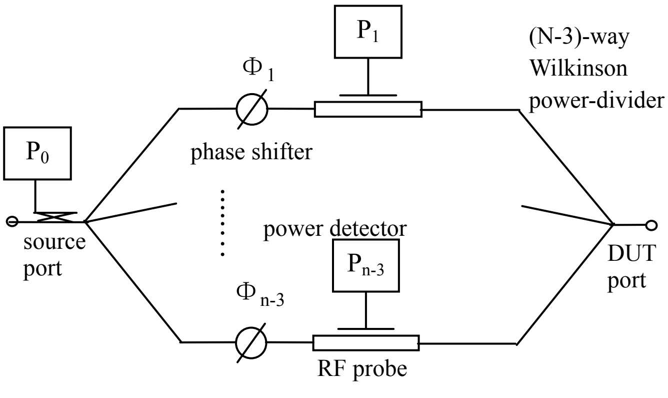

Figure 2.17 Schematic circuit for N-port reflectometer

A (N-3)-way Wilkinson divider is employed in Figure 2.17 to divide the power from the source equally. Included in each of the N-3 arms are a phase-shifter (to provide the requisite level of phase shift) and a RF probe (to provide the power reading). The signals in the N-3 arms are re-combined before the DUT port. There is also a directional coupler with power detector $P_0$ at the source port to monitor the input wave feeding the N-3 arms. For this design, we can readily adjust the magnitude and phase of each q-point (by tuning the associated ratio $\overline{S}_{i1} / \overline{S}_{i2}$ and phase-shift $\Phi_k$ respectively) since the isolation property of the Wilkinson divider allows us to assume that any adjustment performed in one arm does not unduly affect the waves traveling in the other arms.

Since other researchers [2.15]-[2.17] have already reported six-port and seven-port reflectometers yielding optimum measurement performance, we shall choose to implement an eight-port reflectometer for our pilot design based on the N-port network outlined in Figure 2.17. Before proceeding to do so, we need to design the following constituent components at 4GHz (fabricated on Rogers 6010LM substrate with thickness of 50mil, relative permittivity of 10.2 and loss tangent of 0.0023)**:**

(a) The five-way Wilkinson structure is relatively difficult to fabricate as a single component because of the high characteristic impedance of 110Ω required for each of its five arms. A simpler alternative is for us to resort to a composite design comprising four two-way Wilkinson structures (with $Z_{even}$ = 60Ω, $Z_{odd}$ = 42Ω and C =

-15dB) inter-connected as shown in Figure 2.18 so as to perform the five-way power division/combination. The additional lengths of transmission line to be included in the paths numbered 3, 4 and 5 are for phase compensation purposes.

(b) The phase shifters are implemented by inserting the associated transmission-line lengths to introduce the requisite phase delays of 144° and 72° in the paths numbered 4 and 5 respectively. Another possibility is to use lumped components in order to reduce the overall circuit dimensions.

(c) The main function of each RF probe is to detect the forward- and backward-propagating signals. Our design in Figure 2.19 employs two cascaded 90° microstrip coupling line (with $Z_{even} = 67.5\ \Omega$ and $Z_{odd} = 37.5\Omega$). The power detectors placed in the middle of the coupler may be shifted to the left or right so as to adjust the probe ratio $\overline{S}_{i1} / \overline{S}_{i2}$ when fine-tuning the q-point magnitudes.

Depicted in Figure 2.20 is the lay-out for our prototype eight-port reflectometer. For the purpose of calibration based on Hunter and Somlo's procedure [2.10] outlined in Sub-Section 6.1.1(b), our composite reflectometer may be regarded as two six-port reflectometers where the first six-port reflectometer comprises paths 1, 2 and 3 while the second six-port reflectometer comprises paths 3, 4 and 5. Since path 3 is common to both six-port reflectometers, the composite processing of the power readings will yield two sets of values for the parameters associated with this particular path; there is actually not much difference expected for path 3's two sets of parameter values which we simply averaged when computing the q-point results presented in Table 2.2. Even for this rudimentary design (without any special refinements), there is reasonably acceptable correspondence between the predicted and measured results for the tests we conducted on this narrow-band eight-port reflectometer as part of our pilot study.

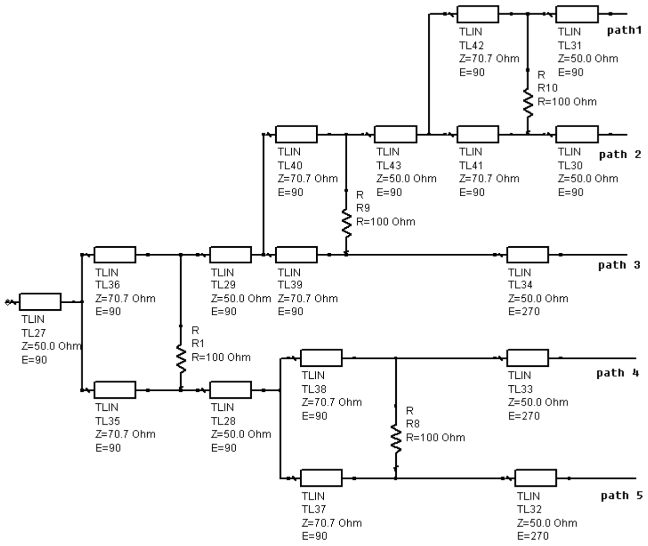

(a) schematic circuit

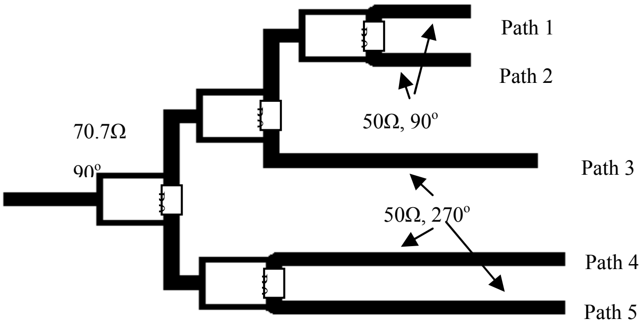

(b) lay-out implementation (with $R_0 = 100\Omega$)

Figure 2.18 Wilkinson divider for use in eight-port reflectometer (Figure 2.20)

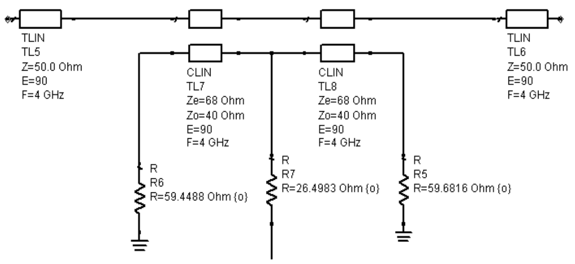

(a) schematic circuit (with $R_1 = 60\Omega$ and $R_2 = 26\Omega$)

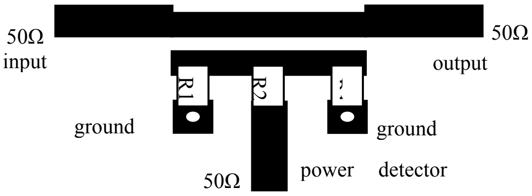

(a) lay-out implementation (with $R_1 = 60\Omega$ and $R_2 = 26\Omega$)

Figure 2.19 RF probe for use in eight-port reflectometer (Figure 2.20)

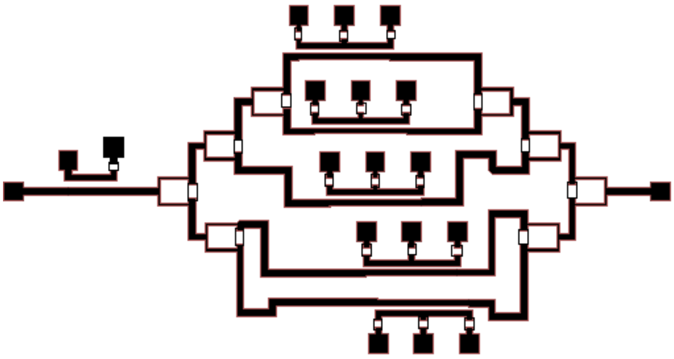

Figure 2.20 Eight-port reflectometer (with details of components provided in Figures 2.18-2.19)

TABLE 2.2 RESULTS FOR Q-POINTS OF EIGHT-PORT REFLECTOMETER (FIGURE 2.20) AT 4GHZ

| path number | Simulations [2.10] | | Measurements | |
|---|---|---|---|---|
| | magnitude | phase | magnitude | phase |
| 1 | 1.71 | $11.5^{0}$ | 1.70 | $5.5^{0}$ |
| 2 | 1.71 | $-59^{0}$ | 1.90 | $-61.5^{0}$ |
| 3 | 1.88 | $82.5^{0}$ | 1.95 | $75^{0}$ |
| 4 | 1.88 | $155^{0}$ | 1.96 | $157^{0}$ |
| 5 | 1.88 | $-131^{0}$ | 1.62 | $-138^{0}$ |

## REFERENCES

[2.1] G.F. Engen, “A (historical) review of the six-port measurement technique,” IEEE Trans. Microwave Theory Tech., vol. 45, pp. 2414-2417, Dec. 1997

[2.2] P.J. Probert and J.E. Carroll, “Design features of multi-port reflectometer”, Proc. Inst. Elec. Eng., pt. H, vol. 129, pp. 245-252, Oct. 1982

[2.3] E.J. Griffin, “Six-port reflectometer circuit comprising three directional couplers”, Electronics Letts., vol. 18, pp. 491-493, Jun. 1982

[2.4] F.M. Ghannouchi, “A comparative worst case error analysis of some proposed six port designs”, IEEE Trans. Microwave Theory Tech., vol 37, Dec. 1988

[2.5] G. Hjipieris, “A millimeter wave six-port reflectometer using dielectric waveguide,” IEEE Trans. Microwave Theory Tech., vol. 38, pp. 54-61, Jan. 1990

[2.6] S.K. Judah, “Planar symmetrical six-port junction,” Proc. Inst. Elec. Eng., pt. H, vol. 134, pp.109-115, Apr. 1987

[2.7] S. Tatu, “Ka-band analog front end for software defined direct conversion receiver,” IEEE Trans. Microwave Theory Tech, vol. 53, pp. 2768-2776, Sep. 2005

[2.8] J. Hesselbarth, “Two new six-port reflectometers covering very large bandwidth”, IEEE Trans. Microwave Theory Tech., vol. 46, pp. 966-969, Aug. 1997

[2.9] H. Cronson, “A 94GHz diode-based single six-port reflectometer,” IEEE Trans. Microwave Theory Tech., vol. 30, pp. 1260-1264, Aug. 1982

[2.10] P. Somlo, Microwave Impedance Measurement (Peregrinus, 1985), pp. 192-193

[2.11] A.L. Cullen and S.P. Yeo, “Six-port reflectometer theory for symmetrical five-port junction with directional coupler”, Proc. Inst. Elec. Eng., vol 133, pt. H, pp. 277-287, Aug. 1986

[2.12] J.J. Yao, Y. Chen and S.P. Yeo, “Modifying hybrid coupler to enhance six-port reflectometer performance,” European Microwave Conf., pp. 256-259, Oct. 2005

[2.13] G.F. Engen, “An improved circuit for implementing the six-port technique of microwave measurement”, IEEE Trans. Microwave Theory Tech., vol. 25, pp. 1080-1083, Dec. 1977

[2.14] J. Juroshek, “A dual six-port network analyzer using diode detectors”, IEEE Trans. Microwave Theory Tech., vol. 32, pp. 78-82, Jan. 1984

[2.15] G. Hjipieris, “A millimeter wave six-port reflectometer using dielectric waveguide,” IEEE Trans. Microwave Theory Tech., vol. 38, pp. 54-61, Jan. 1990

[2.16] S.K. Judah, “Planar symmetrical six-port junction,” Proc. Inst. Elec. Eng., pt. H, vol. 134, pp.109-115, Apr. 1987

[2.17] S. Tatu, “Ka-band analog front end for software defined direct conversion receiver,” IEEE Trans Microwave Theory Tech, vol. 53, pp. 2768-2776, Sep. 2005

# Chapter 3

# ANALYSIS OF SIX-PORT REFLECTOMETER BASED ON FOUR-PORT COUPLERS

Four-port couplers (*eg* hybrid and quadrature couplers) are commonly used as the building blocks for constructing six-port reflectometers (such as those reported in [3.1]-[3.10]). Although the six-port reflectometer concept was originally proposed for use as an instrument for network measurements, there have been extensions to other applications such as radar sensors [3.9] and six-port receivers [3.10]. The reason for the widespread use of these designs is possibly the ready availability of four-port couplers with excellent performance characteristics. However, the six-port reflectometers based on these standard four-port couplers do not yield q-points that comply with the design specifications put forward by Engen [3.1]. Even the six-port reflectometer designs suggested by Engen himself have non-ideal q-point distributions. For this reason, a number of researchers have resorted to novel components (such as symmetrical five- and six-port couplers [3.11]-[3.14]) in their attempts to design six-port reflectometers that offer suitable q-point distributions; however, such non-standard components are not readily available on an off-the-shelf basis and we shall thus re-visit the design of these four-port couplers instead.

## 3.1 Overview of Six-Port Reflectometers based on Hybrid Couplers

We should begin with a review of the designs reported over the past three decades [3.1]-[3.10] for six-port reflectometers based on four-port couplers which invariably take the form of quadrature and 180$^{o}$ hybrid couplers. Many of these six-port reflectometers are derived from the two circuits depicted in Figure 3.1. However, using the 90$^{o}$ and 180$^{o}$ phase-shifting characteristics of these hybrid couplers to design six-port reflectometers will not yield q-points with the requisite angular separations of 120$^{o}$. Instead, the angular separations that have been reported in the literature are typically 90$^{o}$, 135$^{o}$ or even 180$^{o}$; for example, the q-points associated with the six-port reflectometer instrument [3.1] depicted in Figure 3.1(a) are nominally located at $2\angle$-135$^{o}$, $2\angle$-45$^{o}$ and $1.4\angle$90$^{o}$. Figure 3.1(b) presents an example of a seven-port reflectometer design [3.16] with four q-points located at $1.4\angle$-90$^{o}$, $1.4\angle$180$^{o}$ ,$1.4\angle$90$^{o}$ and $1.4\angle$0$^{o}$; although these q-points are symmetrically distributed, the seven-port reflectometer circuit requires more components than the six-port reflectometer counterpart.

It is possible to incorporate delay lines into such reflectometer circuits so as to influence their q-point behavior. Depicted in Figure 3.2 are the modified designs of those shown earlier in Figure 3.1. For the design we modified in Figure 3.2(a), which has now become a seven-port circuit due to the inclusion of another power divider in the six-port circuit of Figure 3.1(a), the addition of prescribed lengths of transmission lines between certain components has allowed us to shift the q-points to 2∠-120°, 2∠120° and 1.4∠0° and we thus obtain angular separations of 120° as required. As for the modified design of Figure 3.2(b), which is actually an eight-port circuit due to the addition of another hybrid coupler in the seven-port circuit of Figure 3.1(b), the availability of yet another port means that we actually have two sets of four power-detector readings giving rise to two sets of q-points at the following locations where all angular separations are 120°:

- first set located at 1.4∠0°, 1.4∠120° and 1.4∠-120°
- second set located at 1.4∠60°, 1.4∠180° and 1.4∠-60°.

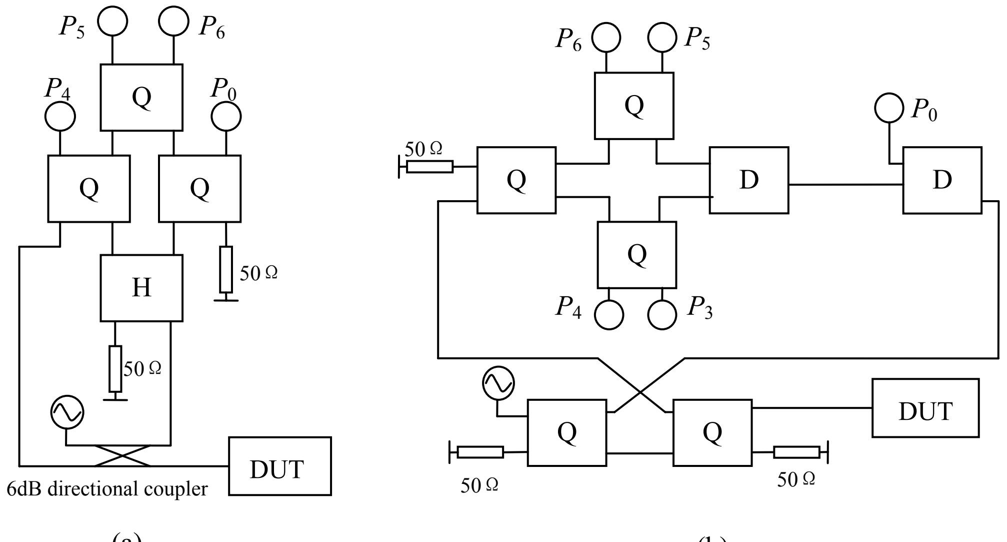

(a) (b)

Figure 3.1 Examples of reflectometer designs based on four-port couplers (where Q represents quadrature hybrid, H represents 180° hybrid and D represents power divider)
(a) proposed by Engen [3.1]
(b) proposed by Cronson [3.16]

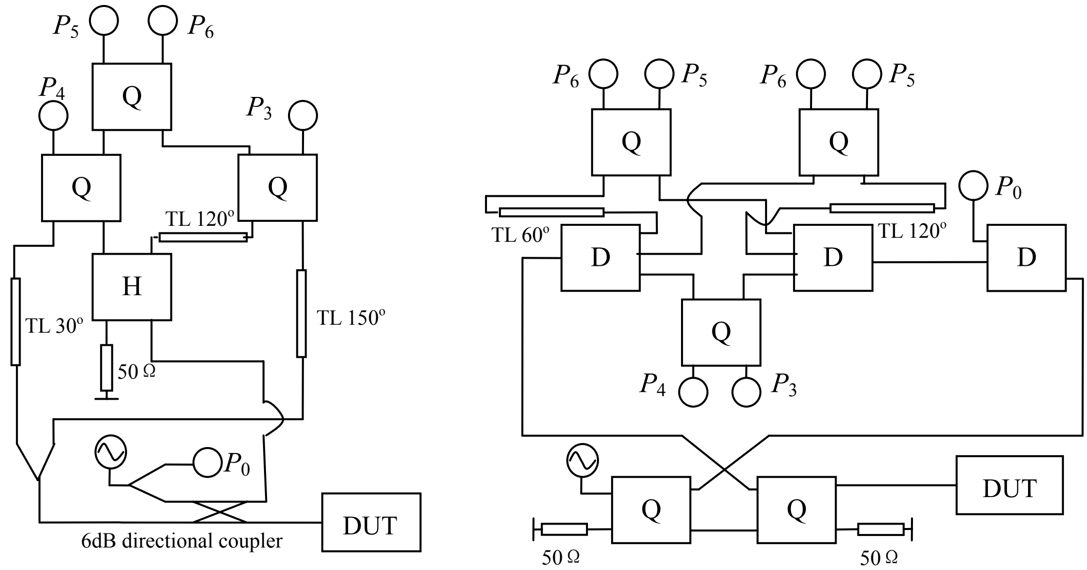

(a)

(b)

Figure 3.2 Modified reflectometer designs derived from examples reproduced in Figure 3.1 (where Q represents quadrature hybrid, H represents $180^{o}$ hybrid, D represents equal power divider, and TL represents transmission line)

However, the two circuits we suggested in Figure 3.2 are narrow-band designs since they utilize transmission lines to shift the q-points so as to obtain $120^{o}$ angular separations. To design wide-band six-port reflectometers with optimum q-point distributions, we need to explore the use of other topologies instead.

## 3.2 Proposed Six-Port Reflectometer Circuit

Depicted in Figure 3.3(a) is the schematic circuit outlining the connections among the various four-port couplers U, V, Y and Z. For ease of incorporating salient information into such circuit diagrams, we shall represent the hybrid coupler in the manner portrayed in Figure

3.3(b) where the coupling between any pair of ports is indicated (with ‘X’ marking those ports that are isolated from each other). We can then use signal flow graph analysis [3.17] to trace the paths of the input signal from the source in order to find configurations that meet the following requirements:

- there must be paths for the wave incident at the input port to travel directly to five ports (one of which is for connection to the DUT while the remaining four ports are terminated in power detectors)
- the wave reflected by the DUT should reach only three of the four power-measurement ports (since we want one of the power detectors to serve as the reference to monitor only the input signal)
- the remaining two ports of our eight-port system will be terminated in loads (such as sliding terminations) with reflection coefficients $\overrightarrow{\Gamma_1}$ and $\overrightarrow{\Gamma_2}$ that may be adjusted in our attempt to fine-tune the q-point distribution of the six-port reflectometer.

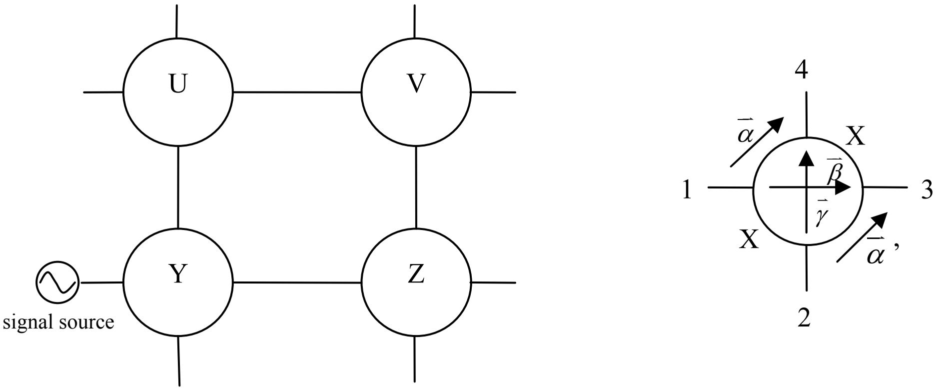

(a) (b)

Figure 3.3 Notation to be employed for (a) six-port reflectometer circuit and (b) hybrid coupler where its isolated ports are denoted by ‘X’ in accordance with scattering matrix in Equation 3.1

After our comprehensive study (outlined in Appendix A) to evaluate all possible permutations in which the DUT, four power detectors and two adjustable loads may be connected to the generic circuit portrayed in Figure 3.3(a), we have chosen the configuration depicted in Figure 3.4 where the pairs of isolated ports for each hybrid coupler are clearly marked by ‘X’. Even with the isolated ports thus specified, there is still flexibility in how we choose to orientate the inter-connections of the four hybrid couplers; in fact, Figure 3.4 actually allows for 12 different inter-connection arrangements. Of these 12 possibilities, we have found the circuit arrangement depicted in Figure 3.5 to be suitable for our purposes.

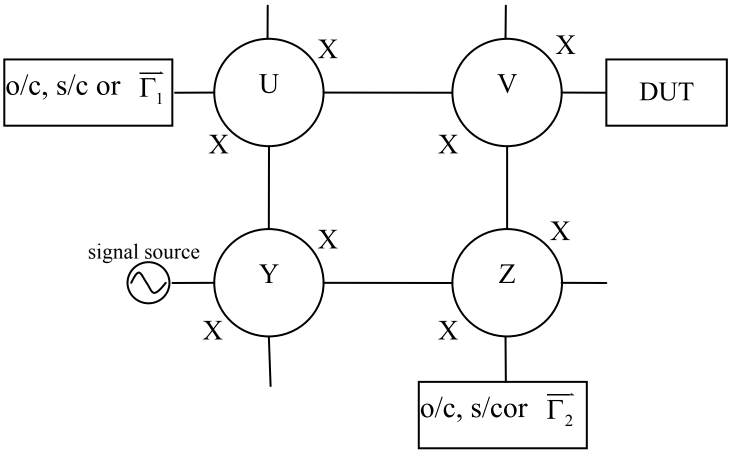

Figure 3.4 Generic topology for six-port reflectometer (where $\Gamma_1$ and $\Gamma_2$ denote adjustable loads)

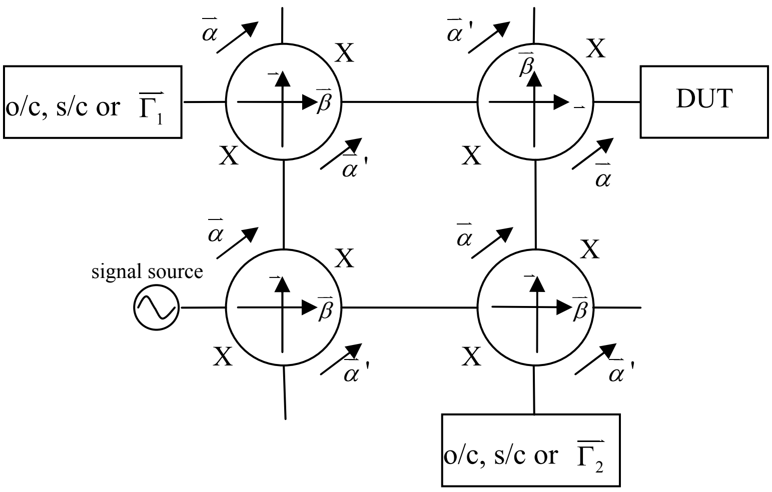

Figure 3.5 Inter-connections of hybrid couplers in six-port reflectometer configuration of Figure 3.4

### 3.2.1 Derivation of q-point expressions

We may implement the configuration depicted in Figure 3.5 by using either the quadrature or 180° versions of the hybrid couplers as shown in Figures 3.6(a) and 3.6(b) respectively. From our experience with such hybrid couplers (including the prototypes we tested in Chapters 4-5), we have found that we may presume $\vec{\alpha}' = \vec{\alpha}$ for our ensuing analysis. Although it is also possible to employ the multi-connection procedure as explained in [3.17], we prefer to continue using signal flow graph analysis for our study of the two six-port reflectometer circuits depicted in Figure 3.6.

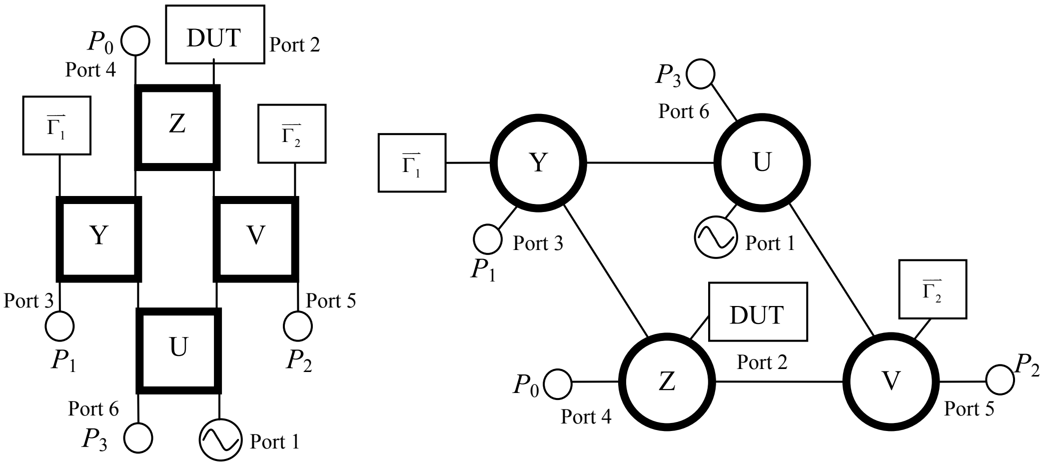

(a) using 90° hybrids

(b) using 180° hybrids

Figure 3.6 Implementing six-port configuration shown in Figure 3.5 by using (a) quadrature hybrids or (b) 180° hybrids

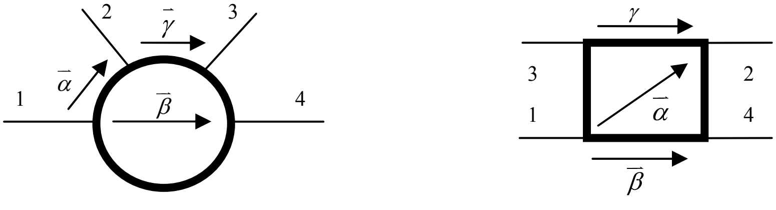

(a) Revised 180° hybrid and its

(b) Revised 90° hybrid and its port

Figure 3.7 Port numbering for (a) 180° hybrids and (b) 90° hybrids

For our analysis, we shall presume that U, V, Y and Z are identical four-port couplers. As already pointed earlier, we prefer not to use the original hybrid-coupler designs since the six-port reflectometers based on such hybrids have thus far yielded q-points with angular separations that are typically 90°, 135° or even 180°. We shall thus have to modify the designs of the 180° and quadrature hybrid couplers sketched in Figures 3.7(a) and 3.7(b) respectively. At this juncture, we may adopt the following scattering matrix to represent a hybrid coupler with zero residual mismatch and perfect isolation characteristics:

$$\overline{S} = \begin{pmatrix} 0 & \overline{\alpha} & 0 & \overline{\beta} \\ \overline{\alpha} & 0 & \overline{\gamma} & 0 \\ 0 & \overline{\gamma} & 0 & \overline{\alpha} \\ \overline{\beta} & 0 & \overline{\alpha} & 0 \end{pmatrix} \tag{3.1}$$

If we additionally assume that the hybrid coupler is loss-free, we then obtain the following relationships between its two scattering coefficients by imposing the unitary-matrix condition S S* = I on Equation 3.1:

$$|\overline{\beta}|=|\overline{\gamma}| \tag{3.2a}$$

$$|\overline{\beta}|^2+|\overline{\alpha}|^2=1 \tag{3.2b}$$

$$2\arg(\overline{\alpha}) = \arg(\overline{\beta}) + \arg(\overline{\gamma}) \pm 180^o \tag{3.2c}$$

By using signal flow graph analysis, we derive the following scattering matrix for the two six-port reflectometer systems depicted in Figure 3.6:

$$\vec{S}_6 = \begin{pmatrix} \vec{\alpha}^2\vec{\gamma}^2\vec{\Gamma}_2 + \vec{\beta}^2\vec{\gamma}^2\vec{\Gamma}_1 & \vec{\alpha}^3 + \vec{\alpha}\vec{\gamma}^2 & \vec{\alpha}\vec{\beta}\vec{\gamma}\vec{\Gamma}_1 & \vec{\alpha}^2(\vec{\beta}+\vec{\gamma}) & \vec{\alpha}\vec{\beta}\vec{\gamma}^2\vec{\Gamma}_2 + \vec{\alpha}\vec{\beta}^2\vec{\gamma}\vec{\Gamma}_1 & \vec{\alpha}^2\vec{\gamma}\vec{\Gamma}_2 \\ \vec{\alpha}^3 + \alpha\vec{\gamma}^2 & 0 & \vec{\gamma}^2 & 0 & \vec{\alpha}^2(\vec{\beta}+\vec{\gamma}) & \vec{\alpha}\vec{\beta} \\ \vec{\alpha}\vec{\beta}\vec{\gamma}\vec{\Gamma}_1 & \vec{\gamma}^2 & \vec{\alpha}^2\vec{\Gamma}_1 & \vec{\alpha}\vec{\gamma} & \vec{\alpha}^2\vec{\beta}\vec{\Gamma}_1 & 0 \\ \vec{\alpha}^2(\vec{\beta}+\vec{\gamma}) & 0 & \vec{\alpha}\vec{\gamma} & 0 & \vec{\alpha}^3 + \alpha\vec{\beta}^2 & \vec{\beta}^2 \\ \vec{\alpha}\vec{\beta}\vec{\gamma}^2\vec{\Gamma}_2 + \vec{\alpha}\vec{\beta}^2\vec{\gamma}\vec{\Gamma}_1 & \vec{\alpha}^2(\vec{\beta}+\vec{\gamma}) & \vec{\alpha}^2\vec{\beta}\vec{\Gamma}_1 & \vec{\alpha}^3 + \vec{\alpha}\vec{\beta}^2 & \vec{\beta}^2\vec{\gamma}^2\vec{\Gamma}_2 + \vec{\alpha}^2\vec{\beta}^3\vec{\Gamma}_1 & \vec{\alpha}\vec{\beta}\vec{\gamma}\vec{\Gamma}_2 \\ \vec{\alpha}^2\vec{\gamma}\vec{\Gamma}_2 & \vec{\alpha}\vec{\beta} & 0 & \vec{\beta}^2 & \vec{\alpha}\vec{\beta}\vec{\gamma}\vec{\Gamma}_2 & \vec{\alpha}^2\vec{\Gamma}_2 \end{pmatrix} \tag{3.3}$$

Equation 3.3 allows us to derive the following expressions for the three q-points of the six-port reflectometers:

$$\begin{aligned} \vec{q}_1 &= -\frac{\vec{\beta}\vec{\Gamma}_1}{\vec{\gamma}(\vec{\gamma}^2 + \vec{\alpha}^2)} \\ \vec{q}_2 &= -\frac{\vec{\beta}\vec{\gamma}(\vec{\gamma}\vec{\Gamma}_2 + \vec{\beta}\vec{\Gamma}_1)}{\vec{\alpha}^2(\vec{\beta}+\vec{\gamma})(\vec{\gamma}^2 + \vec{\alpha}^2)} \\ \vec{q}_3 &= -\frac{\vec{\gamma}\vec{\Gamma}_2}{\vec{\beta}(\vec{\gamma}^2 + \vec{\alpha}^2)} \end{aligned} \tag{3.4}$$

It is more meaningful to obtain the ratios of the three expressions listed in Equation 3.4 since we need to derive expressions for the angular separations of the q-points:

$$\begin{aligned} \arg\left(\frac{\vec{q}_3}{q_1}\right) &= \arg\left(\frac{\vec{\gamma}^2\vec{\Gamma}_2}{\vec{\beta}^2\vec{\Gamma}_1}\right) \\ \arg\left(\frac{\vec{q}_3}{q_2}\right) &= \arg\left(\frac{\vec{\alpha}^2(\vec{\beta}+\vec{\gamma})\vec{\Gamma}_2}{\vec{\beta}^2(\vec{\gamma}\vec{\Gamma}_2 + \vec{\beta}\vec{\Gamma}_1)}\right) \end{aligned} \tag{3.5}$$

An inspection of these q-point expressions indicates that simplification is possible if $\vec{\Gamma}_1 = \vec{\Gamma}_2 = \vec{\Gamma}$. Hence, selecting the same termination for the two adjustable loads will allow Equations 3.4 and 3.5 to become Equations 3.6 and 3.7 respectively:

$$\begin{aligned}
\overline{q_1} &= -\frac{\overrightarrow{\beta}\overrightarrow{\Gamma}}{\overrightarrow{\gamma}(\overrightarrow{\gamma}^2+\overrightarrow{\alpha}^2)} \\
\overline{q_2} &= -\frac{\overrightarrow{\beta}\overrightarrow{\gamma}\overrightarrow{\Gamma}}{\overrightarrow{\alpha}^2(\overrightarrow{\gamma}^2+\overrightarrow{\alpha}^2)} \\
\overline{q_3} &= -\frac{\overrightarrow{\gamma}\overrightarrow{\Gamma}}{\overrightarrow{\beta}(\overrightarrow{\gamma}^2+\overrightarrow{\alpha}^2)}
\end{aligned} \tag{3.6}$$

$$\begin{aligned}
\arg\left(\frac{\overline{q_3}}{\overline{q_1}}\right) &= \arg\left(\frac{\overrightarrow{\gamma}^2}{\overrightarrow{\beta}^2}\right) \\
\arg\left(\frac{\overline{q_3}}{\overline{q_2}}\right) &= \arg\left(\frac{\overrightarrow{\alpha}^2}{\overrightarrow{\beta}^2}\right)
\end{aligned} \tag{3.7}$$

To comply with the design criteria requiring equal magnitudes and angular separations for the three q-points, we infer from Equations 3.6-3.7 that the hybrid coupler must have the following scattering coefficients:

$$\begin{aligned}
&|\overrightarrow{\alpha}| = |\overrightarrow{\beta}| = 1/\sqrt{2} \\
&2(\arg(\overrightarrow{\gamma}) - \arg(\overrightarrow{\beta})) = \pm 120^o \\
&2(\arg(\overrightarrow{\alpha}) - \arg(\overrightarrow{\beta})) = \mp 120^o
\end{aligned} \tag{3.8}$$

Hence, our modified hybrid-coupler designs should have the balanced power-splitting and phase-shift characteristics specified by Equation 3.8. It should be pointed out that the coupler's phase-shift specifications actually apply to the ratios $\overrightarrow{\gamma}/\overrightarrow{\beta}$ and $\overrightarrow{\alpha}/\overrightarrow{\beta}$ (with the phase of $\overrightarrow{\beta}$ still to be specified).

The expressions listed in Equation 3.6 for the three q-point magnitudes can be further simplified after we substitute the design values obtained in Equation 3.8 (which specify that $\alpha$ and $\gamma$ should have the same magnitude and be separated by $120^o$):

$$\left|\overline{q}_i\right| = \left|\frac{\overline{\beta}\overline{\Gamma}}{\overline{\gamma}(\overline{\gamma}^2 + \overline{\alpha}^2)}\right| = \left|\frac{\overline{\Gamma}}{\overline{\gamma}^2 + \overline{\alpha}^2}\right| = 2\left|\overline{\Gamma}\right| \tag{3.9}$$

We infer from Equation 3.9 that, under certain circumstances, the magnitudes of q-points may be determined by the two adjustable loads (where $\overline{\Gamma_1}$ = $\overline{\Gamma_2}$ for this particular scenario). This useful finding indicates that the adjustable loads may be used to fine-tune the q-point magnitudes. As mentioned in Chapter 2, it is preferable to locate the q-points outside the unit circle and so we note from Equation 3.9 that we should choose $|\overline{\Gamma}| > ½$. Since $|\overline{\Gamma}|$ cannot exceed unity for passive loads, the q-points will have magnitudes in the $1 < |\overline{q_i}| < 2$ range.

### 3.2.2 First-order analysis

The analysis performed in Sub-Section 3.2.1 is based on the assumptions of zero mismatch and perfect isolation for the four hybrid couplers. In practice, however, hardware imperfections exist especially when we want to maximize the operating bandwidth that may be achieved for the six-port reflectometer. Hence, we need to evaluate the effects of hardware imperfections on the performance of the reflectometer's performance.

We begin by re-writing Equation 3.1 in the following form so as to take the residual mismatch and isolation leakage of the hybrid coupler into account:

$$\overline{S} = \begin{bmatrix} \overline{\tau_1} & \overline{\alpha_1} & \overline{\xi_1} & \overline{\beta} \\ \overline{\alpha_1} & \overline{\tau_2} & \overline{\gamma} & \overline{\xi_2} \\ \overline{\xi_1} & \overline{\gamma} & \overline{\tau_3} & \overline{\alpha_2} \\ \overline{\beta} & \overline{\xi_2} & \overline{\alpha_2} & \overline{\tau_4} \end{bmatrix} \tag{3.10}$$

If we continue to assume that the hybrid coupler remains loss-free less, we may then substitute the scattering coefficients defined in Equation 3.10 into the following equation since the matrix has to be unitary:

$$\vec{S} \bullet \vec{S}^* \quad = \quad \vec{I} \tag{3.11}$$

The expansion of Equation 3.11 allows us to derive the following relationships among the hybrid coupler's scattering coefficients:

$$\begin{aligned}
&|\vec{\tau}_1|^2 + |\vec{\alpha}_1|^2 + |\vec{\xi}_1|^2 + |\vec{\beta}|^2 = 1 \\
&|\vec{\tau}_2|^2 + |\vec{\alpha}_1|^2 + |\vec{\xi}_2|^2 + |\vec{\gamma}|^2 = 1 \\
&|\vec{\tau}_3|^2 + |\vec{\alpha}_2|^2 + |\vec{\xi}_1|^2 + |\vec{\gamma}|^2 = 1 \\
&|\vec{\tau}_4|^2 + |\vec{\alpha}_2|^2 + |\vec{\xi}_2|^2 + |\vec{\beta}|^2 = 1 \\
&\vec{\tau}_1\vec{\alpha}_1^* + \vec{\alpha}_1\vec{\tau}_2^* + \vec{\xi}_1\vec{\gamma}^* + \vec{\beta}\vec{\xi}_2^* = 0 \\
&\vec{\tau}_1\vec{\xi}_1^* + \vec{\alpha}_1\vec{\gamma}^* + \vec{\xi}_1\vec{\tau}_3^* + \vec{\beta}\vec{\alpha}_2^* = 0 \\
&\vec{\tau}_1\vec{\beta}^* + \vec{\alpha}_1\vec{\xi}_2^* + \vec{\xi}_1\vec{\alpha}_2^* + \vec{\beta}\vec{\tau}_4^* = 0 \\
&\vec{\tau}_2\vec{\gamma}^* + \vec{\alpha}_1\vec{\xi}_1^* + \vec{\gamma}\vec{\tau}_3^* + \vec{\xi}_2\vec{\alpha}_2^* = 0 \\
&\vec{\tau}_2\vec{\xi}_2^* + \vec{\alpha}_1\vec{\beta}^* + \vec{\gamma}\vec{\alpha}_2^* + \vec{\xi}_2\vec{\tau}_4^* = 0 \\
&\vec{\gamma}\vec{\xi}_2^* + \vec{\xi}_1\vec{\beta}_1^* + \vec{\tau}_3\vec{\alpha}_2^* + \vec{\alpha}_2\vec{\tau}_4^* = 0
\end{aligned} \tag{3.12}$$

These equations may be simplified if we capitalize on the physical symmetry of the hybrid coupler's structure so as to introduce the following relationships:

$$\begin{aligned}
&\vec{\xi}_1 = \vec{\xi}_2 = \vec{\xi} \\
&\vec{\alpha}_1 = \vec{\alpha}_2 = \vec{\alpha} \\
&\vec{\tau}_4 = \vec{\tau}_1 \\
&\vec{\tau}_3 = \vec{\tau}_2
\end{aligned} \tag{3.13}$$

The ideal-case values of the hybrid coupler's scattering coefficients are specified in Equation 3.1. For our modified hybrid-coupler design, we expect the prototype to yield scattering coefficients with minor departures from their respective ideal-case values in Equation 3.1. Under such circumstances, we may represent the scattering coefficients in the following manner:

$$\begin{aligned}
\overrightarrow{\alpha} &= (\alpha_0 + \Delta_\alpha)e^{j\phi_\alpha + \Delta\phi_\alpha} \\
\overrightarrow{\beta} &= (\beta_0 + \Delta_\beta)e^{j\phi_\beta + \Delta\phi_\beta} \\
\overrightarrow{\gamma} &= (\gamma_0 + \Delta_\gamma)e^{j\phi_\gamma + \Delta\phi_\gamma} \\
\overrightarrow{\tau_1} &= \Delta_1 e^{j\phi_1} \\
\overrightarrow{\tau_2} &= \Delta_2 e^{j\phi 2} \\
\overrightarrow{\xi} &= \Delta_\xi e^{j\phi_\xi}
\end{aligned} \tag{3.14}$$

The dominant terms in Equation 3.14 ($\alpha_0$, $\gamma_0$, $\beta_0$, $\phi_\alpha$, $\phi_\gamma$ and $\phi_\beta$) will naturally have to satisfy Equation 3.2. By substituting the expressions from Equations 3.2 and 3.13-3.14 into the relationships listed in Equation 3.12, we will obtain the following first-order equations after disregarding all second- and higher-order terms in the respective expansions:

$$\alpha_0\Delta_\alpha = -\beta_0\Delta_\beta = -\gamma_0\Delta_\gamma \tag{3.15a}$$

$$2\Delta\phi_\alpha = \Delta\phi_\beta + \Delta\phi_\gamma \pm \pi \tag{3.15b}$$

$$\overrightarrow{\tau_1}\overrightarrow{\alpha}^* + \overrightarrow{\alpha}\overrightarrow{\tau_2}^* + \overrightarrow{\xi}\overrightarrow{\gamma}^* + \overrightarrow{\beta}\overrightarrow{\xi}^* = 0 \tag{3.15c}$$

$$\Delta\tau_1\beta_0 Cos(\phi_1 + \phi_\beta + \Delta\phi_\beta) = -\Delta\xi\alpha_0 Cos(\phi_\xi + \phi_\alpha + \Delta\phi_\alpha) \tag{3.15d}$$

$$\Delta\tau_2\gamma_0 Cos(\phi_2 + \phi_\gamma + \Delta\phi_\gamma) = -\Delta\xi\alpha_0 Cos(\phi_\xi + \phi_\alpha + \Delta\phi_\alpha) \tag{3.15e}$$

Equation 3.15(a) when coupled together with Equation 3.15(b) provide the inter-relationships among the departures of $\vec{\alpha}$, $\vec{\beta}$ and $\vec{\gamma}$ from their respective ideal-case values; if, for example, we know how much $|\vec{\alpha}|$ and $|\vec{\beta}|$ have departed from their respective ideal-case values, we will then be able to determine from Equation 3.15(a) the departure of $|\vec{\gamma}|$ from its ideal-case value. Another important inference we can draw from Equation 3.15(a) in conjunction with Equation 3.15(b) is that the behavior of $\vec{\alpha}$, $\vec{\beta}$ and $\vec{\gamma}$ for a reasonably well-designed hybrid coupler does not appear to be affected by the residual mismatch and isolation leakage terms represented by $\vec{\tau_i}$ and $\vec{\xi}$ respectively. Hence, we cannot presume that $\Delta_\alpha$, $\Delta_\beta$, $\Delta_\gamma$, $\Delta\phi_\alpha$, $\Delta\phi_\beta$ and $\Delta\phi_\gamma$ will be negligibly small when we are given a prototype with zero mismatch and excellent isolation; in fact, there is no meaningful information available from Equations 3.15(c)-3.15(e) if we substitute $\vec{\tau_i}$ = $\vec{\xi}$ = 0 into these three equations.

### 3.2.3 Empirical findings via simulations

Another approach available to us is to utilize simulations to derive more information on the effects of the hybrid coupler's hardware imperfections on the six-port reflectometer's q-point distribution. From our analysis in Sub-Section 3.2.1, we have found that it is possible to obtain a six-port reflectometer with q-points at their ideal-case locations if we are able to design a modified hybrid coupler with the following scattering matrix (which is based on Equation 3.8):

$$\overline{S} = \begin{bmatrix} 0 & \frac{1}{\sqrt{2}} e^{j(2\pi/3+\phi_0)} & 0 & \frac{1}{\sqrt{2}} e^{j(\pi/3+\phi_0)} \\ \frac{1}{\sqrt{2}} e^{j(2\pi/3+\phi_0)} & 0 & \frac{1}{\sqrt{2}} e^{j\phi_0} & 0 \\ 0 & \frac{1}{\sqrt{2}} e^{j\phi_0} & 0 & \frac{1}{\sqrt{2}} e^{j(2\pi/3+\phi_0)} \\ \frac{1}{\sqrt{2}} e^{j(\pi/3+\phi_0)} & 0 & \frac{1}{\sqrt{2}} e^{j(2\pi/3+\phi_0)} & 0 \end{bmatrix} \qquad (3.16)$$

Simulations will allow us to evaluate the degradation of the six-port reflectometer's q-point distribution when we vary each of the hybrid coupler's scattering coefficients in turn. In this manner, we can ascertain how much departure from the specifications in Equation 3.16 may be tolerated for our modified hybrid-coupler design so as to ensure that the q-point locations will remain the limits of $\boxed{1.1 < |\vec{q_i}| < 2.8 \text{ and } 100^\circ < |\angle \vec{q_i} - \angle \vec{q_j}| < 140^\circ \ (i \neq j)}$ in accordance with our earlier findings in Chapter 2.

## (a) Effects of mismatch on q-point distribution

According to Equation 3.1, the hybrid coupler should ideally be matched with $\vec{\tau_1} = \vec{\tau_2} = 0$. In practice, however, $\vec{\tau_1}$ and $\vec{\tau_2}$ may not be zero over the operating bandwidth ─ especially for a wide-band design. For a well-designed hybrid coupler, we have already inferred from Equations 3.15(a)-3.15(b) that the coupling coefficients $\vec{\alpha}$, $\vec{\beta}$ and $\vec{\gamma}$ should not be affected by the residual-mismatch coefficients $\vec{\tau_1}$ and $\vec{\tau_2}$. For our simulations, we shall evaluate the six-port reflectometer's q-point distribution for selected values of $\vec{\tau_1}$ and $\vec{\tau_2}$ provided that the residual-mismatch perturbations remain low enough for the first-order analysis of Sub-Section 3.2.2 to remain valid.

Table 3.1 Effect of $|\overrightarrow{\tau_1}|$ (where $\angle\overrightarrow{\tau_1} = 240^{o}$) on Q-point distribution

| $\lvert\overrightarrow{\tau_1}\rvert$ | $\lvert\overrightarrow{q_1}\rvert$ | $\lvert\overrightarrow{q_2}\rvert$ | $\lvert\overrightarrow{q_3}\rvert$ | $\angle\overrightarrow{q_1} - \angle\overrightarrow{q_2}$ | $\angle\overrightarrow{q_2} - \angle\overrightarrow{q_3}$ |
|---|---|---|---|---|---|
| -35dB | 1.9 | 2.1 | 2.0 | 118° | 124° |
| -30dB | 1. 8 | 2.2 | 2.0 | 116° | 127° |
| -25dB | 1.7 | 2.3 | 2.1 | 113° | 134° |
| -22dB | 1.6 | 2.5 | 2.2 | 109° | 141° |

Table 3.2 Effect of $|\overrightarrow{\tau_2}|$ (where $\angle\overrightarrow{\tau_2} = 240^{o}$) on Q-point distribution

| $\lvert\overrightarrow{\tau_2}\rvert$ | $\lvert\overrightarrow{q_1}\rvert$ | $\lvert\overrightarrow{q_2}\rvert$ | $\lvert\overrightarrow{q_3}\rvert$ | $\angle\overrightarrow{q_1} - \angle\overrightarrow{q_2}$ | $\angle\overrightarrow{q_2} - \angle\overrightarrow{q_3}$ |
|---|---|---|---|---|---|
| -35dB | 2.0 | 1.8 | 2.0 | 121° | 119° |
| -30dB | 2.0 | 1.7 | 2.0 | 122° | 118° |
| -25dB | 2.0 | 1.4 | 1.9 | 124° | 117° |
| -20dB | 2.0 | 1.0 | 1.9 | 126° | 116° |

Table 3.3 Effect of $\angle\overrightarrow{\tau_1}$ (where $|\overrightarrow{\tau_1}| = -22\text{dB}$) on Q-point distribution

| $\angle\overrightarrow{\tau_1}$ | $\lvert\overrightarrow{q_1}\rvert$ | $\lvert\overrightarrow{q_2}\rvert$ | $\lvert\overrightarrow{q_3}\rvert$ | $\angle\overrightarrow{q_1} - \angle\overrightarrow{q_2}$ | $\angle\overrightarrow{q_2} - \angle\overrightarrow{q_3}$ |
|---|---|---|---|---|---|
| 60° | 2.6 | 1.6 | 1.9 | 126° | 105° |
| 120° | 2.3 | 2.0 | 1.7 | 148° | 103° |
| 180° | 1.8 | 2.7 | 1.8 | 138° | 120° |
| 240° | 1.6 | 2.5 | 2.2 | 109° | 141° |
| 300° | 1.7 | 1.9 | 2.4 | 97° | 134° |
| 360° | 2.1 | 1.6 | 2.1 | 102° | 117° |

Table 3.4 Effect of $\angle\overrightarrow{\tau_2}$ (where $|\overrightarrow{\tau_2}| = -23\text{dB}$) on Q-point distribution

| $\angle\overrightarrow{\tau_2}$ | $\lvert\overrightarrow{q_1}\rvert$ | $\lvert\overrightarrow{q_2}\rvert$ | $\lvert\overrightarrow{q_3}\rvert$ | $\angle\overrightarrow{q_1} - \angle\overrightarrow{q_2}$ | $\angle\overrightarrow{q_2} - \angle\overrightarrow{q_3}$ |
|---|---|---|---|---|---|
| 60° | 2.0 | 3.0 | 2.1 | 113° | 125° |
| 120° | 2.0 | 2.3 | 2.0 | 99° | 137° |
| 180° | 2.0 | 1.6 | 1.9 | 101° | 137° |
| 240° | 2.0 | 1.3 | 1.9 | 125° | 117° |
| 300° | 2.0 | 1.8 | 2.0 | 144° | 99° |
| 360° | 2.0 | 2.7 | 2.1 | 137° | 105° |

The simulation results presented in Tables 3.1-3.4 provide empirical evidence that both magnitudes and phases of the hybrid coupler's residual-mismatch coefficients may affect the six-port reflectometer's q-point distribution. In fact, Tables 3.3-3.4 additionally indicate that the constructive interference of the spurious waves reflected by the four hybrid couplers may aggravate the problem for certain phases of $\vec{\tau_1}$ and $\vec{\tau_2}$; instead of attempting to regulate their phases, the magnitudes of $\vec{\tau_1}$ and $\vec{\tau_2}$ should be minimized during the optimization of the hybrid-coupler design. We recommend from an inspection of the simulation results that the return losses $\vec{\tau_1}$ and $\vec{\tau_2}$ should not exceed -23dB and -20dB respectively: $\boxed{|\vec{\tau_1}| < 0.07 \text{ and } |\vec{\tau_2}| < 0.1}$.

## (b) Effects of isolation on q-point distribution

Equations 3.15(a)-3.15(b) also indicate that the coupling coefficients $\vec{\alpha}$, $\vec{\beta}$ and $\vec{\gamma}$ of a well-designed hybrid coupler should not be affected by its isolation-leakage coefficient (which should ideally be $\vec{\xi}$ = 0). The simulation process we utilized earlier to evaluate the effects of residual mismatches can be used again to study the six-port reflectometer's q-point distribution for selected values of $\vec{\xi}$ provided that the perturbations remain low enough for the first-order analysis of Sub-Section 3.2.2 to remain valid.

The simulation results presented in Tables 3.5-3.6 yield a similar set of empirical findings for the effects of $|\vec{\xi}|$ and $\angle \vec{\xi}$. An inspection of the tabulated data suggests that we should ensure that the magnitude of this isolation-leakage coefficient for our modified hybrid-coupler design should not exceed -25dB: $\boxed{|\vec{\xi}| < 0.06}$ .

TABLE 3.5 EFFECT OF $|\vec{\xi}|$ (WHERE $\angle\vec{\xi}$ = 240O) ON Q-POINT DISTRIBUTION

| $\|\vec{\xi}\|$ | $\|\vec{q}_1\|$ | $\|\vec{q}_2\|$ | $\|\vec{q}_3\|$ | $\angle\vec{q}_1 - \angle\vec{q}_2$ | $\angle\vec{q}_2 - \angle\vec{q}_3$ |
|---|---|---|---|---|---|
| -35dB | 2 | 1.7 | 2 | 117° | 119° |
| -30dB | 1. 9 | 1.5 | 1.9 | 114° | 119° |
| -25dB | 1.8 | 1.3 | 1.9 | 108° | 119° |
| -20dB | 1.7 | 0.9 | 1.8 | 94° | 123° |

TABLE 3.6 EFFECT OF $\angle\vec{\xi}$ (WHERE $|\vec{\xi}|$ = -25DB) ON Q-POINT DISTRIBUTION

| $\angle\vec{\xi}$ | $\|\vec{q}_1\|$ | $\|\vec{q}_2\|$ | $\|\vec{q}_3\|$ | $\angle\vec{q}_1 - \angle\vec{q}_2$ | $\angle\vec{q}_2 - \angle\vec{q}_3$ |
|---|---|---|---|---|---|
| 60° | 2.1 | 3.1 | 2.1 | 126° | 127° |
| 120° | 1.6 | 2.2 | 2.0 | 107° | 139° |
| 180° | 1.5 | 1.5 | 1.9 | 98° | 135° |
| 240° | 1.8 | 1.3 | 1.9 | 108° | 119° |
| 300° | 2.4 | 1.7 | 2.0 | 135° | 97° |
| 360° | 2.6 | 2.9 | 2.1 | 145° | 102° |

## (c) Effects of coupling variations on q-point distribution

Equation 3.15(a)-3.15(b) provide the inter-relationships among the three coupling coefficients $\vec{\alpha}$, $\vec{\beta}$ and $\vec{\gamma}$ of a well-designed hybrid coupler are related to each other. We thus need to study them together in our simulations.

(a) For our simulations to study the effects of varying the hybrid coupler's coupling-coefficient magnitudes on the six-port reflectometer's q-point distribution, Equation 3.15(a) is employed to compute the ratios $|\vec{\alpha}/\vec{\beta}|$ and $|\vec{\alpha}/\vec{\gamma}|$ for selected values of $|\vec{\alpha}|$ while the phases are left unchanged at $\angle\vec{\alpha} = 120^{\circ}$, $\angle\vec{\beta} = 60^{\circ}$ and $\angle\vec{\gamma} = 0^{\circ}$. The simulation results presented in Table 3.7 indicate that we should impose the following limits on the magnitude ratios of our modified hybrid-coupler design: $\boxed{|\vec{\alpha}/\vec{\beta}| < 2\text{dB} \quad \text{and} \quad |\vec{\alpha}/\vec{\gamma}| < 2\text{dB}}$.

(b) For our simulations to study the effects of varying the hybrid coupler's phase imbalances on the six-port reflectometer's q-point distribution, Equation 3.15(b) is employed to compute the phase differences while the magnitudes are left unchanged at $|\vec{\alpha}| = |\vec{\beta}| = |\vec{\gamma}| = 1/\sqrt{2}$. The simulation results presented in Table 3.8 and Table 3.9 (where we vary $\triangle\phi_{\beta}$ and $\triangle\phi_{\gamma}$ respectively) indicate that we should impose the following limits on the phase differences of our modified hybrid-coupler design: $\boxed{|\triangle\phi_{\beta}| < 15^{\circ} \quad \text{and} \quad |\triangle\phi_{\gamma}| < 10^{\circ}}$.

A note of clarification is required for the limits on phase differences. For the definition of the hybrid coupler's scattering coefficients in Equation 3.16, we have to add a common phase $\phi_0$ (which is dependent on the choice of reference planes) to the phases $\phi_{\alpha}$, $\phi_{\beta}$ and $\phi_{\gamma}$ of the three coupling coefficients. For a wide-band coupler design, we usually express this common phase as $k\triangle f$ (where $k$ is a real constant and $\triangle f = f - f_c$, with $f_c$ being the mid-frequency of the specified bandwidth). It will be difficult to insist on $|\triangle\phi_{\beta}| < 15^{\circ}$ and $|\triangle\phi_{\gamma}| < 10^{\circ}$ for wide-band operation with $k \neq 0$. Since $\phi_{\alpha}$, $\phi_{\beta}$ and $\phi_{\gamma}$ are equally affected by this common phase, the q-point locations will remain unchanged so long as Equation 3.8 holds.

Hence, it is preferable to re-write the phase-difference limits in the following form when we are considering wide-band design: $\boxed{|\phi_\alpha - \phi_\gamma| < 15^o \quad \text{and} \quad |\phi_\alpha - \phi_\beta| < 10^o}$.

TABLE 3.7 EFFECTS OF $|\vec{\alpha}|$, $|\vec{\beta}|$ AND $|\vec{\gamma}|$ ON Q-POINT DISTRIBUTION

| $\|\vec{\alpha}\|$ | Power division imbalances $\|\vec{\alpha}/\vec{\beta}\|$ and $\|\vec{\alpha}/\vec{\gamma}\|$ | $\|\vec{q_1}\|$ | $\|\vec{q_2}\|$ | $\|\vec{q_3}\|$ | $\angle\vec{q_1} - \angle\vec{q_2}$ | $\angle\vec{q_2} - \angle\vec{q_3}$ |
|---|---|---|---|---|---|---|
| 0.60 | 2.65dB | 2.8 | 3.2 | 1.6 | 146° | 94° |
| 0.65 | 1.4dB | 2.4 | 2.6 | 1.8 | 133° | 106° |
| 0.70 | 0.17dB | 2.0 | 2.0 | 2.0 | 120° | 120° |
| 0.75 | -1.06dB | 1.8 | 1.5 | 2.4 | 106° | 134° |
| 0.80 | -2.3dB | 1.6 | 1.0 | 2.8 | 94° | 146° |

TABLE 3.8 EFFECT OF $\triangle\phi_\beta$ (WHERE $\triangle\phi_\gamma = 0$ AND $\phi_0 = 0$) ON Q-POINT DISTRIBUTION

| $\triangle\phi_\beta$ | $\|\vec{q_1}\|$ | $\|\vec{q_2}\|$ | $\|\vec{q_3}\|$ | $\angle\vec{q_1} - \angle\vec{q_2}$ | $\angle\vec{q_2} - \angle\vec{q_3}$ |
|---|---|---|---|---|---|
| -20° | 1.6 | 2 | 1.6 | 90° | 130° |
| -15° | 1.6 | 2 | 1.6 | 98° | 128° |
| -10° | 1.7 | 2 | 1.7 | 105° | 125° |
| 10° | 2.4 | 2 | 2.4 | 135° | 115° |
| 15° | 2.6 | 2 | 2.6 | 142° | 113° |
| 20° | 2.9 | 2 | 2.9 | 150° | 110° |

TABLE 3.9 EFFECT OF $\triangle\phi_\gamma$ (WHERE $\triangle\phi_\beta = 0$ AND $\phi_0 = 0$) ON Q-POINT DISTRIBUTION

| $\triangle\phi_\gamma$ | $\|\vec{q_1}\|$ | $\|\vec{q_2}\|$ | $\|\vec{q_3}\|$ | $\angle\vec{q_1} - \angle\vec{q_2}$ | $\angle\vec{q_2} - \angle\vec{q_3}$ |
|---|---|---|---|---|---|
| -10° | 2.4 | 2.9 | 2.4 | 125° | 145° |
| -5° | 2.2 | 2.4 | 2.2 | 123° | 133° |
| 0° | 2 | 2 | 2 | 120° | 120° |
| 5° | 1.9 | 1.7 | 1.9 | 118° | 108° |
| 10° | 1.7 | 1.6 | 1.7 | 115° | 95° |

Having considered each hardware imperfection in turn, we are now in a position to consolidate our empirical findings on how departures from the modified hybrid-coupler's design specifications may affect the six-port reflectometer's q-point distribution:

(a) The q-point distribution does not appear to be particularly sensitive to the magnitude imbalance of the coupling coefficients. It should not be difficult to design hybrid couplers with a tolerance of 2dB for the power-division imbalance.

(b) However, the q-point distribution is sensitive to the phase changes of the coupling coefficients. For certain designs, it may be relatively difficult is keep these phase changes $\vartriangle\phi_\beta$ and $\vartriangle\phi_\gamma$ within the stipulated limits, especially if wide-band operation is required for the hybrid coupler.

(c) Even more challenging is the sensitivity of the q-point distribution to matching and isolation imperfections. Instead of insisting that the phases of those coefficients associated with matching and isolation must be kept within stringent limits, we propose to minimize their magnitudes in our effort to eliminate the spurious waves caused by such imperfections.

## 3.3 Possibility of Fine-tuning Six-Port Reflectometer

It may be difficult to achieve a modified hybrid-coupler design that meets all of the stringent requirements over a sufficiently wide bandwidth. Consider, by way of example, the prototypes recently reported by other researchers in [3.15]-[3.17]: their laboratory tests demonstrated the difficulty they experienced in keeping the residual mismatch below the -20dB threshold.

Another approach we have thus pursued is to employ the adjustable loads $\overrightarrow{\Gamma_1}$ and $\overrightarrow{\Gamma_2}$ for the purpose of fine-tuning the six-port reflectometer system to correct for departures of the q-points from their ideal-case locations. For better understanding of this useful feature, we return to our analysis in Sub-Section 3.2.1 where Equation 3.9 has shown that, under certain circumstances, the magnitudes of q-points may be determined by the adjustable loads. However, Equation 3.9 is not of general application and we should instead re-visit Equation 3.4 from which we obtain the following:

$$\frac{\overrightarrow{q_3}}{\overrightarrow{q_1}} = \frac{\overrightarrow{\gamma}^2\,\overrightarrow{\Gamma_2}}{\overrightarrow{\beta}^2\,\overrightarrow{\Gamma_1}} \tag{3.17a}$$

$$\frac{\overrightarrow{q_2}}{\overrightarrow{q_1}} = \frac{\overrightarrow{\gamma}^2(\overrightarrow{\gamma}\overrightarrow{\Gamma_2}+\overrightarrow{\beta}\overrightarrow{\Gamma_1})}{\overrightarrow{\alpha}^2(\overrightarrow{\beta}+\overrightarrow{\gamma})\overrightarrow{\Gamma_1}} = \frac{\overrightarrow{\gamma}^2((\overrightarrow{\beta}/\overrightarrow{\gamma})(\overrightarrow{q_3}/\overrightarrow{q_1})+1)}{\overrightarrow{\alpha}^2(1+\overrightarrow{\gamma}/\overrightarrow{\beta})} \tag{3.17b}$$

If our modified hybrid-coupler design is able to meet the specifications contained in Equation 3.16, we will then be justified in using $|\overrightarrow{\alpha}| \approx |\overrightarrow{\beta}| \approx |\overrightarrow{\gamma}|$ to simplify Equation 3.17 in the following manner:

$$\frac{\overrightarrow{q_3}}{\overrightarrow{q_1}} = \frac{\overrightarrow{\Gamma_2}}{\overrightarrow{\Gamma_1}}\, e^{j2(\phi_\gamma-\phi_\beta)} \tag{3.18a}$$

$$\frac{\overrightarrow{q_2}}{\overrightarrow{q_1}} = -\left|\frac{\overrightarrow{\gamma}}{\overrightarrow{\alpha}}\right|^2 \frac{(\overrightarrow{q_3}/\overrightarrow{q_1})+e^{j(\phi_\gamma-\phi_\beta)}}{(1+e^{j(\phi_\gamma-\phi_\beta)})} \tag{3.18b}$$

In principle, $\phi_\gamma - \phi_\beta$ should be equal to $2\pi/3$ over the entire bandwidth. In practice, however, we obtain instead $\phi_\beta - \phi_\gamma = 2\pi/3 + \phi_0 + k\triangle f$ where k and $\phi_0$ are constants and $\Delta f$ is the shift from mid-frequency $f_{\mathrm{mid}}$. We infer from Equation 3.18 that we may adjust the relative $q_{\mathrm{k}}$ location by varying $\overline{\Gamma_1}$ and $\overline{\Gamma_2}$. The following possibilities may be considered for either or both of these two terminations in our effort to correct for the $k\Delta f$ term:

(a) <u>delay line</u> (of length d to introduce phase adjustment)

$$\arg(\overline{\Gamma}) = -\phi_{mid} - k\Delta f \tag{3.19}$$

where

$$k = -4\pi\sqrt{\mu\varepsilon_{eff}}\,d$$

and

$$\phi_{mid} = -4\pi f_{mid}\sqrt{\mu\varepsilon_{eff}}\,d$$

(b) <u>reactive components</u> (where ω = $2\pi f_{\mathrm{mid}}$ and $Z_0 = 50\Omega$)

<u>capacitor C</u>:

$$k = -\frac{2CZ_0}{1+(\omega CZ_0)^2} \tag{3.20a}$$

<u>inductor L</u>:

$$k = -\frac{2Z_0L}{(\omega L)^2 + Z_0^2} \tag{3.20b}$$

<u>Practical Example #1</u>

Supposing we performed experiments and found $k$ = 60°/GHz by substituting the measured data into $\phi_\gamma - \phi_\beta = 2\pi/3 + k\triangle f$, we can then opt for:

- either $\overrightarrow{\Gamma_2}$ to be a short-circuited transmission-line with delay of $60^o$ at mid-frequency
- or $\overrightarrow{\Gamma_1}$ to be an open-circuited transmission-line with delay of $60^o$ at mid-frequency.

Practical Example #2

Supposing we use any of the commercially-available software packages to plot the hybrid coupler's scattering coefficients in Figure 3.8 and found $k$ = $10^o$/GHz from the slope of the plot for $\phi_\gamma - \phi_\beta = 2\pi / 3 + k \triangle f$, we may then, by inserting an open-circuited transmission-line with delay of $10^o$ at the port for $\overrightarrow{\Gamma_2}$, be able to adjust the angular separations of the six-port's q-points from the original arrangement in Figure 3.9 (where the q-points are further apart with angular separations ranging from $90^o$ to $150^o$) to the improved arrangement in Figure 3.10 (where the q-points are closer together with angular separations ranging from $105^o$ to $140^o$).

It is also possible to use lumped components which may actually be preferred to delay lines. For this example, we can use an inductor for $\overrightarrow{\Gamma_2}$ and a capacitor for $\overrightarrow{\Gamma_1}$ to obtain the same level of improvement for the q-point distribution.

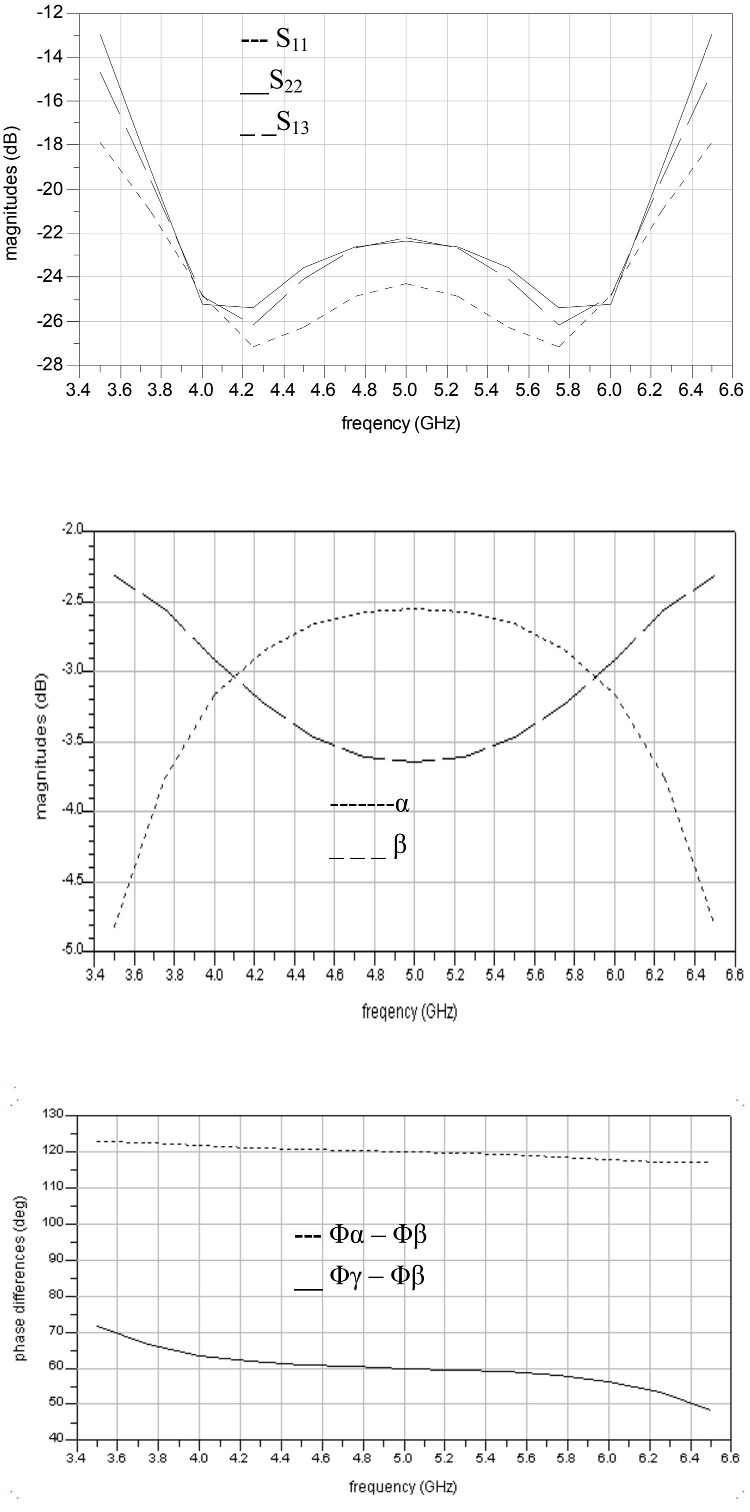

Figure 3.8 Scattering coefficients of rat-race coupler

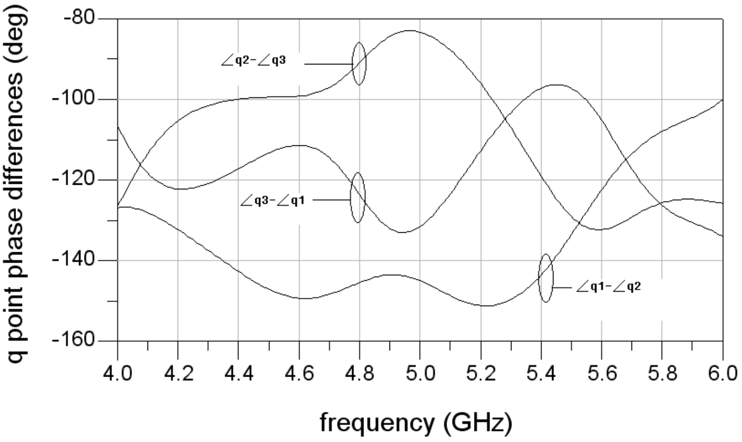

Figure 3.9 Angular separation of q-points for six-port reflectometer based on rat-race couplers of Figure 3.8

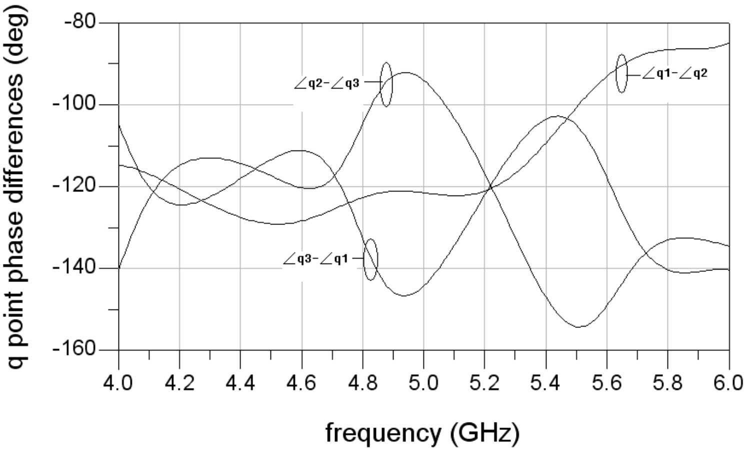

Figure 3.10 Angular separation of q-points for six-port reflectometer with 10° delay line

## REFERENCES

[3.1] G.F. Engen, Microwave Cicruit Theory & Foundations of Microwave Metrology (Peregrinus, 1992), Chapter 17 on six-port reflectometers

[3.2] G.F. Engen and C.A. Hoer, "Application of an arbitrary six-port junction to power-measurement problems", IEEE Trans. Instrum. Meas., vol. 21, pp. 470-474, Jun. 1972

[3.3] M. Weidman, "A semi-automated six-port for measuring millimeter-wave power and complex reflection coefficient", IEEE Trans. Microwave Theory Tech., vol. 25, pp. 1083-1085, Dec. 1977

[3.4] H. Cronson, "A 94-GHz diode-based single six-port reflectometer," IEEE Trans. Microwave Theory Tech., vol.30, pp. 1260-1264, Aug. 1982

[3.5] C.A. Hoer, "A network analyzer incorporating two six-port reflectometers", IEEE Trans. Microwave Theory Tech., vol. 25, pp. 1070-1074, Dec. 1977

[3.6] H. Cronson, "A dual six-port automatic network analyzer", IEEE Trans. Microwave Theory Tech, vol. 29, pp. 372-378, Apr. 1981

[3.7] C.M. Potter and G. Hjipieris, "Six-port reflectometer test arrangement and method including calibration," United States Patent 4,808,912, Feb. 1989

[3.8] H.C. Lu and T.H. Chu, "Microwave diversity imaging using six-port reflectometer," IEEE Trans. Microwave Theory Tech., vol. 47, pp. 84-87, Jan. 1999

[3.9] A. Stelzer, C.G. Diskus, K. Lubke and H.W. Thim, "A microwave position sensor with sub-millimeter accuracy," IEEE Trans. Microwave Theory Tech., vol. 47, pp. 2621-2624, Dec. 1999

[3.10] Y. Liu, "Calibrating an industrial microwave six-port instrument using the artificial neural network technique," IEEE Trans. Instrum. Meas., vol. 45, pp. 651-656, Apr. 1996

[3.11] E.R.B. Hansson and G.P. Riblet, "An ideal six-port network consisting of a matched reciprocal lossless five-port and a perfect directional coupler", IEEE Trans. Microwave Theory Tech., vol. 31, pp. 284-288, Mar. 1991

[3.12] S.P. Yeo and K.H. Lee, "Improvements in design of six-port reflectometer comprising symmetrical five-port junction and directional coupler," IEEE Trans. Instrum. Meas., vol. 39, pp. 184-188, Apr. 1990

[3.13] S.P. Yeo, "Analysis of symmetrical six-port junction when configured as a six-port reflectometer," IEEE Trans. Instrum. Meas., vol. 41, pp. 193-197, Apr. 1992

[3.14] S. K. Judah, "Planar symmetrical six-port junction," Proc. Inst. Elec. Eng., pt. H, vol. 134, pp.109-115, Apr. 1987

[3.15] J.J. Yao, Y. Chen and S.P. Yeo, "Modifying hybrid coupler to enhance six-port reflectometer performance," European Microwave Conf., pp. 256-259, Oct. 2005

[3.16] H. Cronson, “A six-port automatic network analyzer”, IEEE Trans. Microwave Theory Tech, vol. 25, pp. 1086-1091, Dec. 1977

[3.17] K.C. Gupta, “Computer aided design of microwave circuits”, Artech House, 1981

# APPENDIX

Reproduced below are the various possibilities we considered for the six-port reflectometer configurations based on our modified hybrid-coupler designs. The pairs of isolated ports for each hybrid coupler are clearly marked by ‘X’. There are seven ports available for connection to the DUT, four power detectors and two adjustable loads $\overrightarrow{\Gamma_1}$ and $\overrightarrow{\Gamma_2}$**;** three of the seven ports are labeled as (A), (B) and (C) while the remaining four ports are labeled as (1), (2), (3) and (4).

Configuration I: requires different designs for the four modified hybrid couplers

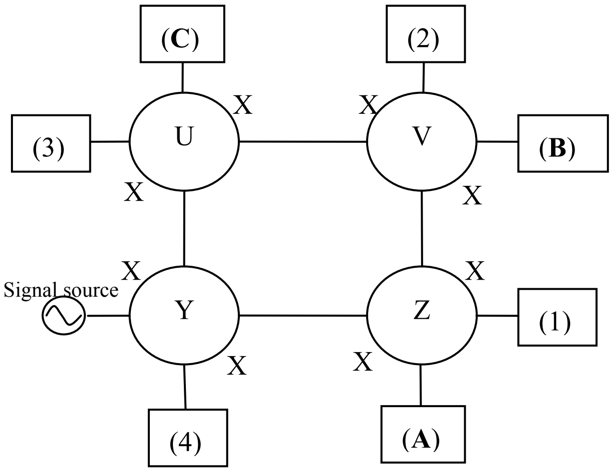

Place the DUT, $\overrightarrow{\Gamma_1}$ and $\overrightarrow{\Gamma_2}$ at any three of the ports labeled as (1), (2), (3) and (4)

Configuration II:  requires different designs for the four modified hybrid couplers

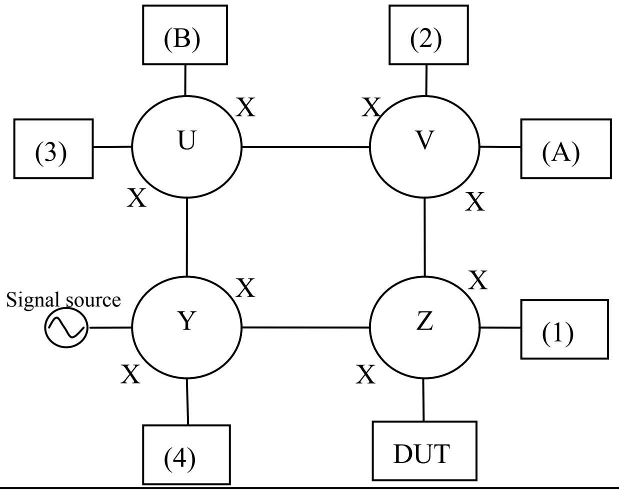

Place the power detectors at the ports labeled as (1), (2), (3) and (4) and place $\overrightarrow{\Gamma_1}$ and $\overrightarrow{\Gamma_2}$ at the ports labeled as (A) and (B)

Configuration III:  requires different designs for the four modified hybrid couplers

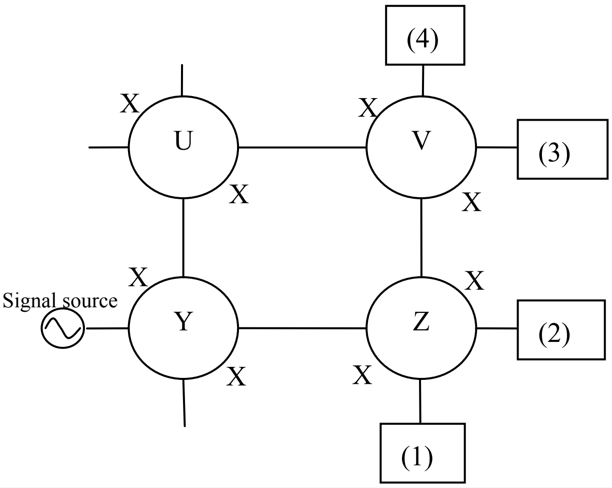

Place the DUT at any of the ports labeled as (1), (2), (3) and (4) before placing the power detectors, $\overrightarrow{\Gamma_1}$ and $\overrightarrow{\Gamma_2}$ at the remaining ports

Configuration IV:

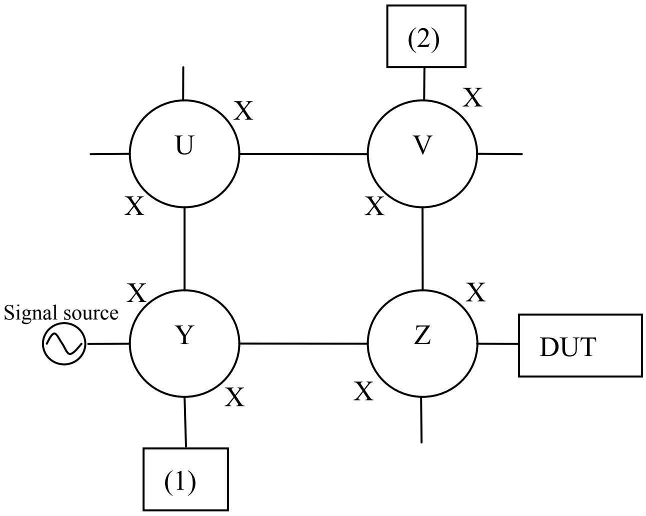

Place $\overrightarrow{\Gamma}_1$ and $\overrightarrow{\Gamma}_2$ at (1) and (2)

Configuration V:

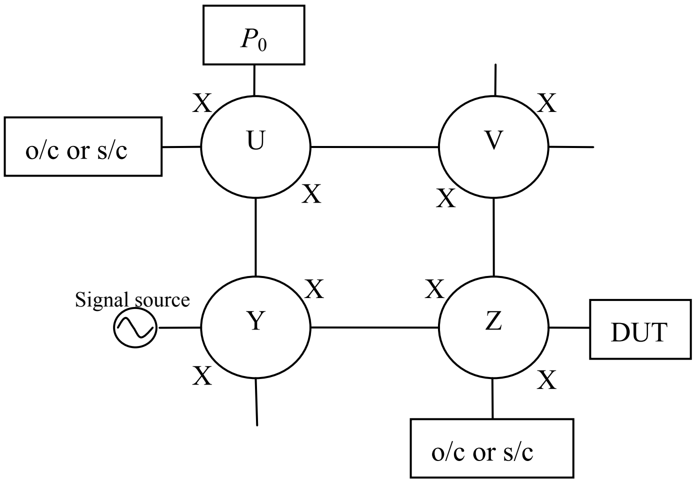

All possible permutations have to be evaluated in turn. As an example, we depict how the DUT, power detectors and adjustable loads may be connected to Configuration V with the resulting scattering matrix given by:

$$\bar{S} = \begin{bmatrix} 0 & \frac{1}{\sqrt{2}} e^{j(3\pi/4+\phi_0)} & 0 & \frac{1}{\sqrt{2}} e^{j\phi_0} \\ \frac{1}{\sqrt{2}} e^{j(3\pi/4+\phi_0)} & 0 & \frac{1}{\sqrt{2}} e^{j(\phi_0+\pi/2)} & 0 \\ 0 & \frac{1}{\sqrt{2}} e^{j(\phi_0+\pi/2)} & 0 & \frac{1}{\sqrt{2}} e^{j(3\pi/4+\phi_0)} \\ \frac{1}{\sqrt{2}} e^{j\phi_0} & 0 & \frac{1}{\sqrt{2}} e^{j(3\pi/4+\phi_0)} & 0 \end{bmatrix}$$

However, the q-points are located at $1.4\angle 0^{\circ}$, $1.4\angle 90^{\circ}$ and $1.4\angle 180^{\circ}$.

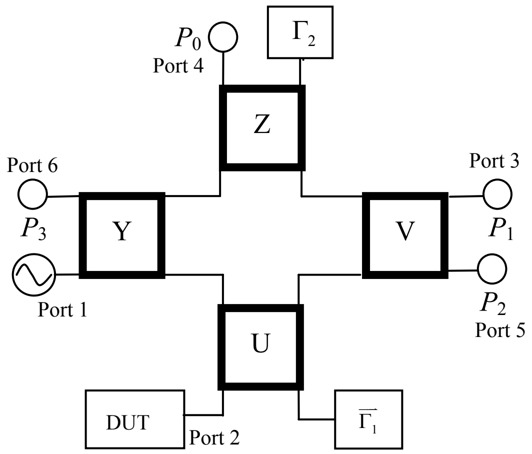

# Chapter 4

# FOUR-PORT COUPLER ANALYSIS

It has already been pointed out in Chapter 3 that we should not use the standard hybrid-coupler designs because the six-port reflectometers based on such readily-available couplers have thus far yielded q-points with angular separations that may be $90^o$, $135^o$ or even $180^o$. We thus need to modify the designs of the quadrature or $180^o$ hybrid couplers so as to meet the criteria spelt out for the six-port reflectometer's q-point distribution.

To fine-tune our modified hybrid-coupler design for wide-band application, we will need to incorporate the effects of junction parasitics and compensation elements. An overview of these higher-order features (which we have included during our design optimization efforts in Chapter 5) is thus presented in Section 4.4 for both microstrip and coplanar-waveguide designs.

## 4.1 Overview of Four-Port Couplers

The most common four-port couplers are based on the coupled-line [4.1]-[4.4], branch-line [4.5]-[4.6] and rat-race [4.7]-[4.10] structures. The coupled-line structure has the advantage of small size but it is difficult to fabricate couplers with tight coupling. The multi-stage structure

[4.14] allows for tight coupling but such designs tend to be larger than other coupler constructions. In recent years, researchers have resorted to broadside-coupled couplers which attempt to obviate this shortcoming; however, we have not opted for this broadside-coupled structure because of the need to address spurious reflections due to structural mismatches at the inter-connections between the four constituent couplers in our proposed six-port reflectometer system. Ultra-wideband four-port couplers with very good matching and isolation characteristics [4.12]-[4.13] have also been attracting attention but their multi-layer structures present fabrication complexities and thus incur higher costs.

For our modified hybrid-coupler design, we shall focus on the branch-line and rat-race structures which are known to offer wider coupling-coefficient range when compared with the coupled-line counterparts. It is straightforward to design 3dB couplers which are often used to divide or combine signals in many microwave applications [4.5]-[4.10]. In addition, it is not difficult to extend the coupler's bandwidth and fabrication is nowadays routine for designs implemented in microstrip, slot-line, CPW, *etc*. The main disadvantage is size especially for multi-section designs based on branch-line or rat-race structures. Lumped-element couplers [4.20]-[4.22] with similar structures as branch-line or rat-race couplers have been attempted in an effort to reduce size at the expense of performance, and other size-reduction techniques [4.15]-[4.19] will have to be considered instead.

It should be pointed out that our primary objective here is to design modified hybrid couplers for use as the core components of our proposed six-port reflectometer. Hence, the focus of our design optimization effort is to meet the criteria spelt out for the six-port reflectometer's q-point distribution. The empirical findings of our simulations in Sub-Section 3.2.3 already suggest that we may be allowed to relax the tolerance limits for certain design specifications of the hybrid coupler so long as the resultant six-port reflectometer continues to meet the q-point requirements. Naturally, the design optimization process outlined in Section 4.3 may be readily adapted if there is a request to design modified hybrid couplers to function in their original role (but with non-standard phase characteristics).

## 4.2 Eigenmode Analysis

Four-port structures such as quadrature and 180$^o$ hybrid couplers are usually symmetrical about one or more mid-planes. The physical symmetry allows us to utilize eigenmode analysis to develop a model that is able to predict the coupler's scattering coefficients. We can extend the analysis to derive general design equations for the coupler to operate at a specific frequency (or over a narrow bandwidth when given the appropriate tolerance limits). In addition, the analytical results lead us to explore the link between branch-line couplers and rat-race couplers. New types of 90$^o$ hybrids may then be devised.

The underlying principle of the even- and odd-mode analysis procedure is to transform the original structure of the four-port coupler into two reduced two-port networks by capitalizing on certain open- or short-circuited properties. Cascading line sections and stubs can be readily included; by multiplying the ABCD matrices of the line sections and stubs, we can obtain the overall ABCD parameters of the even- and odd-mode two-port networks and thereafter convert to the scattering matrix of the four-port network.

### 4.2.1 Analysis of basic hybrid-coupler structures

Consider, by way of example, the branch-line and rat-race couplers depicted in Figures 4.1(a) and 4.1(b) respectively**:** the symmetry about the mid-planes represented by the dash lines allows the four-port structure to be reduced to the two-port structures outlined in Figure 4.2 for their even- and odd-excitation modes (with open- or short-circuit terminations respectively for the shunt stubs affixed to the main lines).

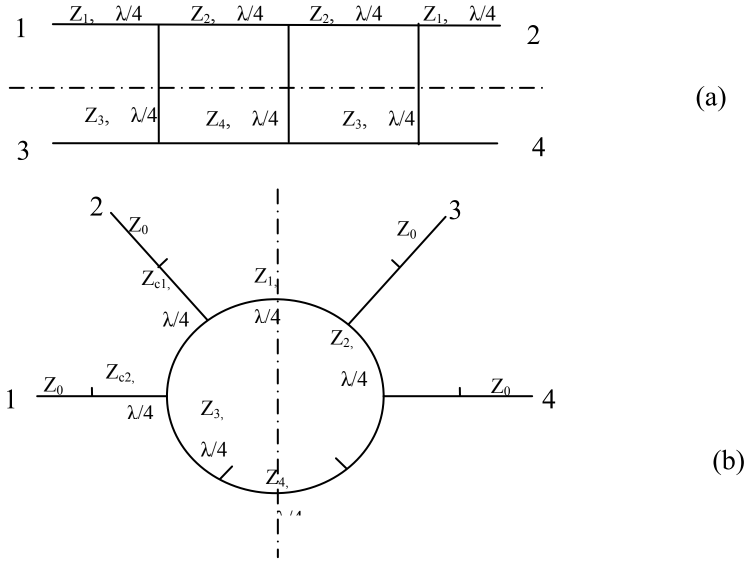

Figure 4.1 Typical structures for hybrid couplers

(a) branch-line four-port coupler (order 3)

(b) rat-race coupler

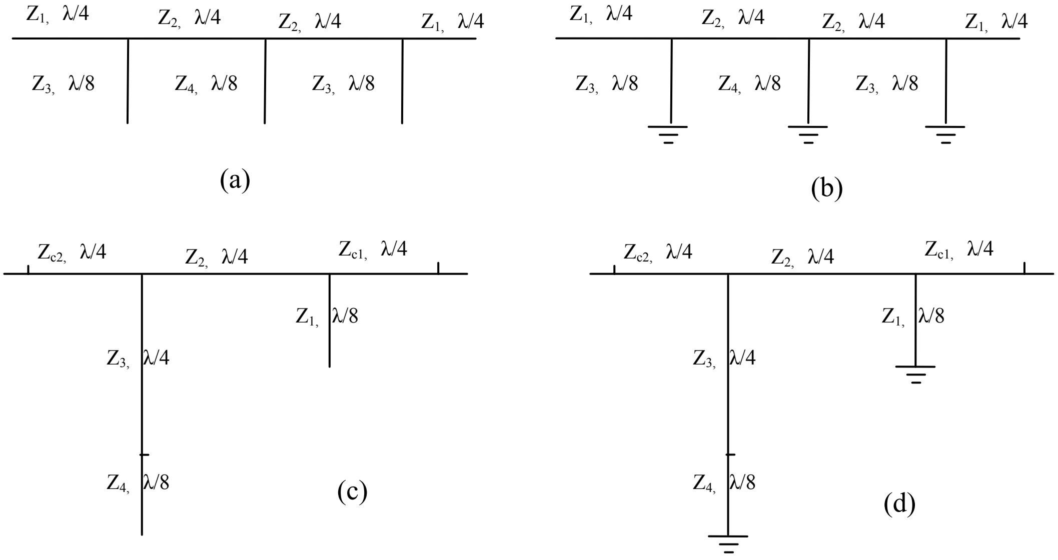

Figure 4.2 Partitioning hybrid couplers (Figure 4.1) for eigenmode analysis
(a) even mode of branch line coupler
(b) odd mode of branch line coupler
(c) even mode of rat-race coupler
(d) odd mode of rat-race coupler

After deriving the ABCD parameters of the even- and odd-mode two-port networks, we can obtain the scattering matrix of the four-port coupler via simple transformations. Listed in Equation 4.1 are the inter-relationships between the coupler's scattering coefficients and the eigenmode results of the reduced two-port networks:

$$\overline{S_{11}} = \frac{1}{2}(\overline{S}_{11\_even} + \overline{S}_{11\_odd}) \tag{4.1a}$$

$$\overline{S_{12}} = \frac{1}{2}(\overline{S}_{12\_even} + \overline{S}_{12\_odd}) \tag{4.1b}$$

$$\overline{S_{13}} = \frac{1}{2}(\overline{S}_{21\_even} - \overline{S}_{21\_odd}) \tag{4.1c}$$

$$\overline{S_{14}} = \frac{1}{2}(\overline{S}_{11\_even} - \overline{S}_{11\_odd}) \tag{4.1d}$$

$$\overline{S_{22}} = \frac{1}{2}(\overline{S}_{22\_even} + \overline{S}_{22\_odd}) \tag{4.1e}$$

$$\overline{S_{23}} = \frac{1}{2}(\overline{S}_{22\_even} - \overline{S}_{22\_odd}) \tag{4.1f}$$

The design specifications for such a coupler to operate at a specific frequency (or over a narrow bandwidth when given the appropriate tolerance limits) can be listed thus:

$$\overrightarrow{S_{11}} = 0 \tag{4.2a}$$

$$\overrightarrow{S_{22}} = 0 \tag{4.2b}$$

$$\overrightarrow{S_{13}} = 0 \tag{4.2c}$$

$$\left|\overrightarrow{S_{12}}\right| = \left|\overrightarrow{S_{14}}\right| \tag{4.2d}$$

The design equations (based on the specifications listed in Equation 4.2) are reproduced in Equations 4.3 and 4.4 for branch-line and rat-race couplers respectively.

<u>for branch-line couplers</u>:

$$\begin{gathered}(-2500Z_2^4Z_3^2Z_4^2(2500+Z_3^2)+5000Z_1^2Z_2^2Z_3Z_4(Z_2^2(2500+Z_3^2)-2500Z_3Z_4)+\ldots \\ Z_1^4(Z_3^2-2500)(Z_2^4(2500+Z_3^2)-5000Z_2^2Z_3Z_4+2500Z_3^2Z_4^2))=0\end{gathered} \tag{4.3a}$$

$$\begin{gathered}50Z_3(-Z_2^2Z_3Z_4+Z_1^2(2Z_2^2-Z_3Z_4))=\ldots \\ (2500Z_2^2Z_3Z_4+Z_1^2(Z_2^2(Z_3^2-2500)+2500Z_3Z_4))\end{gathered} \tag{4.3b}$$

$$\begin{gathered}Z_2^2Z_3Z_4(Z_2^2(2500+Z_3^2)-2500Z_3Z_4)=\ldots \\ Z_1^2(Z_2^4(2500+Z_3^2)-5000Z_2^2Z_3Z_4+2500Z_3^2Z_4^2)\end{gathered} \tag{4.3c}$$

<u>for rat-race coupler</u>:

$$Z_3^2Z_{\mathrm{c}1}^2 = Z_{\mathrm{c}2}^2Z_1Z_4 \tag{4.4a}$$

$$6250000Z_3^8 = 4Z_4^4Z_{c2}^8 \tag{4.4b}$$

$$Z_3^2Z_{c1} = Z_2Z_4Z_{c2} \tag{4.4c}$$

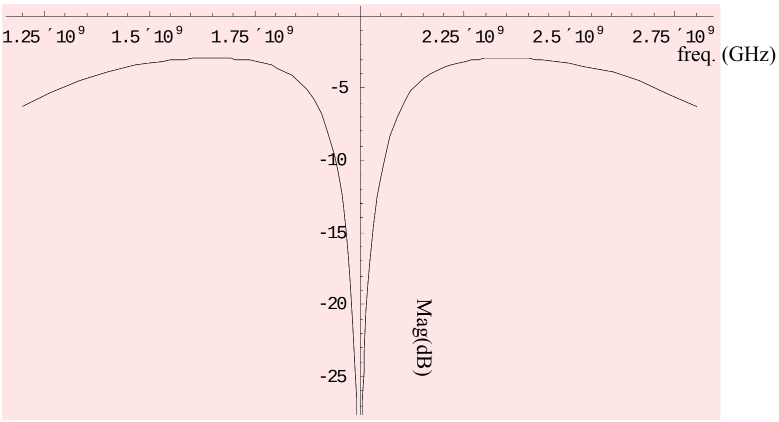

(a) $S_{11}$ and $S_{22}$

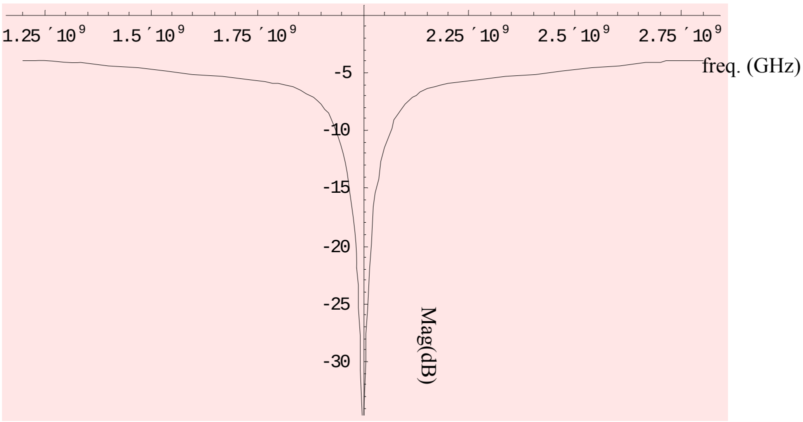

(b) $S_{14}$

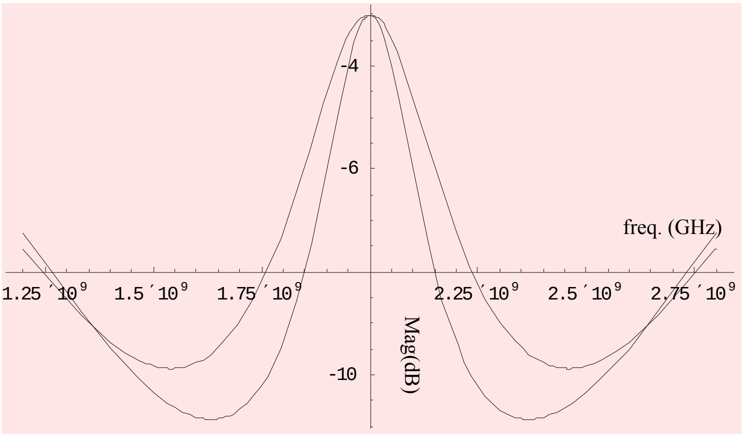

(c) $S_{12}$ and $S_{13}$

Figure 4.3 Example of simulation results for narrow-band branch line coupler design

MATLAB or MATHEMATICA may be employed to solve Equations 4.3 or 4.4 which are undetermined (since the number of unknowns exceeds the number of equations). Figure 4.3 presents the simulation results for a branch-line coupler example where we chose $Z_1 = 40\Omega$ and then utilized Equation 4.3 to obtain $Z_2 = 40\Omega$, $Z_3 = 20\Omega$ and $Z_4 = 455\Omega$ for a design operating at 2GHz. The scattering-coefficient plots clearly show that this design is not for wide-band application.

### 4.2.2 Analysis of cascaded-coupler structures

Muraguchi [4.6] presented a general branch-line coupler structure which can be used to design a $90^o$ hybrid coupler with wider bandwidth. Rehnmark [4.63] described a different structure for the general $180^o$ hybrid coupler with improved bandwidth. We shall assimilate the two so as to develop a consolidated approach that allows the design of both $90^o$ and $180^o$ hybrid couplers.

Depicted in Figure 4.4 is the multi-section branch-line structure reproduced from [4.6]. We shall demonstrate that the $90^o$ and $180^o$ hybrids are actually two variations of the structure proposed in Figure 4.5. The physical symmetry allows for eigenmode analysis and we proceed by applying even- and odd-mode analysis to derive expressions for the scattering coefficients at the specified mid-frequency $f_c$.

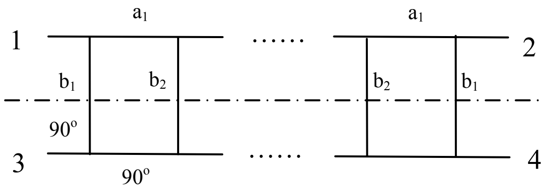

Figure 4.4 Multi-section branch-line structure reproduced from [4.6]

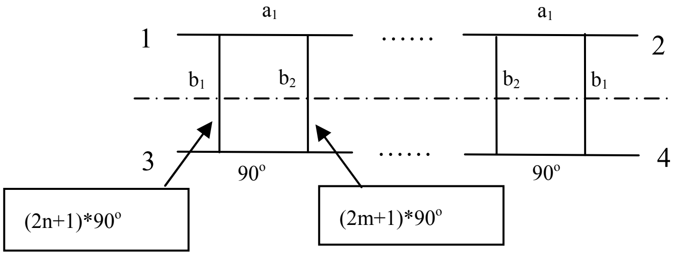

Figure 4.5 Proposed multi-section four-port structure

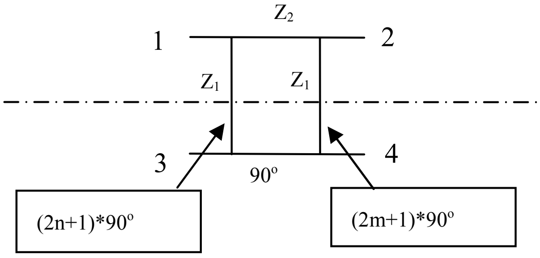

Figure 4.6 Basic one-section unit drawn from midst of four-port structure proposed in Figure 4.5

Depicted in Figure 4.6 is the basic one-section unit we extracted from the midst of the multi-section four-port structure proposed in Figure 4.5. With that as our starting point so as to simplify the analysis, we have been able to derive all of the expressions listed in Appendix III for the scattering coefficients of the multi-section coupler. These scattering-coefficient expressions may be grouped into the following two cases for ease of understanding:

(1) when n and m are both even integers or when n and m are both odd integers

$$S11 = \frac{-12500000\, Z1^2\, Z2^2 + 6250000\, Z2^4 - Z1^4\,(-6250000 + Z2^4)}{6250000\, Z2^4 + 5000\, Z1^2\, Z2^2\,(-2500 + Z2^2) + Z1^4\,(2500 + Z2^2)^2}$$

$$S12 = \frac{100\,\mathrm{i}\; Z1^2\, Z2\,(-2500\, Z2^2 + Z1^2\,(2500 + Z2^2))}{6250000\, Z2^4 + 5000\, Z1^2\, Z2^2\,(-2500 + Z2^2) + Z1^4\,(2500 + Z2^2)^2}$$

$$S13 = \frac{10000\, Z1^3\, Z2^3}{6250000\, Z2^4 + 5000\, Z1^2\, Z2^2\,(-2500 + Z2^2) + Z1^4\,(2500 + Z2^2)^2}$$

$$S14 = \frac{100\,\mathrm{i}\; Z1\, Z2^2\,(2500\, Z2^2 + Z1^2\,(-2500 + Z2^2))}{6250000\, Z2^4 + 5000\, Z1^2\, Z2^2\,(-2500 + Z2^2) + Z1^4\,(2500 + Z2^2)^2} \tag{4.5}$$

(2) when either n or m is an odd integer and the other is an even integer

$$S11 = \frac{2500\, Z2^2 - Z1^2\,(-2500 + Z2^2)}{2500\, Z2^2 + Z1^2\,(2500 + Z2^2)}$$

$$S12 = \frac{100\,\mathrm{i}\; Z1^2\, Z2}{2500\, Z2^2 + Z1^2\,(2500 + Z2^2)}$$

$$S13 = 0$$

$$S14 = \frac{100\,\mathrm{i}\; Z1\, Z2^2}{2500\, Z2^2 + Z1^2\,(2500 + Z2^2)}$$

or

$$S14 = -\frac{100\,\mathrm{i}\; Z1\, Z2^2}{2500\, Z2^2 + Z1^2\,(2500 + Z2^2)}\;; \tag{4.6}$$

We may infer the following from the two sets of scattering-coefficient expressions listed in Equations 4.5-4.6:

(1) when n and m are both even integers or when n and m are both odd integers, either Port 2 or Port 4 of the four-port network is isolated from Port 1 while the remaining two ports (which are coupled to Port 1) have a phase difference of $\pm 90^o$

(2) when either n or m is an odd integer and the other is an even integer, only Port 3 is isolated from Port 1 while the remaining two ports (which are coupled to Port 1) have a phase difference of either $0^o$ or $180^o$.

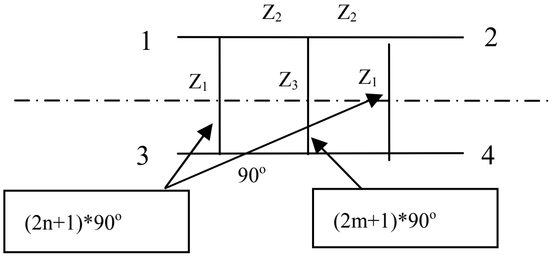

Figure 4.7 Basic two section unit of four-port structure

We now proceed to ascertain whether these findings for the simple one-section unit depicted in Figure 4.6 may be extended to the more complicated two-section unit depicted in Figure 4.7. Listed in Chapter 4's Appendix are the detailed expressions for the scattering coefficients which, once again, may be grouped into the following two cases for ease of understanding:

(1) when n and m are both even integers or when n and m are both odd integers

$$S11 = \frac{-(-6250000 + Z1^4)\ Z2^4 - 25000000\ Z1\ Z2^2\ Z3 + 25000000\ Z1^2\ Z3^2}{(2500 + Z1^2)\ ((2500 + Z1^2)\ Z2^4 - 10000\ Z1\ Z2^2\ Z3 + 10000\ Z1^2\ Z3^2)}$$

$$S12 = \frac{10000\ Z1^3\ Z3\ (-Z2^2 + Z1\ Z3)}{(2500 + Z1^2)\ ((2500 + Z1^2)\ Z2^4 - 10000\ Z1\ Z2^2\ Z3 + 10000\ Z1^2\ Z3^2)}$$

$$S13 = -\frac{100\ i\ Z1^2\ Z3\ ((-2500 + Z1^2)\ Z2^2 + 5000\ Z1\ Z3)}{(2500 + Z1^2)\ ((2500 + Z1^2)\ Z2^4 - 10000\ Z1\ Z2^2\ Z3 + 10000\ Z1^2\ Z3^2)}$$

$$S14 = -\frac{100\ i\ Z1\ (-(2500 + Z1^2)\ Z2^4 + Z1\ (7500 + Z1^2)\ Z2^2\ Z3 - 5000\ Z1^2\ Z3^2)}{(2500 + Z1^2)\ ((2500 + Z1^2)\ Z2^4 - 10000\ Z1\ Z2^2\ Z3 + 10000\ Z1^2\ Z3^2)}$$

$$S22 = \frac{-(-6250000 + Z1^4)\ Z2^4 - 25000000\ Z1\ Z2^2\ Z3 + 25000000\ Z1^2\ Z3^2}{(2500 + Z1^2)\ ((2500 + Z1^2)\ Z2^4 - 10000\ Z1\ Z2^2\ Z3 + 10000\ Z1^2\ Z3^2)}$$

$$S23 = -\frac{100\ i\ Z1\ (-(2500 + Z1^2)\ Z2^4 + Z1\ (7500 + Z1^2)\ Z2^2\ Z3 - 5000\ Z1^2\ Z3^2)}{(2500 + Z1^2)\ ((2500 + Z1^2)\ Z2^4 - 10000\ Z1\ Z2^2\ Z3 + 10000\ Z1^2\ Z3^2)} \qquad (4.7)$$

(2) when either n or m is an odd integer and the other is an even integer

$$\begin{aligned}
S11 &= \frac{-(-6250000 + Z1^4)\, Z2^4 + 25000000\, Z1\, Z2^2\, Z3 + 25000000\, Z1^2\, Z3^2}{(2500 + Z1^2)\, ((2500 + Z1^2)\, Z2^4 + 10000\, Z1\, Z2^2\, Z3 + 10000\, Z1^2\, Z3^2)} \\
S12 &= \frac{10000\, Z1^3\, Z3\, (Z2^2 + Z1\, Z3)}{(2500 + Z1^2)\, ((2500 + Z1^2)\, Z2^4 + 10000\, Z1\, Z2^2\, Z3 + 10000\, Z1^2\, Z3^2)} \\
S13 &= -\frac{100\, i\, Z1^2\, Z3\, ((-2500 + Z1^2)\, Z2^2 - 5000\, Z1\, Z3)}{(2500 + Z1^2)\, ((2500 + Z1^2)\, Z2^4 + 10000\, Z1\, Z2^2\, Z3 + 10000\, Z1^2\, Z3^2)} \\
S14 &= -\frac{100\, i\, Z1\, ((2500 + Z1^2)\, Z2^4 + Z1\, (7500 + Z1^2)\, Z2^2\, Z3 + 5000\, Z1^2\, Z3^2)}{(2500 + Z1^2)\, ((2500 + Z1^2)\, Z2^4 + 10000\, Z1\, Z2^2\, Z3 + 10000\, Z1^2\, Z3^2)} \\
S22 &= \frac{-(-6250000 + Z1^4)\, Z2^4 + 25000000\, Z1\, Z2^2\, Z3 + 25000000\, Z1^2\, Z3^2}{(2500 + Z1^2)\, ((2500 + Z1^2)\, Z2^4 + 10000\, Z1\, Z2^2\, Z3 + 10000\, Z1^2\, Z3^2)} \\
S23 &= -\frac{100\, i\, Z1\, ((2500 + Z1^2)\, Z2^4 + Z1\, (7500 + Z1^2)\, Z2^2\, Z3 + 5000\, Z1^2\, Z3^2)}{(2500 + Z1^2)\, ((2500 + Z1^2)\, Z2^4 + 10000\, Z1\, Z2^2\, Z3 + 10000\, Z1^2\, Z3^2)}
\end{aligned} \tag{4.8}$$

We may infer the following from the two sets of scattering-coefficient expressions listed in Equations 4.7-4.8:

(1) when n and m are both even integers or when n and m are both odd integers, either Port 2 or Port 4 of the four-port network is isolated from Port 1 while the remaining two ports (which are coupled to Port 1) have a phase difference of $0^o$, $90^o$ and $180^o$

(2) when either n or m is an odd integer and the other is an even integer, only Port 3 is isolated from Port 1 while the remaining two ports (which are coupled to Port 1) have a phase difference of $90^o$.

Hence, the multi-section four-port structure proposed in Figure 4.5 may be designed as $0^o$, $90^o$ and $180^o$ hybrid couplers (especially for wide-band $180^o$ hybrids). We must distinguish between the two cases — *either* when m and n are both even/odd integers *or* when one is odd while the other is even.

Furthermore, there is the additional possibility for us to extend the analysis to the three-section unit as the basic building block but the derivation will be more complicated. This may be worth exploring in future should the need arise.

### 4.2.3 Analysis of other hybrid-coupler structures

We can build upon the derivation and findings of Sub-Sections 4.2.1-4.2.2 to develop other interesting variations of the four-port structure. The first two variants (which offer useful insights for our objective to design a hybrid coupler for use in the six-port reflectometer) may be used as dividers to split a wave at the input port into output waves at two other ports. In contrast, the third variant provides the possibility of channeling the wave from the input port to only one output port; since there are two ports without output waves, this particular design may be useful for cross-over application in planar integrated circuits.

(a) two-section 180° hybrid construction (narrow bandwidth)

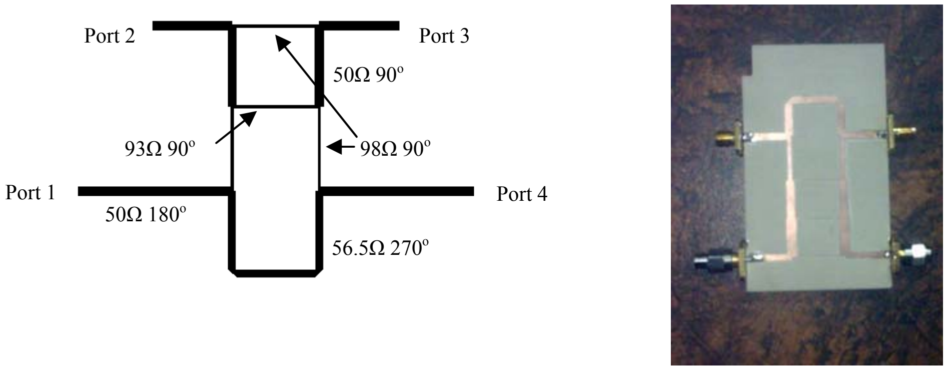

Figure 4.8 Lay-out for two-section 180° hybrid structure

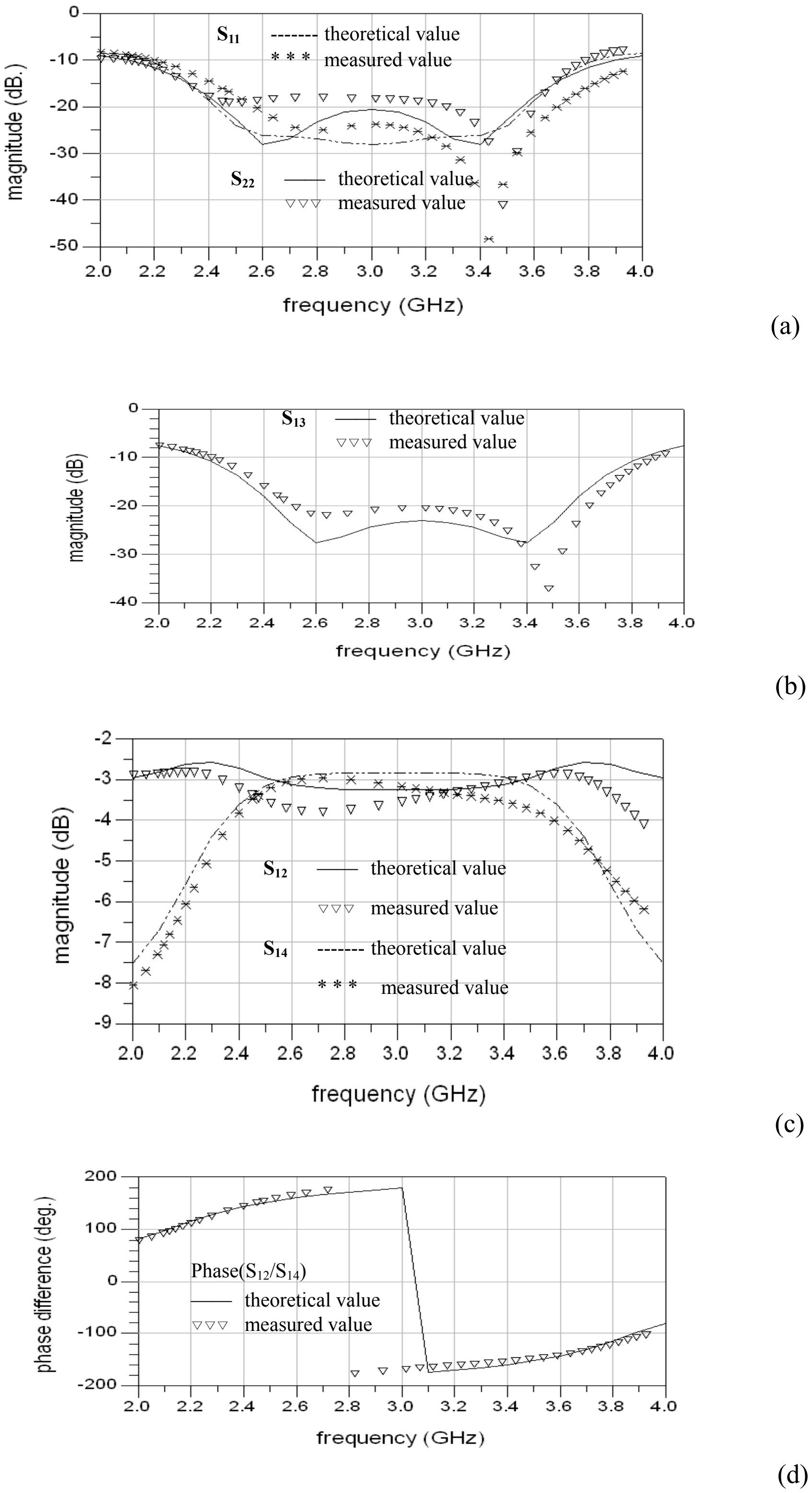

Figure 4.9 Simulation and measured results of two-section 180° hybrid structure

(a) return loss

(b) isolation between two input arms

(c) power division ratio of power dividing arms

(d) phase difference of power dividing arms

### (b) two-section 90° hybrid construction (wider bandwidth)

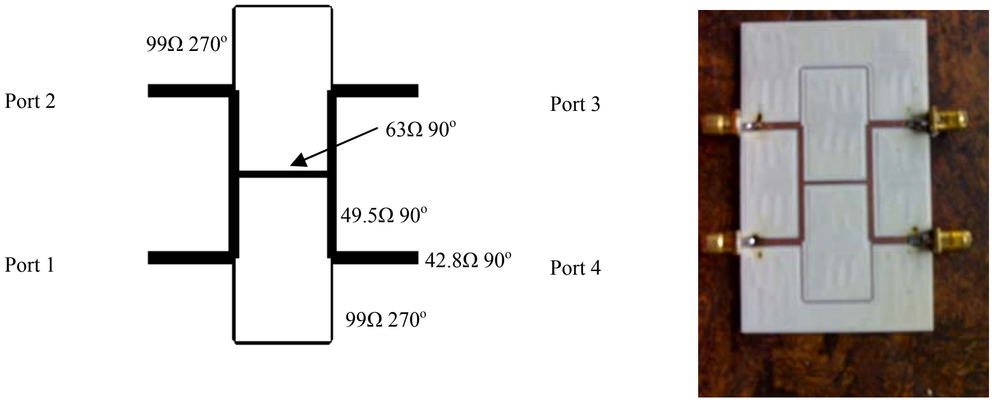

Figure 4.10 Lay-out for two-section 90° hybrid structure

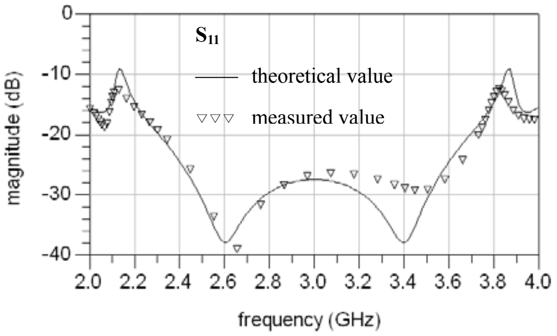

(a)

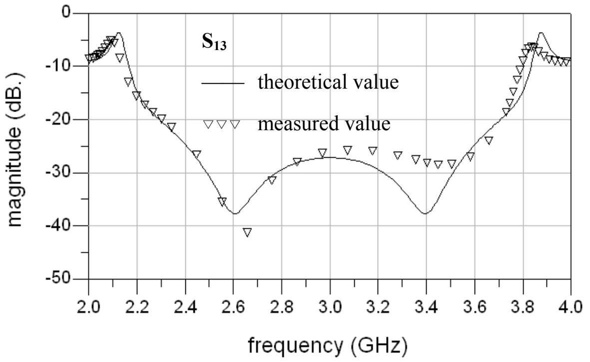

(b)

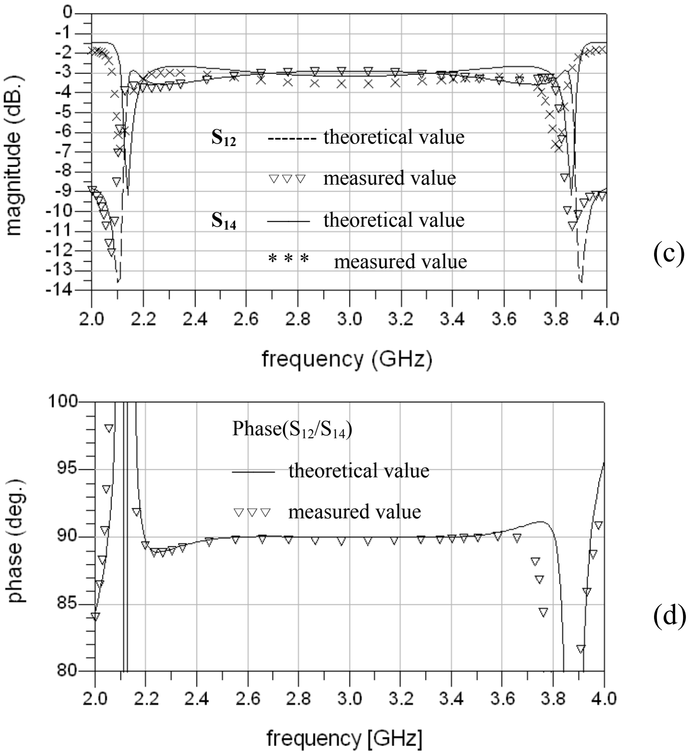

Figure 4.11 Simulation and measured results for two-section 90° hybrid structure

(a) return loss

(b) isolation coefficients

(b) power division ratio of power-dividing arms

(c) phase difference of power-dividing arms

## (c) two-section hybrid cross-over

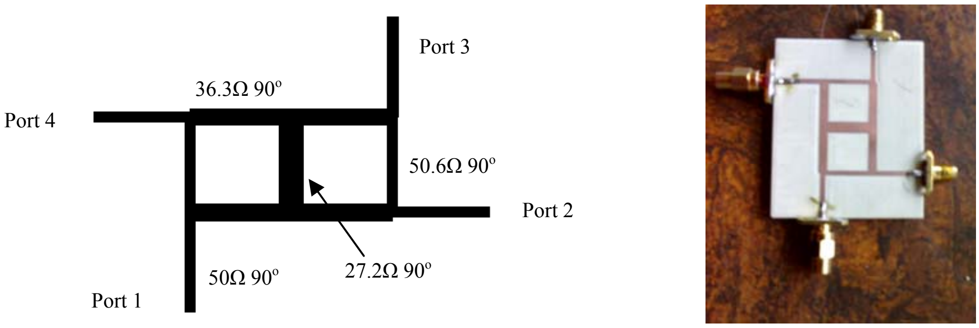

Figure 4.12 lay-out of two-section hybrid cross-over

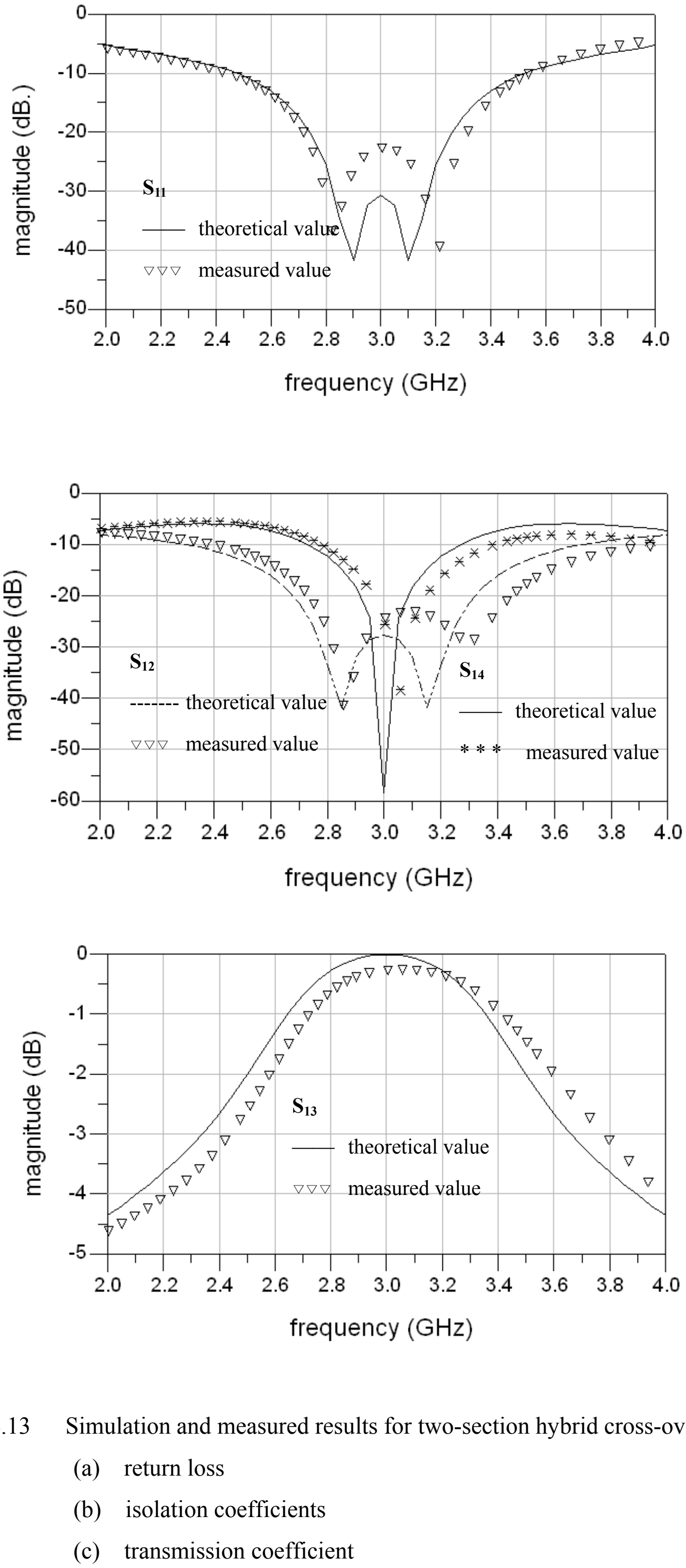

Figure 4.13 Simulation and measured results for two-section hybrid cross-over

(a) return loss

(b) isolation coefficients

(c) transmission coefficient

## 4.3 Modification of Standard Hybrid-Coupler Designs

Although design equations may be available, we still need to resort to optimization because of the requirement for a wider bandwidth or because of the need to impose tighter tolerance for the more critical performance characteristics. The optimization process entails the following:

- define an error function
- choose appropriate algorithm(s) to search through the range of possibilities
- select an initial set of parameter settings as the starting point for the search process.

During the course of our optimization efforts, we have found it important to consider all operational details due to the likelihood of multiple local minima appearing during the search process. In particular, we shall provide an example in Sub-Section 4.3.1 to illustrate that the choice of initial parameter settings plays a pivotal role for our modified hybrid-coupler design.

### 4.3.1 Optimization considerations

The error function to be defined for the optimization process must naturally be based on the ideal-case specifications listed in Equations 4.2. However, our analysis thus far has indicated the need to add other criteria. We have already noted in Section 3.2 that the scattering matrix of the hybrid coupler ought to be written in the following form so as to take hardware imperfections into consideration:

$$\overrightarrow{S}_{prototype} = \begin{bmatrix} \overrightarrow{\zeta_1} & \vec{\xi} & \overrightarrow{\alpha} & \overrightarrow{\beta} \\ \vec{\xi} & \overrightarrow{\zeta_2} & \vec{\gamma} & \vec{\xi} \\ \overrightarrow{\alpha} & \vec{\gamma} & \overrightarrow{\zeta_2} & \vec{\delta} \\ \overrightarrow{\beta} & \overrightarrow{\alpha} & \vec{\xi} & \overrightarrow{\zeta_1} \end{bmatrix} \tag{4.9}$$

Accordingly, we may define the error function in the following manner:

$$F_{error}(Z_1, Z_2, Z_3, ......) = \sum_{i=1}^{6} w_i g_i \tag{4.10}$$

where

$$g_1 = \sum_{j=1}^{N} |\overrightarrow{\zeta_1}(f_j)|^2 \qquad g_2 = \sum_{j=1}^{N} |\overrightarrow{\zeta_2}(f_j)|^2$$

$$g_3 = \sum_{j=1}^{N} |\vec{\xi}(f_j)|^2, \qquad g_4 = \sum_{j=1}^{N} ||\overrightarrow{\alpha}(f_j)/\overrightarrow{\beta}(f_j)|-1|$$

$$g_5 = \sum_{j=1}^{N} |\overrightarrow{\alpha}^2(f_j)/\overrightarrow{\beta}^2(f_j) - e^{-j2\pi/3}| \qquad g_6 = \sum_{j=1}^{N} |\vec{\gamma}^2(f_j)/\overrightarrow{\beta}^2(f_j) - e^{j2\pi/3}|$$

$$f_j = f_L + (j-1)(f_H - f_L)/(N-1), \qquad \text{j = 1, 2, …, N}$$

with $f_H$ and $f_L$ being the highest and lowest frequency respectively of the requisite bandwidth.

We have found from experience that there should be flexibility for us to adapt the error function defined in Equation 4.10 in accordance with the design details. Even a minor modification of the error-function definition will change the relative contributions of the constituent errors to the total error and thus affect the optimization speed and convergence results. Returning to Equation 4.10 for illustration, we may re-define $g_4$, $g_5$ and $g_6$ as

$$\begin{aligned} g_4 &= \sum_{j=1}^{N} (|\overrightarrow{\alpha}(f_j)/\overrightarrow{\beta}(f_j)|-1)^2 \\ g_5 &= \sum_{j=1}^{N} |\overrightarrow{\alpha}(f_j)/\overrightarrow{\beta}(f_j) - e^{-j\pi/3}|^2 \\ g_6 &= \sum_{j=1}^{N} |\vec{\gamma}(f_j)/\overrightarrow{\beta}(f_j) - e^{j\pi/3}|^2 \end{aligned} \tag{4.11}$$

In addition, there is the need to impose constraints so as to ensure that the design parameters returned by the optimization software can actually be implemented in practice. Consider, by way of example, the characteristic impedance of a microstrip line which should not exceed certain bounds due to fabrication practicalities for its line-width. Such constraints may be incorporated into the error function by employing Lagrange multipliers. Returning again to Equation 4.10 for illustration, it is possible for us to impose the constraint of $Z_i < R$ by introducing slack variables into the error function in the following manner:

$$\begin{aligned} F'_{error} &= F_{error}(Z'_1, Z'_2 ......, Z'_n) \\ Z'_i &= R - Z^2_{n+i} \end{aligned} \tag{4.12}$$

Equation 4.12 is an unconstrained extreme problem which can be approached by employing any or a combination of techniques (*eg* quasi-Newton, least path, steepest gradient, *etc*). Details of such algorithms are available in [4.23]-[4.26].

A simple trial will help to highlight the considerations to be taken into account. One of our preliminary designs is a hybrid coupler based on the rat-race structure depicted in Figure 4.14 for operation over a 50% bandwidth. When we first chose the following set of initial parameter settings to initiate the search for the minimum of the error function (Equation 4.10)

$Z_1 = 90\Omega$, $Z_2 = 75\Omega$, $Z_3 = 45\Omega$, $Z_4 = 35\Omega$, $Z_{c1} = 55\Omega$, $Z_{c2} = 45\Omega$, $Z_{c3} = 50\Omega$ and $Z_{c4} = 50\Omega$ ,

we obtained the following design by using the quasi-Newton algorithm:

$Z_1 = 57\Omega$, $Z_2 = 47\Omega$, $Z_3 = 38\Omega$, $Z_4 = 29\Omega$, $Z_{c1} = 47\Omega$, $Z_{c2} = 38\Omega$, $Z_{c3} = 50\Omega$ and $Z_{c4} = 50\Omega$.

(4.13a)

When we performed a second round of optimization with the following set of initial parameter settings (with changes in the initial settings of only two parameters)

$Z_1 = 120\Omega$, $Z_2 = 75\Omega$, $Z_3 = 45\Omega$, $Z_4 = 35\Omega$, $Z_{c1} = 80\Omega$, $Z_{c2} = 45\Omega$, $Z_{c3} = 50\Omega$ and $Z_{c4} = 50\Omega$

using the quasi-Newton algorithm a second time yielded the following design with a difference of more than 15% for the $Z_{c1}$ parameter:

$Z_1 = 130\Omega$, $Z_2 = 74\Omega$, $Z_3 = 41\Omega$, $Z_4 = 31\Omega$, $Z_{c1} = 94\Omega$, $Z_{c2} = 40\Omega$, $Z_{c3} = 70\Omega$ and $Z_{c4} = 50\Omega$.

(4.13b)

Plotted in Figures 4.15 and 4.16 are the scattering coefficients for the coupler designs listed in Equations 4.13(a) and 4.13(b) respectively. By merely changing the initial parameter settings, we obtained coupler designs with dissimilar performance characteristics (even when using the same search algorithm); for this case, the coupler design we obtained during the second round of optimization yields a poorer phase response as shown in Figure 4.16(c).

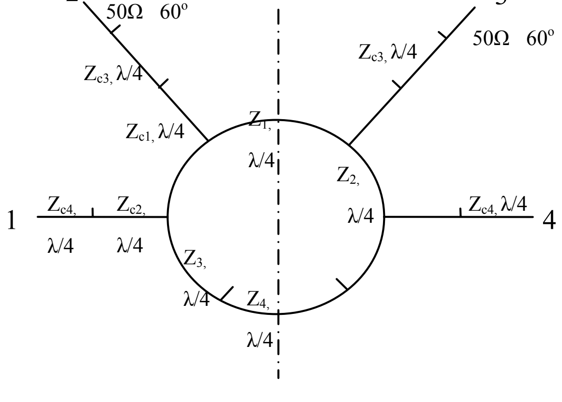

Figure 4.14 Wideband 180o hybrid coupler design example

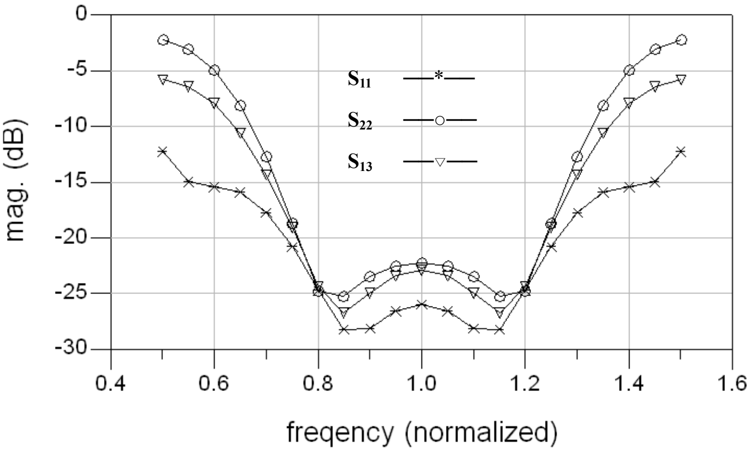

(a) mismatch and isolation coefficients (denoted by $S_{11}$, $S_{22}$ and $S_{13}$ respectively)

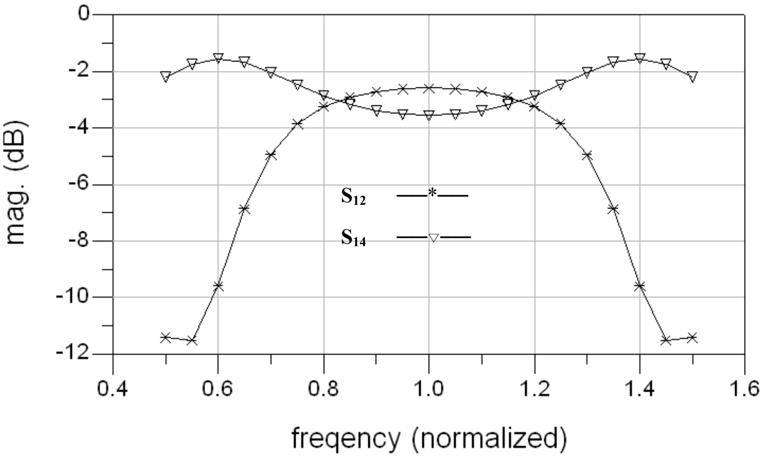

(b) coupling coefficients (denoted by $S_{12}$ and $S_{14}$)

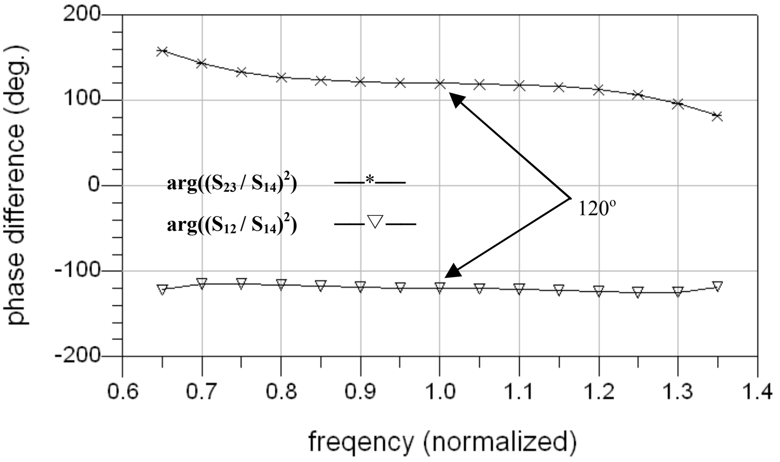

(c) phases of $S_{12}/S_{14}$ and $S_{23}/S_{14}$

Figure 4.15 Simulation results for rat-race coupler based on parameter settings listed in Equation 4.13(a)

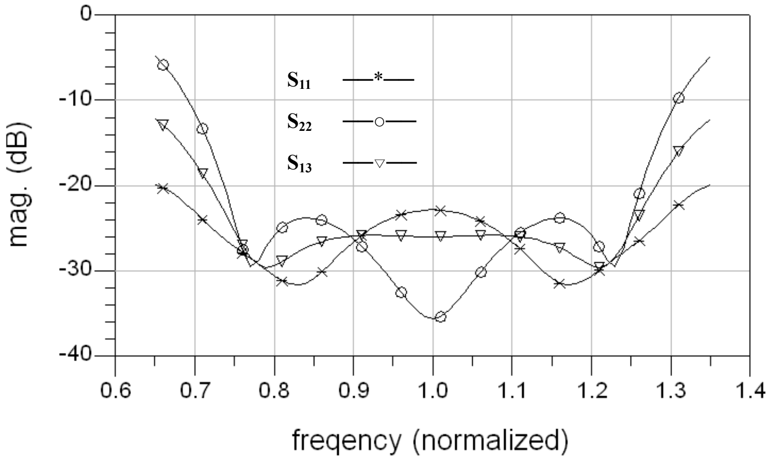

(a) mismatch and isolation coefficients (denoted by $S_{11}$, $S_{22}$, and $S_{13}$ respectively)

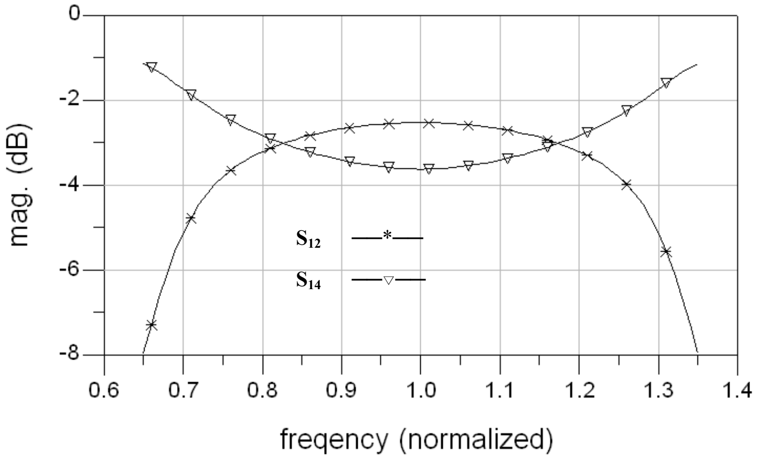

(b) coupling coefficients (denoted by $S_{12}$ and $S_{14}$)

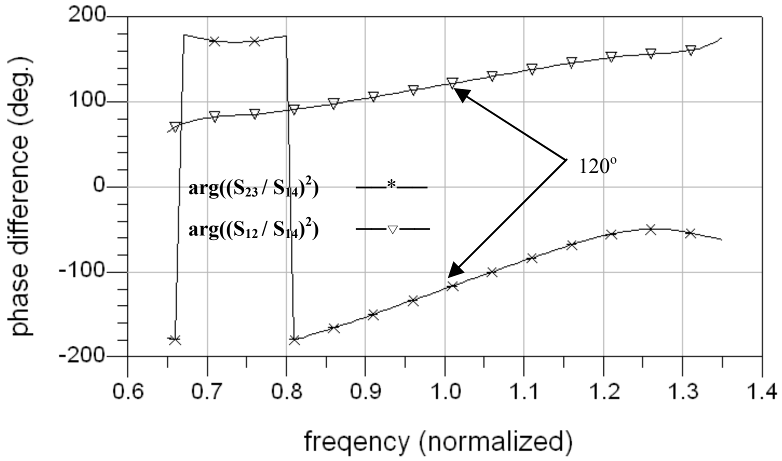

(c) phases of $S_{12}/S_{14}$ and $S_{23}/S_{14}$

Figure 4.16 Simulation results for rat-race coupler based on initial parameter settings listed in Equation 4.13(b)

Yet another variation we attempted is to employ a combination of algorithms to search for the global minimum of the error function defined in Equations 4.11-4.12. We first employed the least path technique and initiated the process with the parameter settings listed in Equation 4.13(b); we then continued the optimization by employing the gradient search technique and obtained the design yielding the scattering coefficients presented in figure 5.10. Hence, there is clearly a need to double-check the design data provided by the optimization software for our task at hand.

### 4.3.2 Modified branch-line structure for 90$^o$ hybrid coupler

Investigations have shown that the typical branch-line structure depicted in Figure 4.1(a) for the quadrature hybrid coupler is able to yield satisfactory performance over a 30% bandwidth. To widen the operating bandwidth of this type of coupler, we will employ what Muraguchi proposed in [4.6]. Outlined in Figure 4.16 is a typical extended structure (which is actually one of the possibilities we envisaged for the general structure proposed in Figure 4.5).

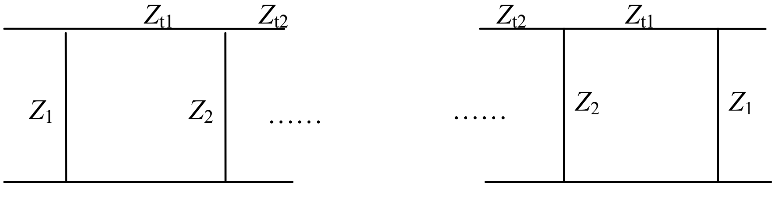

Figure 4.17 Extended structure for branch-line couplers proposed by Muraguchi [4.6]

Since the structure shown in Figure 4.16 involves more arms and links, we need to include additional variables in the error function. The coupler design we obtained after the optimization process has a wider bandwidth of 50-60%. In practice, it will be difficult to design couplers with operating bandwidths exceeding 60% because of the difficulty of fabricating microstrip lines with high characteristic impedances and the need to compensate junction parasitics for large differences in characteristic impedances of adjoining lines. One approach when attempting to design higher-order branch-line couplers is to choose a different medium; for example, although it is possible to continue using microstrip to achieve a bandwidth of 35% with $Z_1 = 105\ \Omega$. $Z_2 = 71\ \Omega$, $Z_{t1} = 44\ \Omega$ for the structure depicted in Figure 4.1(a), we will have to resort to slot-line or coplanar-waveguide (CPW) for a higher-order design with $Z_1 = 168\ \Omega$. $Z_2 = 107\ \Omega$, $Z_{t1} = 48\ \Omega$, $Z_{t1} = 47\ \Omega$.

Apart from return loss and isolation, we have to consider the coupler's phase characteristics which, according to our six-port reflectometer analysis in Section 3.2, need to meet the phase-difference specifications listed in Equation 3.8. Hence, we have to add lengths of transmission lines (to introduce the appropriate phase delays) at certain ports of the branch-line couplers as depicted in Figure 4.18. As can be seen from the simulation results presented in Figure 4.19, it is possible to meet the phase-difference requirements over a frequency range of only 20% for the structure depicted in Figure 4.18(a). For such structures, we have found it difficult to extend the operating bandwidth beyond 30% due to the constraints discussed in Sub-Section 4.3.1. There is the possibility of resorting to the reflectometer-tuning feature we proposed in Section 3.3 but the range of adjustment is likely to be limited for this particular case and we should thus consider alternative designs instead.

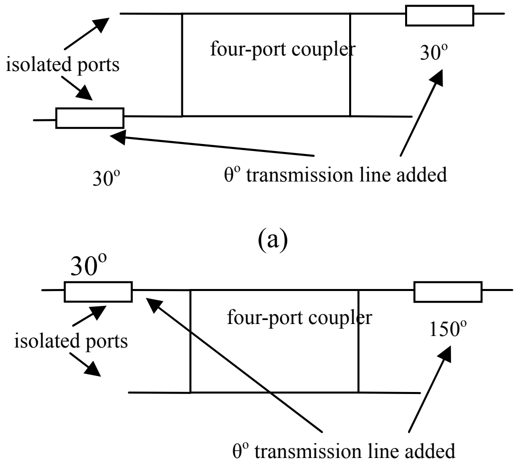

(a)

(b)

Figure 4.18 Modified branch-line structures with delay lines to meet phase requirements of Equation 3.8

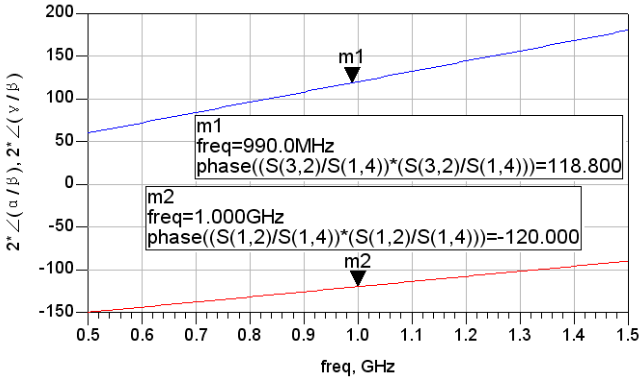

Figure 4.19 Phase responses for modified branch-line structure depicted in Figure 4.18(a)

## 4.3.3 Modified rat-race structure for 180° hybrid coupler

Investigations have shown that the typical rat-race structure depicted in Figure 4.1(b) for the 180° hybrid coupler is able to yield satisfactory performance over a 30% bandwidth. The initial modifications we explored are sketched in Figure 4.20. The results compiled during our exploratory study indicate that it is possible to obtain bandwidths of 40% and 60% for the preliminary designs depicted in Figures 4.20(a) and 4.20(b) respectively. Naturally, we need to be mindful of the hardware imperfections due to the fabrication tolerance limits discussed in Sub-Section 4.3.2 since the discrepancy between measured and predicted results may be unacceptable for designs with even wider bandwidths.

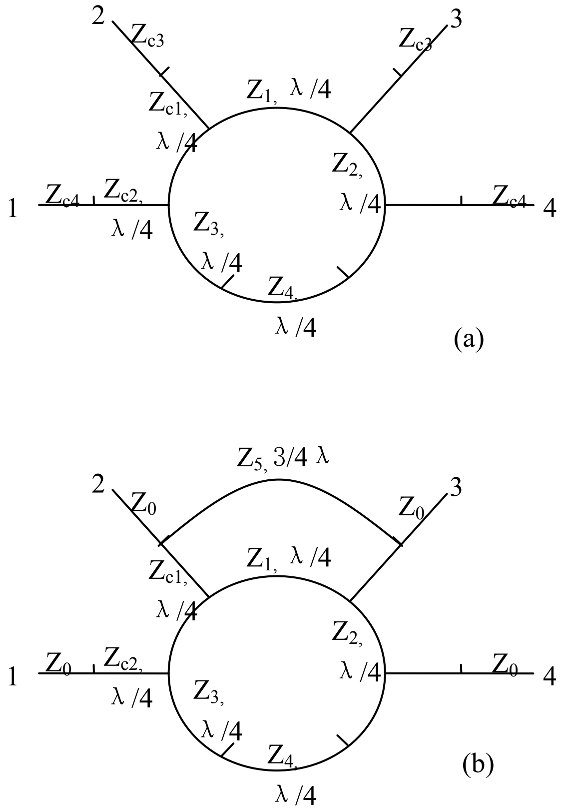

Figure 4.20 Modified rat-race coupler structures with improved performance

For six-port reflectometer application, the important advantage of using the rat-race structure is the range of phase differences that may be accommodated. Consider, by way of example, the modified rat-race structure depicted in figure 5.9 with the following set of design parameters

$Z_1 = 46\Omega$, $Z_2 = 41\Omega$, $Z_3 = 40\Omega$, $Z_4 = 40\Omega$, $Z_{c1} = 40\Omega$, $Z_{c2} = 34\Omega$, $Z_{c3} = 47\Omega$, $Z_{c2} = 49\Omega$

(4.14a)

where we can arrange the phase difference for the $s_{12}$ and $s_{14}$ pair and the $s_{23}$ and $s_{14}$ pair to be $70^o$ at 3GHz by merely adding phase-delay lines of $110^o$ and $140^o$ at Ports 2 and 3 respectively. As can be seen from the simulation results plotted in Figure 4.22, the bandwidth is rather limited because of the gradients of the plots for the phase difference between $s_{12}$ and $s_{14}$ and the phase difference between $s_{23}$ and $s_{14}$.

We have subsequently improved the bandwidth by using the error function defined in Equation 4.12 instead for the optimization process which then resulted in the following set of design parameters

$Z_1 = 60\Omega$, $Z_2 = 90\Omega$, $Z_3 = 77\Omega$, $Z_4 = 40\Omega$, $Z_{c1} = 40\Omega$, $Z_{c2} = 112\Omega$, $Z_{c3} =42\ \Omega$, $Z_{c2} = 85\Omega$

(4.14b)

As can be seen from the simulation results plotted in Figure 4.23, we have thus managed to obtain flatter plots for the corresponding phase differences.

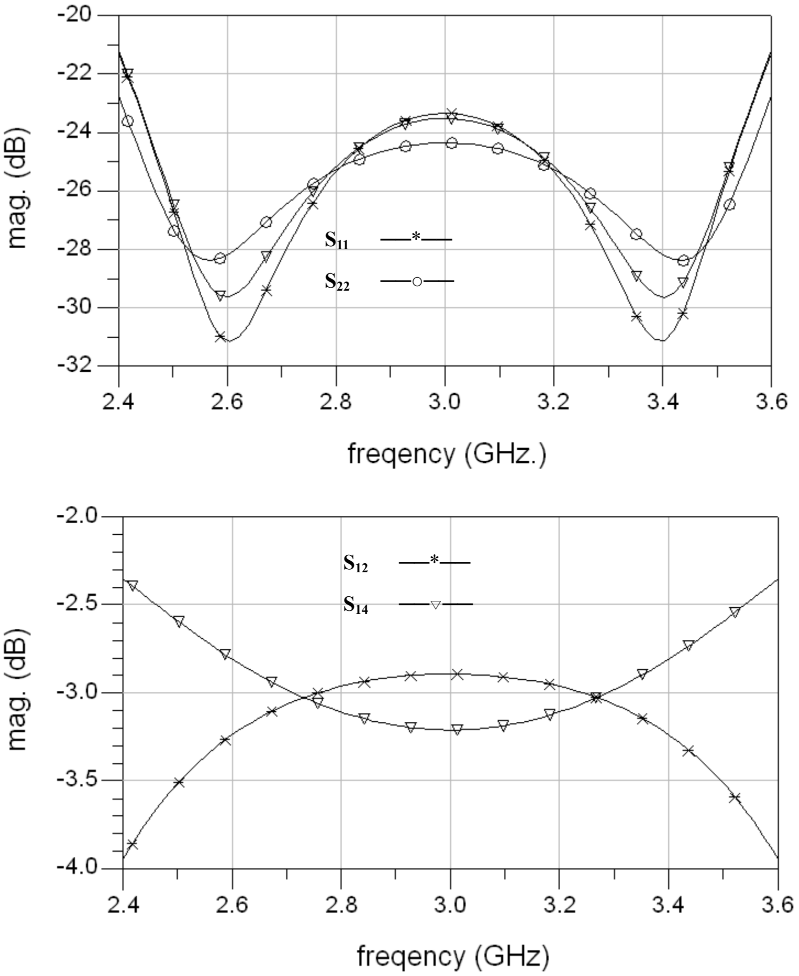

Figure 4.21 Simulation results for rat-race coupler based on design parameters listed in Equation 4.14(a) before taking phase specifications into consideration

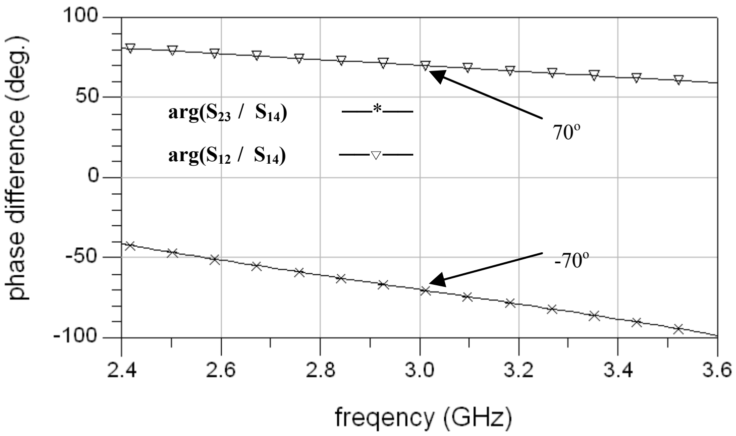

Figure 4.22 Simulation results for rat-race coupler based on design parameters listed in Equation 4.14(a) after adding phase-delay lines of 110° and 140° at Ports 2 and 3 respectively

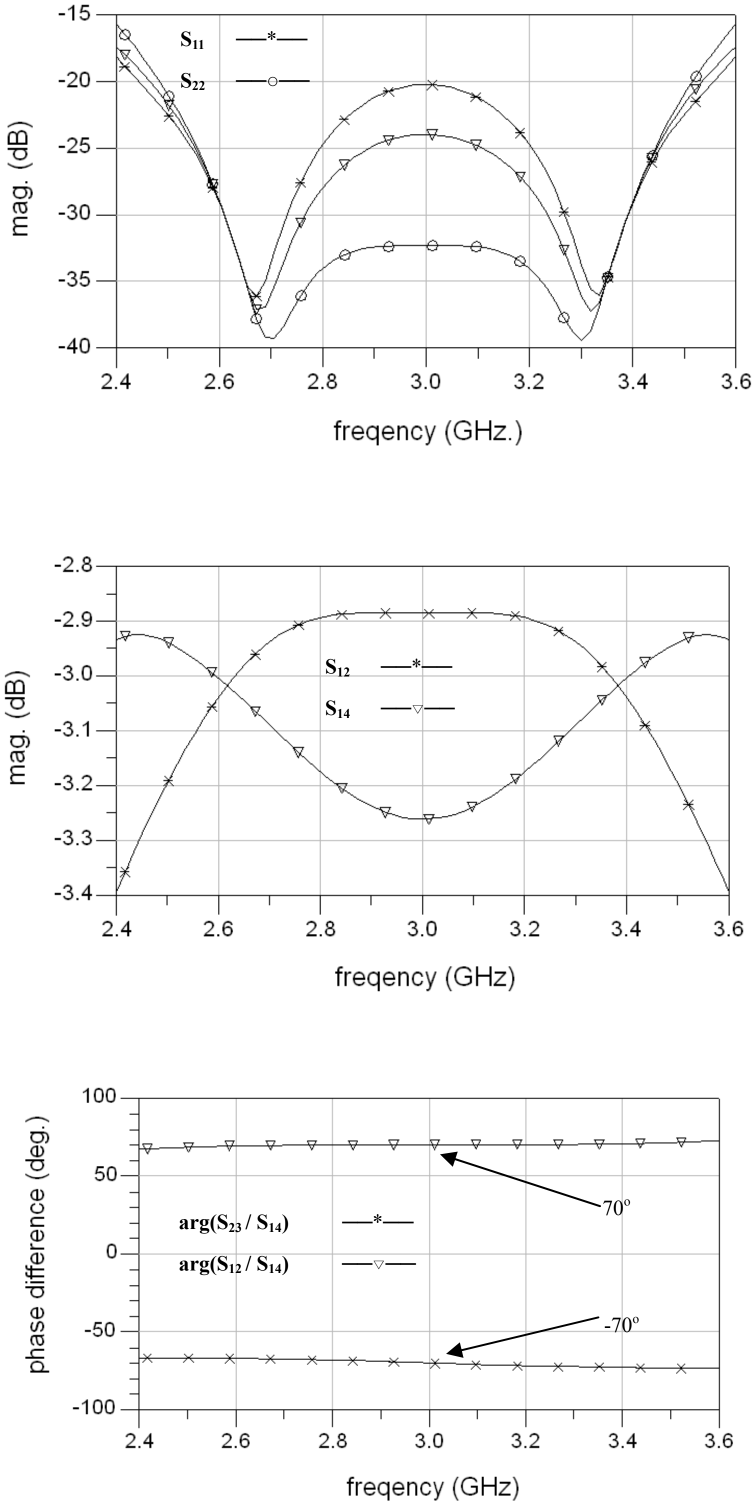

Figure 4.23 Simulation results for rat-race coupler based on design parameters listed in Equation 4.14(b)

## 4.4 Discontinuity Models with Junction Parasitics and Compensation Elements

Simulation models which do not take all hardware imperfections and compensation elements into account will degrade the effectiveness of the optimization process in searching for the most appropriate design. Since there may be constructive interference among the spurious waves caused by various hardware imperfections, neglecting second- and higher-order effects will be detrimental to our overall objective of meeting the criteria spelt out for the six-port reflectometer's q-point distribution. Hence, our study here must additionally include an appreciation of the junction parasitics, compensation elements and other secondary features so that we can accordingly tailor the detailed design specifications of the hybrid couplers and other constituent components for six-port reflectometer application.

The designs we reported in Chapter 5 have been implemented in either microstrip or coplanar-waveguide (CPW). For our microstrip designs, the discontinuities we encountered are steps and T-junctions. For our CPW prototypes, we also need to pay special attention to the $180^{\circ}$ phase inverters we incorporated into the modified hybrid-coupler design.

### 4.4.1 Microstrip discontinuities

There are many papers and books providing details for all forms of microstrip discontinuities. Our focus here is on those discontinuities that directly affect the modified hybrid-coupler designs we implemented in microstrip in Sections 5.1 and 5.2 (for the branch-line and rat-race structures respectively).

(a) <u>microstrip step</u>

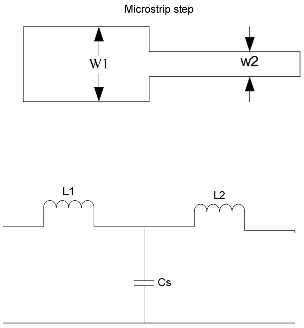

Figure 4.24 Lumped-element model of microstrip step discontinuity

Step discontinuities arise whenever we need to vary the characteristic impedances of transmission lines. According to Gupta [4-34], the microstrip step can be modeled as a T lumped-component circuit with the following expressions for the key parameters:

$$L_1 = \frac{L_{w1}}{L_{w1} + L_{w2}} L_s, \qquad L_2 = \frac{L_{w2}}{L_{w1} + L_{w2}} L_s$$

$$L_{w1} = \frac{Z_{0w1}\sqrt{\varepsilon_{re}}}{c}, \qquad L_{w2} = \frac{Z_{0w2}\sqrt{\varepsilon_{re}}}{c} \tag{4.15}$$

and $$L_s = 0.000987h\left(1 - \frac{Z_{0w1}}{Z_{0w2}}\sqrt{\frac{\varepsilon_{re1}}{\varepsilon_{re2}}}\right) \quad \text{(pF)}$$

$$C_s = 0.00137\frac{\sqrt{\varepsilon_{re1}}}{Z_{0w1}}(1 - \frac{W_1}{W_2})h\left(\frac{\varepsilon_{re1} + 0.3}{\varepsilon_{re1} - 0.258}\right)\left(\frac{W_1/h + 0.264}{W_1/h + 0.8}\right) \quad \text{(nH)}$$

where $Z_{0wi}$ and $\varepsilon_{rei}$ are the characteristic impedance and effective dielectric constant respectively for each microstrip line.

(b) <u>microstrip T-junction</u>

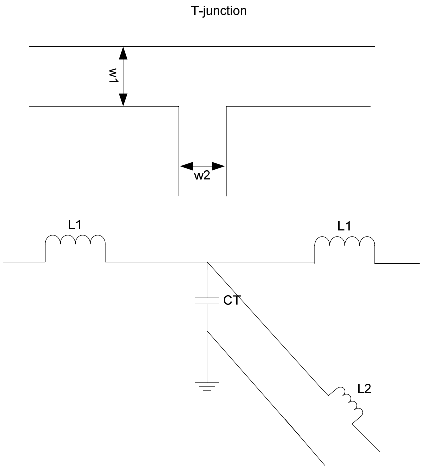

Figure 4.25 Lumped-element model for microstrip symmetrical T-junction

We have found it important to account for the junction parasitics of T-junctions. Reproduced below are the expressions from [4-34] for the lumped-component model parameters of the symmetrical T-junction:

$$\frac{C_T}{W_1}(pF/m) = \frac{100}{\tanh(0.0072 * Z_2)} + 0.64Z_2 - 261 \qquad (25 < Z_2 < 100)$$

$$\frac{L_1}{h}(nH/m) = -\frac{W_2}{h}\left(\frac{W_2}{h}\left(-0.016\frac{W_1}{h} + 0.064\right) + \frac{0.016}{W_1/h}\right)L_{w1} \tag{4.16}$$

$$0.5 < W_1/h, \qquad W_2/h < 0.2$$

$$\frac{L_2}{h}(nH/m) = \left(\frac{W_2}{h}\left(0.12\frac{W_1}{h} - 0.74\right) + 0.195\frac{W_1}{h} - 0.357 + 0.0283\sin(\frac{W_1}{h}\pi - 0.75\pi)\right)L_{w2}$$

$$1 < W_1/h < 2, \qquad 0.5 < W_2/h < 0.2$$

where $L_{w1}$ and $L_{w2}$ are the inductance per unit length for microstrip of width $w_i$.

For greater flexibility during our coupler design attempts, we also need to consider the possibility of allowing for asymmetrical T-junction structures. Depicted in figure 4.26 is the lumped-component element model from [4.36] to be used in such a situation. There are also other models for T-junctions such as [4.37] and [4.38]. When using these models, attention has to be paid to the junction reactance $jB_T$ which we found to be troublesome because of possible simulation errors during our coupler design optimization efforts.

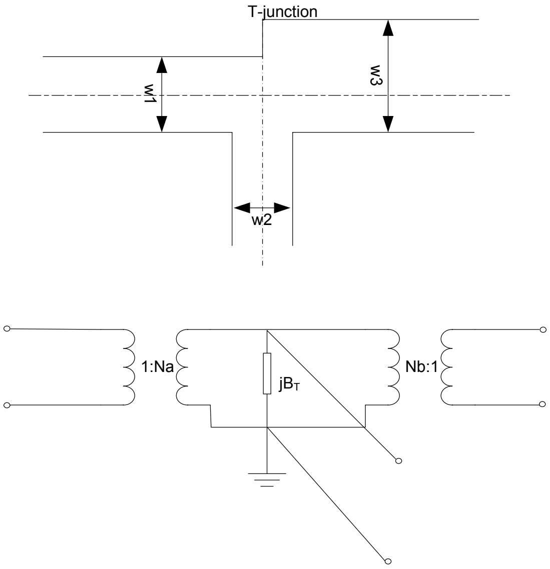

Figure 4.26 Lumped-element model for asymmetrical microstrip T-junction

(c) <u>microstrip open-circuit terminations</u>

The inclusion of open-circuit stubs offers greater design flexibility. The fringing fields that exist at the termination can be taken into account by using the simple models depicted in Figures 4.27(b) or 4.27(c) with the following expressions for the lumped component or extended length respectively obtained from [4-39]:

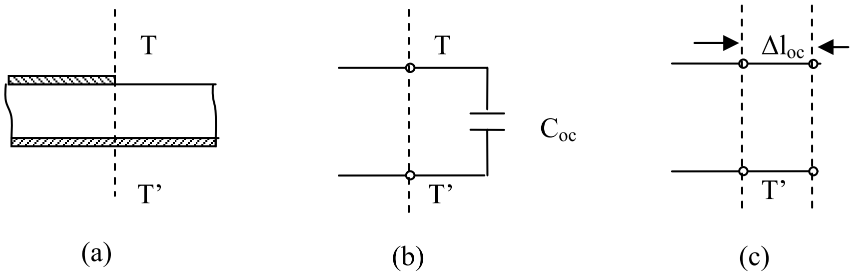

Figure 4.27 Models for microstrip open-circuit termination
(a) physical structure
(b) lumped-element model
(c) extended-length model

$$\frac{C_{oc}}{W} = \exp\left(2.3026\sum_{i=1}^{5} C_i(\varepsilon_r)\left(\log\left(\frac{W}{h}\right)\right)^{i-1}\right) \quad \text{(pF/m)} \tag{4.17a}$$

$$\frac{\Delta l_{oc}}{h} = \frac{C_{oc}}{W}\frac{cZ_{om}W/h}{\sqrt{\varepsilon_{re}}} \tag{4.17b}$$

A common approach to compensate for open-circuit terminations is to simply adjust the line length as can be inferred from Equation 4.17 for the extended-length model depicted in Figure 4.27(c).

### 4.4.2 Coplanar-waveguide discontinuities

We have also resorted in Chapter 5 to CPW implementation so as to extend the coupler's bandwidth. An additional discontinuity we employed for the CPW coupler design reported in Section 5.3 is the $180^o$ phase inverter (which we have not found to be necessary for the two microstrip coupler designs reported in Sections 5.1-5.2).

### (a) CPW open-circuit termination

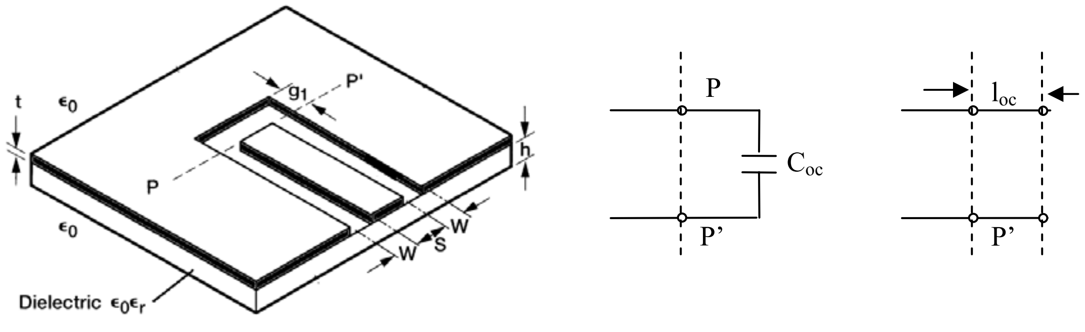

(a) (b) (c)

Figure 4.28 Models for CPW open-circuit termination
(a) physical structure
(b) lumped-element model
(c) extended-length model

As for the microstrip counterparts, the CPW open-circuit termination can be modeled as the lumped component or extended length depicted in Figures 4.27(a) or 4.27(b) respectively. Their corresponding expressions may be obtained from [4-40]-[4.43]:

(i) for the case of $g_1 \geqslant S + 2W$ and $0.2 \leqslant S/(S + 2W) \leqslant 0.8$

$$C_{oc} = \frac{\tan(\beta l_{oc})}{\omega Z_0} \tag{4.18}$$

$$l_{oc} = \frac{S + 2W}{4} \tag{4.19}$$

(ii for the case of $S/(S + 2W) \geqslant 0.25$ and $h/(S + 2W) \geqslant 1.0$

$$C_{oc} = C_{oc(air)}\varepsilon_{eff} \tag{4.20}$$

where

$$C_{\mathrm{oc(air)}} = \frac{2\varepsilon_0}{\pi}\left\{(S+W)\left[\frac{\ln(\eta+\sqrt{1+\eta^2})}{\eta} + \ln\left(\frac{\sqrt{1+\eta^2}+1}{\eta}\right)\right.\right.$$
$$\left.\left. - \frac{1}{3}\left(\frac{1}{1+\sqrt{1+\eta^2}} + \frac{1}{\eta+\sqrt{1+\eta^2}}\right)\right] - \left(S+\frac{2}{3}W\right)\right\}$$
$$\eta = \frac{g_1}{S+W}. \qquad (4.21)$$

(b) CPW steps

Depicted in Figure 4.28 is the model provided by Simons [4-46] for the CPW step discontinuity. It has been pointed out that the junction capacitor denoted as $C_s$ "… effectively lengthens the low-impedance CPW line towards the higher-impedance CPW line" [4-47].

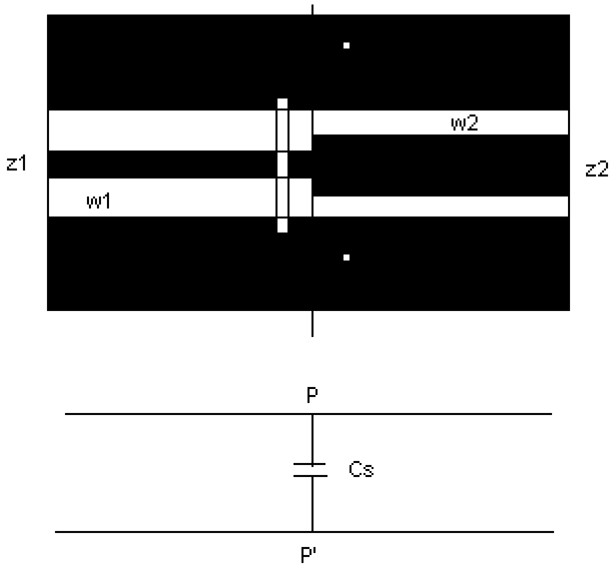

Figure 4.29 Lumped-element model reproduced from [4.46] for CPW step

(c) CPW T-junction

Depicted in Figure 4.29 is the model provided by Mirshekar-Syahkal [4-47] for the CPW T-junction with quasi-static approximations for the determination of the various lumped-component values. It should be pointed out, however, that his model still requires intensive computations with integration.

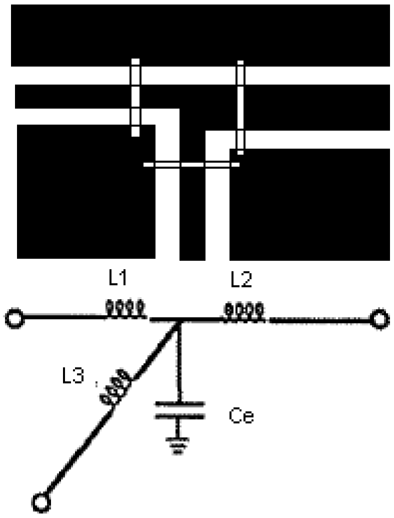

Figure 4.30 Lumped-element model reproduced from [4.47] for asymmetrical CPW T-junction

(d) CPW 180° phase inverter

The 180° phase inverter is an important element in our CPW coupler design (details of which are described in Section 5.3). For the ideal case, we expect the 180° phase inverter to meet the following scattering-coefficient requirements over the entire operating bandwidth:

$$\begin{aligned} &|S_{12}| = 1 \\ &\angle S_{12} = 180^o \\ &|S_{11}| = 0 \end{aligned} \tag{4.22}$$

The most frequently used CPW phase inverter structures compiled by Wang [4-48] are reproduced in Figure 4.30. Depicted in Figure 4.30(a)-(d) are four structures which do not require mode conversion in view of the direct phase change at the crossing point. As for the other four structures shown in Figure 4.30(e)-(h), mode conversion is required from CPW to slot-line and then back to CPW. Without any mode conversion, the four simpler structures depicted in Figure 4.30(a)-(d) are expected to yield better phase inversion, lower insertion loss and wider bandwidth than the other four phase inverters shown in Figures 4.30(e)-(h).

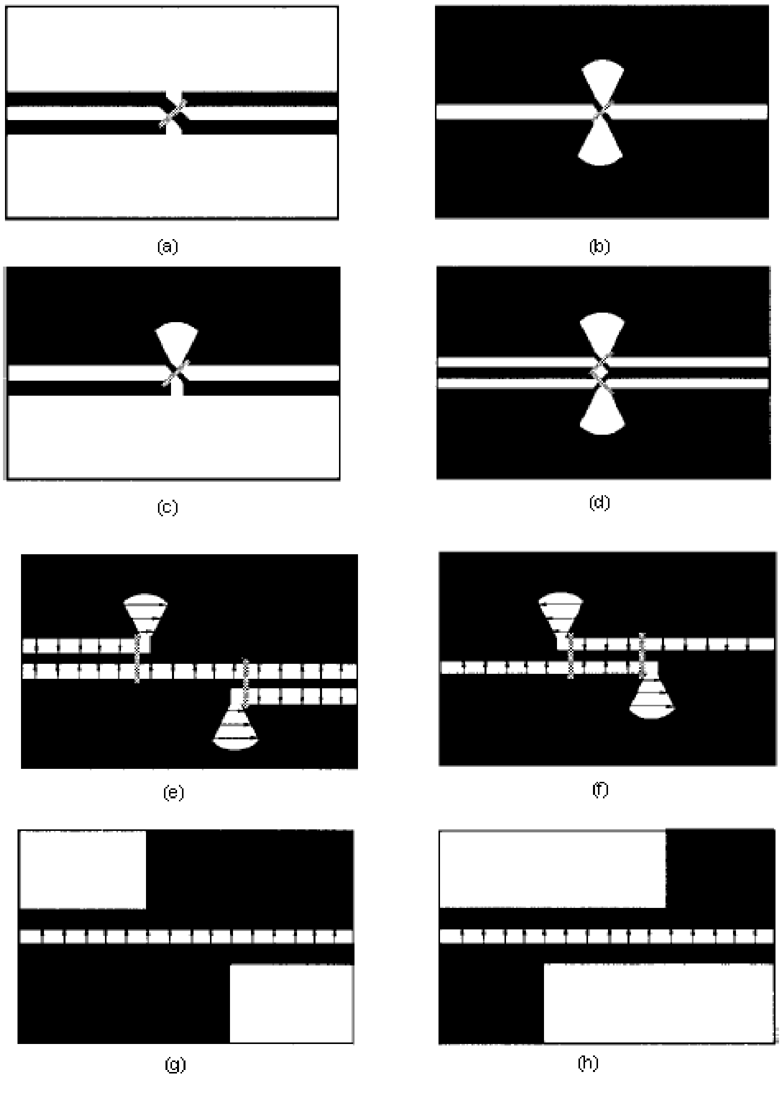

Figure 4.31 Different designs reproduced from [4.48] for CPW 180° phase inverter

### 4.4.3 Discontinuity compensation techniques

There are various discontinuity compensation techniques available; for example, we have already noted in Sub-Section 4.4.1 that it is possible to account for the fringing fields at the termination of an open-circuit stub by shifting the reference plane (and thus effectively change the line length). We shall also briefly consider here the other discontinuity compensation techniques which have been found to be useful for our coupler design efforts in Chapter 5.

(a) <u>structure re-shaping</u>

The additional reactances which have to be included in equivalent models to account for various spurious junction effects offer clues as to how designs may be fine-tuned. A typical example is the bend depicted in Figure 4.32; by adding the chamfer, Hammerstad and Bekkadal [4-55] demonstrated that the bend should have the lowest VSWR up to 12GHz when $w_c = 1.83w$ for any bend angle $\varphi$ while Douville [4-56] recommended the optimum amount of chamfering to be

$$M = 52 + 65e^{-1.35w/h} \tag{4.23}$$

when $w/h > 0.25$ and $\varepsilon_r < 25$ and where $M = (x/d)\ 100\%$, w is the width of the transmission line and h is the thickness of the substrate.

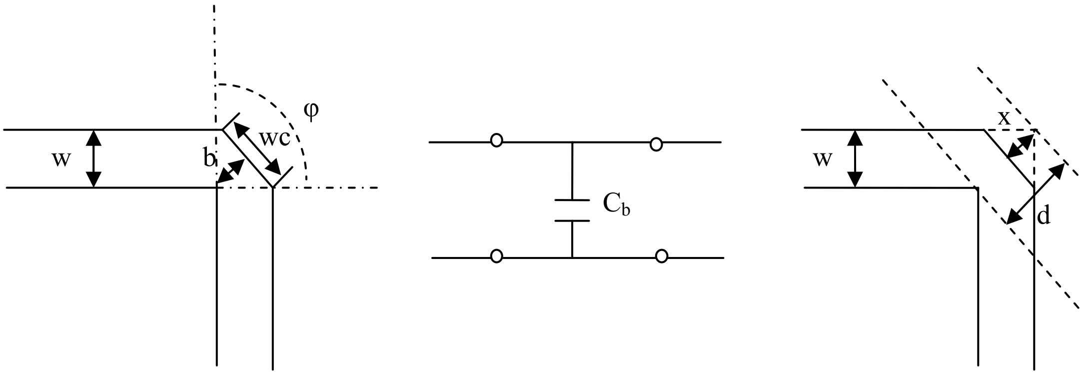

Figure 4.32 Microstrip bend structure with chamfering

Depicted in Figure 4.33 is the T-junction which has also benefited from compensation techniques under certain operating conditions; for example, Gupta [4-34] recommended the use of the simpler re-shaped structures sketched in Figure 4.33(a)-(b) only when $h/\lambda << 1$. More complicated re-shaping is also possible and we reproduce in Figure 4.34 the T-junction design proposed by Dydyk [4-50].

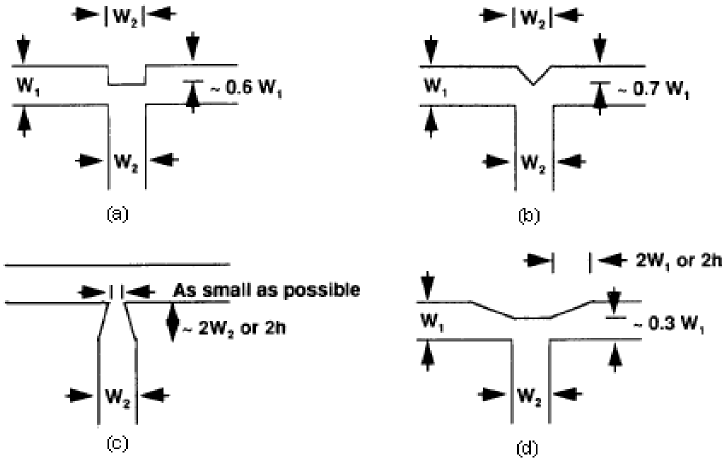

Figure 4.33 T junction compensation possibilities reproduced from [4.34]

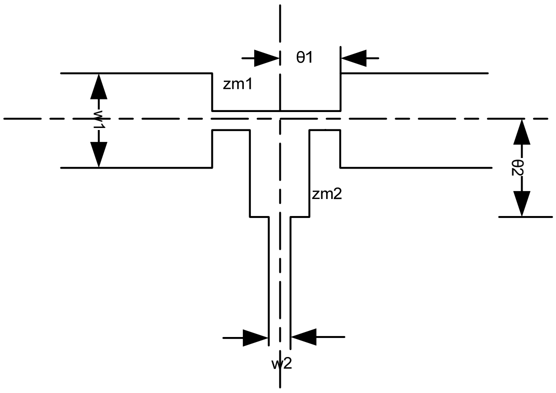

Figure 4.34 More complicated compensation scheme proposed by Dydyk [4.50] for T junction

We have also found it necessary to re-shape other basic structures during our coupler design efforts. Examples of such re-shaped structures are provided in Figure 4.35 (for the microstrip step junction) and Figure 4.36 (for the various CPW elements required in Section 5.3).

One of most commonly used CPW bend structure is shown in Figure 4.36(c). Omar and Watson [4.64] suggested that the optimum chamfering for the central conductor strip corner should be $\frac{mS}{W+S}$ with the optimum chamfering for minimum return loss given by:

$$\left(\frac{m}{m_{\max}}\right)_{\text{opt}} = \begin{cases} 0.2102 \ln\left(\frac{S}{W}\right) + 0.7677 & \text{for } 0 \leqslant S/W \leqslant 2, \\ 1 & \text{for } S/W > 2.5. \end{cases} \tag{4.24}$$

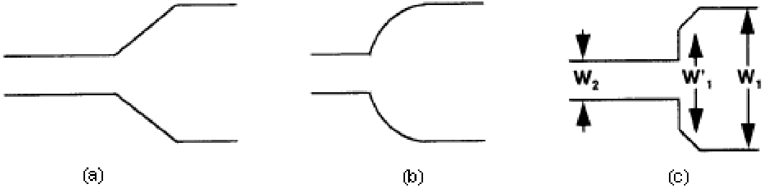

Figure 4.35 Step junction compensation possibilities reproduced from [4.49]

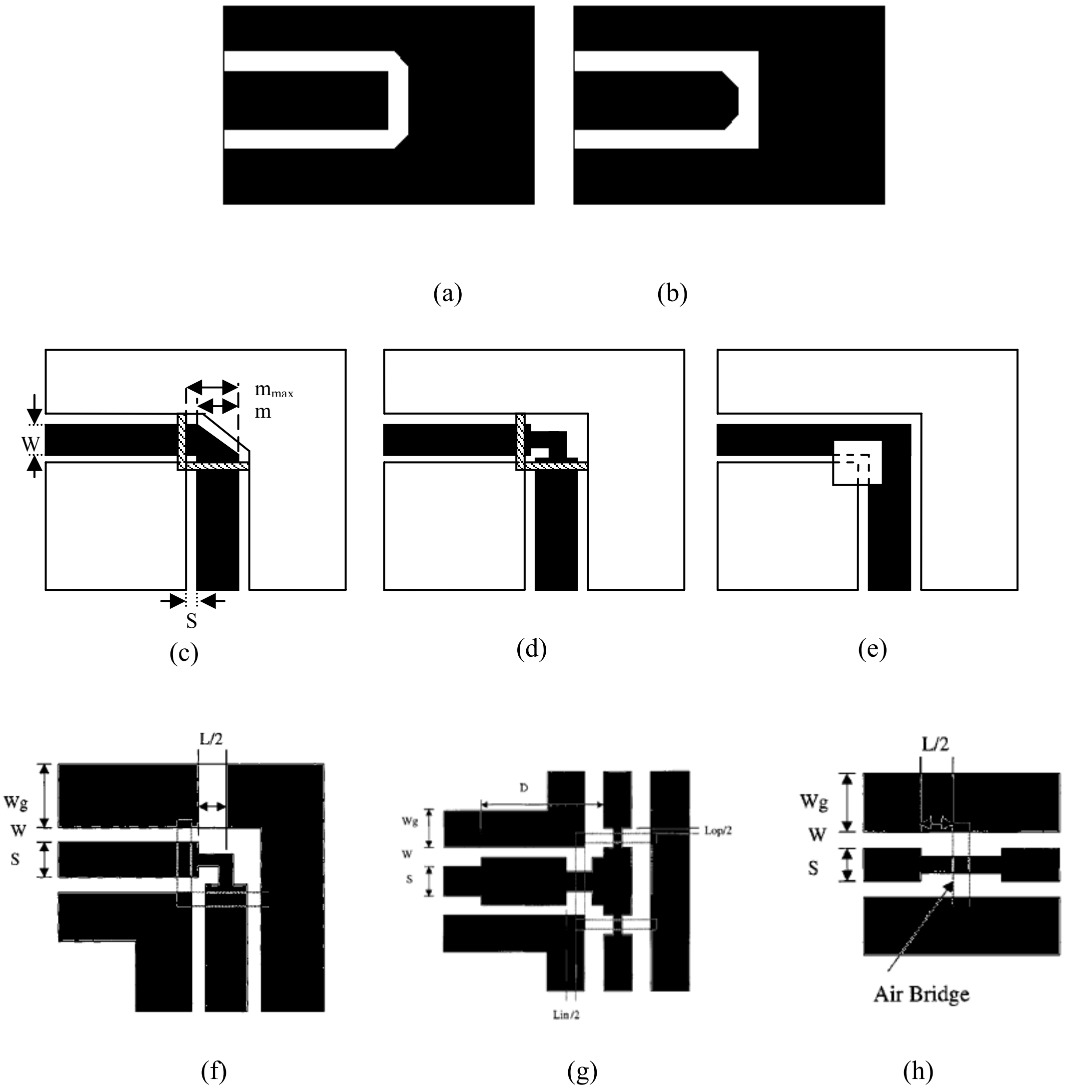

Figure 4.36 CPW structures with discontinuity compensation

(a) stub with outer chamfer [4.57]
(b) stub with inner chamfer [4.57]
(c) bend with chamfer [4.62]
(d) bend with step change at corner [4.62]
(e) bend with dielectric overlay [4.62]
(f) re-shaped bend proposed by Weller [4.58]
(g) re-shaped T junction proposed by Weller [4.58]
(h) re-shaped air bridge proposed by Weller [4.58]

### (b) structure re-scaling

During our discussion of the open-circuit stub, we have already inferred that it is necessary to define an effective length in order to account for the fringing fields appearing at the end. For the analysis of microstrip lines, there is similarly a need to define effective widths so as to account for the fringing fields appearing at the edges.

Extrapolating from these simple illustrations, it is also possible [4.51]-[4.52] to change the physical widths and lengths of selected transmission lines in order to account for certain spurious effects. This is commonly applied in the design of four-port networks. For the example presented in Table 4.1, we have optimized a 6GHz branch-line coupler design before and after taking junction effects into account; the two sets of tabulated design data show that there are differences of 20-30% in the lengths of selected branch arms (*viz* $L_1$ and $L_4$) after taking spurious effects into consideration whilst still meeting the same design objectives.

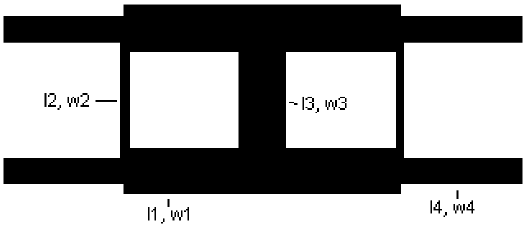

Figure 4.37 Branch-line coupler structure

TABLE 4.1 DESIGN DATA FOR BRANCH LINE COUPLER (FIGURE 4.36) WITH AND WITHOUT DISCONTINUITY COMPENSATION

| Coupler parameter | Optimized design data without considering spurious discontinuity parasitics | Optimized design data after taking spurious discontinuity parasitics into consideration |
|---|---|---|
| L1 | 360 | 290 |
| L2 | 250 | 250 |
| L3 | 250 | 250 |
| L4 | 340 | 305 |
| W1 | 120 | 120 |
| W2 | 20 | 20 |
| W3 | 120 | 120 |
| W4 | 62 | 65 |

### (c) adding compensating lumped/distributed components

Figure 4.38(a) depicts the design reported by Dydyk [4.53] who found that the performance might be improved by adding lumped capacitances (or inductors) to compensate for the spurious effects in his directional coupler designs. As shown in Figure 4.38(b), Gruszczynski [4.54] chose instead to add distributed capacitive components in his directional coupler design.

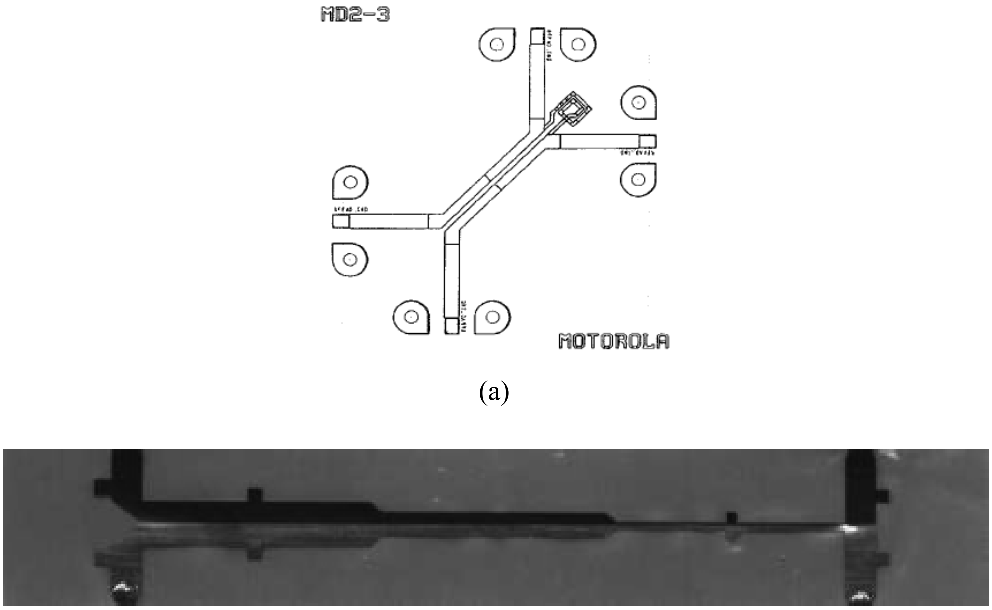

(a)

(b)

Figure 4.38 Microstrip directional coupler designs with (a) lumped compensating components as reported by Dydyk [4.53] and (b) distributed compensating components as reported by Gruszczynski [4.54]

In view of the difficulty to accurately predict the spurious effects that may arise in any planar structure, it is advisable to incorporate adjustable elements so as to allow for the possibility of fine-tuning the design during laboratory testing. As demonstrated by Gruszczynski [4.54] for his design depicted in Figure 4.38(b), a simple way to add adjustable reactive components is to insert shunt stubs at appropriate sites within the circuit. As an example, we have similarly attempted to improve the performance of the four-port coupler portrayed in Figure 4.39(a) by adding adjustable open-circuit stubs as shown in Figure 4.39(b) and the performance results we measured for the prototype before and after fine-tuning are presented in Figures 4.39(c) and 4.39(d) respectively; a comparison of the two sets of measured data confirms that adding open-circuit stubs at the four arms has not only improved the isolation and return loss of our prototype coupler but also allowed us to shift back the center frequency which had strayed from the original target of 5GHz specified for the design.

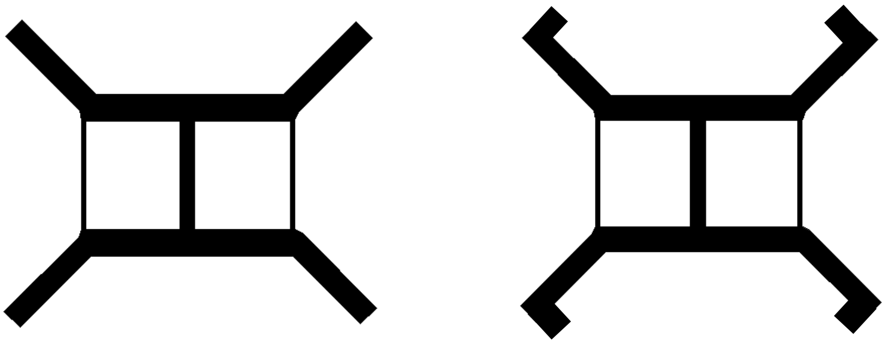

(a) original design (b) revised design

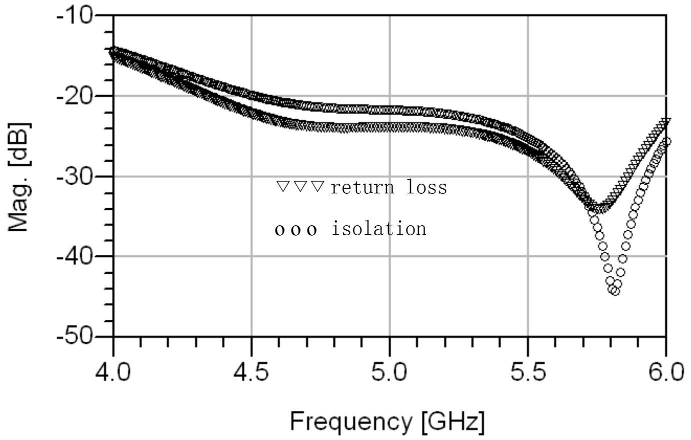

(c) measured return loss and isolation of original design

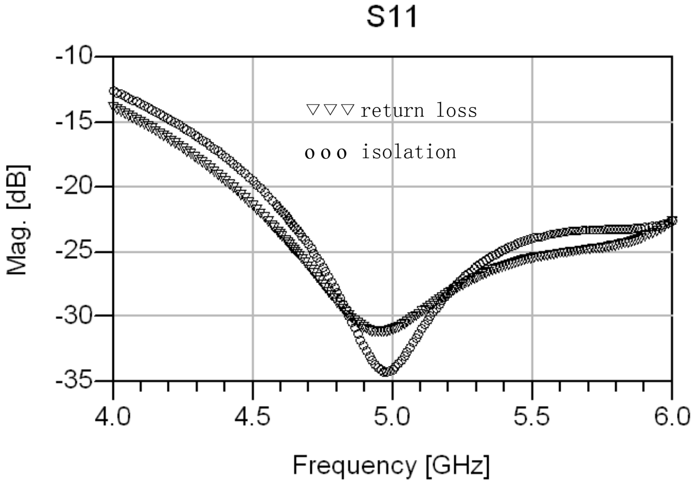

Figure 4.39 Branch coupler with and without tuning capacitive tuning stubs

(a) lay-out of coupler without tuning stubs

(b) lay-out of coupler with tuning stubs

(c) measured performance of coupler without tuning stubs

(d) measured performance of coupler with tuning stubs

## REFERENCES

[4.1] W.J. Getsinger, "A coupled strip-line configuration using printed circuit construction that allows very close coupling," IRE Trans. Microwave Theory Tech., vol. 9, pp. 535–544, Nov.1961

[4.2] E.G. Cristal and L. Young, "Theory and tables of optimum symmetrical TEM-mode coupled-transmission-line directional couplers," IEEE Trans. Microwave Theory Tech., vol. MTT-13, pp. 544–558, Sep. 1965

[4.3] J.P. Shelton and J.A. Mosko, "Synthesis and design of wideband equal ripple TEM directional couplers and fixed phase shifters," IEEE Trans. Microwave Theory Tech., vol. MTT-14, pp. 462–473, Oct. 1966

[4.4] Y. Konishi, "A directional coupler of a vertically installed planar circuit structure", IEEE Trans. Microwave Theory Tech., vol. MTT-36, Jun. 1988

[4.5] R. Levy and L. Lind, "Synthesis of symmetrical branch-guide directional couplers," IEEE Trans. Microwave Theory Tech., vol. MTT-16, pp. 80-89, Feb. 1968

[4.6] M. Muraguchi, "Optimum design of 3-dB branch line couplers using microstrip lines", IEEE Trans. Microwave Theory Tech., vol. 31, Aug. 1983

[4.7] C.Y. Pen, "Hybrid-ring direction coupler for arbitrary power division," IRE Trans. Microwave Theory Tech., vol. MTT-9, pp. 529-535, Nov.1961

[4.8] J. Reed and G.J. Wheeler, "A Method of analysis of symmetrical four-port network," IRE Trans. Microwave Theory Tech., vol. MTT-4, pp. 246-252, Oct. 1956

[4.9] S. March, "A wideband- stripline hybrid ring," IEEE Trans. Microwave Theory Tech., vol. MTT-16, no, 6, p. 361, June 1968.

[4.10] D.I. Kim, "Broad-band design of improved hybrid-ring 3-dB directional coupler", IEEE Trans. Microwave Theory Tech., vol. 30, pp. 2040-2046, Nov. 1982

[4.11] J. Lange, "Interdigitated stripline quadrature hybrid", IEEE Trans. Microwave Theory Tech., pp. 1150-1151, Aug. 1969

[4.12] A. Sawicki, '"Novel coupled-line conductor-backed coplanar and microstrip directional couplers for PCB and LTCC applications", IEEE Trans. Microwave Theory Tech., vol. 51, pp.1743-1751, Jun. 2003

[4.13] K. Sachse, "Quasi-ideal multilayer two- and three-strip directional couplers for monolithic and hybrid MICs", IEEE Trans. Microwave Theory Tech., vol. 47, pp. 1873- 1882, Sep. 1999

[4.14] S. Gruszczynski, "design of compensated coupled stripline 3dB directional couplers phase shifters and magic Ts", IEEE Trans. Microwave Theory Tech., vol. 54, pp. 3501- 3507, Sep. 2006

[4.15] S.S. Liao," A novel compact-size branch-line coupler", IEEE Microwave Wireless Comp. Lett., vol. 15, pp. 588-590, Sep. 2005

[4.16] T. Hirota, A. Minakaw and M. Muraguchi, “Reduced-size branch-line and rat-race hybrids for uniplanar MMIC’s,” IEEE Trans. Microwave Theory Tech., vol. MTT-38, pp. 270–275, Mar. 1990

[4.17] R.B. Singh and T.M. Weller, “Miniaturized 20GHz CPW quadrature coupler using capacitive loading,” Microw. Opt. Technol. Lett., vol. 30, pp. 3-5, Jul. 2001

[4.18] M.C. Scardelletti, G.E. Ponchak and T.M. Weller, “Miniaturized Wilkinson power dividers utilizing capacitive loading,”IEEE Microw. Wireless Compon. Lett., vol. 12, no. 1, pp. 6–8, Jan. 2002

[4.19] G.E. Ponchak, “Experimental analysis of reduced-sized coplanar waveguide transmission lines,” in IEEE MTT-S Dig., 2003,pp. 971–974

[4.20] C.Y. Ho, “Lumped element quadrature coupler design,” Microwave J. , vol. 22, no. 9, pp. 67-70, Sept. 1979.

[4.21] R.W. Vogel, “Directional couplers with lumped and distributed elements,” in Proc. 26 Intern. Wies. Koll., TH Ilmenau, Vortragsr. Mikrowellentechnik, 1981, pp. 79-81

[4.22] R.K. Gupta and W.J. Getsinger, “Quasi-lumped-element 3- and 4-port networks for MIC and MMIC applications,” IEEE MTT-S Int. Microwave Symp. Dig., San Francisco, 1984, pp. 409-411

[4.23] G. Michael, “Advanced Engineering Mathematics”, Prentice Hall, 1998

[4.24] R. Malek-Madani, “Advanced Engineering Mathematics with Mathematica and MATLAB ” Addison-Wesley, 1998

[4.25] T.L. Harman, J.B. Dabney and N.J. Richert, “Advanced engineering mathematics with MATLAB ” Pacific Grove, CA: Brooks/Cole Pub., 2000

[4.26] C.R. Wylie, Jr , “Advanced Engineering Mathematics”, McGraw-Hill [1966]

[4.27] D.M. Pozar, “Microwave Engineering”, John Wiley & Sons Inc., 1998

[4.28] C.Y. Chang, “A novel broadband chebychev-response rat-race ring coupler”, IEEE Trans. Microwave Theory Tech., vol. 47, pp.455- 462, Apr. 1999

[4.29] A.F. Celliers, “Design curves for 3-dB branch-line couplers”, IEEE Trans. Microwave Theory Tech., vol. 33, pp.1226- 1228, Nov. 1985

[4.30] D.I. Kim and Y. Naito, “Broad-band design of improved hybrid-ring 3-dB directional coupler,” IEEE Trans. Microwave Theory Tech., vol. MTT-30, pp. 2040–2046, Nov. 1982

[4.31] J. Wright, “Equivalent circuits of microstrip impedance discontinuities and launchers”, IEEE Trans. Microwave Theory Tech., vol. 22. pp.48-52, Jan. 1974

[4.32] T. Itoh and R. Mittra, “A new method for solving discontinuity problems in microstrip lines”, 1972 IEEE GMTT Int. Microwave Symp. Digest, pp.68-70

[4.33] T.C. Edwards, “Foundations of microwave circuit design”, Wiley, New York, 1981

[4.34] K.C. Gupta, “Microstrip lines and slotlines”, Artech house, 1996

[4.35] A. Agrawal, “A printed –circuit hybrid ring directional coupler for arbitrary power divisions”, IEEE Trans. On MTT , VOL.34, No.12, Dec. 1986

[4.36] E. Hammerstad, “Accurate Models for microstrip computer aided design ”, IEEE MTT-S Int. Symp. Digest, 1980, pp 407-409

[4.37] A.F. Thompson, “Calculation of microstrip discontinuity inductance”, IEEE Trans. On MTT, VOL. 23, 1975, pp.648-655

[4.38] P. Silvester and P. Benedek, “Microstrip discontinuity capacitances for right-angle bends, T-junctions and crossings”, IEEE Trans. Microwave Theory Tech., vol. 21, pp. 341-346, Mar. 1973

[4.39] P. Silvester and P. Benedek, “Equivalent capacitance of microstrip open circuits”, IEEE Trans. Microwave Theory Tech., vol. 20, pp. 511-516, Apr. 1972

[4.40] R.N. Simons and G.E. Ponchak, ‘‘Modeling of Some Coplanar Waveguide Discontinuities,’’ IEEE Trans. Microwave Theory Tech., vol. 36, pp. 1796-1803, Dec. 1988

[4.41] K. Beilenhoff, H. Klingbeil, W. Heinrich, and H.L. Hartnagel, ‘‘Open and short circuits in coplanar MMIC’s,’’ IEEE Trans. Microwave Theory Tech., vol. 41, pp. 1534-1537, Sep. 1993

[4.42] K. Beilenhoff, W. Heinrich, and H.L. Hartnagel, ‘‘Finite-difference analysis of open and short circuits in coplanar MMIC’s including finite metallization thickness and mode conversion,’’ 1992 IEEE MTT-S Int. Microwave Symp. Dig., vol. 1, pp. 103-106, Albuquerque, NM, June 1-5, 1992

[4.43] M.H. Mao, R.B. Wu, C.H. Chen, and C.H. Lin, ‘‘Characterization of coplanar waveguide open-end capacitance – theory and experiment,’’ IEEE Trans. Microwave Theory Tech., vol. 42, pp. 1016-1024, Jun. 1994

[4.44] N. Dib, “Comprehensive study of CAD models of several coplanar waveguide discontinuities”, IEE. Proc. Microwave Antenna Prop., vol. 152, pp. 69-76, Apr. 2005

[4.45] D. Mirshekar-Syahkal, “Computation of equivalent circuits of CPW discontinuities using quasi-static spectral domain method”, IEEE Trans. Microwave Theory Tech., vol. 44, pp. 979-984, Jun. 1996

[4.46] R., Simons, “Modeling of some coplanar waveguide discontinuities”, IEEE Trans. Microwave Theory Tech., vol. 36, pp. 1796-1803, Dec. 1988

[4.47] D. Mirshekar-Syahkal, “Computation of Equivalent Circuits of CPW Discontinuities Using Quasi-static Spectral Domain Method”, IEEE Trans. Microwave Theory Tech., vol. 44, No. 6, pp. 979-984, Jun. 1996

[4.48] T.Q. Wang, “Experimental study of wideband uniplanar phase inverters for MICs”. 1997 IEEE MTT-S Int. Microwave Symp. Digest, pp.777-780

[4.49] E. Hammerstad, “Accurate Models for microstrip computer aided design ”, IEEE MTT-S Int. Symp. Digist, 1980, pp 407-409

[4.50] M. Dydyk, "Master the T-junction and sharpen your MIC designs", Microwaves, vol.16, pp. 184-186, May 1977

[4.51] R.Vogel, "Effects of the T-Junction Discontinuity on the design of microstrip directional coplers", IEEE Trans. Microwave Theory Tech., pp. 145-146, Mar. 1973

[4.52] W. Leighton, "Junction reactance and dimensional tolerance effects on X-band 3dB directional effects", IEEE Trans. Microwave Theory Tech., vol. MTT-19, pp. 818-824, Oct. 1999

[4.53] M. Dydyk, "Microstrip directional couplers with ideal performance via single-element compensation," IEEE Trans. Microwave Theory Tech., vol. MTT-47, pp. 956-964, Jun. 1999

[4.54] S. Gruszczynski, "design of compensated coupled stripline 3dB directional couplers phase shifters and magic Ts", IEEE Trans. Microwave Theory Tech., vol. MTT-54, pp. 3501-3507, Sep. 2006

[4.55] E. Hammerstad, "Accurate models for microstrip computer aided design ", IEEE MTT-S Int. Symp. Digist, 1980, pp 407-409

[4.56] R.J.P. Douville and D.J. James, "Experimental study of symmetrical microstrip bends and their compensation", IEEE Trans. Microwave Theory Tech., vol. 26, pp. 175-182, Feb. 1978

[4.57] N. Dib, "The Effect of Mitering on CPW Discontinuities", IEE. Proc. Microwave Antennas Prop., vol. 152, pp. 223-228, Apr. 2005

[4.58] T. Weller, "Three-dimensional high-frequency distribution networks. I. Optimization of CPW discontinuities", IEEE Trans. Microwave Theory Tech., vol. MTT-48, pp. 1635-1642, Oct. 1997

[4.59] A.A. Omar, Y.L. Chow, L. Roy, and M.G. Stubbs, ''Effect of Air-Bridges and Mitering on Coplanar Waveguide 90° Bends:Theory and Experiments,'' 1993 IEEE MTT-S Int. Microwave Symp. Dig., vol. 2, pp. 823-826, June 14-18, 1993, Atlanta, GA.

[4.60] P.M. Watson and K.C. Gupta, ''Design and Optimization of CPW Circuits Using EM-ANN Models for CPW Components,'' IEEE Trans. Microwave Theory Tech., vol. 45, pp. 2515-2523, Dec. 1997.

[4.61] T.M. Weller, R.M. Henderson, S.V. Robertson and L.P.B. Katehi, ''Optimization of MM-Wave Distribution Networks Using Silicon-Based CPW,'' 1998 IEEE MTT-S Int. Microwave Symp. Dig., vol. 2, pp. 537-540, June 7-12, 1998, Baltimore, MD.

[4.62] R.N. Simons and G.E. Ponchak, ''Modeling of Some Coplanar Waveguide Discontinuities,'' IEEE Trans. Microwave Theory Tech., vol. 36, pp. 1796-1803, Dec. 1988

[4.63] Rehnmark S., "Wideband balanced line microwave hybrids", IEEE Trans. Microwave Theory Tech., vol. 25, pp. 825-830, Oct. 1977

[4.64] A.A. Omar et al., “Effects of air-bridges and mitering on CPW $90^o$ bends: theory and experiments ”, IEEE MTT-S Int. Microwave Symp. Dig., Atlanta Ga, June 1993, pp. 823-826

# APPENDIX

## I. MATHEMATIC PROGRAM FOR ANALYSIS OF BRANCH-LINE COUPLERS

$$L_{z5} = \frac{\lambda 0}{4};$$

$$L_{zc2} = \frac{\lambda 0}{4};$$

$$L_{z3} = \frac{\lambda 0}{8};$$

$$L_{z4} = \frac{\lambda 0}{4};$$

$$L_{z2} = \frac{\lambda 0}{8};$$

$$L_{z1} = \frac{\lambda 0}{8};$$

$$L_{zc1} = \frac{\lambda 0}{4};$$

$$\beta = \frac{2\,\pi}{\lambda};$$

$$Z0 = 50;$$

$$oA_{zc1} = \left\{\{Cos\,[\beta\, L_{zc1}],\ i\, Zc1\ Sin\,[\beta\, L_{zc1}]\},\ \left\{\frac{i\ Sin\,[\beta\, L_{zc1}]}{Zc1},\ Cos\,[\beta\, L_{zc1}]\right\}\right\};$$

$$oA_{zc2} = \left\{\{Cos\,[\beta\, L_{zc2}],\ i\, Zc2\ Sin\,[\beta\, L_{zc2}]\},\ \left\{\frac{i\ Sin\,[\beta\, L_{zc2}]}{Zc2},\ Cos\,[\beta\, L_{zc2}]\right\}\right\};$$

$$oA_{z4} = \left\{\{Cos\,[\beta\, L_{z4}],\ i\, Z4\ Sin\,[\beta\, L_{z4}]\},\ \left\{\frac{i\ Sin\,[\beta\, L_{z4}]}{Z4},\ Cos\,[\beta\, L_{z4}]\right\}\right\};$$

$$oA_{z5} = \left\{\{Cos\,[\beta\, L_{z5}],\ i\, Z5\ Sin\,[\beta\, L_{z5}]\},\ \left\{\frac{i\ Sin\,[\beta\, L_{z5}]}{Z5},\ Cos\,[\beta\, L_{z5}]\right\}\right\};$$

$$oZ_{z1} = \frac{Z1}{i\ Tan\,[\beta\, L_{z1}]};$$

$$oA_{z1} = \left\{\{1,\ 0\},\ \left\{\frac{1}{oZ_{z1}},\ 1\right\}\right\};$$

$$oZ_{z2} = \frac{Z2}{i\ Tan\,[\beta\, L_{z2}]};$$

$$o\ A_{z2} = \left\{\{1,\ 0\},\ \left\{\frac{1}{oZ_{z2}},\ 1\right\}\right\};$$

$$oZ_{z3} = \frac{Z3}{i\ Tan\,[\beta\, L_{z3}]};$$

$$o\ A_{z3} = \left\{\{1,\ 0\},\ \left\{\frac{1}{oZ_{z3}},\ 1\right\}\right\};$$

$$oA_{summary} = oA_{zc1}\,.\,oA_{z1}\,.\,oA_{z4}\,.\,oA_{z3}\,.\,oA_{z5}\,.\,oA_{z2}\,.\,oA_{zc2};$$

$$oS = \{\{0,\ 0\},\ \{0,\ 0\}\};$$

$$oS[[1,\ 1]] = 1 \Big/ \left(oA_{summary}[[1,\ 1]] + \frac{oA_{summary}[[1,\ 2]]}{Z0} + Z0\ oA_{summary}[[2,\ 1]] + oA_{summary}[[2,\ 2]]\right) \left(oA_{summary}[[1,\ 1]] + \frac{oA_{summary}[[1,\ 2]]}{Z0} - Z0\ oA_{summary}[[2,\ 1]] - oA_{summary}[[2,\ 2]]\right);$$

$$oS[[1,\ 2]] = 2 \Big/ \left(oA_{summary}[[1,\ 1]] + \frac{oA_{summary}[[1,\ 2]]}{Z0} + Z0\ oA_{summary}[[2,\ 1]] + oA_{summary}[[2,\ 2]]\right) (oA_{summary}[[1,\ 1]]\ oA_{summary}[[2,\ 2]] - oA_{summary}[[1,\ 2]]\ oA_{summary}[[2,\ 1]]);$$

$$oS[[2,\ 1]] = 2 \Big/ \left(oA_{summary}[[1,\ 1]] + \frac{oA_{summary}[[1,\ 2]]}{Z0} + Z0\ oA_{summary}[[2,\ 1]] + oA_{summary}[[2,\ 2]]\right);$$

$$\text{oS[[2, 2]]} = 1\Big/\left(\text{oA}_{\text{summary}}\text{[[1, 1]]} + \frac{\text{oA}_{\text{summary}}\text{[[1, 2]]}}{\text{Z0}} + \text{Z0 oA}_{\text{summary}}\text{[[2, 1]]} + \text{oA}_{\text{summary}}\text{[[2, 2]]}\right)$$
$$\left(-\text{oA}_{\text{summary}}\text{[[1, 1]]} + \frac{\text{oA}_{\text{summary}}\text{[[1, 2]]}}{\text{Z0}} - \text{Z0 oA}_{\text{summary}}\text{[[2, 1]]} + \text{oA}_{\text{summary}}\text{[[2, 2]]}\right);$$

$$\text{sA}_{\text{zc1}} = \left\{\{\text{Cos}\,[\beta\,\text{L}_{\text{zc1}}],\ \mathbb{i}\ \text{Zc1 Sin}\,[\beta\,\text{L}_{\text{zc1}}]\},\ \left\{\frac{\mathbb{i}\ \text{Sin}\,[\beta\,\text{L}_{\text{zc1}}]}{\text{Zc1}},\ \text{Cos}\,[\beta\,\text{L}_{\text{zc1}}]\right\}\right\};$$
$$\text{sA}_{\text{zc2}} = \left\{\{\text{Cos}\,[\beta\,\text{L}_{\text{zc2}}],\ \mathbb{i}\ \text{Zc2 Sin}\,[\beta\,\text{L}_{\text{zc2}}]\},\ \left\{\frac{\mathbb{i}\ \text{Sin}\,[\beta\,\text{L}_{\text{zc2}}]}{\text{Zc2}},\ \text{Cos}\,[\beta\,\text{L}_{\text{zc2}}]\right\}\right\};$$
$$\text{sA}_{\text{z4}} = \left\{\{\text{Cos}\,[\beta\,\text{L}_{\text{z4}}],\ \mathbb{i}\ \text{Z4 Sin}\,[\beta\,\text{L}_{\text{z4}}]\},\ \left\{\frac{\mathbb{i}\ \text{Sin}\,[\beta\,\text{L}_{\text{z4}}]}{\text{Z4}},\ \text{Cos}\,[\beta\,\text{L}_{\text{z4}}]\right\}\right\};$$
$$\text{sA}_{\text{z5}} = \left\{\{\text{Cos}\,[\beta\,\text{L}_{\text{z5}}],\ \mathbb{i}\ \text{Z5 Sin}\,[\beta\,\text{L}_{\text{z5}}]\},\ \left\{\frac{\mathbb{i}\ \text{Sin}\,[\beta\,\text{L}_{\text{z5}}]}{\text{Z5}},\ \text{Cos}\,[\beta\,\text{L}_{\text{z5}}]\right\}\right\};$$

$$\text{sZ}_{\text{z1}} = \text{Z1}\ \mathbb{i}\ \text{Tan}\,[\beta\,\text{L}_{\text{z1}}];$$
$$\text{sA}_{\text{z1}} = \left\{\{1,\ 0\},\ \left\{\frac{1}{\text{sZ}_{\text{z1}}},\ 1\right\}\right\};$$
$$\text{sZ}_{\text{z3}} = \text{Z3}\ \mathbb{i}\ \text{Tan}\,[\beta\,\text{L}_{\text{z3}}];$$
$$\text{s A}_{\text{z3}} = \left\{\{1,\ 0\},\ \left\{\frac{1}{\text{sZ}_{\text{z3}}},\ 1\right\}\right\};$$
$$\text{sZ}_{\text{z2}} = \text{Z2}\ \mathbb{i}\ \text{Tan}\,[\beta\,\text{L}_{\text{z2}}];$$
$$\text{s A}_{\text{z2}} = \left\{\{1,\ 0\},\ \left\{\frac{1}{\text{sZ}_{\text{z2}}},\ 1\right\}\right\};$$

$$\text{sA}_{\text{summary}} = \text{sA}_{\text{zc1}}.\text{sA}_{\text{z1}}.\text{sA}_{\text{z4}}.\text{sA}_{\text{z3}}.\text{sA}_{\text{z5}}.\text{sA}_{\text{z2}}.\text{sA}_{\text{zc2}};$$

$$\text{sS} = \{\{0,\ 0\},\ \{0,\ 0\}\};$$
$$\text{sS[[1, 1]]} = 1\Big/\left(\text{sA}_{\text{summary}}\text{[[1, 1]]} + \frac{\text{sA}_{\text{summary}}\text{[[1, 2]]}}{\text{Z0}} + \text{Z0 sA}_{\text{summary}}\text{[[2, 1]]} + \text{sA}_{\text{summary}}\text{[[2, 2]]}\right)$$
$$\left(\text{sA}_{\text{summary}}\text{[[1, 1]]} + \frac{\text{sA}_{\text{summary}}\text{[[1, 2]]}}{\text{Z0}} - \text{Z0 sA}_{\text{summary}}\text{[[2, 1]]} - \text{sA}_{\text{summary}}\text{[[2, 2]]}\right);$$
$$\text{sS[[1, 2]]} = 2\Big/\left(\text{sA}_{\text{summary}}\text{[[1, 1]]} + \frac{\text{sA}_{\text{summary}}\text{[[1, 2]]}}{\text{Z0}} + \text{Z0 sA}_{\text{summary}}\text{[[2, 1]]} + \text{sA}_{\text{summary}}\text{[[2, 2]]}\right)$$
$$(\text{sA}_{\text{summary}}\text{[[1, 1]] sA}_{\text{summary}}\text{[[2, 2]]} - \text{sA}_{\text{summary}}\text{[[1, 2]] sA}_{\text{summary}}\text{[[2, 1]]});$$
$$\text{sS[[2, 1]]} = 2\Big/\left(\text{sA}_{\text{summary}}\text{[[1, 1]]} + \frac{\text{sA}_{\text{summary}}\text{[[1, 2]]}}{\text{Z0}} + \text{Z0 sA}_{\text{summary}}\text{[[2, 1]]} + \text{sA}_{\text{summary}}\text{[[2, 2]]}\right);$$
$$\text{sS[[2, 2]]} = 1\Big/\left(\text{sA}_{\text{summary}}\text{[[1, 1]]} + \frac{\text{sA}_{\text{summary}}\text{[[1, 2]]}}{\text{Z0}} + \text{Z0 sA}_{\text{summary}}\text{[[2, 1]]} + \text{sA}_{\text{summary}}\text{[[2, 2]]}\right)$$

$$\text{S11} = \text{Simplify}\left[\text{Abs}\left[\text{Limit}\left[\frac{1}{2}\ (\text{oS[[1, 1]]} + \text{sS[[1, 1]]}),\ \lambda \to \lambda0\right]\right]\right]$$
$$\text{S12} = \text{Simplify}\left[\text{Abs}\left[\text{Limit}\left[\frac{1}{2}\ (\text{oS[[2, 1]]} + \text{sS[[2, 1]]}),\ \lambda \to \lambda0\right]\right]\right]$$
$$\text{S13} = \text{Simplify}\left[\text{Abs}\left[\text{Limit}\left[\frac{1}{2}\ (\text{oS[[2, 1]]} - \text{sS[[2, 1]]}),\ \lambda \to \lambda0\right]\right]\right]$$
$$\text{S14} = \text{Simplify}\left[\text{Abs}\left[\text{Limit}\left[\frac{1}{2}\ (\text{oS[[1, 1]]} - \text{sS[[1, 1]]}),\ \lambda \to \lambda0\right]\right]\right]$$
$$\text{S22} = \text{Simplify}\left[\text{Abs}\left[\text{Limit}\left[\frac{1}{2}\ (\text{oS[[2, 2]]} + \text{sS[[2, 2]]}),\ \lambda \to \lambda0\right]\right]\right]$$
$$\text{S23} = \text{Simplify}\left[\text{Abs}\left[\text{Limit}\left[\frac{1}{2}\ (\text{oS[[2, 2]]} - \text{sS[[2, 2]]}),\ \lambda \to \lambda0\right]\right]\right]$$

## II. MATHEMATIC PROGRAM FOR ANALYSIS of RAT-RACE COUPLERS

$$L_{z0} = \frac{\lambda 0}{4};$$

$$L_{z3} = \frac{5\,\lambda 0}{8};$$

$$L_{z1} = \frac{\lambda 0}{4};$$

$$L_{z4} = \frac{3\,\lambda 0}{8};$$

$$L_{z2} = \frac{\lambda 0}{4};$$

$$L_{z5} = \frac{\lambda 0}{8};$$

$$\beta = \frac{2\,\pi}{\lambda};$$

$$Z0 = 50;$$

$$oA_{z0} = \left\{\{\mathrm{Cos}\,[\beta\, L_{z0}],\ i\ Z0\ \mathrm{Sin}\,[\beta\, L_{z0}]\},\ \left\{\frac{i\ \mathrm{Sin}\,[\beta\, L_{z0}]}{Z0},\ \mathrm{Cos}\,[\beta\, L_{z0}]\right\}\right\};$$

$$oA_{z1} = \left\{\{\mathrm{Cos}\,[\beta\, L_{z1}],\ i\ Z1\ \mathrm{Sin}\,[\beta\, L_{z1}]\},\ \left\{\frac{i\ \mathrm{Sin}\,[\beta\, L_{z1}]}{Z1},\ \mathrm{Cos}\,[\beta\, L_{z1}]\right\}\right\};$$

$$oA_{z2} = \left\{\{\mathrm{Cos}\,[\beta\, L_{z2}],\ i\ Z2\ \mathrm{Sin}\,[\beta\, L_{z2}]\},\ \left\{\frac{i\ \mathrm{Sin}\,[\beta\, L_{z2}]}{Z2},\ \mathrm{Cos}\,[\beta\, L_{z2}]\right\}\right\};$$

$$oZ_{z3} = \frac{Z3}{i\ \mathrm{Tan}\,[\beta\, L_{z3}]};$$

$$oA_{z3} = \left\{\{1,\ 0\},\ \left\{\frac{1}{oZ_{z3}},\ 1\right\}\right\};$$

$$oZ_{z4} = \frac{Z4}{i\ \mathrm{Tan}\,[\beta\, L_{z4}]};$$

$$oA_{z4} = \left\{\{1,\ 0\},\ \left\{\frac{1}{oZ_{z4}},\ 1\right\}\right\};$$

$$oZ_{z5} = \frac{Z5}{i\ \mathrm{Tan}\,[\beta\, L_{z5}]};$$

$$oA_{z5} = \left\{\{1,\ 0\},\ \left\{\frac{1}{oZ_{z5}},\ 1\right\}\right\};$$

$$oA_{summary} = oA_{z0}\,.\,oA_{z3}\,.\,oA_{z1}\,.\,oA_{z4}\,.\,oA_{z2}\,.\,oA_{z5}\,.\,oA_{z0};$$

$$oS = \{\{0,\ 0\},\ \{0,\ 0\}\};$$

$$oS[[1,\ 1]] = 1 \Big/ \left(oA_{summary}[[1,\ 1]] + \frac{oA_{summary}[[1,\ 2]]}{Z0} + Z0\ oA_{summary}[[2,\ 1]] + oA_{summary}[[2,\ 2]]\right) \left(oA_{summary}[[1,\ 1]] + \frac{oA_{summary}[[1,\ 2]]}{Z0} - Z0\ oA_{summary}[[2,\ 1]] - oA_{summary}[[2,\ 2]]\right);$$

```
oS[[1, 2]] =
 2 / (oA_summary[[1, 1]] + oA_summary[[1, 2]]/Z0 + Z0 oA_summary[[2, 1]] + oA_summary[[2, 2]])
  (oA_summary[[1, 1]] oA_summary[[2, 2]] - oA_summary[[1, 2]] oA_summary[[2, 1]]);
oS[[2, 1]] =
 2 / (oA_summary[[1, 1]] + oA_summary[[1, 2]]/Z0 + Z0 oA_summary[[2, 1]] + oA_summary[[2, 2]]);
oS[[2, 2]] =
 1 / (oA_summary[[1, 1]] + oA_summary[[1, 2]]/Z0 + Z0 oA_summary[[2, 1]] + oA_summary[[2, 2]])
  (-oA_summary[[1, 1]] + oA_summary[[1, 2]]/Z0 - Z0 oA_summary[[2, 1]] + oA_summary[[2, 2]]);



sA_z0 = {{Cos [β L_z0], ⅈ Z0 Sin [β L_z0]}, {ⅈ Sin [β L_z0]/Z0, Cos [β L_z0]}};
sA_z1 = {{Cos [β L_z1], ⅈ Z1 Sin [β L_z1]}, {ⅈ Sin [β L_z1]/Z1, Cos [β L_z1]}};
sA_z2 = {{Cos [β L_z2], ⅈ Z2 Sin [β L_z2]}, {ⅈ Sin [β L_z2]/Z2, Cos [β L_z2]}};

sZ_z3 = Z3 ⅈ Tan [β L_z3];
sA_z3 = {{1, 0}, {1/sZ_z3, 1}};
sZ_z4 = Z4 ⅈ Tan [β L_z4];
sA_z4 = {{1, 0}, {1/sZ_z4, 1}};
sZ_z5 = Z5 ⅈ Tan [β L_z5];
sA_z5 = {{1, 0}, {1/sZ_z5, 1}};

sA_summary = sA_z0 . sA_z3 . sA_z1 . sA_z4 . sA_z2 . sA_z5 . sA_z0;


sS = {{0, 0}, {0, 0}};
 sS[[1, 1]] =
  1 / (sA_summary[[1, 1]] + sA_summary[[1, 2]]/Z0 + Z0 sA_summary[[2, 1]] + sA_summary[[2, 2]])
   (sA_summary[[1, 1]] + sA_summary[[1, 2]]/Z0 - Z0 sA_summary[[2, 1]] - sA_summary[[2, 2]]);
 sS[[1, 2]] =
  2 / (sA_summary[[1, 1]] + sA_summary[[1, 2]]/Z0 + Z0 sA_summary[[2, 1]] + sA_summary[[2, 2]])
   (sA_summary[[1, 1]] sA_summary[[2, 2]] - sA_summary[[1, 2]] sA_summary[[2, 1]]);
 sS[[2, 1]] =
  2 / (sA_summary[[1, 1]] + sA_summary[[1, 2]]/Z0 + Z0 sA_summary[[2, 1]] + sA_summary[[2, 2]]);
 sS[[2, 2]] =
  1 / (sA_summary[[1, 1]] + sA_summary[[1, 2]]/Z0 + Z0 sA_summary[[2, 1]] + sA_summary[[2, 2]])
   (-sA_summary[[1, 1]] + sA_summary[[1, 2]]/Z0 - Z0 sA_summary[[2, 1]] + sA_summary[[2, 2]]);
 S11 = Simplify[Abs[Limit[1/2 (oS[[1, 1]] + sS[[1, 1]]), λ → λ0]]]
 S12 = Simplify[Abs[Limit[1/2 (oS[[2, 1]] + sS[[2, 1]]), λ → λ0]]]
 S13 = Simplify[Abs[Limit[1/2 (oS[[2, 1]] - sS[[2, 1]]), λ → λ0]]]
 S14 = Simplify[Abs[Limit[1/2 (oS[[1, 1]] - sS[[1, 1]]), λ → λ0]]]
 S22 = Simplify[Abs[Limit[1/2 (oS[[2, 2]] + sS[[2, 2]]), λ → λ0]]]
 S23 = Simplify[Abs[Limit[1/2 (oS[[2, 2]] - sS[[2, 2]]), λ → λ0]]]
```

## III. DERIVATION RESULTS FOR GENERAL FOUR-PORT NETWORK

The derived S parameters of the structure shown in Figure 4.6

$$S11=\frac{1}{2}\left(\frac{50\,Z2^2\,\text{Cot}[\frac{1}{4}(1+2m)\pi]\,(Z1-50\,i\,\text{Cot}[\frac{1}{4}(1+2n)\pi])+Z1\,(-i\,Z1\,(-2500+Z2^2)-50\,Z2^2\,\text{Cot}[\frac{1}{4}(1+2n)\pi])}{50\,Z2^2\,\text{Cot}[\frac{1}{4}(1+2m)\pi]\,(Z1-50\,i\,\text{Cot}[\frac{1}{4}(1+2n)\pi])+Z1\,(i\,Z1\,(2500+Z2^2)+50\,Z2^2\,\text{Cot}[\frac{1}{4}(1+2n)\pi])}+\frac{50\,Z2^2\,\text{Tan}[\frac{1}{4}(1+2m)\pi]\,(Z1+50\,i\,\text{Tan}[\frac{1}{4}(1+2n)\pi])+i\,Z1\,(Z1\,(-2500+Z2^2)+50\,i\,Z2^2\,\text{Tan}[\frac{1}{4}(1+2n)\pi])}{50\,Z2^2\,\text{Tan}[\frac{1}{4}(1+2m)\pi]\,(Z1+50\,i\,\text{Tan}[\frac{1}{4}(1+2n)\pi])+Z1\,(-i\,Z1\,(2500+Z2^2)+50\,Z2^2\,\text{Tan}[\frac{1}{4}(1+2n)\pi])}\right)$$

$$S12=50\,i\,Z1^2\,Z2\left(\frac{1}{-50\,i\,Z2^2\,\text{Cot}[\frac{1}{4}(1+2m)\pi]\,(Z1-50\,i\,\text{Cot}[\frac{1}{4}(1+2n)\pi])+Z1\,(Z1\,(2500+Z2^2)-50\,i\,Z2^2\,\text{Cot}[\frac{1}{4}(1+2n)\pi])}+\frac{1}{50\,i\,Z2^2\,\text{Tan}[\frac{1}{4}(1+2m)\pi]\,(Z1+50\,i\,\text{Tan}[\frac{1}{4}(1+2n)\pi])+Z1\,(Z1\,(2500+Z2^2)+50\,i\,Z2^2\,\text{Tan}[\frac{1}{4}(1+2n)\pi])}\right)$$

$$S13=-50\,i\,Z1^2\,Z2\left(\frac{1}{-50\,i\,Z2^2\,\text{Tan}[\frac{1}{4}(1+2m)\pi]\,(Z1-50\,i\,\text{Tan}[\frac{1}{4}(1+2n)\pi])+Z1\,(Z1\,(2500+Z2^2)-50\,i\,Z2^2\,\text{Tan}[\frac{1}{4}(1+2n)\pi])}-\frac{1}{50\,i\,Z2^2\,\text{Tan}[\frac{1}{4}(1+2m)\pi]\,(Z1+50\,i\,\text{Tan}[\frac{1}{4}(1+2n)\pi])+Z1\,(Z1\,(2500+Z2^2)+50\,i\,Z2^2\,\text{Tan}[\frac{1}{4}(1+2n)\pi])}\right)$$

$$S14=\left(100\,i\,Z1\,Z2^2\left(-2500\,Z1^2\,\text{Sec}[n\pi]+Z2^2\,\text{Sec}[m\pi]\,(2500+Z1^2+100\,i\,Z1\,\text{Tan}[n\pi])\right)\right)\Big/\left(\left(-50\,i\,Z2^2\,\text{Cot}[\frac{1}{4}(1+2m)\pi]\,(Z1-50\,i\,\text{Cot}[\frac{1}{4}(1+2n)\pi])+Z1\,(Z1\,(2500+Z2^2)-50\,i\,Z2^2\,\text{Cot}[\frac{1}{4}(1+2n)\pi])\right)\left(50\,i\,Z2^2\,\text{Tan}[\frac{1}{4}(1+2m)\pi]\,(Z1+50\,i\,\text{Tan}[\frac{1}{4}(1+2n)\pi])+Z1\,(Z1\,(2500+Z2^2)+50\,i\,Z2^2\,\text{Tan}[\frac{1}{4}(1+2n)\pi])\right)\right)$$

$$S22=\frac{1}{2}\left(\left(-50\,Z2^2\,\text{Cot}[\frac{1}{4}(1+2m)\pi]\,(Z1+50\,i\,\text{Cot}[\frac{1}{4}(1+2n)\pi])+Z1\,(-i\,Z1\,(-2500+Z2^2)+50\,Z2^2\,\text{Cot}[\frac{1}{4}(1+2n)\pi])\right)\Big/\left(50\,Z2^2\,\text{Cot}[\frac{1}{4}(1+2m)\pi]\,(Z1-50\,i\,\text{Cot}[\frac{1}{4}(1+2n)\pi])+Z1\,(i\,Z1\,(2500+Z2^2)+50\,Z2^2\,\text{Cot}[\frac{1}{4}(1+2n)\pi])\right)+\left(-50\,Z2^2\,\text{Tan}[\frac{1}{4}(1+2m)\pi]\,(Z1-50\,i\,\text{Tan}[\frac{1}{4}(1+2n)\pi])+Z1\,(i\,Z1\,(-2500+Z2^2)+50\,Z2^2\,\text{Tan}[\frac{1}{4}(1+2n)\pi])\right)\Big/\left(50\,Z2^2\,\text{Tan}[\frac{1}{4}(1+2m)\pi]\,(Z1+50\,i\,\text{Tan}[\frac{1}{4}(1+2n)\pi])+Z1\,(-i\,Z1\,(2500+Z2^2)+50\,Z2^2\,\text{Tan}[\frac{1}{4}(1+2n)\pi])\right)\right)$$

$$S23=\left(100\,i\,Z1\,Z2^2\left(-2500\,Z1^2\,\text{Sec}[m\pi]+Z2^2\,\text{Sec}[n\pi]\,(2500+Z1^2+100\,i\,Z1\,\text{Tan}[m\pi])\right)\right)\Big/\left(\left(-50\,i\,Z2^2\,\text{Cot}[\frac{1}{4}(1+2m)\pi]\,(Z1-50\,i\,\text{Cot}[\frac{1}{4}(1+2n)\pi])+Z1\,(Z1\,(2500+Z2^2)-50\,i\,Z2^2\,\text{Cot}[\frac{1}{4}(1+2n)\pi])\right)\left(50\,i\,Z2^2\,\text{Tan}[\frac{1}{4}(1+2m)\pi]\,(Z1+50\,i\,\text{Tan}[\frac{1}{4}(1+2n)\pi])+Z1\,(Z1\,(2500+Z2^2)+50\,i\,Z2^2\,\text{Tan}[\frac{1}{4}(1+2n)\pi])\right)\right)$$

## IV. DERIVATION RESULTS FOR GENERAL FOUR-PORT NETWORK

The derived S parameters of the structure shown in figure 4.7

$$\begin{aligned}
&S11 = \\
&\{-(50\,(Z1\,Z3\,(12500000 + 124900\,\mathrm{i}\,Z1 + Z1^2\,(1 - 125000\,\mathrm{i}\,\mathrm{oA} - 2500\,\mathrm{i}\,z5)) + \\
&\qquad(-50\,\mathrm{i} + Z1)\,Z2^2\,(125000\,\mathrm{i} + Z1 + 50\,Z1^2\,(50\,\mathrm{oA} + z5))))\,/ \\
&\quad((-50\,\mathrm{i} + Z1)\,((-50\,\mathrm{i} + Z1)\,Z2^2 - 100\,\mathrm{i}\,Z1\,Z3)\,(125000 + Z1\,(-\mathrm{i} + 125000\,\mathrm{oA} + 2500\,z5))), \\
&\ -(50\,\mathrm{i}\,((6250000 + 124950\,\mathrm{i}\,Z1 + Z1^2)\,Z2^4 + 2500\,Z1^2\,Z3^2\,(5000 + Z1\,(50\,\mathrm{i} + 50\,\mathrm{oA} + z5)) + \\
&\qquad Z1\,Z2^2\,Z3\,(18750000 + Z1^2\,(1 + 2500\,\mathrm{i}\,\mathrm{oA} + 50\,\mathrm{i}\,z5) + 100\,Z1\,(2499\,\mathrm{i} + 1250\,\mathrm{oA} + 25\,z5))))\,/ \\
&\quad((-50\,\mathrm{i} + Z1)\,((-50\,\mathrm{i} + Z1)\,Z2^2 - 100\,\mathrm{i}\,Z1\,Z3)\,((125000\,\mathrm{i} + Z1)\,Z2^2 - 2500\,Z1\,Z3\,(-50\,\mathrm{i} + 50\,\mathrm{oA} + z5)))\}
\end{aligned}$$

$$S12 = \{-\frac{50\,\mathrm{i}\,Z1\,(50\,\mathrm{i}\,(-50\,\mathrm{i} + Z1)^2\,Z2^2 + Z1\,Z3\,((125000 - 250000\,\mathrm{i}) + Z1\,((5000 - \mathrm{i}) + 125000\,\mathrm{oA} + 2500\,z5)))}{(-50\,\mathrm{i} + Z1)\,((-50\,\mathrm{i} + Z1)\,Z2^2 - 100\,\mathrm{i}\,Z1\,Z3)\,(125000 + Z1\,(-\mathrm{i} + 125000\,\mathrm{oA} + 2500\,z5))},$$

$$\begin{aligned}
&(50\,\mathrm{i}\,Z1\,Z3\,((-125000\,\mathrm{i} + (5000 - 125000\,\mathrm{i})\,Z1 - (1 - 50\,\mathrm{i})\,Z1^2)\,Z2^2 + \\
&\qquad 2500\,Z1\,Z3\,(-100\,\mathrm{i} + Z1\,((2 - 50\,\mathrm{i}) + 50\,\mathrm{oA} + z5))))\,/ \\
&\quad((-50\,\mathrm{i} + Z1)\,((-50\,\mathrm{i} + Z1)\,Z2^2 - 100\,\mathrm{i}\,Z1\,Z3)\,((125000\,\mathrm{i} + Z1)\,Z2^2 - 2500\,Z1\,Z3\,(-50\,\mathrm{i} + 50\,\mathrm{oA} + z5)))\}
\end{aligned}$$

$$S13 = \{\frac{50\,Z1\,(50\,(-50\,\mathrm{i} + Z1)^2\,Z2^2 + \mathrm{i}\,Z1\,Z3\,((125000 + 250000\,\mathrm{i}) + Z1\,((-5000 - \mathrm{i}) + 125000\,\mathrm{oA} + 2500\,z5)))}{(-50\,\mathrm{i} + Z1)\,((-50\,\mathrm{i} + Z1)\,Z2^2 - 100\,\mathrm{i}\,Z1\,Z3)\,(125000 + Z1\,(-\mathrm{i} + 125000\,\mathrm{oA} + 2500\,z5))},$$

$$\frac{50\,Z1\,Z3\,((125000 - (125000 - 5000\,\mathrm{i})\,Z1 - (50 - \mathrm{i})\,Z1^2)\,Z2^2 - 2500\,\mathrm{i}\,Z1\,Z3\,(100\,\mathrm{i} + Z1\,((-2 - 50\,\mathrm{i}) + 50\,\mathrm{oA} + z5)))}{(-50\,\mathrm{i} + Z1)\,((-50\,\mathrm{i} + Z1)\,Z2^2 - 100\,\mathrm{i}\,Z1\,Z3)\,((125000\,\mathrm{i} + Z1)\,Z2^2 - 2500\,Z1\,Z3\,(-50\,\mathrm{i} + 50\,\mathrm{oA} + z5))}\}$$

$$\begin{aligned}
&S14 = \\
&\{(\mathrm{i}\,Z1\,((-50\,\mathrm{i} + Z1)\,Z2^2\,(6250000\,\mathrm{oA} - Z1 + 125000\,(-\mathrm{i} + z5)) + \\
&\qquad 50\,Z1\,Z3\,(125000\,\mathrm{oA}\,(-100\,\mathrm{i} + Z1) - 125000\,\mathrm{i}\,(-\mathrm{i} + 2\,z5) + Z1\,(\mathrm{i} + 2500\,z5))))\,/ \\
&\quad((-50\,\mathrm{i} + Z1)\,((-50\,\mathrm{i} + Z1)\,Z2^2 - 100\,\mathrm{i}\,Z1\,Z3)\,(125000 + Z1\,(-\mathrm{i} + 125000\,\mathrm{oA} + 2500\,z5))), \\
&\ (Z1\,((6250000 + 124950\,\mathrm{i}\,Z1 + Z1^2)\,Z2^4 + \\
&\qquad 50\,Z2^2\,Z3\,(2499\,\mathrm{i}\,Z1^2 - 125000\,\mathrm{i}\,\mathrm{oA}\,(-50\,\mathrm{i} + Z1) + 2500\,Z1\,(100 - \mathrm{i}\,z5) - 125000\,z5) + \\
&\qquad 125000\,Z1\,Z3^2\,(-50\,\mathrm{i}\,\mathrm{oA}\,(-100\,\mathrm{i} + Z1) + Z1\,(50 - \mathrm{i}\,z5) - 100\,z5)))\,/ \\
&\quad((-50\,\mathrm{i} + Z1)\,((-50\,\mathrm{i} + Z1)\,Z2^2 - 100\,\mathrm{i}\,Z1\,Z3)\,((125000\,\mathrm{i} + Z1)\,Z2^2 - 2500\,Z1\,Z3\,(-50\,\mathrm{i} + 50\,\mathrm{oA} + z5)))\}
\end{aligned}$$

$$\begin{aligned}
&S22 = \\
&\{-(50\,Z1\,((-50\,\mathrm{i} + Z1)\,Z2^2\,(2501 + 2500\,\mathrm{oA}\,Z1 + 2500\,\mathrm{i}\,z5) + \\
&\qquad Z1\,Z3\,(-125100\,\mathrm{i} + Z1 - 125000\,\mathrm{i}\,\mathrm{oA}\,Z1 + 250000\,z5 + 2500\,\mathrm{i}\,Z1\,z5)))\,/ \\
&\quad((-50\,\mathrm{i} + Z1)\,((-50\,\mathrm{i} + Z1)\,Z2^2 - 100\,\mathrm{i}\,Z1\,Z3)\,(125000 + Z1\,(-\mathrm{i} + 125000\,\mathrm{oA} + 2500\,z5))), \\
&\ (50\,Z1\,(-2501\,\mathrm{i}\,(-50\,\mathrm{i} + Z1)\,Z2^4 + 2500\,Z1\,Z3^2\,(Z1\,(-50 - 50\,\mathrm{i}\,\mathrm{oA} + \mathrm{i}\,z5) + 100\,z5) + \\
&\qquad Z2^2\,Z3\,((-2501\,\mathrm{i} + 2500\,\mathrm{oA})\,Z1^2 - 100\,\mathrm{i}\,Z1\,(-2501\,\mathrm{i} + 1250\,\mathrm{oA} - 25\,z5) + 125000\,z5)))\,/ \\
&\quad((-50\,\mathrm{i} + Z1)\,((-50\,\mathrm{i} + Z1)\,Z2^2 - 100\,\mathrm{i}\,Z1\,Z3)\,((125000\,\mathrm{i} + Z1)\,Z2^2 - 2500\,Z1\,Z3\,(-50\,\mathrm{i} + 50\,\mathrm{oA} + z5)))\}
\end{aligned}$$

$$\begin{aligned}
&S23 = \\
&\{(50\,\mathrm{i}\,Z1\,Z3\,(-12500000\,\mathrm{i} + 125000\,(1 - 100\,\mathrm{i}\,\mathrm{oA})\,Z1 + Z1^2\,(\mathrm{i} + 125000\,\mathrm{oA} - 2500\,z5)) + \\
&\qquad(-50\,\mathrm{i} + Z1)\,Z2^2\,(6250000\,\mathrm{i} + 6250000\,\mathrm{i}\,\mathrm{oA}\,Z1 + Z1^2\,(-\mathrm{i} + 2500\,z5)))\,/ \\
&\quad((-50\,\mathrm{i} + Z1)\,((-50\,\mathrm{i} + Z1)\,Z2^2 - 100\,\mathrm{i}\,Z1\,Z3)\,(125000 + Z1\,(-\mathrm{i} + 125000\,\mathrm{oA} + 2500\,z5))), \\
&\ ((312500000\,\mathrm{i} - 6250000\,Z1 - 50\,\mathrm{i}\,Z1^2 + Z1^3)\,Z2^4 - 125000\,\mathrm{i}\,Z1^2\,Z3^2\,(-5000 + 50\,\mathrm{oA}\,(-100\,\mathrm{i} + Z1) - Z1\,(50\,\mathrm{i} + z5)) - \\
&\qquad 50\,Z1\,Z2^2\,Z3\,(-18750000\,\mathrm{i} + 125000\,\mathrm{oA}\,(50 + \mathrm{i}\,Z1) + 2500\,Z1\,(100 - \mathrm{i}\,z5) + Z1^2\,(\mathrm{i} + 50\,z5)))\,/ \\
&\quad((-50\,\mathrm{i} + Z1)\,((-50\,\mathrm{i} + Z1)\,Z2^2 - 100\,\mathrm{i}\,Z1\,Z3)\,((125000\,\mathrm{i} + Z1)\,Z2^2 - 2500\,Z1\,Z3\,(-50\,\mathrm{i} + 50\,\mathrm{oA} + z5)))\}
\end{aligned}$$

# Chapter 5

# FOUR-PORT COUPLER IMPLEMENTATION

We have already noted in Chapter 4 that the branch-line and rat-race ring couplers are preferred because of their performance characteristics and fabrication ease. These couplers may be implemented in various forms ─ microstrip [5.1]-[5.4], slot-line [5.5], coplanar-waveguide (CPW) [5.6]-[5.9], *etc*. Among these, microstrip-line structures are most widely used and we shall explore in Sections 5.1-5.2 the implementation of our modified-coupler designs in microstrip form. In our effort to widen the bandwidth even further, we shall also proceed with CPW implementation in Section 5.3.

## 5.1 Microstrip Prototype based on Modified Branch-Line Structure

Although there are many papers/textbooks [5.1]-[5.17] relating to branch-line coupler design, we have already found in Sub-Section 4.3.1 that the six-port reflectometer based on standard branch-line couplers will not yield an operating bandwidth exceeding 25%. Nevertheless, such a structure is convenient to fabricate and it provides us with the opportunity to build up our experience as we seek to move up the learning curve in our objective to develop six-port reflectometers with the ideal-case q-point distribution outlined in Chapter 3.

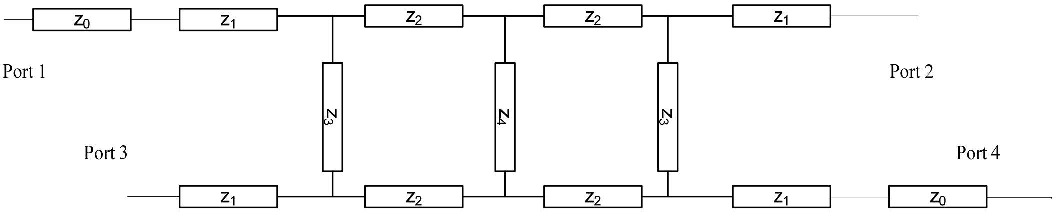

Figure 5.1 Schematic circuit diagram of proposed branch-line coupler structure

For the microstrip branch-line structure sketched in Figure 5.1, we have chosen to use the Rogers RT/Duroid 5870 substrate (with relative permittivity of 2.33, loss tangent of 0.0012, laminate thickness of 31mil and ½oz of copper cladding) from the stock already available in our laboratory. As discussed in Sub-Section 4.3.1, we ought to begin our optimization from the narrow-band design with the following set of initial parameter settings for a 5GHz coupler: $Z_1 = 40\Omega$, $Z_2 = 40\Omega$, $Z_3 = 20\Omega$ and $Z_4 = 45\Omega$.

We have also found from our trials that we ought to re-cast our optimization error function in the following form:

$$F_{error} = \sum_{i=1}^{6} W_i g_i \tag{5.1}$$

$$g_1 = \sum_{j=1}^{N} |S_{11}(f_j)|^2 , \qquad g_2 = \sum_{j=1}^{N} |S_{22}(f_j)|^2$$

$$g_3 = \sum_{j=1}^{N} |S_{13}(f_j)|^2 , \qquad g_4 = \sum_{j=1}^{N} (|S_{12}(f_j)| - \frac{1}{\sqrt{2}})^2$$

$$g_5 = \sum_{j=1}^{N} (|S_{14}(f_j)| - \frac{1}{\sqrt{2}})^2 \qquad g_6 = \sum_{j=1}^{N} \angle \frac{S_{12}(f_j)}{S_{14}(f_j)} - 120^o$$

where

$$f_j = f_L + (j-1)\Delta f\ , \quad \text{j=1,……,N}$$

$$\Delta f = (f_H - f_L)/(N-1)$$

$f_L$ is the lowest frequency of the specified bandwidth

$f_H$ is the highest frequency of the specified bandwidth

N is the number of sampling points and

$W_i$ are the weighting factors.

Table 5.1 Key parameters for preliminary design of branch-line coupler (without discontinuity compensation)

| Coupler arm | Characteristic impedance (Ω) | Electrical length (degree) |
|---|---|---|
| $Z_1$ | 46 | 90 |
| $Z_2$ | 30 | 90 |
| $Z_3$ | 98 | 90 |
| $Z_4$ | 34 | 90 |
| $Z_0$ | 50 | 30 |

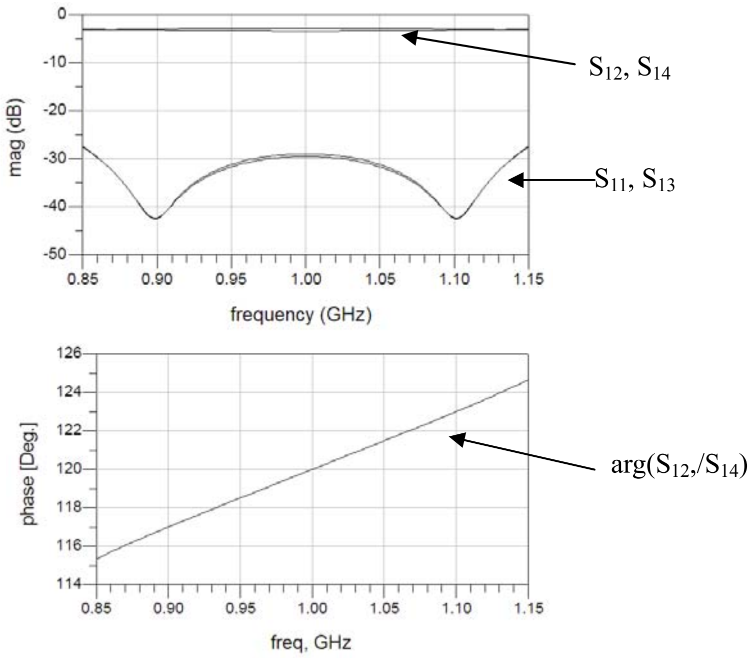

Figure 5.2 Simulation results for branch-line coupler with design parameters listed in Table 5.1

The simulation results presented in Figure 5.2 do not explicitly take discontinuity compensation into account. For operating frequencies higher than 5 GHz, it is naturally advisable to consider junction parasitic effects as well. We therefore need to re-scale the widths and lengths of the branch lines in order to compensate for the discontinuities as explained in Sub-Section 4.4.3. Including also the T-junction model in the optimization, we have been able to obtain the design parameters listed in Table 5.2 from a second run of the algorithm. Presented in Figure 5.4 are the simulation results for the design with discontinuity compensation now taken into consideration. Laboratory tests have also been performed on the modified branch-line prototype with the lay-out depicted in Figure 5.3. After de-embedding the raw measurement data, the experimental results presented in Figure 5.4 confirm that the return loss and isolation of our prototype exceed 25dB over a bandwidth of 26%. For the magnitude results, there is close agreement between the predicted and measured data in Figures 5.2 and 5.4 respectively. The measured phase differences are, however, somewhat larger than predicted by the simulation results (approximately 2°/GHz) and this may lead to some deterioration in the performance of the six-port reflectometer as discussed in Sub-Section 4.3.2.

TABLE 5.2 KEY PARAMETERS OF MODIFIED BRANCH-LINE COUPLER AFTER INCLUDING DISCONTINUITY COMPENSATION

| Coupler arm | Characteristic impedance (Ω) | Line width (mil) | Electrical length (degree) | Line length (mil) |
|---|---|---|---|---|
| $Z_1$ | 48 | 97 | 80 | 375 |
| $Z_2$ | 36 | 150 | 82 | 380 |
| $Z_3$ | 111 | 20 | 71 | 345 |
| $Z_4$ | 38 | 135 | 75 | 345 |
| $Z_0$ | 50 | 92 | 30 | 140 |

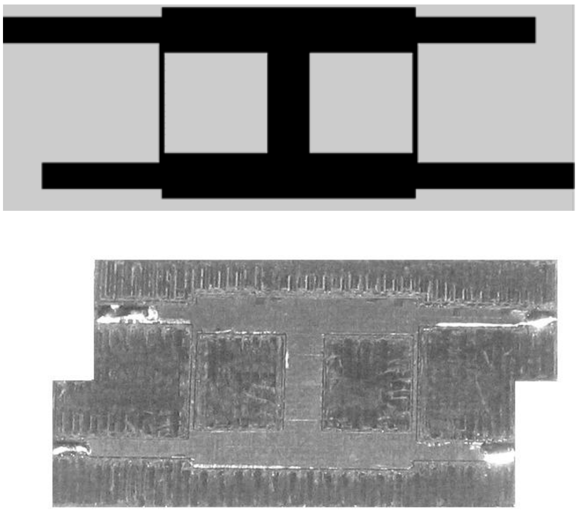
(a)

(b)

Figure 5.3 Layout of modified branch-line coupler after including discontinuity compensation (with design parameters listed in Table 5.2 and overall dimensions of 48mm X 25mm)

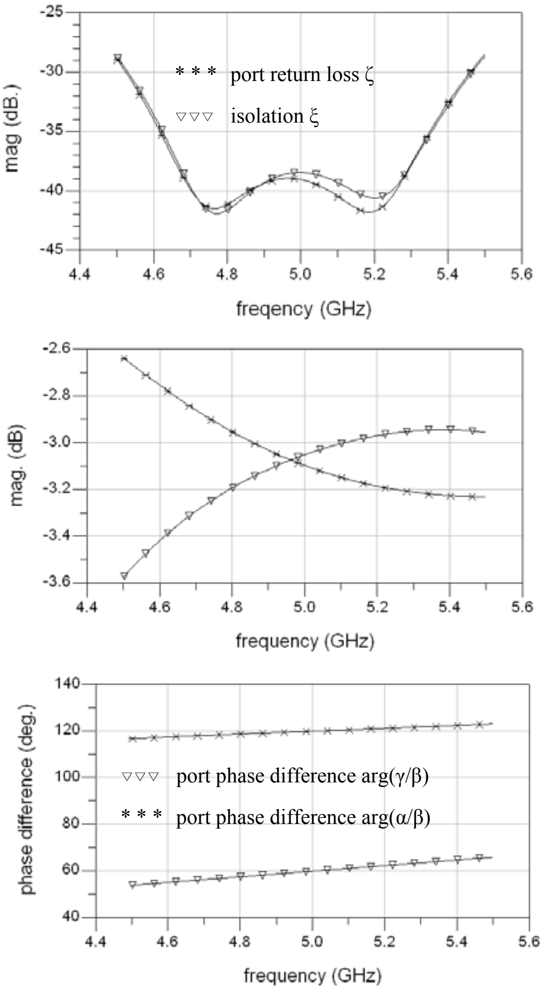

Figure 5.4 Simulation results for modified branch-line coupler (with design parameters listed in Table 5.2)

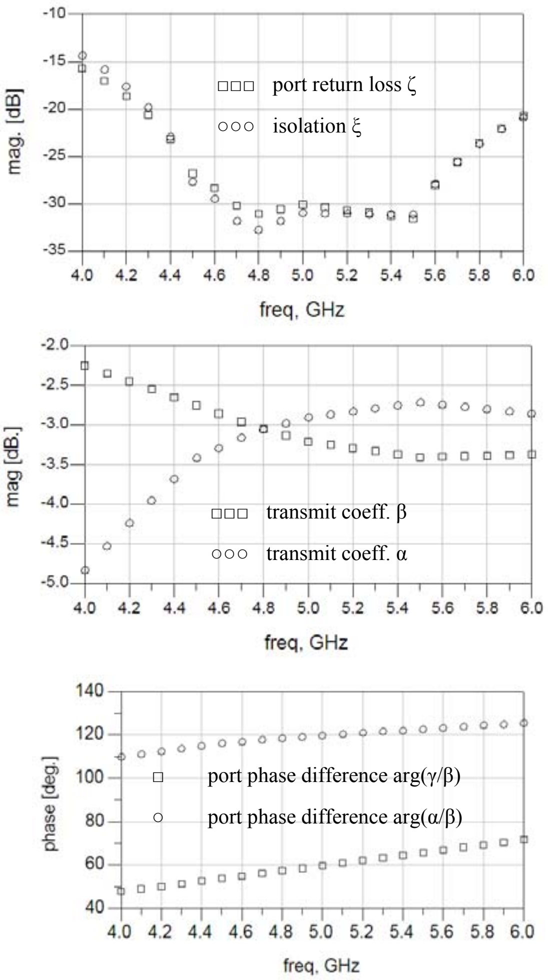

Figure 5.5 Measured results (after de-embedding) for modified branch-line coupler with design parameters listed in Table 5.2

These measured results confirm that it is, in practice, possible to meet the residual-mismatch, isolation, magnitude-imbalance and phase-difference requirements (as discussed in Sub-Section 3.2.3) over the frequency range from 4.4GHz to 5.8GHz.

## 5.2 Microstrip Prototype based on Modified Rat-Race Structure

Rat-race couplers are as popular as branch-line couplers. We note from the experimental results reported thus far in the literature for standard rat-race couplers [5.9]-[5.12] that the actual performance of such a coupler may deviate from what is expected during the design phase. For our modified-design attempts, we shall thus have to resort to re-scaling techniques in order to take discontinuity compensation into account.

The schematic design for our modified rat-race structure is depicted in Figure 5.6. Listed in Table 5.3 are the design data obtained by our optimization software for our initial attempt without discontinuity compensation. It is evident from a comparison of the predicted and measured results presented in Figures 5.7 and 5.8 respectively that there is, not unexpectedly, a shift of the center frequency from the original design specification of 3GHz.

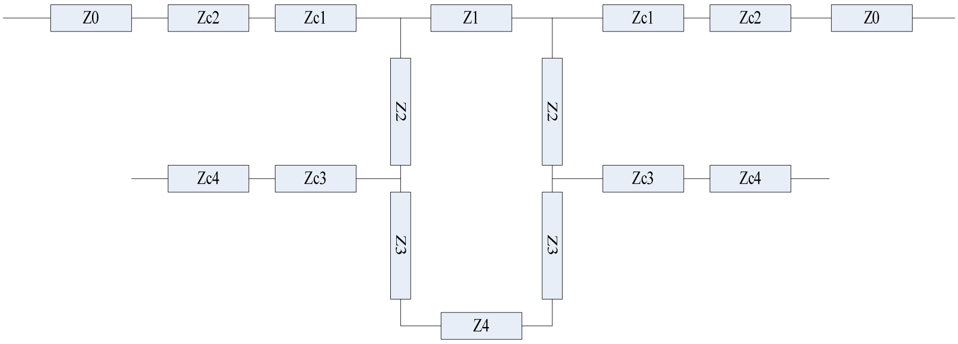

Figure 5.6 Schematic circuit diagram for proposed rat-race coupler structure

TABLE 5.3 KEY PARAMETERS FOR PRELIMINARY DESIGN OF RAT-RACE COUPLER (WITHOUT DISCONTINUITY COMPENSATION)

| Coupler arm | Characteristic impedance (Ω) | Electrical length (degree) |
|---|---|---|
| $Z_1$ | 107 | 90 |
| $Z_2$ | 65 | 90 |
| $Z_3$ | 36 | 90 |
| $Z_4$ | 30 | 90 |
| $Z_{c1}$ | 77 | 90 |
| $Z_{c2}$ | 62 | 90 |
| $Z_{c3}$ | 35 | 90 |
| $Z_{c4}$ | 47 | 90 |
| $Z_0$ | 50 | 60 |

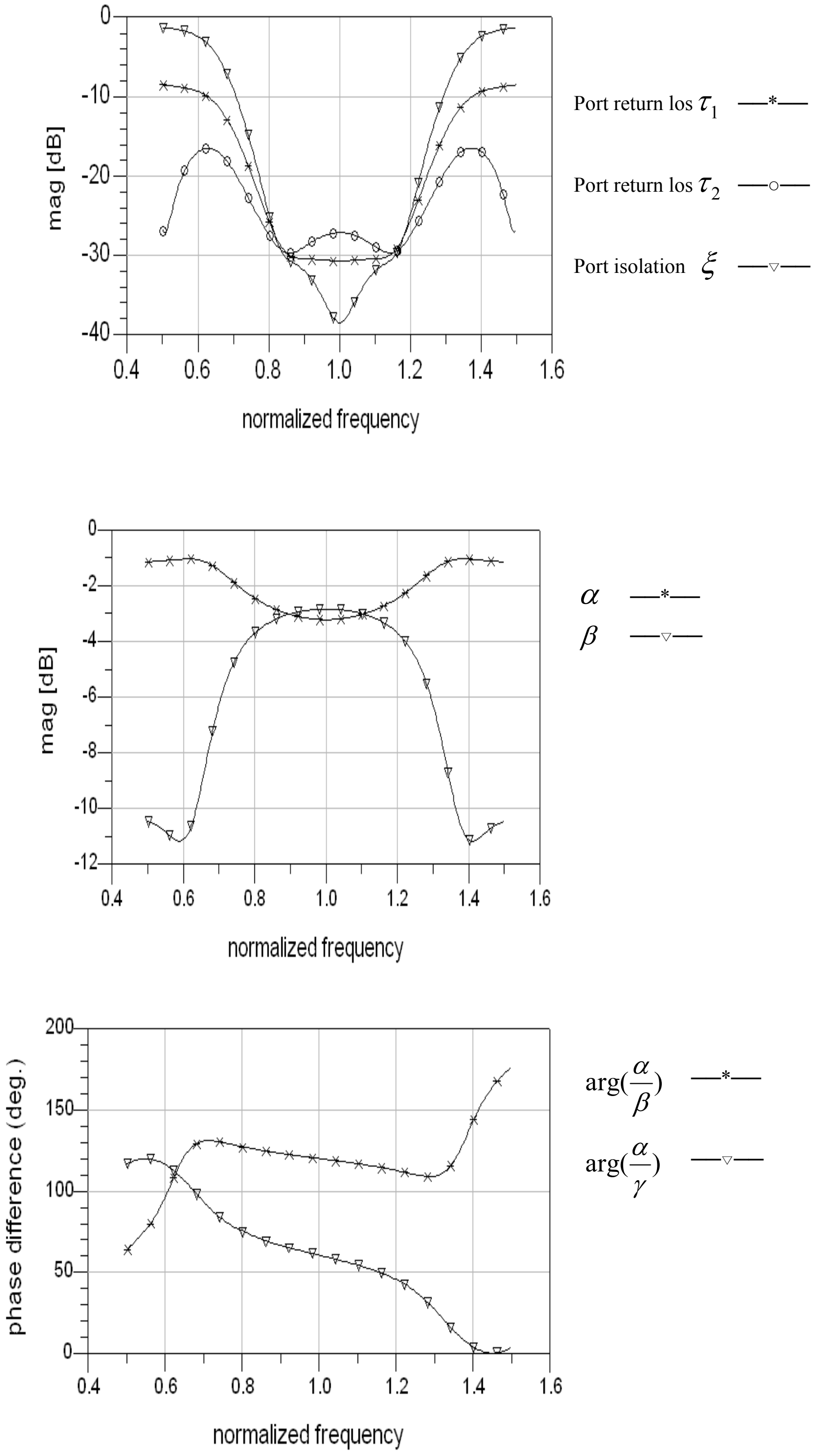

Figure 5.7 Simulation results for modified rat-race coupler with design parameters listed in Table 5.3

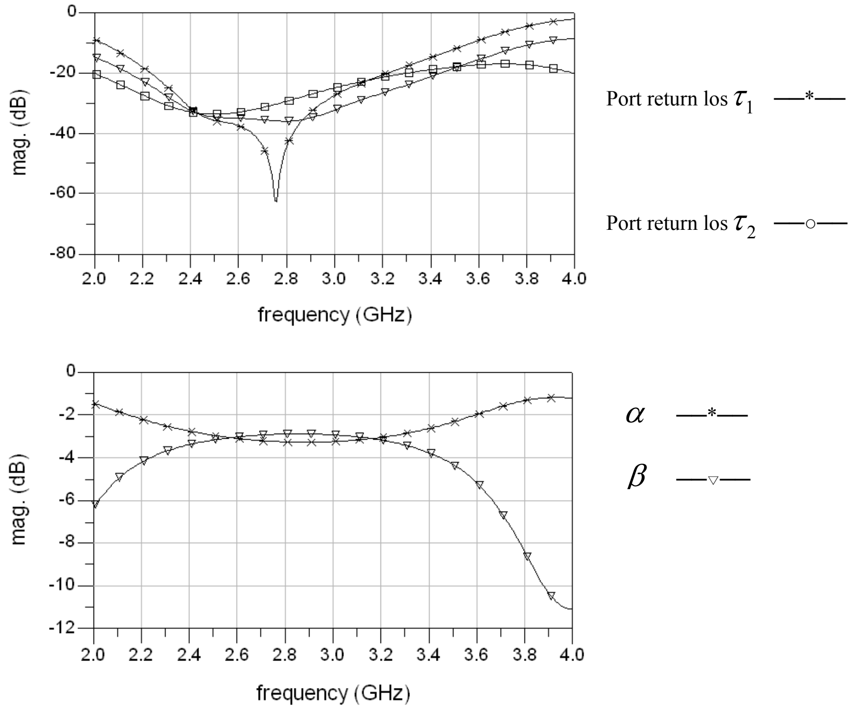

Figure 5.8 Simulation results for modified rat-race coupler implemented on RT5880 31 mil (without taking discontinuity compensation into consideration)

It is thus necessary to incorporate discontinuity compensation in order to account for parasitic effects. To improve our design, we have again resorted to re-scaling by systematically adjusting the width and length of each branch of the coupler. We have also found it useful to adjust the weights in Equation 5.1. Listed in Table 5.5 are the design data we obtained after several iterations during our follow-up attempts. The lay-out for the improved design depicted in Figure 5.9 is different from that for the original design we obtained during our initial attempt without any compensations. The measured results presented in Figure 5.10 confirm that the improved design yields a bandwidth of approximately 32% with negligible shift of the center frequency. With both residual mismatch and insertion loss better than -25dB, such a coupler is certainly suitable for use in the optimum reflectometer set-up proposed in Section 3.2.

TABLE 5.4 KEY PARAMETERS FOR OPTIMIZED DESIGN OF MODIFIED RAT-RACE COUPLER AFTER DISCONTINUITY COMPENSATION

| Coupler arm | Characteristic impedance (Ω) | Line width (mil) | Electrical length (deg) | Line length (mil) |
|---|---|---|---|---|
| $Z_1$ | 88 | 35 | 97 | 790 |
| $Z_2$ | 76 | 47 | 93 | 755 |
| $Z_3$ | 56 | 79 | 93 | 750 |
| $Z_4$ | 42 | 120 | 81 | 640 |
| $Z_{c1}$ | 50 | 94 | 79 | 630 |
| $Z_{c2}$ | 36 | 150 | 71 | 560 |
| $Z_{c3}$ | 61 | 69 | 77 | 620 |
| $Z_{c4}$ | 62 | 67 | 112 | 900 |
| $Z_0$ | 41 | 125 | 78 | 615 |

Note: definitions of Z provided in Figure 5.6

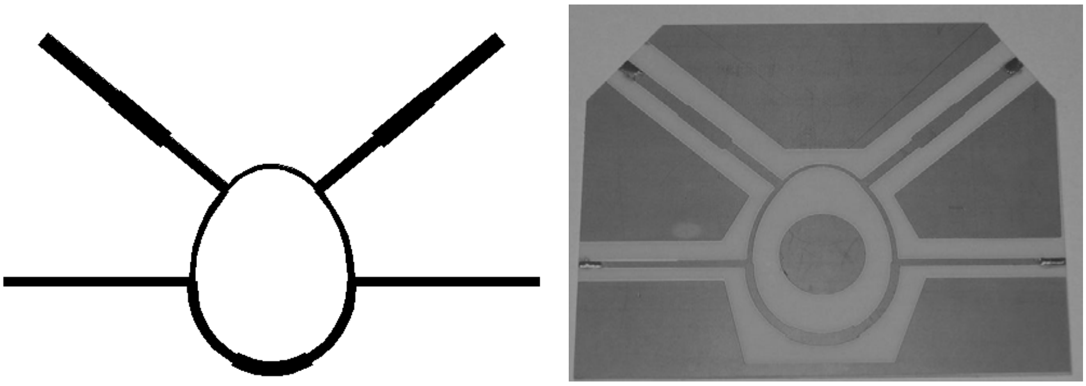

Figure 5.9 Layout of modified rat-race coupler after including discontinuity compensation (with design parameters listed in Table 5.5 and overall dimensions of 113mm X 85mm)

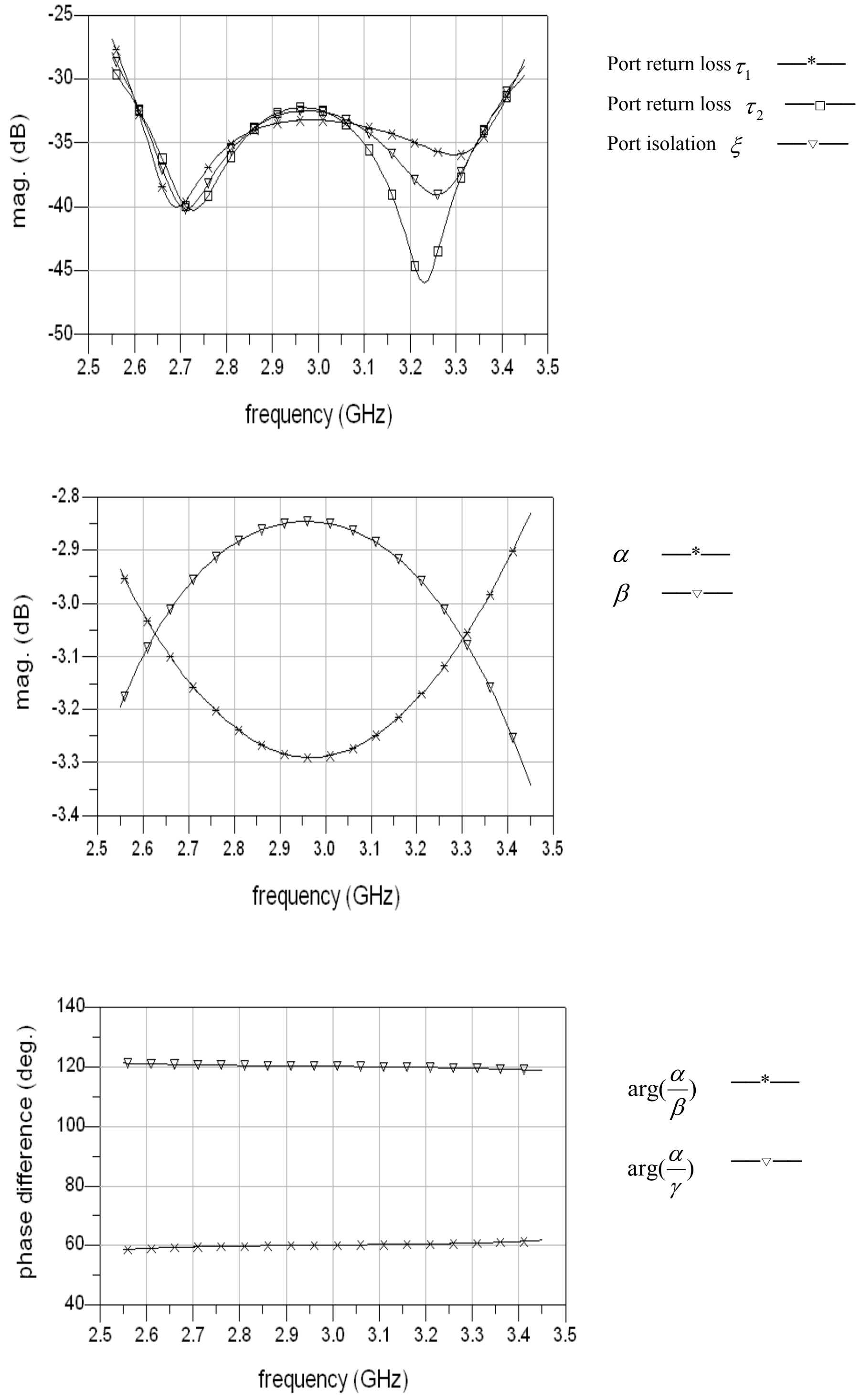

Figure 5.10 Simulation results for modified rat-race coupler with design parameters listed in Table 5.4

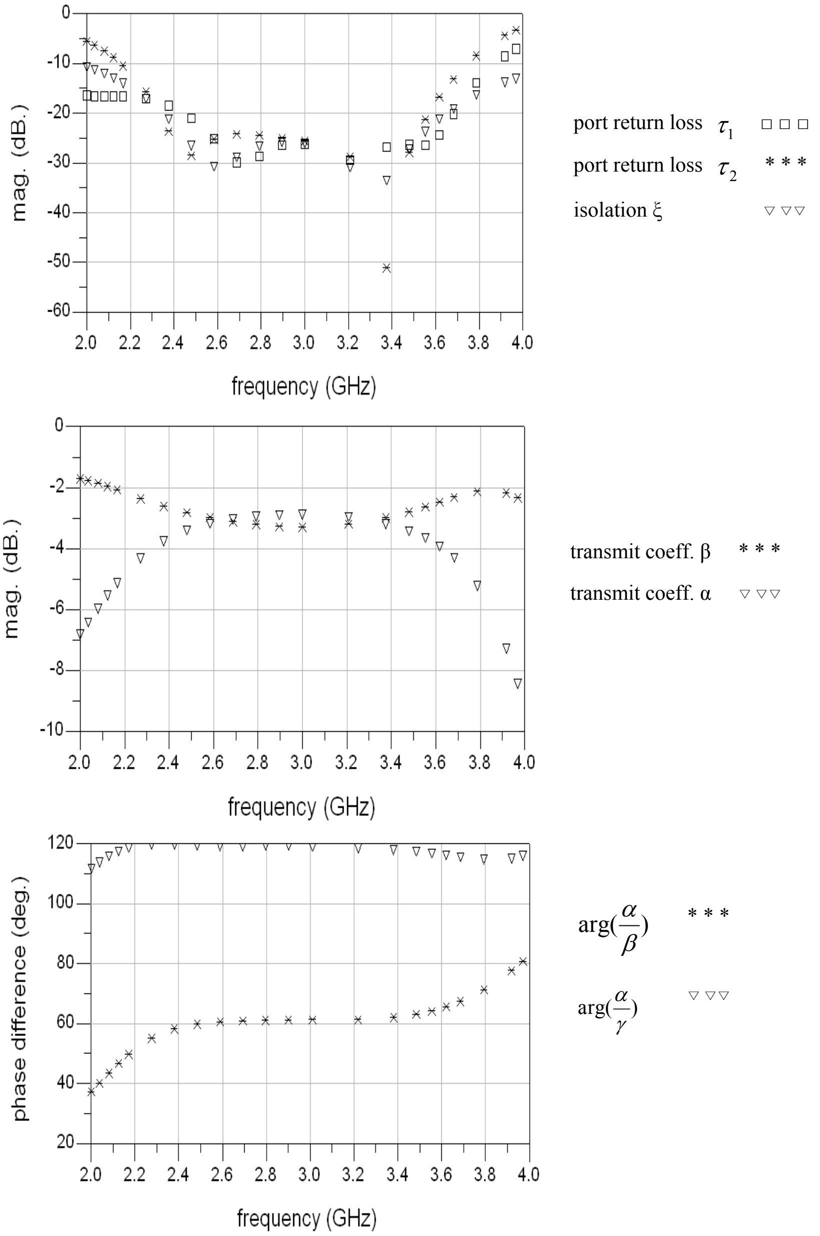

Figure 5.11 Measured results for modified rat-race coupler with design parameters listed in Table 5.4

## 5.3 Wide-Band Prototype based on CPW Structure

The microstrip prototypes we attempted in Sections 5.1 and 5.2 for the branch-line and rat-race couplers respectively are relatively easy to design and fabricate. Although their resulting performance characteristics are suitable for optimum reflectometer operation, there is a limit to how much we can extend their bandwidths because of the inherent limitations of microstrip-implemented designs. As for the branch-line coupler, its bandwidth should, in principle, increase with the number of sections; however, the maximum/minimum impedance ratio of the branch lines will become too large to be physically realizable when the number of sections increases beyond 4. Similar constraints apply for the rat-race coupler as well. Having found it difficult to design microstrip couplers with bandwidths exceeding 50% for both of these structures, we shall now explore CPW implementation instead in view of the possibility of wider bandwidths.

Various hybrid couplers implemented in coplanar forms have been reported in the 1990s; for example, Ho *et al* [5.35] proposed the wideband CPW-to-slotline transition designs while Heimer *et al* [5.36] utilized asymmetrical coplanar stripline in place of CPW. Although the prototypes reported in [5.35] and [5.36] yielded isolation better than -20dB over an octave bandwidth, their residual-mismatch results were not as impressive (typically between -10dB and -20dB) over the requisite operating frequency range. Wang *et al* [5.37] attempted to improve the matching by varying the characteristic impedances of the ring segments in Figure 5.12(a) but what they achieved was still not good enough. Chang *et al* [5.38] suggested further improvement by increasing the response order of the circuit in Figure 5.12(b) in their effort to design prototypes yielding Chebyshev responses; their phase-inverter was implemented in finite-ground CPW (FCPW) and the designs they proposed in [5.38] required very low CPW impedances (of approximately 30Ω for the lowest case). Actually, we may trace the structures proposed in [5.37] and [5.38] to the hybrid-ring coupler designed by Kim [5.39] using a scheme with higher response order.

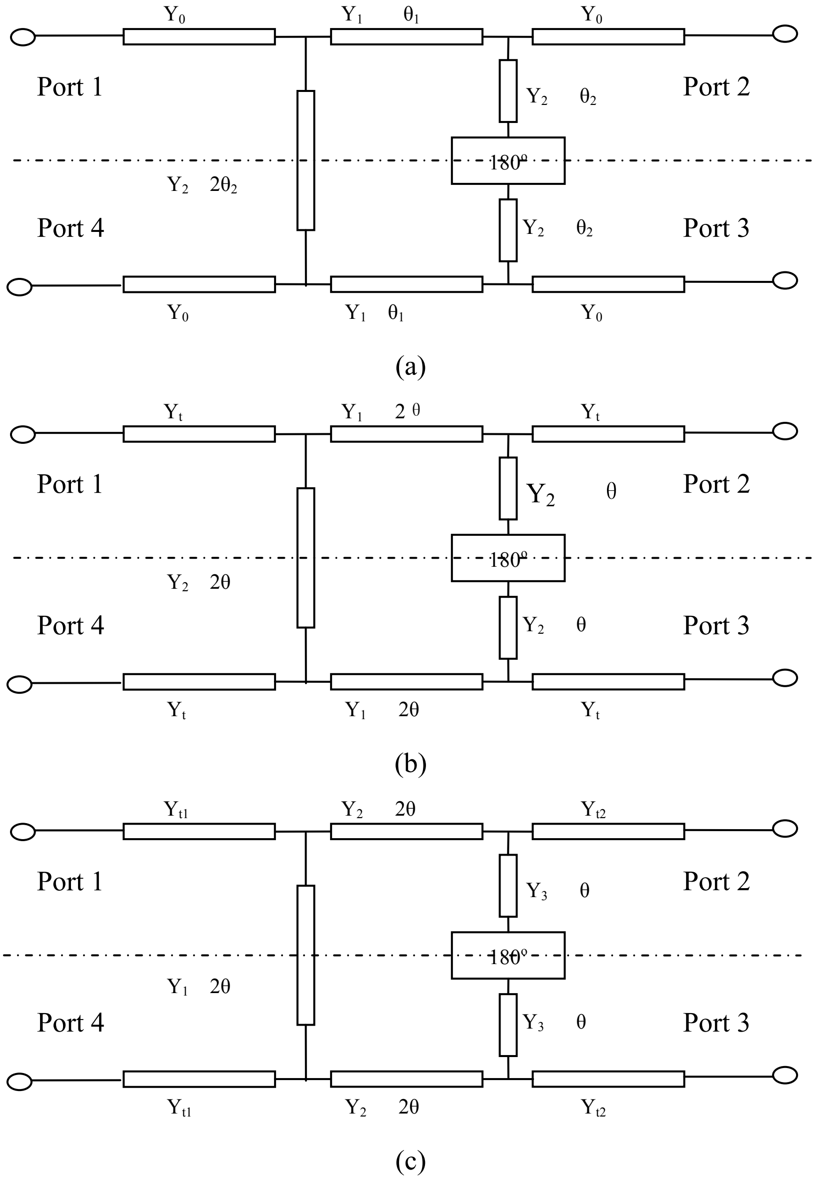

Figure 5.12 Schematic circuit diagrams for CPW couplers

(a) reported by Wang *et al* [5.37]

(b) reported by Chang *et al* [5.38]

(c) our proposed design

Drawing upon the experience accrued by Wang *et al* [5-37] and Chang *et al* [5.38], we have subsequently found that it is possible to improve the design by increasing the response order. Our coupler design process starts from the scattering analysis of the circuit structure depicted in Figure 5.12(c). With the detailed expressions derived from eigenmode analysis (for both odd and even modes), we are able to determine the design conditions satisfying the following performance requirements at the center frequency $f_c$:

$$\begin{aligned} &\overrightarrow{S_{ii}} = 0 \\ &\overrightarrow{S_{13}}, \overrightarrow{S_{24}} = 0 \qquad \text{where i = 1, 2, 3, 4} \\ &|\overrightarrow{S_{12}} / \overrightarrow{S_{14}}| = 1 \end{aligned} \tag{5.2}$$

It is convenient to employ the symbol processing toolbox of Mathematic (or MATLAB) to derive the following equations where we set θ=90$^o$:

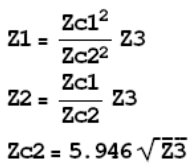

$$\begin{aligned} Z1 &= \frac{Zc1^2}{Zc2^2} Z3 \\ Z2 &= \frac{Zc1}{Zc2} Z3 \\ Zc2 &= 5.946\sqrt{Z3} \end{aligned} \tag{5.3}$$

This system of 3 equations contains 5 unknowns. We thus need to choose appropriate values for 2 of the 5 unknowns before we can proceed to use Equation 5.3 to solve for the remaining 3 unknowns to obtain a narrow-band design for the 3dB four-port coupler. This narrow-band design is useful in serving as the initial design to launch our optimization search for us to obtain a wide-band design for the modified CPW couplers.

During our search trials, we have once again found that we ought to re-cast our optimization error function in the following form:

$$F_{error}(Y_1, Y_2, Y_3, Y_{t1}, Y_{t2}) = \sum_{i=1}^{5} W_i g_i$$

where $$g_1 = \sum_{j=1}^{N} |\overline{S_{11}}(f_j)|^2 \quad , \quad g_2 = \sum_{j=1}^{N} |\overline{S_{22}}(f_j)|^2$$

$$g_3 = \sum_{j=1}^{N} |\overline{S_{13}}(f_j)|^2 \quad , \quad g_4 = \sum_{j=1}^{N} (|\overline{S_{12}}(f_j)| - \frac{1}{\sqrt{2}})^2$$

$$g_5 = \sum_{j=1}^{N} (|\overline{S_{14}}(f_j)| - \frac{1}{\sqrt{2}})^2 \qquad (5.4)$$

$f_j = f_L + (j-1)\Delta f$ , j=1,……,N

$\Delta f = (f_H - f_L)/(N-1)$

$f_L$ is the lowest frequency of the designed band

$f_H$ is the highest frequency of the designed band

N is the number of sampling points

$W_i$ are the weighting factors.

The algorithms are based on the composite quasi-Newton and gradient search. Starting from the previous set of initial parameters, we have thus been able to obtain the first-cut design parameters: $Y_1 = Y_3 = 1.07$, $Y_2 = 1.04$, $Y_{t1} = Y_{t2} = 1.25$ (or $Z_1 = Z_3 = 46.5\Omega$, $Z_2 = 48.5\Omega$, $Z_{t1} = Z_{t2} = 40.5\Omega$). Presented in Figure 5.13 are the scattering-coefficient plots predicted for this first-cut design (without taking any enhancement/compensation features into consideration).

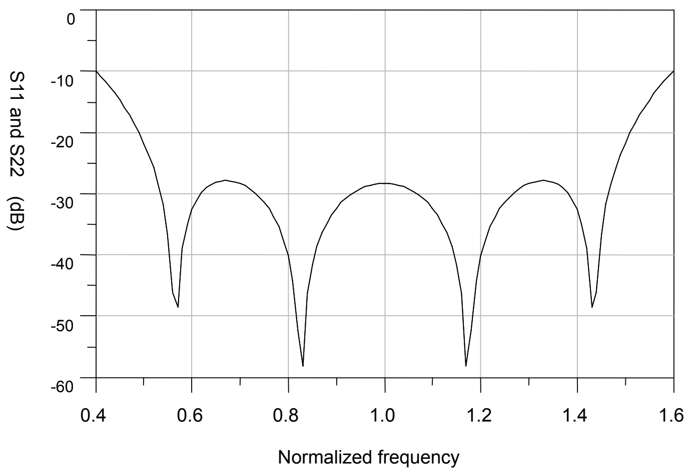

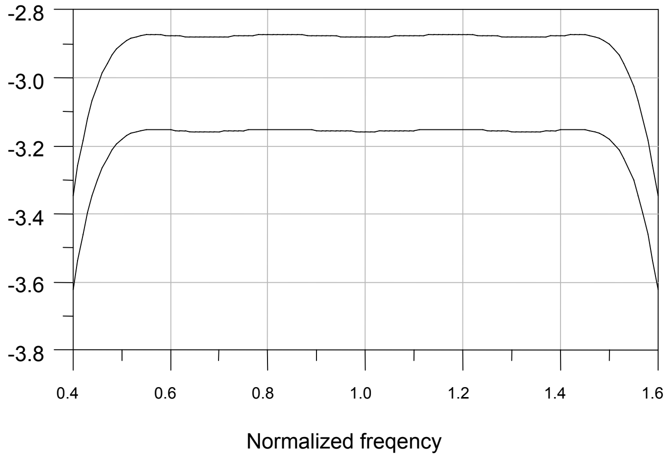

Figure 5.13 Simulation results for preliminary design of our proposed CPW coupler (without discontinuity compensation) NB: $|s_{13}| = 0$ over entire bandwidth and thus not presented here

## 5.3.1 Discontinuity effects of 180$^o$ phase inverter

We need to pay attention to the 180$^o$ phase inverter which may adversely affect the overall coupler's performance as pointed out by Chang *et al* [5-36]. In general, the scattering matrix of a (non-ideal) phase inverter may be represented in the following manner:

$$\overline{S}_{phase\_inverter} = \begin{bmatrix} Ae^{i\theta 1} & Be^{i\theta 2} \\ Be^{i\theta 2} & Ae^{i\theta 1} \end{bmatrix} \tag{5.5}$$

where the magnitude parameters A and B and phase parameters $\theta_1$ and $\theta_2$ will have to satisfy the following equations drawn from the unitary-matrix conditions for the loss-free case:

$$A^2 + B^2 = 1$$

and

$$\theta 1 - \theta 2 = \pm\pi / 2 + n\pi \quad \text{(where n is integer)} \qquad \text{when } |A| \neq 0.$$

For the ideal case, the transmission coefficient of the 180° phase inverter should have magnitude of B = 1 and phase of $\theta_2 = 180^{\circ}$ and consequently the magnitude of its reflection coefficient will drop to A = 0 (with $\theta_1$ taking on any value). If we allow for non-zero reflection coefficient whilst insisting on the 180° phase-shift requirement, Equation 5.5 may then be re-written in the following form:

$$\overline{S}_{phase\_inverter1} = \begin{bmatrix} \sqrt{1-B^2}\,e^{i\pi/2} & -B \\ -B & \sqrt{1-B^2}\,e^{i\pi/2} \end{bmatrix} \tag{5.6}$$

By writing S11 in the following Mathematica format (where $S11_0$ is the S11 parameter of the phase inverter with ideal-case matching)

$$\overline{S11} = \overline{S11}_0 \left(1 + \sqrt{\frac{1-B}{2B}} F(freq, Y_1, Y_2, Y_3, Y_{t1}, Y_{t2})\right) \ , \tag{5.7}$$

and allowing for the normalized admittance to vary from 0.42 to 1.25 and the normalized frequency to vary from 0.5 to 1.5, we have found that the value of the function *F*(*freq*, $Y_1$, $Y_2$,

$Y_3$, $Y_{t1}$, $Y_{t2}$,) is in the vicinity of 2 and by so doing we can derive approximate limits for our optimization goals:

$$\sqrt{\frac{1-B}{B}} < 0.1 \qquad \text{that is} \qquad \mathbf{B} > 0.991 \text{ or } A < 0.14 \text{ (-17dB)} \tag{5.8}$$

There is another near-ideal scenario that we ought to consider. If we insist on no return losses whilst allowing for the transmission phase-shift to stray from the design specification of $180^o$, we may then re-cast Equation 5.7 as

$$\overrightarrow{S11} = \overrightarrow{S11}_0 (1 + e^{-\frac{\theta 2}{2} i} \sqrt{-(1+e^{-\theta 2 i})^2} F'(freq, Y_1, Y_2, Y_3, Y_{t1}, Y_{t2})) \quad , \tag{5.9}$$

and thus employ a similar procedure to derive the following approximate limit for $\theta_2$ after noting that the value of the function $F'(freq$, $Y_1$, $Y_2$, $Y_3$, $Y_{t1}$, $Y_{t2}$,) is in the vicinity of 1:

$$174^o < \theta_2 < 186^o \tag{5.10}$$

Although we have derived these two approximate limits separately, such hardware imperfections co-exist in practice and there may be a need for the tolerance limits to be tightened. They are nevertheless useful as a first-order guide for our design process and we should additionally be mindful of the overall need to meet the system design requirements for optimum reflectometer operation.

Depicted in Figure 5.14 are the two $180^o$ phase inverter designs we fabricated on Rogers 6010LM substrate (with $\varepsilon_r = 10.2$, tan $\delta = 0.0023$ and substrate thickness = 50mil). Unlike other researchers who utilized radial stubs and slotline short stubs (which are more suitable for circuits with narrow-band requirements), we have chosen the hollow patches of circular or rectangular geometries as portrayed in Figures 5.14(a) and 5.14(b) respectively. Implemented on Rogers 6010LM substrate (with $\varepsilon_r$ = 10.2, tanδ = 0.0023 and substrate thickness = 50mil), the two 2GHz designs are based on CPW lines with slot width of 16mil, central-strip width of 40 mil and line length of 640mil (corresponding to 90° transmission line with characteristic impedance of 48.5Ω). The measured results for both inverters are presented in Figures 5.15-5.16. For the inverter tested in Figure 5.15 (where the radius of the hollow patch is 250 mil), we have found that increasing the radius will cause the operating frequency to be lower by virtue of the larger size. The measured results also indicate that the phase shifter based on the hollow patch has a wider bandwidth; actually, the performance differences between the two designs are not significant enough and either of them may be selected for use in the prototype system.

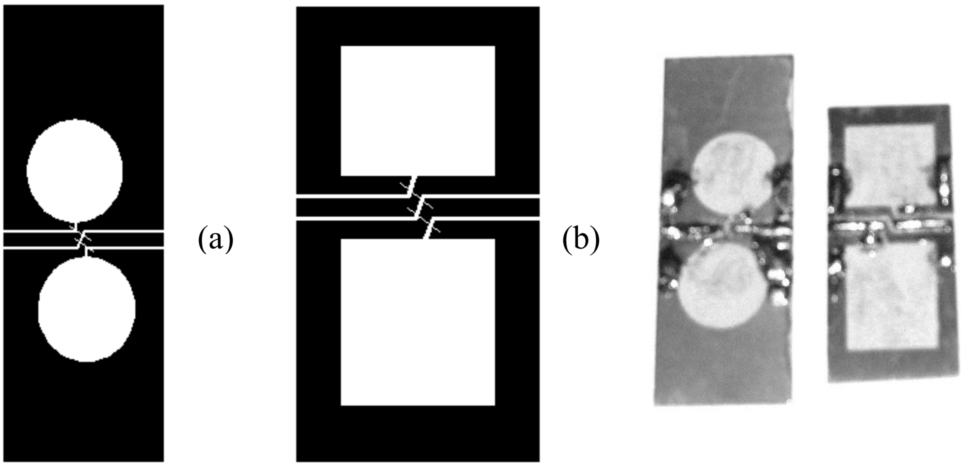

Figure 5.14 Proposed phase inverter designs based on (a) hollow patch and (b) finite-ground CPW

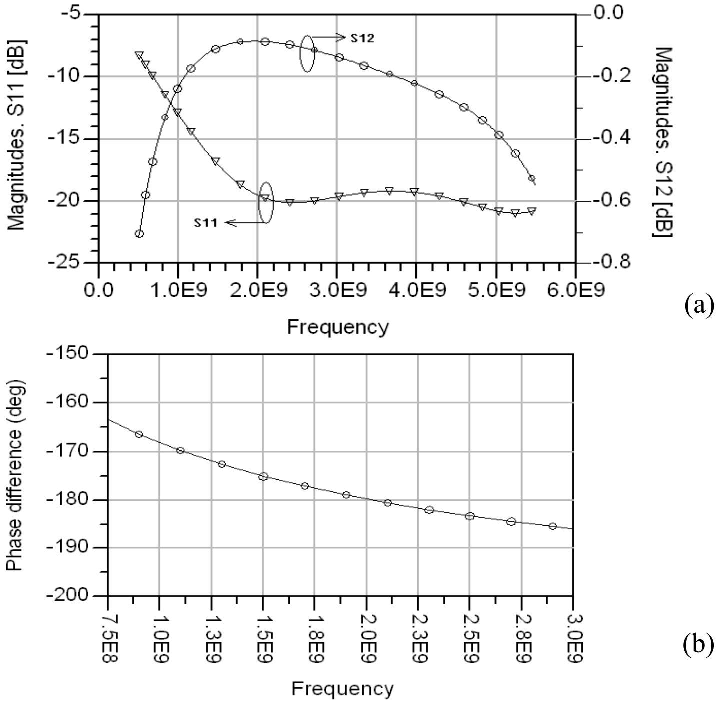

Figure 5.15 Measured results for 180° phase inverter with hollow patch depicted in Figure 5.14(a)

(a) return loss and insertion loss

(b) phase difference between phase inverter and normal 90° length of CPW line

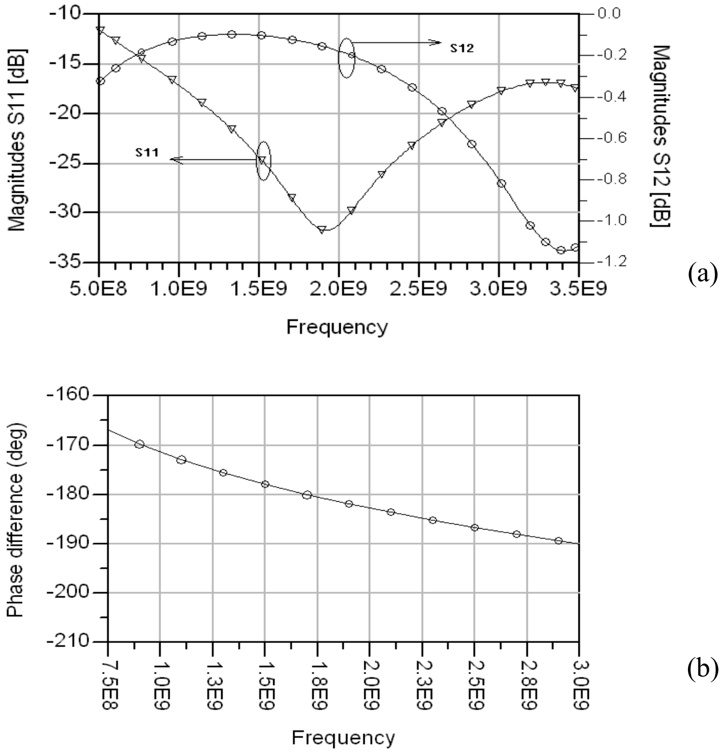

Figure 5.16 Measured results for finite-ground CPW inverter depicted in Figure 5.14(b)

(a) return loss and insertion loss

(b) phase difference between phase inverter and normal 90° length of CPW line

## 5.3.2 CPW coupler design with compensation elements

We have since studied the two structures portrayed in Figure 5.14 for use as the 180° phase inverter required in the schematic circuit we proposed in Figure 5.12(c). Of these two possibilities, we have decided to adopt the finite-ground CPW structure portrayed in Figure 5.14(b). Depicted in Figure 5.17 is the initial design we obtained for the coupler (without taking discontinuity effects into consideration).

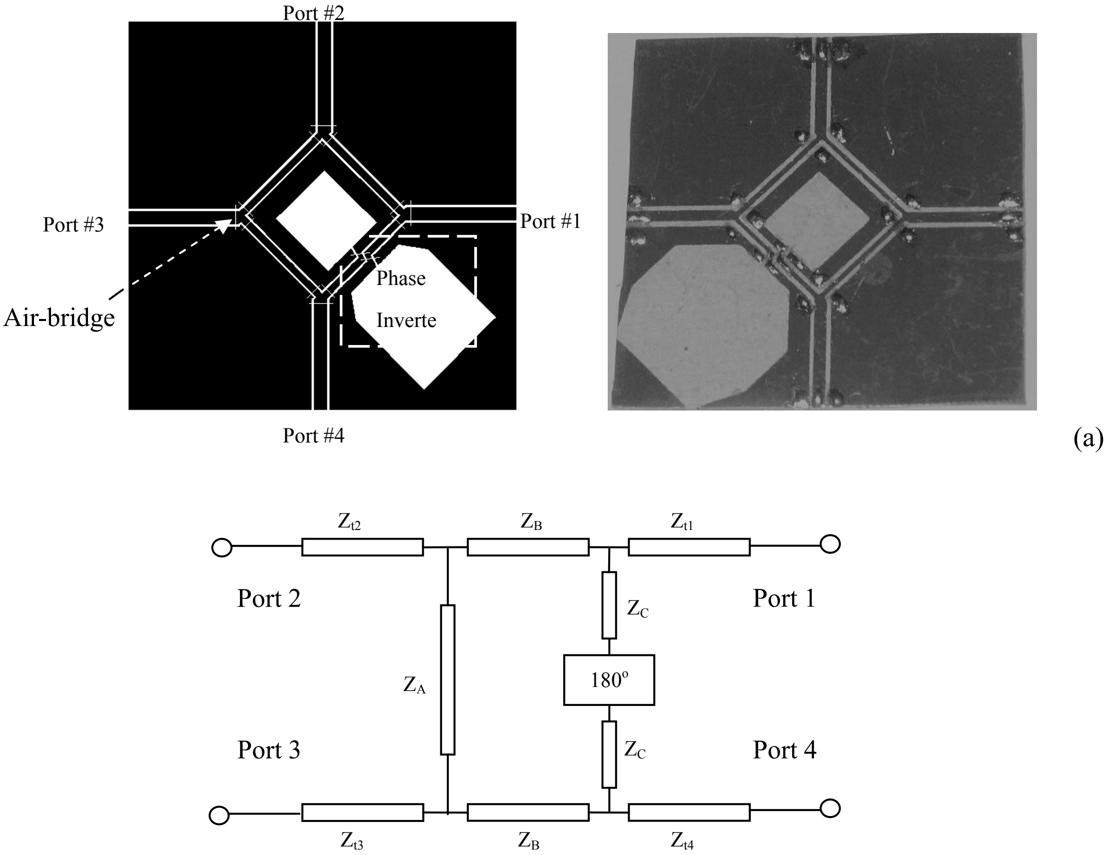

Figure 5.17 Preliminary CPW hybrid-coupler design (without compensating elements) using finite-ground phase inverter structure portrayed in Figure 5.15(b)

(a) physical lay-out (with overall dimensions of 57mm X 57mm)

(b) schematic circuit (with $Z_{t1} = Z_{t3}$, $Z_{t2} = Z_{t4}$ for 180° phase inverter)

Since it is important to take discontinuity effects into account, we need to iteratively improve our design. By adapting the approach employed by Dydyk (for his own microstrip coupler design) [5.27], we have also attempted to add compensating elements to the initial design adopted in Figure 5.17 to launch our iterative search. The final design we selected after many experimental trials is depicted in Figure 5.18 (fabricated on Rogers 6010LM substrate with relative permittivity of 10.2, loss tangent of 0.002 and thickness of 50mil). Listed in Table 5.5 are the key coupler parameters corresponding to the minimum value of $F_{\text{error}}$. We note from the measured results plotted in Fig. 5.18 that our improved coupler is able to satisfy our design goals over a 80% bandwidth (from 1.2 GHz to 2.8 GHz). We will discuss in Chapter 6 the minor refinements we need to additionally incorporate when fabricating four of this CPW coupler in order to construct our six-port reflectometer.

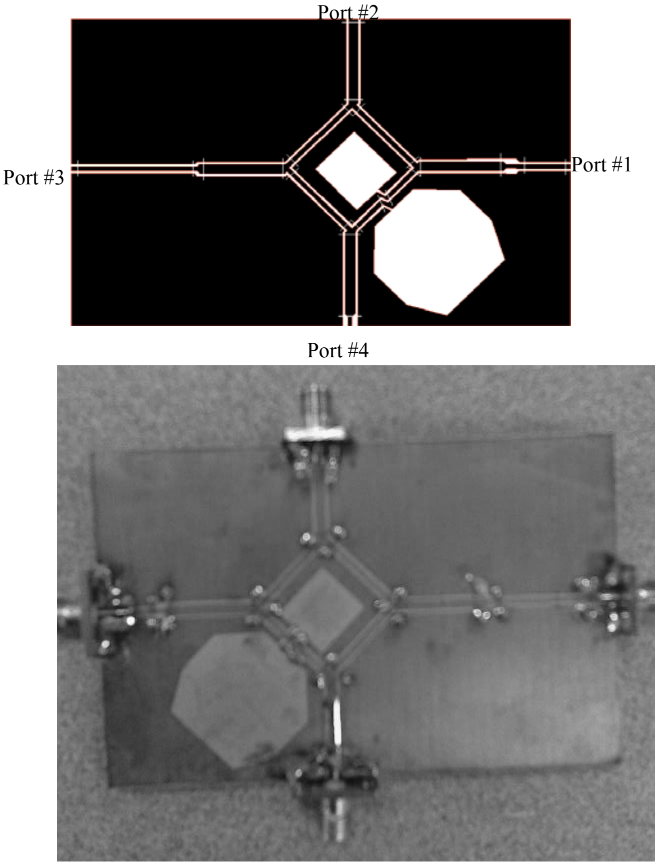

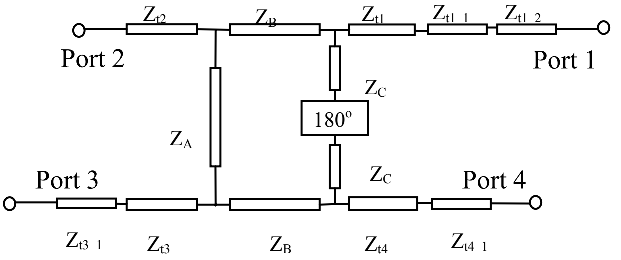

Figure 5.18 Final CPW hybrid-coupler design after incorporating compensating elements

(a) physical lay-out (with design parameters listed in Table 5.5)

(b) photograph of CPW coupler with compensating elements (94mm X 60mm)

(c) schematic circuit (with $Z_{t1} = Z_{t3}$ and $Z_{t2} = Z_{t4}$ for 180° phase inverter)

TABLE 5.5 KEY PARAMETERS FOR OPTIMIZED DESIGN OF CPW COUPLER DEPICTED IN FIGURE 5.18

| Coupler arm | Characteristic impedance (Ω) | Electrical length (deg at $f_{mid}$=2GHz) | Central strip width (mil) | Slot width (mil) | Line length (mil) |
|---|---|---|---|---|---|
| $Z_A$ | 46.5 | 90 | 50 | 16 | 650 |
| $Z_B$ | 48.5 | 90 | 40 | 16 | 640 |
| $Z_C$ | 46.5 | 90 | 50 | 16 | 650 |
| $Z_{t1}$, $Z_{t2}$, $Z_{t3}$, $Z_{t4}$ | 40.5 | 90 | 80 | 16 | 670 |
| $Z_{t1\_1}$ | 70 | 10 | 32 | 40 | 75 |
| $Z_{t1\_2}$ | 50 | 60 | 38 | 16 | 400 |
| $Z_{t3\_1}$ | 50 | 130 | 38 | 16 | 950 |
| $Z_{t4\_1}$ | 70 | 10 | 32 | 40 | 75 |

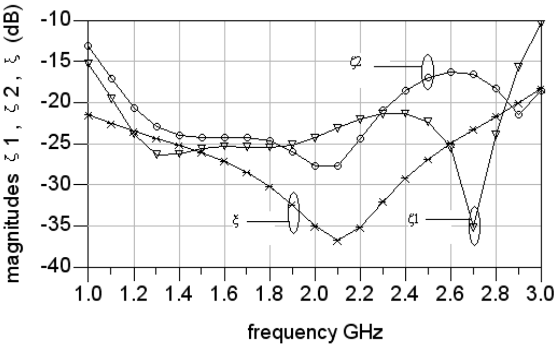

(a)

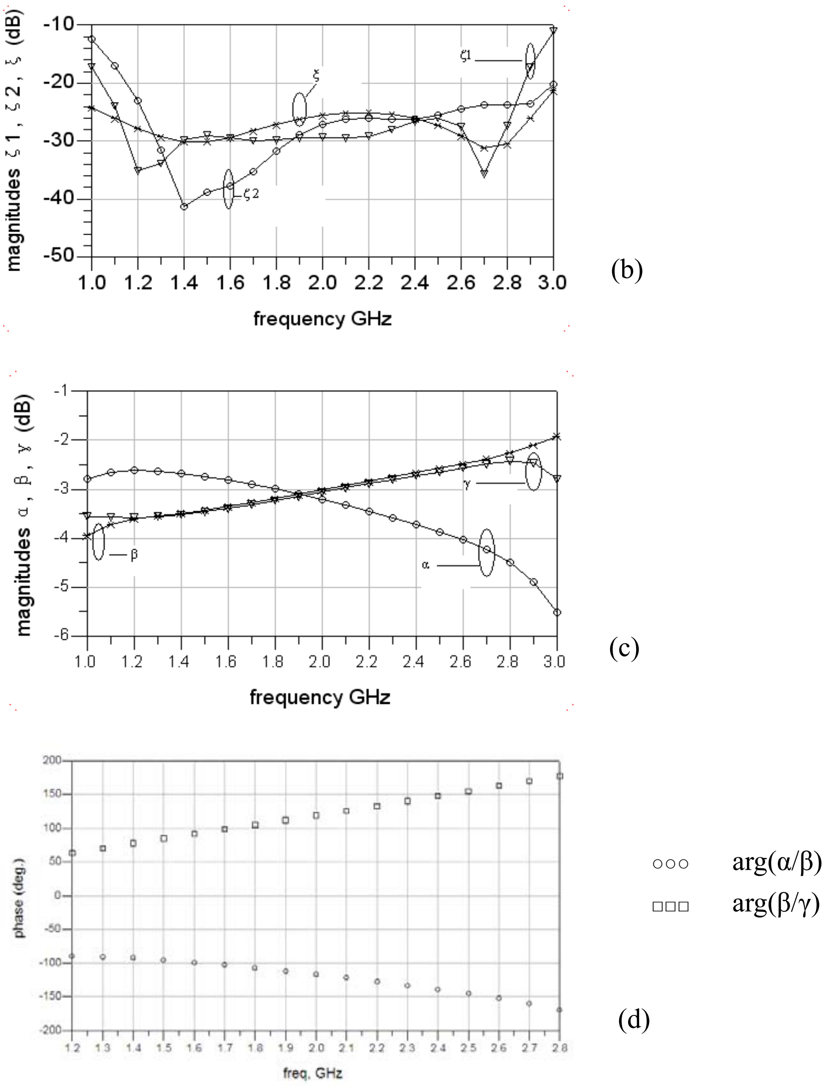

Figure 5.19 Measured results for scattering coefficients of CPW hybrid couplers

(a) return loss and isolation for design in Figure 5.17(a) before compensation

(b) return loss and isolation for design in Figure 5.18(a) with compensation elements

(c) coupling coefficients for design in Figure 5.18(a) with compensation elements

(d) phase responses for design in Figure 5.18(a) with compensation elements

It is evident from the measured results that we are able to improve both matching and isolation after compensating for discontinuity effects. Although the magnitude-imbalance results are acceptable, we need to correct for the imperfections in the phase responses obtained in Figure 5.19(d) by incorporating tuning features as described in Chapter 6 for the prototype system.

## REFERENCES

[5.1] R. Levy and L.F. Lind, “Synthesis of symmetrical branch-guide directional couplers,” IEEE Trans. Microwave Theory Tech., vol. MTT-16, pp. 80–89, Feb. 1968.

[5.2] R. Levy, “Zolotarev branch-guide couplers,” IEEE Trans. Microwave Theory Tech., vol. MTT-21, pp. 95–99, Feb. 1973.

[5.3] M. Muraguchi, T. Yukitake and Y. Naito, “Optimum design of 3-dB branch-line couplers using microstrip lines,” IEEE Trans. Microwave Theory Tech., vol. MTT-31, pp. 674–678, Aug. 1983

[5.4] M. Muraguchi, “Optimum Design of 3-dB Branch-Line Couplers Using Mlcrostrip Lines”, IEEE Trans. Microwave Theory Tech., vol. MTT-31, pp. 674-678, Aug. 1983

[5.5] C.H. Ho, “A broadband uniplanar branch-line coupler using a coupled rectangular slotline ring”, IEEE Microwave Guided Wave Lett., vol. 3, pp. 175-176, Jun. 1993

[5.6] C.H. Ho, “Broadband uniplanar hybrid-ring and branch-line couplers”, IEEE Trans. Microwave Theory Tech., vol. 41, pp. 2116-2125, Dec. 1993

[5.7] J.A. Navarro, L. Fan, and K. Chang, “The coplanar waveguide-fed electronically tunable slotline ring resonator,” in IEEE MTT-S Int. Microwave Symp. Dig., 1992, pp. 951-954.

[5.8] C.H. Ho, L. Fan, and K. Chang, “Broad-band uniplanar hybrid-ring coupler,” Electron. Lett., vol. 29, pp. 44-45, Jan. 1993.

[5.9] T. Hirota, Y. Tarusawa, H. Ogawa and K. Owada, “Planar MMIC hybrid circuit and frequency converter,” in IEEE MTT-S Int. Microwave Svmu. Dip.. 1986. KID. 103-105.

[5.10] D.I. Kim and Y. Naito, “Broad-band design of improved hybrid-ring 3-dB directional coupler,” IEEE Trans. Microwave Theory Tech., vol. MTT-30, pp. 2040–2046, Nov. 1982.

[5.11] D.I. Kim and G.S. Yang, “Design of a new hybrid-ring directional coupler using λ/8 orλ/6 sections,” IEEE Trans. Microwave Theory Tech., vol. 39, pp. 1779–1783, Oct. 1991.

[5.12] K. Ashok, “A printed-circuit hybrid-ring directional coupler for arbitrary power divisions” IEEE Microwave Theory Tech., vol. MTT-34, pp. 1401-1407, Dec. 1996

[5.13] J. Wright, “Equivalent circuits of microstrip impedance discontinuities and launchers”, IEEE Trans. on Microwave Theory Tech., vol. 22. pp. 48-52, Jan. 1974

[5.14] T. Itoh and R. Mittra, “A new method for solving discontinuity problems in microstrip lines”, IEEE GMTT Int. Microwave Symp. Digest, 1972, pp.68-70

[5.15] T.C. Edwards, “Foundations of Microwave Circuit Design”, Wiley, 1981

[5.16] D. Pozar, “Microwave Engineering”, John Wiley, 1998

[5.17] K.C. Gupta, “Microstrip Lines and Slotlines”, Artech House, 1996

[5.18] A. Agrawal, “A printed-circuit hybrid ring directional coupler for arbitrary power divisions”, IEEE Trans. Microwave Theory Tech., vol. 34, Dec. 1986

[5.19] E. Hammerstad, “Accurate Models for microstrip computer aided design ”, IEEE MTT-S Int. Symp. Digist, 1980, pp 407-409

[5.20] A.F. Thompson. “Calculation of microstrip discontinuity inductance ”, IEEE Trans. Microwave Theory Tech., vol. 23, pp. 648-655, May 1975

[5.21] P. Silvester and P. Benedek, “Microstrip discontinuity capacitances for right-angle bends, T-junctions and crossings”, IEEE Trans. Microwave Theory Tech., vol. 21, pp. 341-346, Feb. 1973

[5.22] N. Dib, “Comprehensive study of CAD models of several coplanar waveguide (CPW) discontinuities”, IEE. Proc. Microwave Antenna Prop., vol. 152, pp. 69-76, Apr. 2005

[5.23] D. Mirshekar-Syahkal, “Computation of equivalent circuits of CPW discontinuities using quasi-static spectral domain method”, IEEE Trans. Microwave Theory Tech., vol. 44, pp. 979-984, Jun. 1996

[5.24] R., Simons, “Modeling of some coplanar waveguide discontinuities”, IEEE Trans. Microwave Theory Tech, vol. 36, pp. 1796-1803, Dec. 1988

[5.25] D. Mirshekar-Syahkal, “Computation of equivalent crcuits of CPW discontinuities using quasi-static spectral domain method”, IEEE Trans. Microwave Theory Tech., vol. 44, pp. 979-984, Jun. 1996

[5.26] T.Q. Wang, “Experimental study of wideband uniplanar phase inverters for MICs”. 1997 IEEE MTT-S Int. Microwave Symp. Digest, pp.777-780

[5.27] M. Dydyk, “Microstrip directional couplers with ideal performance via single-element compensation,” IEEE Trans. Microwave Theory Tech., vol. MTT-47, pp. 956-964, Jun. 1999

[5.28] R.Vogel, “Effects of the T-Junction Discontinuity on the design of microstrip directional couplers”, IEEE Trans. Microwave Theory Tech., pp. 145-146, March. 1973

[5.29] W. Leighton, “Junction reactance and dimensional tolerance effects on X-band 3dB directional effects”, IEEE Trans. Microwave Theory Tech., vol. MTT-19, pp. 818-824, Oct. 1999

[5.30] C.H. Ho, L. Fan and K. Chang, “New uniplanar coplanar-waveguide hybrid-ring couplers and magic-Ts,” IEEE Trans. Microwave Theory Tech., vol. MTT-42, pp. 2440-2448, Dec. 1994

[5.31] M. Dydyk, “Master the T-junction and sharpen your MIC designs”, Microwaves, Vol.16, May 1977, pp. 184-186

[5.32] S. Gruszczynski, “design of compensated coupled stripline 3dB directional couplers phase shifters and magic Ts”, IEEE Trans. Microwave Theory Tech., vol. MTT-54, pp. 3501-3507, Sep. 2006

[5.33] N. Dib, "Effect of mitering on CPW discontinuities", IEE. Proc. Microwave Antenna Prop., vol. 152, pp. 223-228, Apr. 2005

[5.34] T. Weller, "Three-dimensional high-frequency distribution networks. I. Optimization of CPW discontinuities", IEEE Trans. Microwave Theory Tech., vol. MTT-48, pp. 1635-1642, Oct. 1997

[5.35] C.H. Ho, L. Fan and K. Chang, "New uniplanar coplanar-waveguide hybrid-ring couplers and magic-Ts," *IEEE Trans. Microwave Theory Tech.*, vol. MTT-42, pp. 2440-2448, Dec. 1994

[5.36] B.R. Heimer, L. Fan and K. Chang, "Uniplanar hybrid couplers using asymmetrical coplanar striplines," IEEE Trans. Microwave Theory Tech., vol. MTT-45, pp. 2234-2240, Dec. 1997

[5.37] T. Wang and K. Wu, "Size reduction and band-broadening design technique of uniplanar hybrid ring coupler using phase inverter for M(H)MICs," IEEE Trans. Microwave Theory Tech., vol. MTT-47, pp. 198-206, Feb. 1999

[5.38] C.Y. Chang and C.C. Yang, "A novel broadband Chebyshev-response rat-race ring coupler," IEEE Trans. Microwave Theory Tech., vol. MTT-47, pp. 455-462, Apr. 1999.

[5.39] A. Sawicki and K. Sachse, "Novel coupled-line conductor-backed coplanar and microstrip directional couplers for PCB and LTCC applications," IEEE Trans. Microwave Theory Tech., vol. MTT-51, pp. 1743-1751, Jun. 2003.

[5.40] M. Dydyk, "Microstrip directional couplers with ideal performance via single-element compensation," *IEEE Trans. Microwave Theory Tech.*, vol. MTT-47, pp. 956-964, June. 1999.

[5.41] T.Q. Ho, "A broad-band coplanar waveguide to slotline transition", *IEEE Microwave and guided wave letters.*, vol.2, pp. 415-416, Oct. 1992.

# Chapter 6

# SIX-PORT REFLECTOMETERS BASED ON MODIFIED FOUR-PORT COUPLERS

In Chapter 2, we have already studied the general criteria for designing a six-port reflectometer [SPR] which finds ready application as an impedance-measuring instrument [6.1]. In Chapter 3, our analysis has indicated that it is, in principle, possible for SPRs based on modified four-port couplers to yield optimum q-point distributions (with magnitudes in the range of 1.2 to 3 and angular separations in the range of $100^o$ to $140^o$). In Chapters 4-5, we have specifically focused on the analysis, design and testing of modified four-port coupler structures which allow us to meet the requirements for optimum SPR-performance criteria. In the present chapter, we shall proceed to construct microstrip-based SPRs in Sections 6.2 and 6.3 (by using the branch-line and rat-race couplers designed in Sections 5.1 and 5.2 respectively) and a CPW-based SPR in Section 6.4 (by using the wider-bandwidth coupler designed in Sub-Section 5.3.2). All of these prototype SPRs need to be calibrated and we shall thus have to begin with a review of selected calibration procedures in Section 6.1.

## 6.1 Six-Port Reflectometer Calibration

Figure 6.1 depicts the schematic SPR system where the DUT is commonly replaced by known standards during calibration. Researchers have already proposed a number of approaches to determine the unknown coefficients of the SPR's system equations by using 4, 5, 6 or even more known standards. Our choice is based on a review of selected calibration procedures.

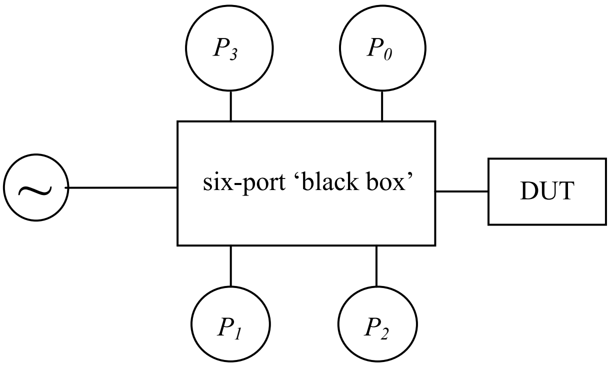

Figure 6.1 Schematic six-port reflectometer set-up (with DUT replaced by known standards during calibration)

In general, the system equations for the generic SPR set-up contain a total of 11 unknown scalar parameters that need to be determined during calibration. There are different ways to formulate these system equations. The most obvious is the following formulation derived directly from scattering analysis:

$$p_i = k_i \frac{\left|\overline{A}_i \overline{\Gamma} + 1\right|}{\left|\overline{A}_0 \overline{\Gamma} + 1\right|} \quad \text{where i = 1, 2, 3} \qquad (6.1)$$

where $p_\text{i}$ is the ratio of power-meter reading $P_\text{i}$ to reference power-meter reading $P_0$

$\overrightarrow{A_0}$, $\overrightarrow{A_1}$, $\overrightarrow{A_2}$ and $\overrightarrow{A_3}$ are 4 complex unknowns (containing 8 scalar unknowns)

and $k_1$, $k_2$ and $k_3$ are 3 scalar unknowns.

Equation 6.1 may be re-cast to yield the following formulation which is also commonly used for SPR-related applications:

$$\overline{\Gamma} = \frac{\sum_{i=0}^{3} F_i p_i + j\sum_{i=0}^{3} G_i p_i}{1 + \sum_{i=1}^{3} H_i p_i} \tag{6.2}$$

where the eleven unknowns to be determined are the scalar parameters $F_0$, $F_1$, $F_2$, $F_3$, $G_0$, $G_1$, $G_2$, $G_3$, $H_1$, $H_2$ and $H_3$.

### 6.1.1 Review of selected calibration procedures

(a) Engen's calibration procedure

Engen, who was one of the pioneers for SPRs [6.2]-[6.3], suggested that the six-port system be reduced to a four-port system to facilitate calibration. Instead of searching for the 11 unknowns simultaneously, he proposed the following transformation:

$$\overline{\Gamma} = \frac{\overline{a}\,\overline{w} + \overline{b}\,\overline{w}}{\overline{c}\,\overline{w} + 1} \tag{6.3}$$

Equation 6.3 allows the original set of three equations contained in Equation 6.1 to be converted from the $\Gamma$ plane to the w plane so as to yield the following three circle equations (with the first circle centered at the origin and the center $w_1$ of another circle sited on the real axis of the w plane):

$$\begin{aligned} \left|\overline{w}\right|^2 &= p_1 \\ \left|\overline{w} - w_1\right|^2 &= \xi \cdot p_2 \\ \left|\overline{w} - \overline{w_2}\right|^2 &= \rho \cdot p_3 \end{aligned} \tag{6.4}$$

where ρ, ξ, $w_1$ are scalar parameters and $\overrightarrow{w_2}$ is complex (with $p_1$, $p_2$ and $p_3$ being the power ratios defined earlier). The first stage of this six-to-four-port reduction procedure is to use five sliding-short terminations as calibration standards for determining ρ, ξ, $w_1$, $\mathrm{Re}(\overrightarrow{w_2})$ and $\mathrm{Im}(\overrightarrow{w_2})$. The remaining six scalar unknown parameters contained in the complex coefficients a, b and c defined in Equation 6.3 are determined via an iterative process during the second stage.

This six-to-four-port reduction procedure appears to be lengthy and complicated. In addition, there is the ambiguity of having to choose square-root signs when solving the paraboliod equation for ρ, ξ, $w_1$ and $\overrightarrow{w_2}$ during the fist step. Other researchers [6.4]-[6.5] have subsequently offered various suggestions to improve the procedure proposed by Engen.

(b) <u>Hunter and Somlo's calibration procedure</u>

For the calibration procedure proposed by Hunter and Somlo [6.7]-[6.9], it is recommended that one of the five known standards should be a matched (or nearly matched) load. The other four known standards may be sliding terminations with similar reflection-coefficient magnitudes.

It is obvious from the detailed description provided in [6.9] that what Hunter and Somlo have proposed is more explicit and avoids the ambiguity inherent in Engen's algorithm. Without any iterative searches, this direct and fast calibration procedure is spared from the need for computationally-intensive number crunching. In addition, the use of a matched load offers enhanced accuracies for most DUT-measurement applications.

(c) Qiao and Yeo's calibration procedure

The calibration procedure proposed by Qiao and Yeo [6.10] allows the requisite number of known standards to be reduced to the minimum of only four standards (*viz* matched load and three sliding-short terminations). After using the matched load to determine the three scalar unknown parameters $k_1$, $k_2$ and $k_3$, Qiao and Yeo introduced the following re-arrangement for Equation 6.1:

$$\frac{1}{R_{i,n}}\left|\overline{A_i}-\frac{e^{j\phi_n}}{\left|\overline{\Gamma}_n\right|}\right|=\lambda_n \qquad \text{where} \quad i=0,1,2,3 \quad \text{and n} = 1,2,3 \tag{6.5}$$

where

$$R_{i,n}=\sqrt{\frac{p_{i,n}}{k_i}}$$

with $i$ and n referring to the known standard and measurement port respectively.

By so doing, Qiao and Yeo showed that solving for the remaining four complex unknown coefficients $\overline{A_0}$, $\overline{A_1}$, $\overline{A_2}$ and $\overline{A_3}$ can be reduced to merely solving for the three new scalar parameters $\lambda_1$, $\lambda_2$ and $\lambda_3$ introduced in Equation 6.5. Instead of searching an eight-dimensional space for the real and imaginary parts of $\overline{A_0}$, $\overline{A_1}$, $\overline{A_2}$ and $\overline{A_3}$, their simplified algorithm needs only to search a three-dimensional space for the values of $\lambda_1$, $\lambda_2$ and $\lambda_3$.

(d) Jachim and Gutscher's calibration procedure

Jachim and Gutscher [6.11] chose to start from the formulation of Equation 6.2 instead. Their statistical approach required them to derive the following set of linear equations for evaluating $F_i$, $G_i$ and $H_i$:

$$\left[\sum_{k=1}^{m} W_k [[C_u^k][U^k] + [C_v^k][V^k]]\right] \cdot [X] = \sum_{k=1}^{m} W_k P_4^k [[C_u^k \mid C_v^k]\begin{bmatrix} r^k \\ x^k \end{bmatrix}] \tag{6.6}$$

where $[U^k] = [P_1^k \quad P_2^k \quad P_3^k \quad P_0^k \quad 0 \quad 0 \quad 0 \quad 0 \quad -r^k P_1^k \quad -r^k P_2^k \quad -r^k P_3^k]$ ,

$[V^k] = [0 \quad 0 \quad 0 \quad 0 \quad P_1^k \quad P_{21}^k \quad P_3^k \quad P_0^k \quad -x^k P_1^k \quad -x^k P_2^k \quad -x^k P_3^k]$ ,

$[C_u^k] = [P_1^k \quad P_2^k \quad P_3^k \quad P_0^k \quad 0 \quad 0 \quad 0 \quad 0 \quad r^k P_1^k \quad r^k P_2^k \quad r^k P_3^k]^T$ ,

$[V^k] = [0 \quad 0 \quad 0 \quad 0 \quad P_1^k \quad P_{21}^k \quad P_3^k \quad P_0^k \quad x^k P_1^k \quad x^k P_2^k \quad x^k P_3^k]^T$ ,

$[X] = [F_1 \quad F_2 \quad F_3 \quad F_4 \quad G_1 \quad G_2 \quad G_3 \quad G_4 \quad H_1 \quad H_2 \quad H_3]^T$ ,

$m$ is the number of standards, $r_k$ is the real part of the $k$th standard, $x_k$ is the imaginary part of the $k$th standard, and $W_k$ is the weight associated with the $k$th standard.

The principal advantage of this statistically-optimum procedure is that there is no need for high-precision standards since it is possible for calibration errors to be reduced by using more than six standards; *eg* Jachim and Gutscher chose to use seven standards in [6.11]. The 11 X 11 matrix introduced in Equation 6.6 may pose computational challenges for matrix inversion; hence, there are constraints on the choice of standards so as to obviate ill-conditioned matrix situations.

TABLE 6.1 COMPARISON OF SELECTED CALIBRATION PROCEDURES FOR SIX-PORT REFLECTOMETERS

|  | Procedure proposed by Engen [6.2] | Procedure proposed by Hunter and Somlo [6.7] | Procedure proposed by Jachim and Gutscher [6.11] | Procedure proposed by Qiao and Yeo [6.10] |
|---|---|---|---|---|
| Minimum number of standards | 5 | 5 | 6 | 4 |
| Algorithm complexity | high | low | low | moderate |
| Hardware integration complexity | difficult | easy | moderate | moderate |
| Calibration accuracy | moderate | moderate | low | high |
| Verification of results | easy | easy | difficult | easy |

### 6.1.2 Calibration trials

After a careful consideration of the advantages and disadvantages tabulated in Table 6.1 for the calibration procedures included in our study, we have decided to adopt the one proposed by Hunter and Somlo to calibrate the three prototype SPRs we developed in Sections 6.2-6.4.

(a) <u>calibration standards</u>

It is possible to use the calibration kit provided for the commercially-available vector network analyzer (VNA) as the known standards required for the calibration procedure proposed by Hunter and Somlo. Alternatively, we may fabricate the requisite standards in-house on PCBs instead.

For quality assurance purposes, we had to employ the VNA to measure the performance characteristics of all the four-port couplers we fabricated (based on the designs reported in Chapter 5) before using them as building blocks for our prototype SPRs. Since the return losses of these matched couplers must be less than -20dB, we had to resort to de-embedding as recommended by the VNA manufacturer [6.12]-[6.14]. Hence, we also found it necessary to fabricate the following standards which we used not only for VNA de-embedding but also for SPR calibration**:** λ/4 50Ω open line, λ/4 50Ω short line, λ/4 50Ω load line and λ/2 50Ω thru-line as shown in Figure 6.2.

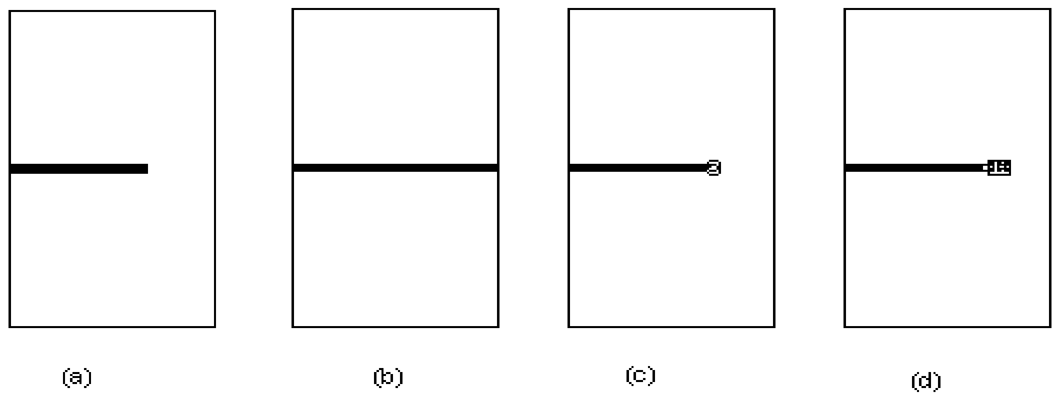

Figure 6.2 Calibration standards: (a) open line, (b) thru-line, (c) short line, and (d) load line

(b) <u>experimental set-up</u>

The general set-up for our calibration trials is depicted in Figure 6.3 with each PCB standard connected in turn to the prototype SPR at its DUT port. As shown in the photograph of Figure 6.4, we have chosen the HP E8257D signal source and R&S NRVS power meters which ought to be available in most well-equipped microwave laboratories.

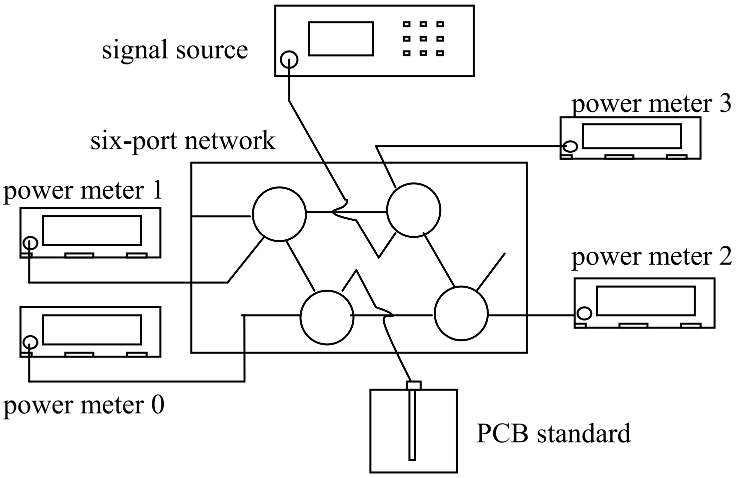

Figure 6.3 Prototype six-port reflectometer set-up

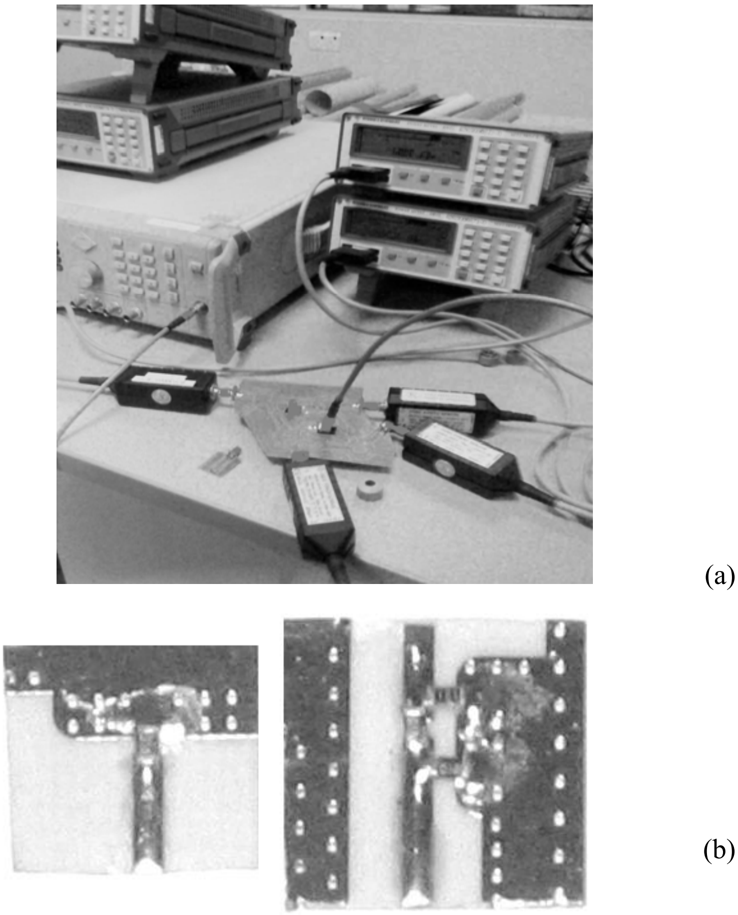

Figure 6.4 Photographs of prototype six-port reflectometer and selected DUTs
100Ω, 330Ω and 1000Ω loads shown in the left of (b)
3dB attenuation and 10dB attenuation shown in the right of figure (b)

(c) need for de-embedding

When using the VNA (to measure the performance characteristics of our four-port couplers), we should pay attention to the shift of the reference planes (as illustrated in Figure 6.5) due to the SMA connectors serving as interfaces. For the VNA calibration procedure SOLT (short, open, load and through), it is assumed that that the standards have compatible connectors with the test cables and hence the reference planes ought to be at the inputs of these connectors. Although this might not pose a serious problem at lower frequencies, we affirmed from our test results the need for de-embedding when operating beyond 3GHz**;** for example, the two return-loss plots presented in Figure 6.6 (for a 6GHz coupler as the DUT) clearly indicate the effect of SMA connectors on the raw measurements (*ie* before de-embedding). After applying the VNA calibration procedure LRL (line, reflect and line) to perform the de-embedding, we obtained the smoother and more accurate plot presented in Figure 6.6 without the spurious effects masking the actual return-loss behavior of the four-port coupler (which was designed for operation from 5GHz to 7GHz).

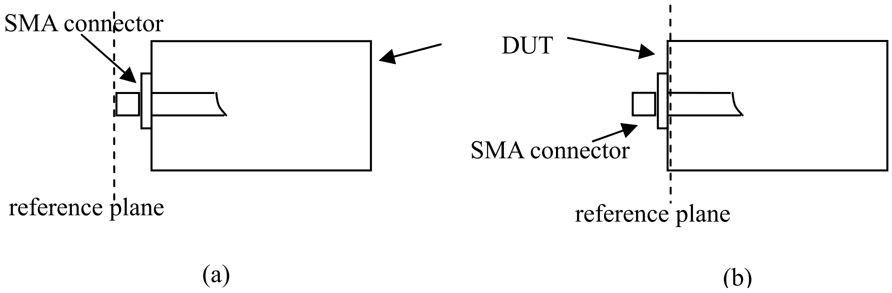

Figure 6.5 Illustration of measurements with reference plane at (a) input terminal of connector and (b) input terminal of DUT

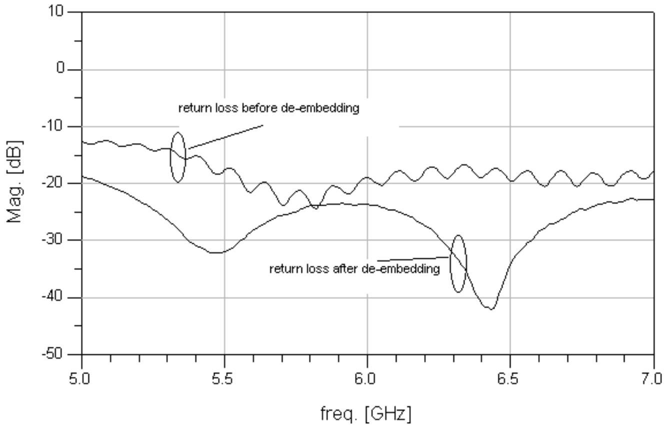

Figure 6.6 Return loss plots obtained by VNA before and after de-embedding SMA-connector effects

In Sections 6.2-6.4, the DUT measurement results obtained by each of our three prototype SPRs will be compared with those taken by the VNA. For such comparisons, the standards utilized to calibrate the VNA and SPRs ought to be the same. The flow-chart in Figure 6.7 presents the two possible calibration scenarios (*viz* with and without de-embedding to account for the DUT's SMA connectors)**:**

- For the procedure outlined in the left branch of the flow-chart in Figure 6.7, the wide-band load and open/short terminations (from the VNA calibration kit) and another two PCB open/short standards are used to calibrate the VNA and SPR with the SMA connector's input terminal taken as the reference plane. This option may be used only when operating at the lower-frequency end (below, say, 3GHz).

- For the procedure outlined in the right branch of the flow-chart in Figure 6.7, we also used the five standards employed in the VNA's LRL (or LRM) procedure to calibrate each SPR with the reference plane now sited at the DUT's input terminal. The characteristics of the five 'standards' we fabricated on PCB must naturally be determined before they can be used for the VNA/SPR calibration**;** where circumstances allowed, we chose instead the wide-band load and open/short terminations (from the VNA calibration kit) plus another two PCB open/short offsets as the standards. This option is recommended when the operating frequency is no longer low enough for us to disregard the need for de-embedding.

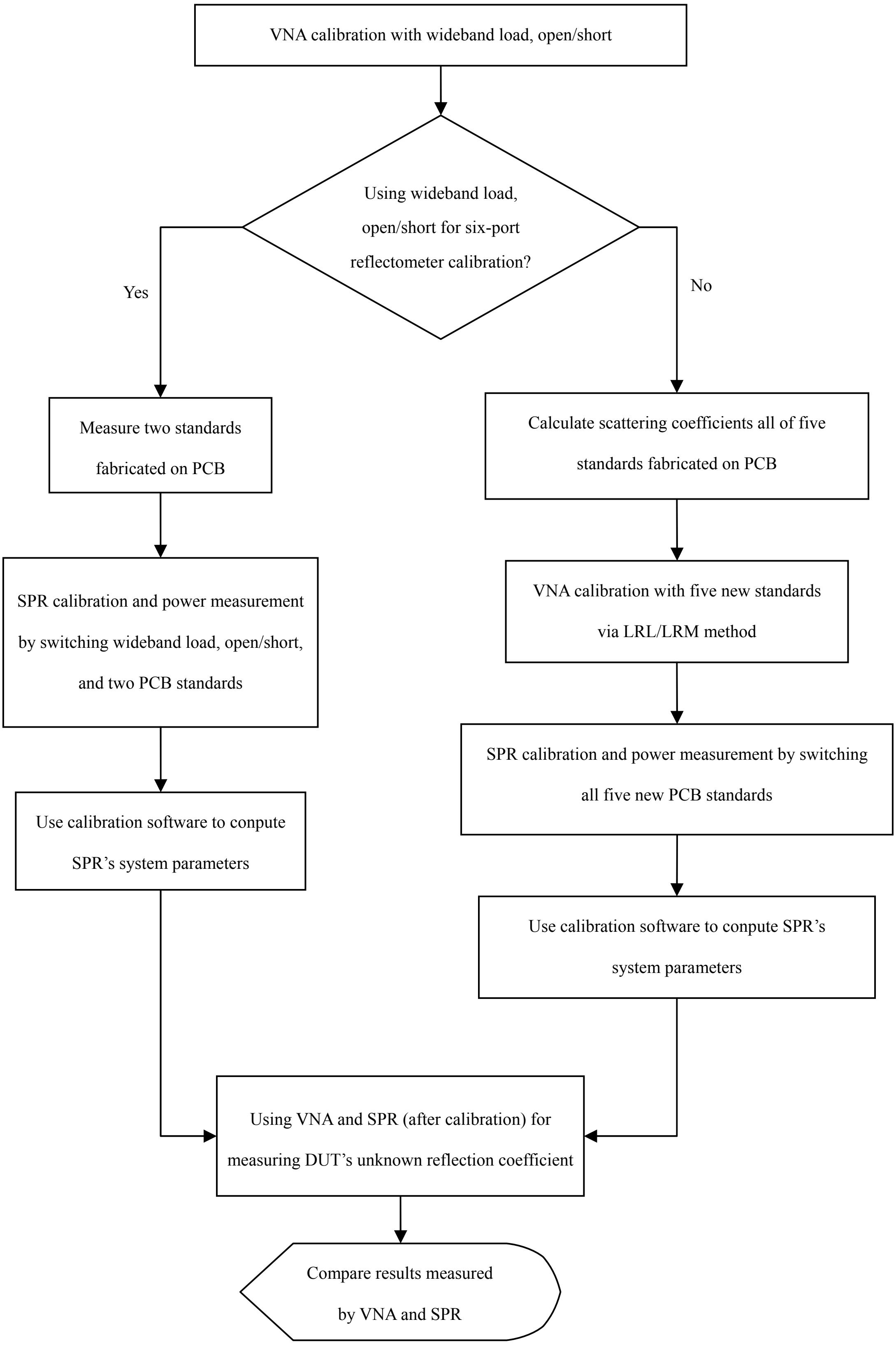

Figure 6.7 Flow-chart for calibration of vector network analyzer (VNA) and six-port reflectometer (SPR) with or without de-embedding

(d) calibration error simulations

In general, it is difficult to perform experiments in the laboratory for the purpose of conducting an unbiased comparison of the two calibration scenarios outlined in the flow-chart of Figure 6.7 since there are too many factors outside our immediate control affecting the empirical evaluation. Instead, we shall resort to Monte Carlo simulations so as to statistically analyze the calibration errors that may be expected when applying Hunter and Somlo's procedure.

The SPR utilized for our computational study is the one based on modified four-port couplers previously considered in Sub-Section 2.6.3. The data at our disposal allowed us to compute the ideal-case power-meter readings for the SPR with the various standards connected under noise-free conditions at 2GHz. The Monte Carlo simulations involved the addition of increasing levels of Gaussian noise to the ideal-case power-meter readings followed by the use of the noise-corrupted power readings thus obtained to re-compute the SPR's system coefficients. For comparison purposes, we adopted the following parameters to serve as indicators of how much the SPR's system parameters strayed from their original settings:

- $\frac{Std(k_1)}{k_1}$ where std($k_1$) is the standard deviation of coefficient $k_1$ in Equation 6.1
- $\frac{\sqrt{EVMS(\overline{A_i})}}{|\overline{A_i}|}$ where $EVMS(\overline{A_i})$ is the error vector mean square of the complex coefficient $\overline{A_i}$.

The simulation results presented in Figure 6.8 indicate that the errors in the SPR's system parameters $k_i$ and $\overrightarrow{A_i}$ increase in an approximately linear manner with the level of Gaussian noise injected into the ideal-case power-meter readings. In particular, the parameters $A_i$ appear to be more sensitive; this is not unexpected if we recall that the magnitudes of q-points will in the limit approach $q_i \approx \frac{1}{|\overline{A_i}|}$ when $A_0$ is sufficiently large (above, say, 10GHz).

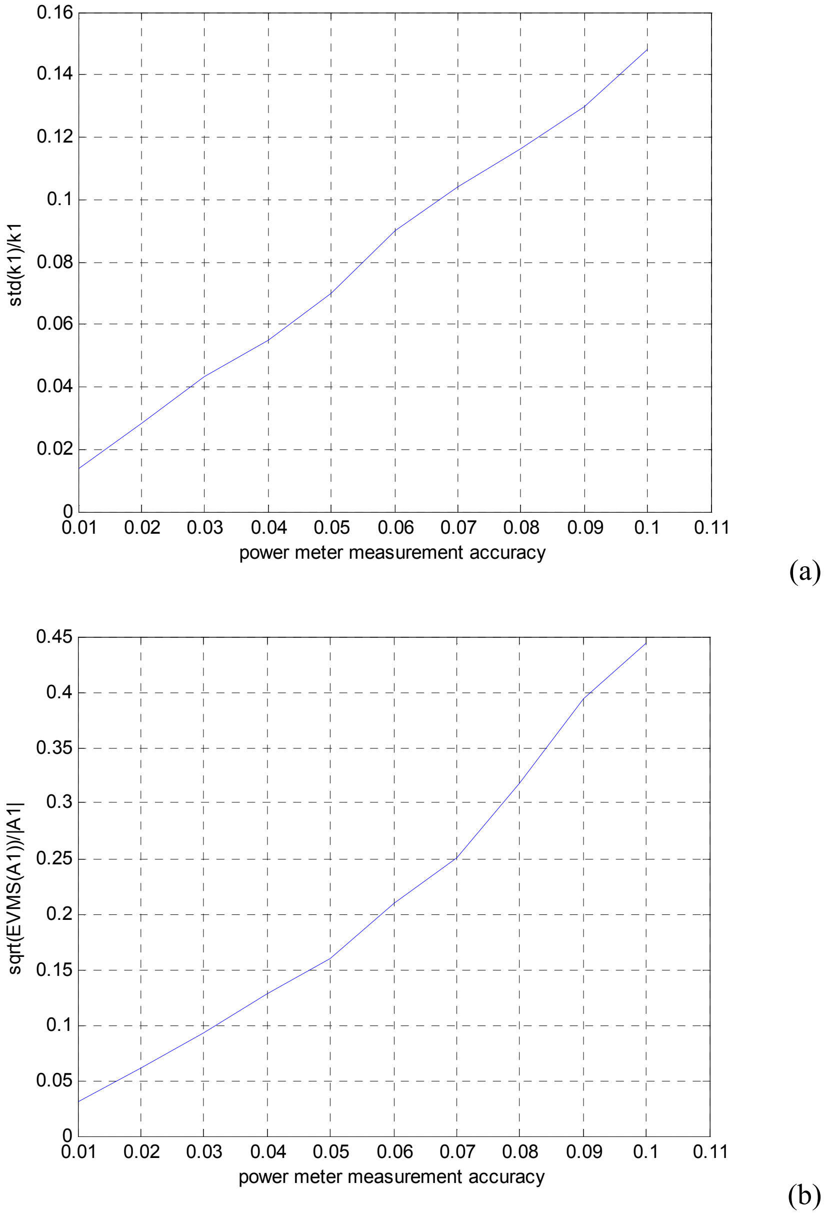

Figure 6.8 Monte Carlo simulation results for Hunter and Somlo's calibration algorithm under Gaussian noise

## 6.2 Prototype Reflectometer based on Modified Branch-Line Couplers

The first SPR we constructed employs four of the modified branch-line couplers we designed earlier in Section 5.1 (with the details of the key coupler parameters given in Figure 5.3 and Table 5.2). Figure 6.9 depicts the lay-out of our microstrip circuit implemented on Rogers 5870 laminate (with relative permittivity of 2.3, loss tangent of 0.0012, thickness of 31mil and 1/2 oz copper foil). Preliminary tests indicate that the following compensation elements have to be included before our prototype SPR is ready for DUT measurements**:**

(a) chamfering the bends (with $M_{opt} \approx 53\%$ in accordance with Equation 4.23) when inter-connecting the four couplers

(b) adjusting the lengths of the open-circuit terminations at two of the coupler arms (with $\Delta l_{oc1} = 5\text{mil}$ for arm #1 and $\Delta l_{oc2} = 20\text{mil}$ for arm #2)

(c) adding short stubs at the two open-circuit terminations as explained in Section 3.3 for fine-tuning the ratio $\Gamma_1/\Gamma_2$ in an effort to correct for q-point deviations.

As can be seen from the predicted results plotted in Figure 6.10, the three q-points for such a SPR (after having incorporated all the final-stage refinements depicted in Figure 6.9) meet the design specifications of $120^o \pm 20^o$ and $2 \pm 0.5$ for angular separations and magnitudes respectively over a 29% bandwidth (from 4.5GHz to 5.9GHz). The corresponding results we subsequently obtained in Figure 6.10 (during the laboratory experiments conducted on our prototype SPR) are largely similar.

Listed in Table 6.2 are the sample results obtained by our prototype SPR for selected DUTs with different values of Γ. Table 6.3 records the measurements of Γ taken at different frequencies for the 100Ω load as the DUT. A comparison with the corresponding readings obtained by the HP8510C VNA confirms that our prototype SPR is able to measure the magnitude and phase of Γ to within ±0.01 and ±2° respectively. We also note from the measured q-point plots in Figure 6.10 that the angular separations remain within the 120° ± 20° range over a 29% bandwidth; this is a marked improvement when compared with the results already reported in the literature for the other SPR instruments which utilized standard four-port couplers (*eg* 90°, 135° and 135° for the SPR circuit proposed by Engen [6.4]).

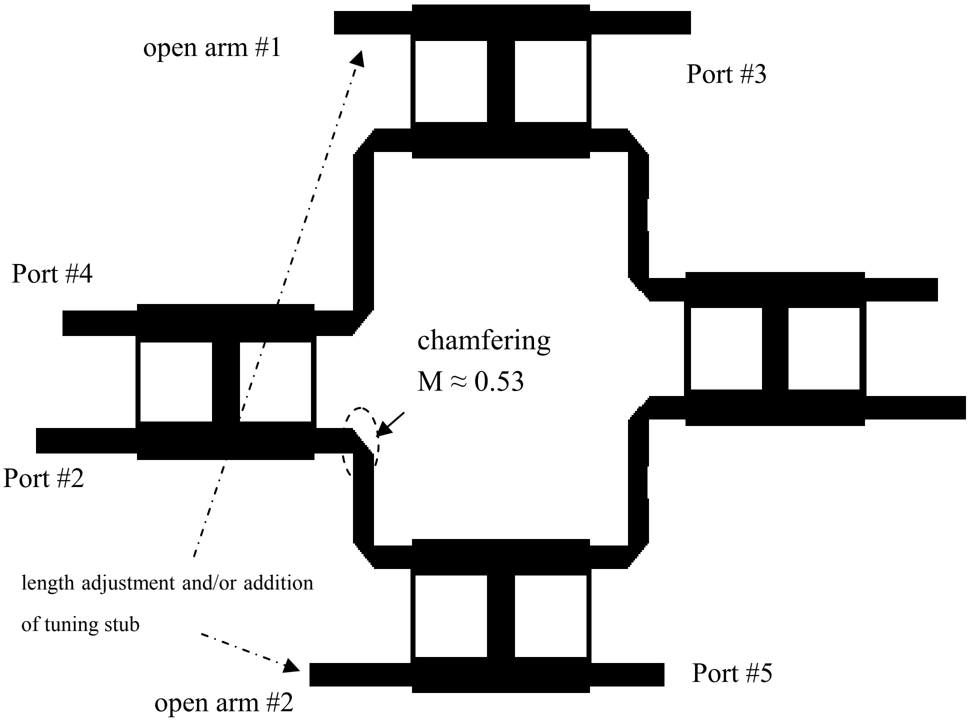

(a) layout illustration

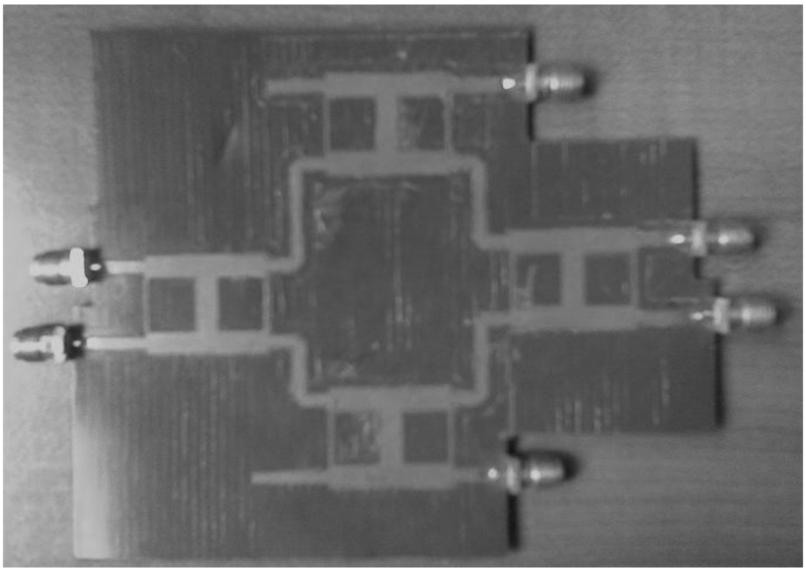

(b) photo of prototype (with overall dimensions of 122mm X 88mm)

Figure 6.9 Prototype SPR based on modified branch-line couplers designed in Section 5.1

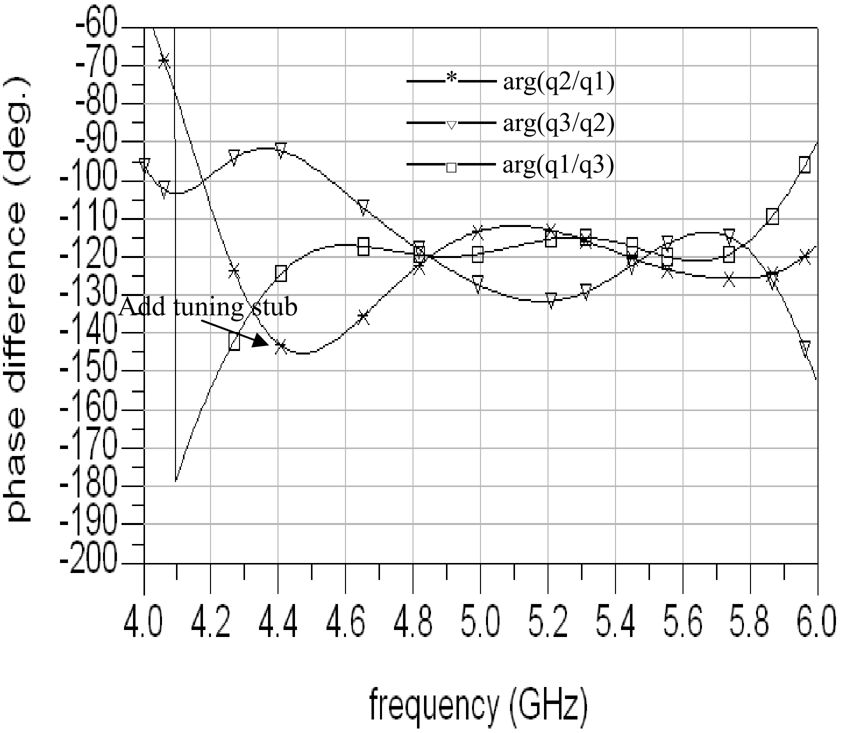

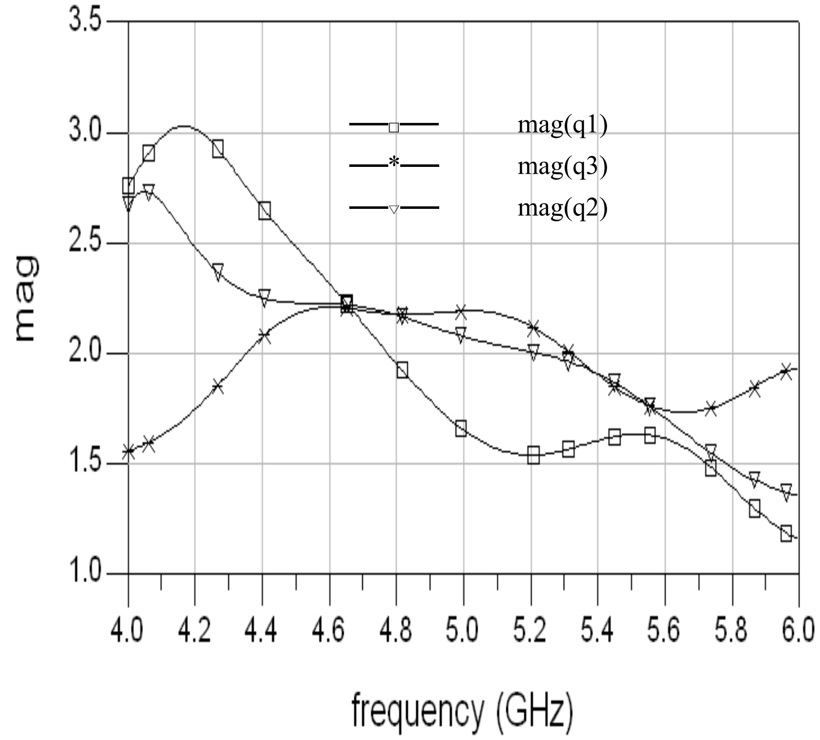

Figure 6.10 Predicted results for q-points of prototype SPR (Figure 6.8) based on modified branch-line couplers (Figure 5.3)

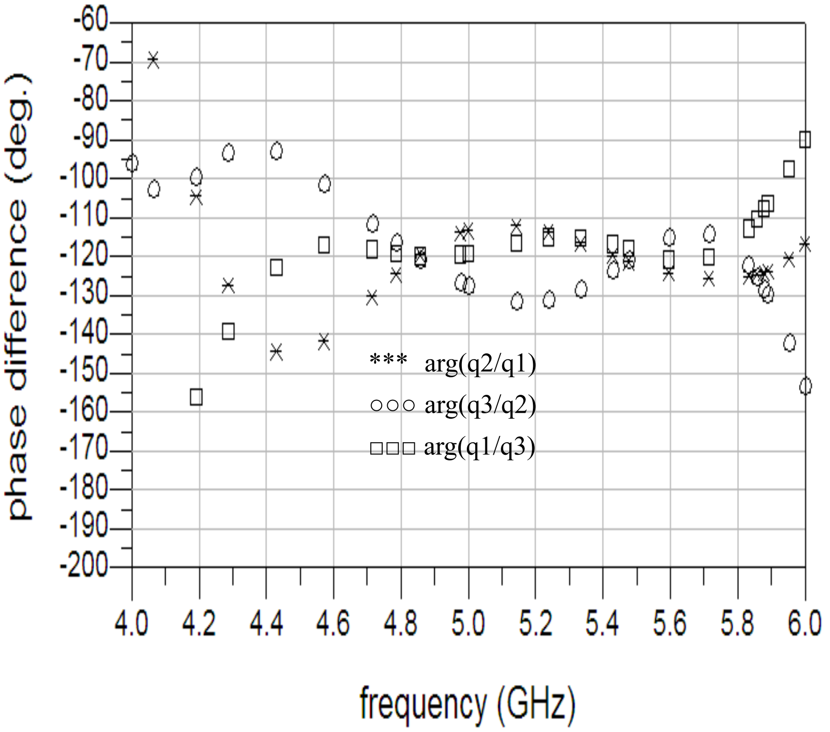

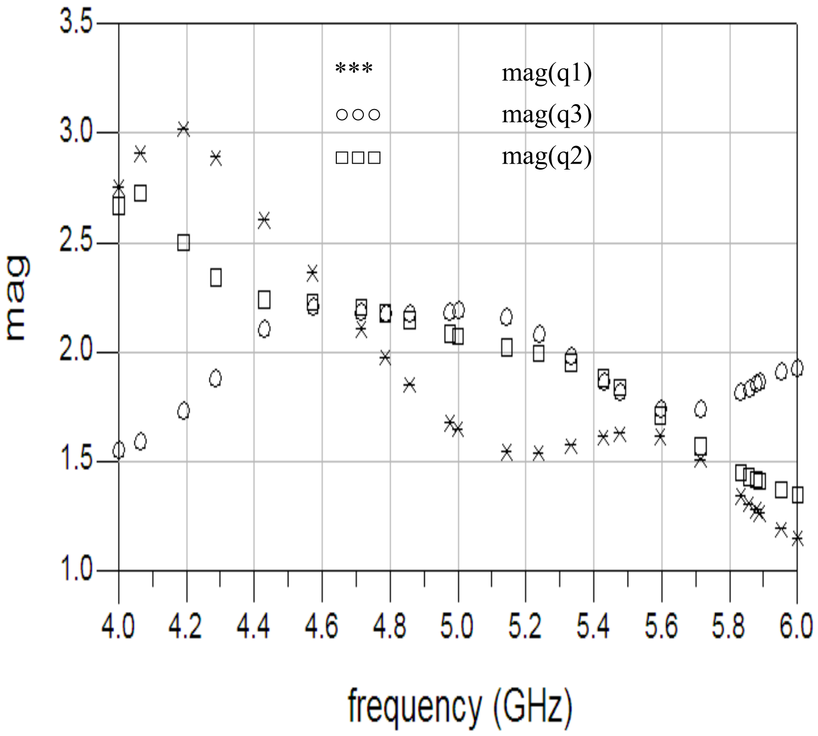

Figure 6.11 Measured results for q-points of prototype SPR (Figure 6.8) based on modified branch-line couplers (Figure 5.3)

TABLE 6.2 COMPARISON OF MEASUREMENT RESULTS TAKEN BY PROPOSED SPR (DEPICTED IN FIGURE 6.8) AND HP8510C VNA FOR SELECTION OF DUTS AT 5GHZ

| Device Under Test | Measured value of Γ taken by | |
|---|---|---|
| | Prototype SPR | HP8510C |
| 3dB attenuator | 0.53∠-38.3° | 0.54∠-39.4° |
| 10dB attenuator | 0.11∠-53.6° | 0.12∠-54.5° |
| 100Ω resistor | 0.35∠−115.8° | 0.34∠−116.1° |
| 330Ω resistor | 0.74∠−114.4° | 0.73∠−115.9° |
| 1000Ω resistor | 0.91∠−116.1° | 0.90∠−116.5° |

TABLE 6.3 COMPARISON OF MEASUREMENT RESULTS TAKEN AT DIFFERENT FREQUENCIES BY PROPOSED SPR (DEPICTED IN FIGURE 6.8) AND HP8510C VNA FOR 100Ω RESISTOR AS DUT

| Frequency (GHz) | Measured value of $\Gamma$ taken by | |
|---|---|---|
| | Prototype SPR | HP8510C |
| 4.6 | $0.33\angle{-106.1}^{\circ}$ | $0.34\angle{-107.8}^{\circ}$ |
| 4.8 | $0.33\angle{-111.8}^{\circ}$ | $0.34\angle{-112.5}^{\circ}$ |
| 5.0 | $0.35\angle{-115.8}^{\circ}$ | $0.34\angle{-116.1}^{\circ}$ |
| 5.2 | $0.35\angle{-120.1}^{\circ}$ | $0.34\angle{-121.4}^{\circ}$ |
| 5.4 | $0.36\angle{-125.4}^{\circ}$ | $0.34\angle{-127.5}^{\circ}$ |
| 5.6 | $0.34\angle{-130.6}^{\circ}$ | $0.35\angle{-129.3}^{\circ}$ |
| 5.8 | $0.35\angle{-134.7}^{\circ}$ | $0.33\angle{-133.9}^{\circ}$ |

## 6.3 Prototype Reflectometer based on Modified Rat-Race Couplers

Depicted in Figure 6.12 is another microstrip circuit we also fabricated on Rogers 5870 laminate (with relative permittivity of 2.3, loss tangent of 0.0012, thickness of 31mil and 1/2 oz copper foil). Unlike our first SPR's configuration in Section 6.2 (where the geometry of the branch-line couplers allowed for some symmetry in the overall lay-out portrayed in Figure 6.9), it is necessary for us to add bends in a non-symmetric manner when arranging in Figure 6.12 for the inter-connection of the four modified rat-race couplers we designed earlier in Section 5.2 (with the details of the key coupler parameters given in Figure 5.9 and Table 5.5). In addition, the following compensation elements have to be included during the final-stage refinement of our second prototype SPR**:**

(a) chamfering for the bends inserted in two of the inter-connecting lines (with $M_{opt}$ of approximately 30% and 50% for angles of $90^o$ and $78^o$ respectively as depicted in Figure 6.12)

(b) adjustment of lengths for two open-circuit terminations (with $\Delta l_{oc1}$ = 276mil for arm #1 and $\Delta l_{oc2}$ = 256mil for arm #2)

(c) adding capacitors or short stubs at the two open-circuit terminations for fine-tuning the ratio $\Gamma_1/\ \Gamma_2$ in Equations 3.17-3.18.

As can be seen from the predicted and measured results plotted in Figures 6.13 and 6.14 respectively, the q-points for our second prototype SPR also meet the design specifications of $120^o \pm 20^o$ and $2 \pm 0.5$ for angular separations and magnitudes respectively over a 33% bandwidth (from 2.5GHz to 3.5GHz). For the DUT-measurement tests, we once again compare the results taken by both SPR and VNA**;** the data recorded in Tables 6.4 and 6.5 show similar levels of measurement accuracies as in Tables 6.2 and 6.3, and it thus appears that the difference between our first two prototype SPRs is minor in terms of overall performance. Although there is a marginally wider bandwidth for our second prototype SPR (based on modified rat-race couplers) when compared with our first prototype SPR (based on modified branch-line couplers), we have subsequently not been able to obtain further improvement unless we look beyond microstrip-based circuits to consider other forms of planar implementation.

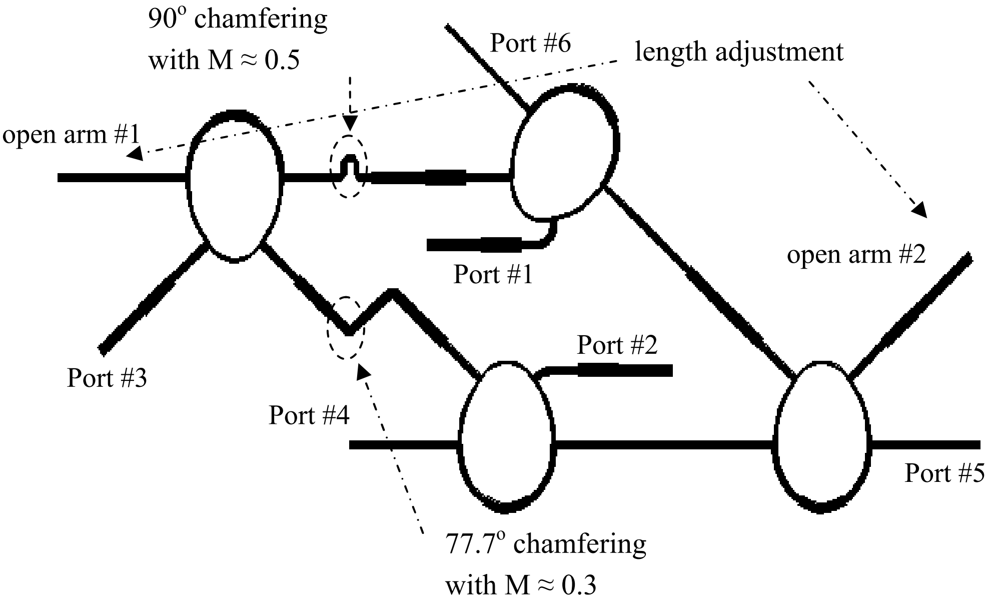

(a) layout illustration

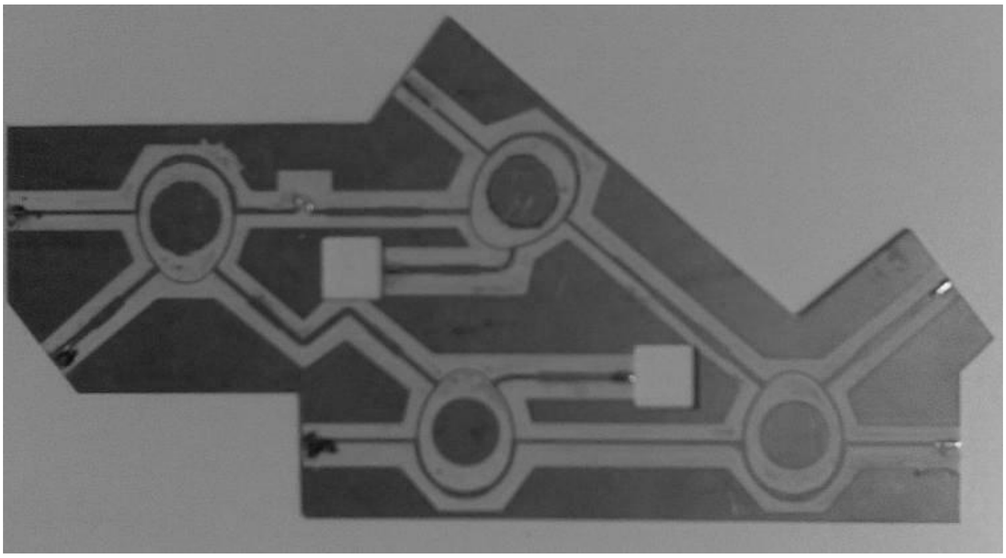

(b) photo of prototype (with overall dimensions of 330mm X 168mm)

Figure 6.12 Prototype SPR based on modified rat-race couplers designed in Section 5.2

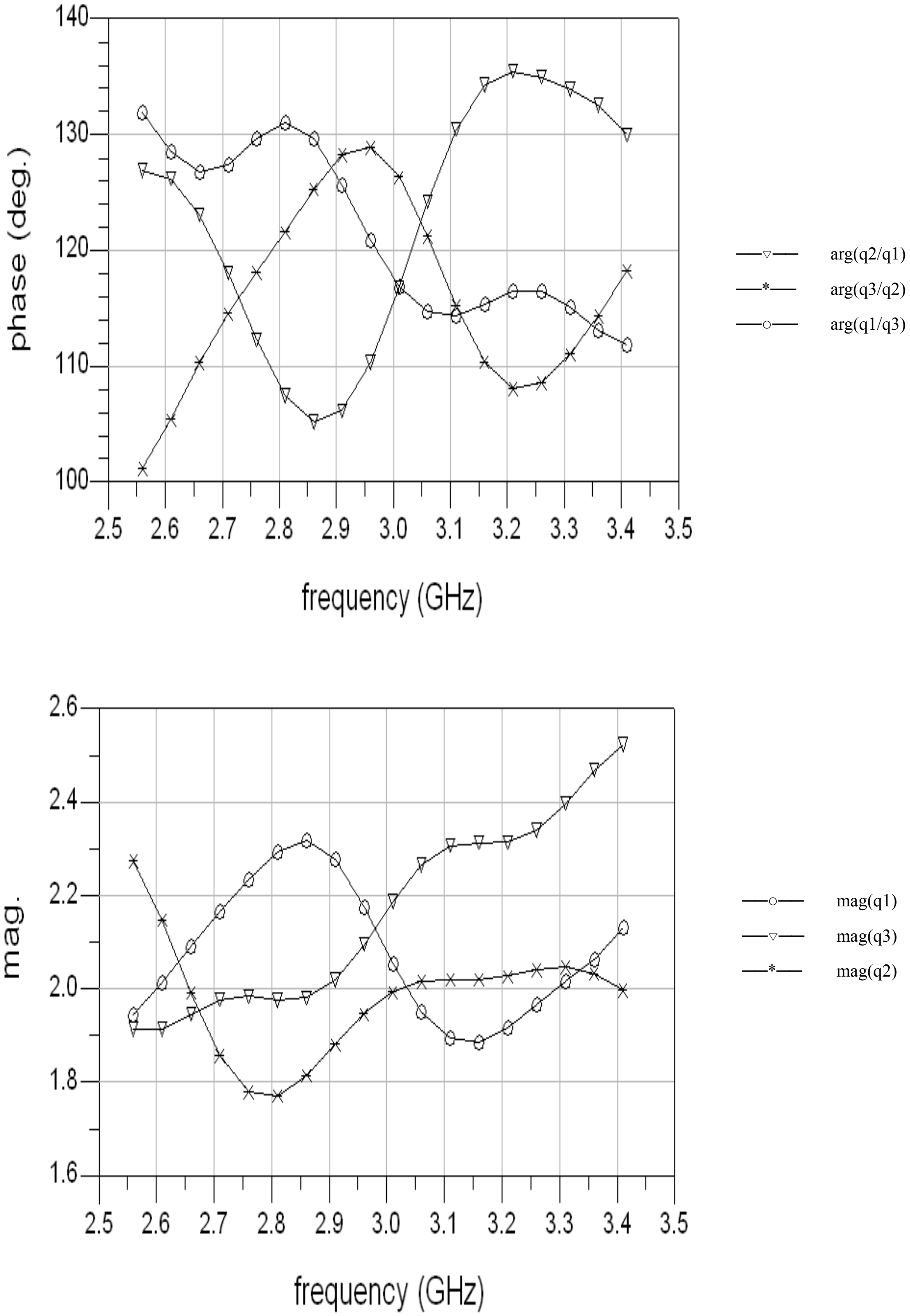

Figure 6.13 Predicted results for q-points of prototype SPR (Figure 6.12) based on modified rat-race couplers (Figure 5.9)

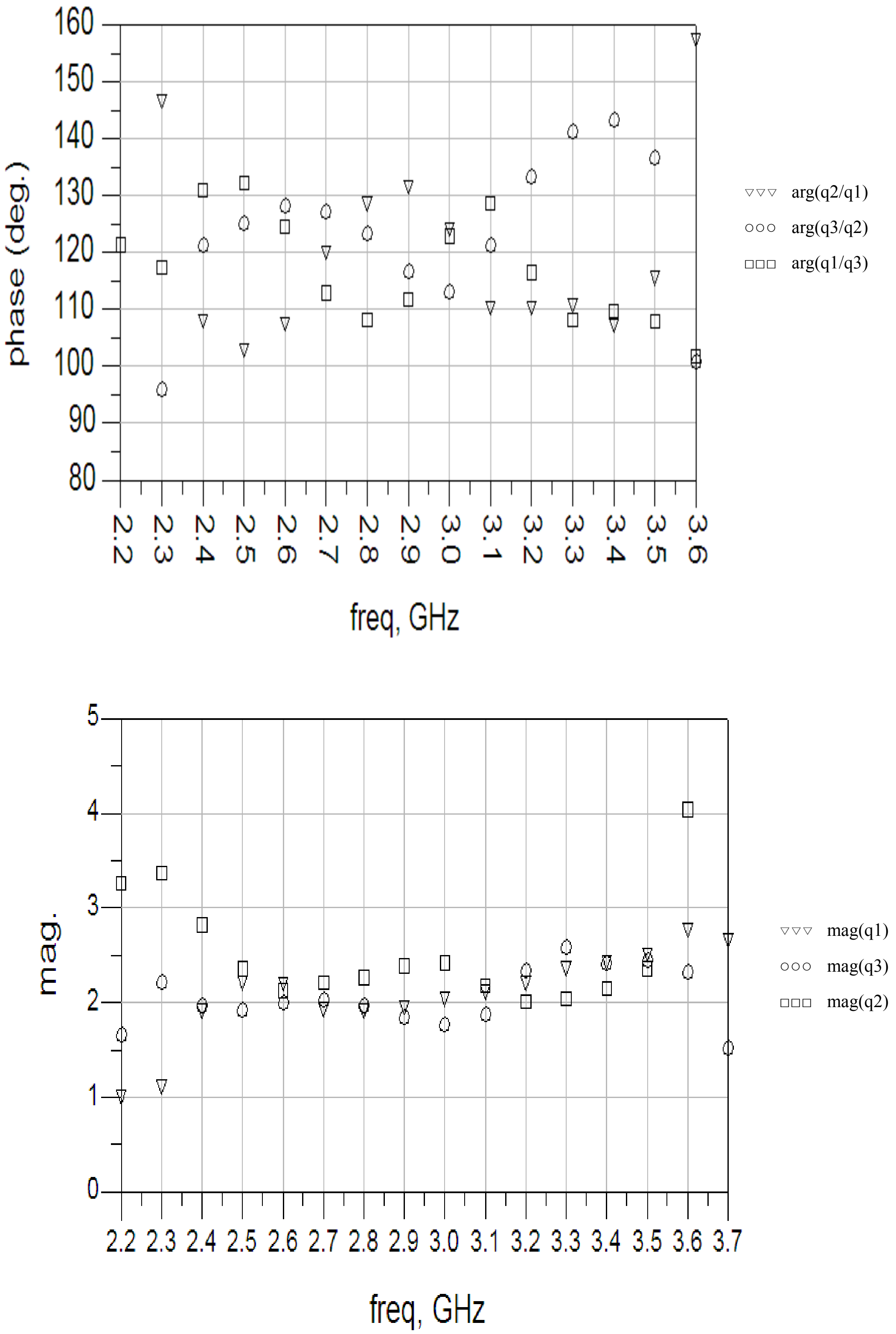

Figure 6.14 Measured results for q-points of prototype SPR (Figure 6.12) based on modified rat-race couplers (Figure 5.9)

Table 6.4 Comparison of measurement results taken by proposed SPR (depicted in Figure 6.12) and HP8510C VNA for selection of DUTs at 3GHz

| Device Under Test | Measured value of $\Gamma$ taken by | |
|---|---|---|
| | Prototype SPR | HP8510C |
| 3dB attenuator | $0.56\angle 42.3^{\circ}$ | $0.54\angle 39.6^{\circ}$ |
| 10dB attenuator | $0.15\angle 27.4^{\circ}$ | $0.12\angle 29.6^{\circ}$ |
| 100 Ω resistor | $0.36\angle 73.6^{\circ}$ | $0.37\angle 71.2^{\circ}$ |
| 330 Ω resistor | $0.76\angle 71.5^{\circ}$ | $0.74\angle 72.8^{\circ}$ |
| 1000 Ω resistor | $0.89\angle 71.2^{\circ}$ | $0.90\angle 73.7^{\circ}$ |

Table 6.5 Comparison of measurement results taken at different frequencies by proposed SPR (depicted in Figure 6.12) and HP8510C VNA for 100Ω resistor as DUT

| Frequency (GHz) | Measured value of $\Gamma$ taken by | |
|---|---|---|
| | Prototype SPR | HP8510C |
| 2.6 | $0.35\angle 59.7^{\circ}$ | $0.34\angle 60.9^{\circ}$ |
| 2.8 | $0.34\angle 67.6^{\circ}$ | $0.34\angle 66.7^{\circ}$ |
| 3.0 | $0.35\angle 73.6^{\circ}$ | $0.35\angle 71.2^{\circ}$ |
| 3.2 | $0.34\angle 77.3^{\circ}$ | $0.34\angle 78.2^{\circ}$ |
| 3.4 | $0.36\angle 81.9^{\circ}$ | $0.34\angle 80.2^{\circ}$ |

## 6.4 Prototype Reflectometer based on CPW Hybrid Couplers

We have found it necessary to resort to CPW implementation in our attempt to overcome the inherent limitations encountered for microstrip-based circuits in Sections 6.2-6.3. The CPW hybrid coupler we designed earlier in Sub-Section 5.3.2 (with the details of the key coupler parameters given in Figure 5.18 and Table 5.6) has already been shown to yield suitable scattering-coefficient behavior over a bandwidth of 80% (from 1.2GHz to 2.8GHz) when fabricated on Rogers 6010LM substrate (with relative permittivity of 10.2, loss tangent of 0.002 and thickness of 50mil). In Figure 6.15, we depict how four of these CPW couplers are to be inter-connected to construct our third prototype SPR. For the schematic circuit diagram sketched in Figure 6.15(a), each rhombus represents a CPW coupler where the emboldened edge denotes the coupler arm with the 180° phase shifter (based on the coupler design reproduced in Figure 5.18). Special attention has to be paid to the following compensation elements when trying to fit all the components within the 17cm X 13cm board lay-out**:**

(a) metering of CPW central strip corner in accordance with Equation 4.24

$$M_1 = \frac{m}{m_{\max}} = 0.59 \qquad \text{for} \quad 50\Omega \text{ CPW line}$$

$$M_2 = \frac{m}{m_{\max}} = 0.44 \text{ for} \quad 40\Omega \text{ CPW line}$$

(b) chamfering with $M_{opt}$ of approximately 50% for bends with different line impedance transitions

(c) adjustment of lengths for two open-circuit terminations (with $\Delta l_{oc1}$ = 17mil for arm #1 and $\Delta l_{oc2}$ = 16mil for arm #2)

(d) adding SMT capacitors or inductors at the two open-circuit terminations for fine-tuning the ratio $\Gamma_1/\Gamma_2$ in Equations 3.17-3.18.

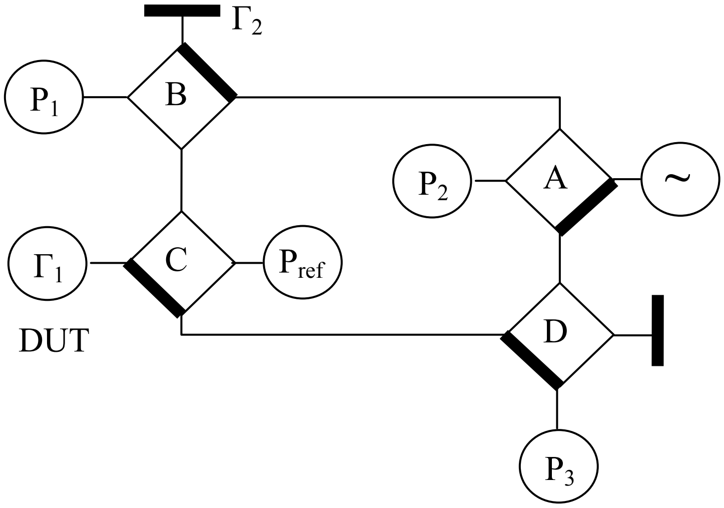
Γ2
P1
B
P2
A
~
Γ1
C
Pref
DUT
D
P3

(a)

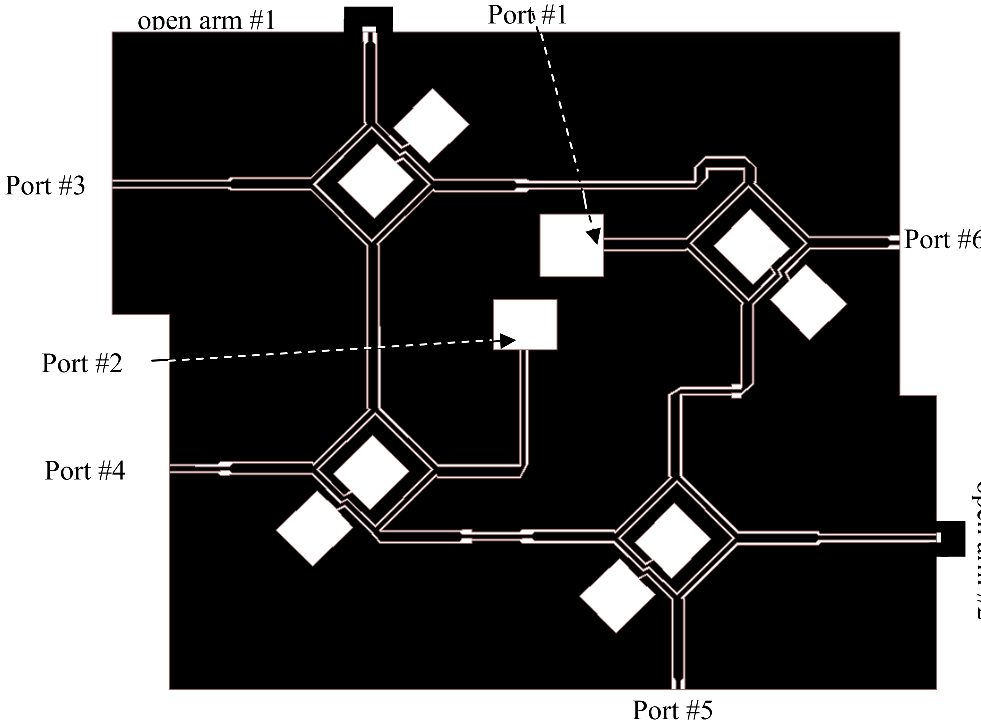
open arm #1
Port #1
Port #3
Port #6
Port #2
Port #4
open arm #2
Port #5

(b)

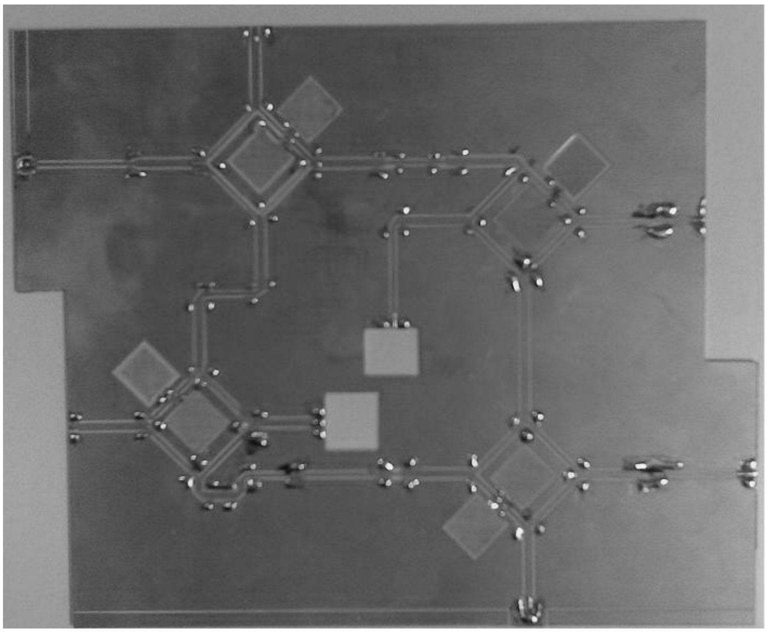

(c)

Figure 6.15 Prototype SPR based on modified CPW hybrid couplers designed in Sub-Section 5.3.2

(a) schematic circuit where emboldened rhombus edge denotes coupler arm with 180° phase inverter

(b) physical lay-out with overall dimensions of 17cm X 13cm

(c) photo of prototype (with overall dimensions of 165mm X 134mm)

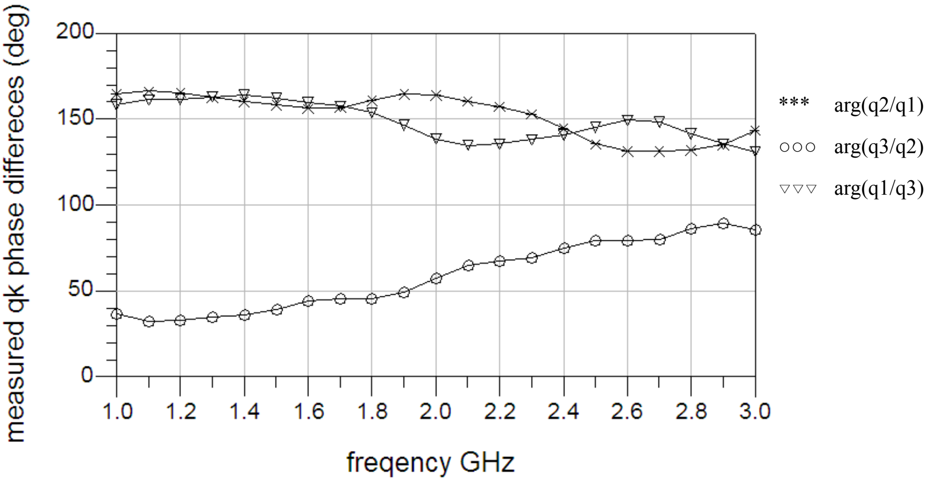

Figure 6.16 Measured results for q-points of prototype SPR (Figure 6.15) obtained during preliminary tests without using tuning elements at open arms

Plotted in Figure 6.16 are some of the q-point data we obtained during the initial tests we conducted without any tuning elements at the terminations represented by $\Gamma_1$ and $\Gamma_2$. It is clear from such plots that there is a need to use adjustable capacitances or inductances for tuning the ratio $\Gamma_1/\Gamma_2$ in accordance with Equations 3.17-3.18. Another observation we noted from these preliminary trials is that it is not advisable to choose the same termination for both $\Gamma_1$ and $\Gamma_2$. In fact, our simulations indicate that we ought to connect a 6nH inductor at arm #2 while leaving $\Gamma_1$ as an open-circuit termination. What we finally chose after the tuning trials is an 8.2nH inductor for $\Gamma_2$ (with $\Gamma_1$ remaining unchanged), and the q-point results thus obtained are presented in Figure 6.17 which show the angular separations remaining within the $120^o \pm 20^o$ specification over a 80% bandwidth (from 1.2GHz to 2.8GHz). Alternatively, we have additionally found from our tuning trials that the same level of improvement in the q-point distribution may also be obtained if we connect a 4.7pF capacitor at arm #1 while extending the length of open arm #2 by 160mil.

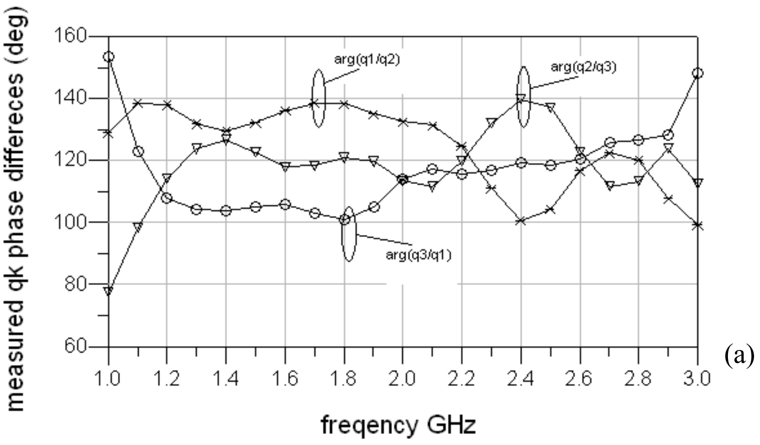

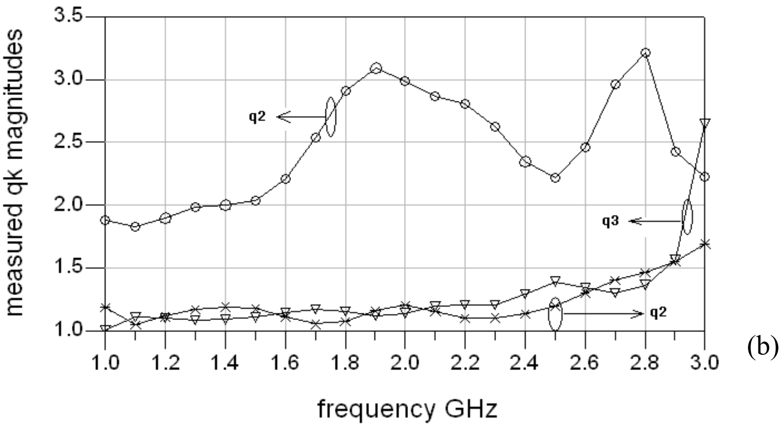

Figure 6.17 Measured results for q-points of prototype SPR (Figure 6.15) based on CPW hybrid couplers (Figure 5.18)

Listed in Table 6-6 are the sample results obtained by our third prototype SPR for the same selection of DUTs as in Tables 6.2 and 6.4 (for our first and second SPRs respectively). In view of the wider bandwidth now available, Table 6-7 records the measurements of Γ for one particular DUT over the 80% bandwidth from 1.2GHz to 2.8GHz. Finally, we also present the measured q-point plots in Figure 6.18 where the DUT is a variable two-port attenuator shorted at one end**;** these test results confirm that the angular separations vary by less than $10^o$ as we systematically change |Γ| from 0 to 1 for the passive DUT.

Other researchers have resorted to non-standard components (such as symmetrical five-port and six-port couplers) in their attempts to design SPRs with optimum q-point distributions**;** for example, Yeo and Lee [6.28] employed a symmetrical five-port coupler together with a directional junction (to provide the additional sixth port) to develop their SPR. The results we presented in Figures 6.17-6.18 and Tables 6.6-6.7 compare favorably with the following findings reported earlier by Yeo and Lee**:**

- angular separations of q-points remaining within 20° of optimum 120° specification
- angular separations of q-points varying by less than 10° for changes of DUT
- q-point magnitude differences of less than 100%
- ±0.01 and ±2° for magnitude and phase respectively of DUT's reflection coefficient Γ.

Table 6.6 Comparison of measurement results taken by proposed SPR (depicted in Figure 6.15) and HP8510C VNA for selection of DUTs at 2GHz

| Device Under Test | Measured value of Γ taken by | |
|---|---|---|
| | Prototype SPR | HP8510C |
| 3dB attenuator | 0.53∠-28.3° | 0.54∠-29° |
| 10 attenuator | 0.11∠43.3° | 0.12∠45° |
| 100Ω resistor | 0.34∠-39.0° | 0.34∠-41° |
| 330Ω resistor | 0.74∠-40.4° | 0.73∠-42° |
| 1000Ω resistor | 0.91∠-39.3° | 0.90∠-41° |

Table 6.7 Comparison of measurement results taken at different frequencies by proposed SPR (depicted in Figure 6.15) and HP8510C VNA for 100Ω resistor as DUT

| Frequency (GHz) | Measured value of Γ taken by | |
|---|---|---|
| | Prototype SPR | HP8510C |
| 1.2 | 0.33 ∠-96.5° | 0.34∠-95° |
| 1.6 | 0.33 ∠ 111.2° | 0.34∠112° |
| 2.0 | 0.34 ∠ -39.0° | 0.33∠-41° |
| 2.4 | 0.32 ∠ 168.0° | 0.33∠169° |
| 2.8 | 0.33 ∠ 18.5° | 0.32∠17° |

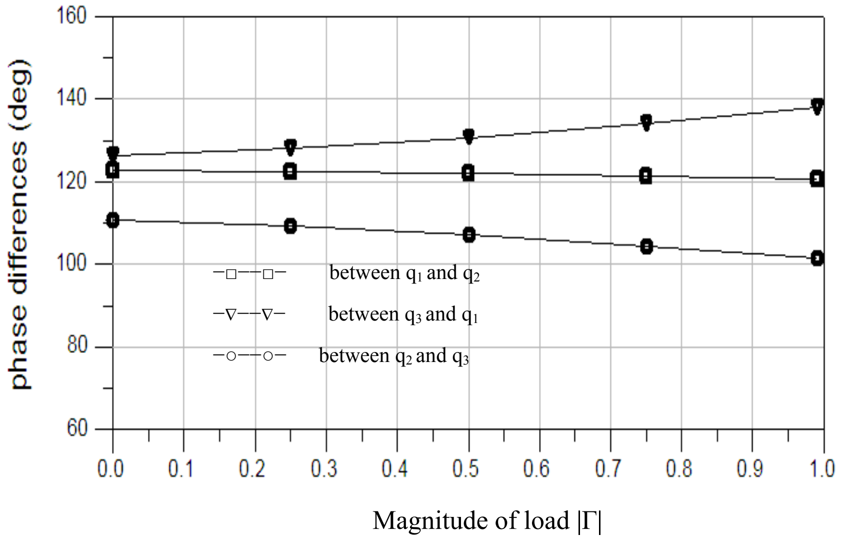

Figure 6.18 Measured results for angular separations of q-points for prototype SPR (Figure 6.15) based on CPW hybrid couplers (Figure 5.18) where DUT is variable attenuator with |Γ| ranging from 0 to 1 at test frequency of 2GHz

## REFERENCES

[6.1] G.F. Engen, "A historical review of the six-port measurement technique," IEEE Trans. Microwave Theory Tech., vol. MTT-45, pp. 2414-2417, Dec. 1997

[6.2] G.F. Engen, "Calibrating the six-port reflectometer by means of sliding terminations," IEEE Trans. Microwave Theory Tech., vol. MTT-26, pp. 951-957, Dec. 1978

[6.3] G.F. Engen, "A least squares solution for use in six-port measurement technique," IEEE Trans. Microwave Theory Tech., vol. MTT-28, pp. 1477-1482, Dec. 1980

[6.4] H. Ebbeson and G.F. Engen, "Singularities in the calibration of six-port network analyzers", Microwave Symposium Digest, MTT-S International, Volume 81, Issue 1, Jun 1981 Page(s): 149 - 150

[6.5] A. Wright, "A robust six-to-four port reduction technique for the calibration of six-port microwave network analysers", Instrumentation and Measurement Technology Conference, 1990. IMTC-90. Conference Record., 7th IEEE Volume , Issue , 13-15 Feb 1990 Page(s):111 - 114

[6.6] G.F. Engen, "A Least Squares Solution for Use in the Six-Port Measurement Technique," IEEE Trans. Microwave Theory Tech., vol. MTT-28, pp. 1477-1482, Dec. 1980

[6.7] J.D. Hunter and P.I. Somlo, "An explicit six-port calibration method using five standards", IEEE Trans. Microwave Theory Tech., vol. MTT-33, pp. 69-72, Jan. 1985

[6.8] P.I. Somlo and J.D. Hunter, "A six-port reflectometer and its complete characterization by convenient calibration procedures", IEEE Trans. Microwave Theory Tech., vol. MTT-30, pp. 186-192, Feb. 1982

[6.9] P.I. Somlo and J.D. Hunter, "Microwave Impedance Measurements", Peter Peregrinus, 1985, pp.193-198

[6.10] L. Qiao and S.P. Yeo, "Improved implementation of four-standard procedure for calibrating six-port reflectometers", IEEE Trans. Instrument. & Measurement, vol. 44, pp. 632-636, Jun. 1995

[6.11] S.P. Jachim and W.D. Gutscher, "A statistical method for calibrating the six-port reflectometer using nonideal standards", ", IEEE Trans. Microwave Theory Tech., vol. MTT-37, pp. 1825-1828, Nov. 1989

[6.12] Agilent Technologies, "In-fixture measurements using vector network analyzers", Agilent AN1287-9, Agilent Technologies Ltd., 5968-5329, 2006

[6.13] Agilent Technologies, "8510C Network Analyzer System – Operating and Programming Manual", 08510-90281, May 2001

[6.14] Agilent Technologies, "Specifying calibration standards and kits for Agilent vector network analyzer", AN1287-11, 5989-4840, Apr. 2006

[6.15] E. Hammerstad, "Accurate models for microstrip computer aided design ", IEEE MTT-S Int. Symp. Digist, 1980, pp. 407-409

[6.16] P. Silvester and P. Benedek, "Microstrip discontinuity capacitance for right-angle bends, T-junctions and crossings", IEEE Trans. Microwave Theory Tech, vol. 21, pp. 341-346, feb. 1973

[6.17] R. Garg, and I.J. Bahl, "Microstrip discontinuities", Int. J. Electron, vol. 45, pp. 81-87, Jul. 1978

[6.18] B. Easter, "The equivalent circuit of some microstrip discontinuities", IEEE Trans. Microwave Theory Tech., vol. 23, pp. 655-660, May 1975

[6.19] R.J.P. Douville and D.J. James, "Experimental study of symmetrical microstrip bends and their compensation", IEEE Trans. Microwave Theory Tech., vol. 26, pp. 175-182, Jan. 1978

[6.20] A.A. Omar, Y.L. Chow, L. Roy, and M.G. Stubbs, ''Effect of air-bridges and mitering on coplanar waveguide 90° bends – theory and experiments,'' 1993 IEEE MTT-S Int. Microwave Symp. Dig., vol. 2, pp. 823-826, June 14-18, 1993, Atlanta, GA

[6.21] P.M. Watson and K.C. Gupta, ''Design and Optimization of CPW Circuits Using EM-ANN Models for CPW Components,'' IEEE Trans. Microwave Theory Tech., vol. 45, pp. 2515-2523, Dec. 1997

[6.22] T.M. Weller, R.M. Henderson, S.V. Robertson, and L.P.B. Katehi, ''Optimization of mm-wave distribution networks using silicon-based CPW,'' 1998 IEEE MTT-S Int. Microwave Symp. Dig., Vol. 2, pp. 537-540, June 7-12, 1998, Baltimore, MD

[6.23] R.N. Simons and G.E. Ponchak, ''Modeling of some coplanar waveguide discontinuities,'' IEEE Trans. Microwave Theory Tech., vol. 36, pp. 1796-1803, Dec. 1988

[6.24] P. Silvester and P. Benedek, "Equivalent capacitance of microstrip open circuits", IEEE Trans. Microwave Theory Tech., vol. 20, pp. 511-516, Apr. 1972

[6.25] K. Beilenhoff, H. Klingbeil, W. Heinrich, and H.L. Hartnagel, ''Open and short circuits in coplanar MMIC's,'' IEEE Trans. Microwave Theory Tech., vol. 41, pp. 1534-1537, Sep. 1993

[6.26] K. Beilenhoff, W. Heinrich, and H.L. Hartnagel, ''Finite-Difference Analysis of Open and Short Circuits in Coplanar MMIC's Including Finite Metallization Thickness and Mode Conversion,'' 1992 IEEE MTT -S Int. Microwave Symp. Dig., vol. 1, pp. 103-106, Albuquerque, NM, June 1-5, 1992

[6.27] M.H. Mao, R.B. Wu, C.H. Chen and C.H. Lin, ''Characterization of coplanar waveguide open end capacitance – theory and experiment,'' IEEE Trans. Microwave Theory Tech., vol. 42, pp. 1016-1024, Jun. 1994

[6.28] S.P. Yeo and K.H. Lee, "Improvements in design of six-port reflectometer comprising symmetrical five-port waveguide junction and directional coupler", IEEE Trans. Instrum. Meas., vol. IM-39, pp. 184-188, Feb. 1990

# Chapter 7

# CONCLUSIONS

Six-port reflectometers based on standard four-port couplers are inexpensive instruments that can be easily developed in-house since their constituent components are readily available in any reasonably well-equipped microwave laboratory. However, it is known that such designs do not meet the optimum q-point specifications laid down by Engen [7.20] and other researchers [7.21]-[7.22]. During the course of our investigations, we have successfully re-designed different four-port coupler structures for use in Chapter 6 to build three prototype six-port reflectometers yielding the requisite q-point distributions.

In addition, we have found it necessary to conduct empirical trials to determine the maximum design tolerances that may be allowed. Instead of dwelling only on six-port reflectometers, our preliminary analysis in Chapter 2 has been extended to the more general case of N-port reflectometers. We have also included in Chapter 2 a pilot design of an eight-port reflectometer in order to reinforce our understanding of the generic design criteria for application to the follow-up exploration in Chapter 3 of various topologies for possible use in our proposed six-port reflectometer. The empirical results provide useful insight to help us determine the key parameter specifications for our three coupler designs in Chapter 5 (*viz* the microstrip couplers with bandwidths of 26% and 32% for the branch-line and rat-race structures in Sections 5.1 and 5.2 respectively as well as the CPW coupler with the wider bandwidth of 80% in Sub-Section 5.3.2).

## 7.1 Principal Results

The preliminary analysis and empirical trials we conducted for the N-port reflectometer in Chapter 2 have yielded the following findings:

(1) We have found that the performance of the N-port reflectometer may be improved by increasing the number of ports if all the q-points lie on a common circle with its center at the origin and an optimum radius of 1. Under such conditions, the measurement error EVMS due to power-meter uncertainty $\varepsilon$ will decrease. Our tolerance trial results show that q-point magnitudes from 1 to 3 are also acceptable with the EVMS increasing slightly over this range.

(2) If the N-3 q-points of the N-port reflectometer lie on a common circle centered at the origin, their angular separations should all be equal to $360^o/(N-3)$ for optimum performance. For the case of the six-port reflectometer where N = 6, the optimum angular separation of the three q-points is thus $120^o$ and our tolerance trial results show that the acceptable range of angular separations should not exceed $120^o \pm 20^o$ if the EVMS is to remain less than twice the minimum EVMS value.

(3) If the q-points of the N-port reflectometer do not lie on a common circle centered at the origin, their optimum locations will vary in accordance with the specific details of the case under study. Our Monte Carlo simulations have yielded helpful findings for

the following cases:

(a) The six-port reflectometer proposed by Engen [7.20] has two q-points with equal magnitudes where $|\overline{q_2}| = |\overline{q_3}| = 1.5$ and $\angle \overline{q_1} = 0^{\circ}$. If we vary the magnitude of $\overline{q_1}$ while keeping all the other parameters unchanged, we have found that the optimum angular separation between $\overline{q_2}$ and $\overline{q_3}$ varies with the magnitude of $\overline{q_1}$. If we choose $|\overline{q_1}| = 1.5$ (and thus revert to the case of the three q-points lying on a common circle centered at the origin), we naturally expect $\angle \overline{q_2} = 120^{\circ}$ and $\angle \overline{q_3} = 240^{\circ}$ to be the optimum configuration. When $|\overline{q_1}|$ is increased beyond 1.5, our simulation results show a decrease in the optimum angular separation between $q_2$ and $q_3$.

(b) For the six-port reflectometer reported by Juroshek [7.24] where $\angle \overline{q_1} = 0^{\circ}$, $\angle \overline{q_2} = 135^{\circ}$, $\angle \overline{q_3} = -135^{\circ}$ and $|\overline{q_1}| = 1.5$, our simulation results show that we ought to choose $|\overline{q_2}| = |\overline{q_3}| = 1$ for optimum performance. If the q-points' angular positions are given by $\angle \overline{q_1} = 0^{\circ}$, $\angle \overline{q_2} = 90^{\circ}$, $\angle \overline{q_3} = -90^{\circ}$ instead, we have found that the optimum magnitudes should then be $|\overline{q_2}| = |\overline{q_3}| = 1.6$ when $|\overline{q_1}| = 1.5$.

(c) The six-port reflectometer studied by Cullen and Yeo [7.23] permits a variety of inter-connecting arrangements for their constituent components. Our comparative EVMS analysis has allowed us to confirm their choice of Configuration II (instead of the other possible configurations) for optimum performance on the basis of measurement accuracies.

The empirical findings in Chapter 2 indicate that we should choose the following tolerance limits for our six-port reflectomter design:

- q-point magnitudes between 1 and 3
- q-point angular separations between $100^o$ and $140^o$.

The detailed analysis and simulations we conducted in Chapter 3 have provided useful insights into the performance that may be expected for the six-port reflectometer when based on modified four-port couplers with the following scattering-matrix representation (which takes hardware imperfections into consideration):

$$\vec{S} = \begin{bmatrix} \vec{\tau_1} & \vec{\alpha_1} & \vec{\xi_1} & \vec{\beta} \\ \vec{\alpha_1} & \vec{\tau_2} & \vec{\gamma} & \vec{\xi_2} \\ \vec{\xi_1} & \vec{\gamma} & \vec{\tau_3} & \vec{\alpha_2} \\ \vec{\beta} & \vec{\xi_2} & \vec{\alpha_2} & \vec{\tau_4} \end{bmatrix} . \tag{7.1}$$

For the topology we selected, our simulation results in Sub-Section 3.2.3 have yielded the following design specifications for the four-port couplers that we need to modify in our effort to meet the objective of optimum q-point distributions for such six-port reflectometers:

$$\begin{aligned}
&|\vec{\tau_1}| \text{ and } |\vec{\tau_2}| < -23\text{dB} \\
&|\vec{\xi}| < -25\text{dB} \\
&|\vec{\alpha}/\vec{\beta}| \text{ and } |\vec{\alpha}/\vec{\gamma}| < 2\text{dB} \\
&|\triangle\phi_\gamma| < 10^o \\
&|\triangle\phi_\beta| < 15^o \\
&|\phi_\alpha - \phi_\beta| < 10^o \\
&|\phi_\alpha - \phi_\gamma| < 15^o
\end{aligned} \tag{7.2}$$

Even with careful design, the actual performance may deviate from ideal-case expectations due to various spurious effects and we should thus devise some means of fine-tuning for us to adjust the relative positions of certain q-points. The analysis in Section 3.3 has indicated how this can be accomplished by adding open/short stubs, capacitors or inductors at either or both of the terminations labeled as $\overrightarrow{\Gamma_1}$ and $\overrightarrow{\Gamma_2}$. We have thus incorporated such features when designing our prototype six-port reflectometers.

The analysis, design and tests we performed in Chapters 4-5 for three modified four-port structures (with close attention having been paid to address discontinuity compensation and other spurious effects) yielded three prototype couplers for use as building blocks of the three prototype six-port reflectometers we built and tested in Chapter 6. The experimental data obtained for our two microstrip-implemented reflectometers (based on the branch-line and rat-race couplers as described in Sections 6.2 and 6.3 respectively) as well as our CPW-implemented reflectometer in Section 6.4 have confirmed that their measured q-point distributions all meet the design targets of $1 < |\overrightarrow{q_i}| < 3$ and $100^o < |\arg(\overrightarrow{q_i} / \overrightarrow{q_j})| < 140^o$. A comparison of the DUT measurements taken by our three prototype six-port reflectometers with the corresponding Γ readings obtained by the commercially-available HP8510C vector network analyzer has demonstrated that measurement accuracies of ±0.02 and $\pm 2^o$ can be readily achieved for $|\overline{\Gamma}|$ and $\arg(\overline{\Gamma})$ respectively. Since the bandwidths we obtained during laboratory tests for the two microstrip-based reflectometers in Sections 6.2 and 6.3 are only 29% and 33% respectively, we have also explored other planar implementations and successfully developed in Section 6.3 the CPW-based version yielding an improved bandwidth of 80%.

## 7.2 Suggestions for Future Research

We have already considered a range of aspects during the course of our investigations. There are, nevertheless, other aspects that may be worth exploring as possible follow-up in the future.

(a) CPW discontinuity modeling

Without enhanced numerical accuracies for the performance data predicted by computer-aided models for the more complicated CPW structures, we had to resort to cut-and-try iterations (instead of relying solely on the optimization algorithms outlined in Chapter 4) in our attempts to arrive at a design that minimizes practical problems associated with fabrication yield or operational reliability. Trying to incorporate some computationally-intensive software (for computing the scattering coefficients of CPW structures) into the optimization process is time-consuming and inefficient. It will naturally be advantageous to have more flexibility in tweaking the physical dimensions of various CPW discontinuities during the optimization of our six-port reflectometer design but this requires the availability of enhanced lumped-element models for the various non-uniform CPW discontinuities (including their higher-order parasitics).

(b) Novel broadband four-port couplers

It is relatively easy to implement in microstrip the two prototype six-port reflectometers based on branch-line and rat-race couplers in Sections 6.2 and 6.3 respectively. However, it is difficult to extend the bandwidth of such microstrip-implemented designs beyond 35% (due to the inherent limitations generally associated with microstrip structures) and we thereafter proceeded with the CPW-implemented design yielding a bandwidth of 80% in Section 6.4. Actually, the concept allows for other forms of planar implementation as well and another possible follow-up is to explore novel four-port coupler designs that can meet the specifications listed in Equation 7.2 over a bandwidth exceeding 80%. In addition, it will be helpful (for incorporation into MMICs) to opt for simpler structures than that designed in Sub-Section 5.3.2.

(c) Optimum seven-port reflectometer

Our analysis of the N-port reflectometer in Chapter 3 has indicated that the overall measurement accuracies ought to improve with the number of ports, and we briefly digressed in Section 3.3 to consider the pilot design of the eight-port reflectometer. It may be useful to pursue this in more detail, starting perhaps with the seven-port reflectometer, based on the findings reported in Chapter 3. One such possibility is the schematic diagram sketched in Figure 7.1 which is our modification of the seven-port reflectometer proposed by Engen [7.19]; instead of opting for open/short stubs or SMT inductors/capacitors for fine-tuning purposes as in Section 6.4, we suggest the insertion of an attenuator to provide the means of adjusting the relative q-point distribution.

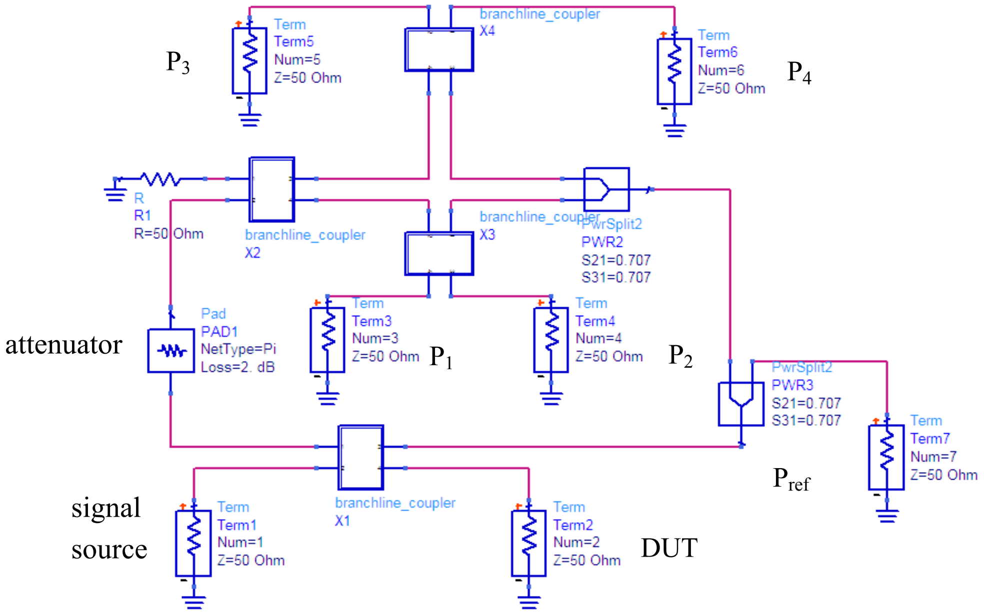

Figure 7.1 Schematic diagram for seven-port reflectometer (based on modification of circuit proposed by Engen [7.19]) where X and P denote 90° hybrid couplers and power detectors respectively

## REFERENCES

[7.1] N. Dib, “Comprehensive study of CAD models of several coplanar waveguide discontinuities”, IEE. Proc. Microwave Antenna Prop., vol. 152, pp. 69-76, Apr. 2005

[7.2] D. Mirshekar-Syahkal, “Computation of equivalent circuits of CPW discontinuities using quasi-static spectral domain method”, IEEE Trans. Microwave Theory Tech., vol. 44, pp. 979-984, Jun. 1996

[7.3] Rainee, Simons, “Modeling of some coplanar waveguide discontinuities”, IEEE Trans. Microwave Theory Tech., vol. 36, pp. 1796-1803, Dec. 1988

[7.4] D. M.-Syahkal, “Computation of Equivalent Circuits of CPW Discontinuities Using Quasi-static Spectral Domain Method”, IEEE Trans. Microwave Theory Tech., Vol. 44, No. 6, pp. 979-984, June 1996.

[7.5] T.W. Wang, “Experimental study of wideband uniplanar phase inverters for MICs”. 1997 IEEE MTT-S Int. Microwave Symp. Digest, pp.777-780

[7.6] Lin, F., and Wu, R.: ‘Analysis of CPW discontinuities with finite metallisation thickness and nonrectangular edge profile’, IEEE Trans. Microw. Theory Tech., 1997, 45, pp. 2131–2138

[7.7] R.M. Vahldieck and K. Wu, “Theoretical and experimental characterization of coplanar waveguide discontinuities”, IEEE Trans. Microw. Theory Tech., 1993, 41, pp. 1638–1640

[7.8] B.R. Heimer, L. Fan and K. Chang, “Uniplanar hybrid couplers using asymmetrical coplanar striplines,” IEEE Trans. Microwave Theory Tech., vol. MTT-45, pp. 2234-2240, Dec. 1997.

[7.9] T. Wang and K. Wu, “Size reduction and band-broadening design technique of uniplanar hybrid ring coupler using phase inverter for M(H)MICs,” IEEE Trans. Microwave Theory Tech., vol. MTT-47, pp. 198-206, Feb. 1999.

[7.10] C.Y. Chang and C.C. Yang, “A novel broadband Chebyshev-response rat-race ring coupler,” IEEE Trans. Microwave Theory Tech., vol. MTT-47, pp. 455-462, Apr. 1999

[7.11] T.Y. Chang, “Coplanar-waveguide tandem couplers with backside conductor”, Microwave Wireless Comp. Lett., vol.13, pp. 214-216, Jun. 2003

[7.12] S. Gruszczynski, “Design of compensated coupled-stripline 3-dB directional couplers, phase shifters and Magic-T’s — Part II: Broadband Coupled-Line Circuits”, IEEE Trans. Microwave Theory Tech, vol. 54, pp. 3501-3507, Sep. 2006

[7.13] K. Sachse and A. Sawicki, “Quasi-ideal multilayer two- and three-strip directional couplers for monolithic and hybrid MIC’s”, IEEE Trans. Microwave Theory Tech., vol. 47, pp. 1873-1882, Sep. 1999

[7.14] A.M. Abbosh and M.E. Bialkowski” Design of compact directional couplers for UWB applications,” IEEE Trans. Microwave Theory Tech., vol.. 55, pp. 189-194, Feb. 2007

[7.15] F. Tefiku, “Novel directional couplers using broadside-coupled coplanar waveguides for double-sided printed antennas” IEEE Trans. Microwave Theory Tech., vol. 44, pp. 275-282, Feb. 1996

[7.16] A. Sawicki, “Novel coupled-line conductor-backed coplanar and microstrip directional couplers for PCB and LTCC applications”, IEEE Trans. Microwave Theory Tech., vol. 51, pp. 1743-1751, Jun. 2003

[7.17] R.W. Vogel, “Analysis and design of lumped- and lumped-distributed-element directional couplers for MIC and MMIC applications”, IEEE Trans. Microwave Theory Tech., vol. 40, pp. 253-262, Feb. 1992

[7.18] T.Y. Song, “design of novel lumped element backward directional coupler based on parallel coupled line theory”, IEEE MTT-S Digest 2002, pp. 213-216

[7.19] G.F. Engen, “An Improved Circuit for Implementing the Six-Port Technique of Microwave Measurements”, IEEE Trans. Microwave Theory Tech., vol 25, pp. 1080-1083, Dec. 1977

[7.20] G.F. Engen, “A historical review of the six port measurement technique”, IEEE Trans. Microwave Theory Tech, vol. 45, no.12, pp. 2414-2417, Dec. 1997

[7.21] S.P. Yeo, “Analysis of symmetrical six-port junction when configured as a six-port reflectometer”, IEEE Trans. Instrum. Meas., vol. 41, no. 2, pp. 193-197, Apr. 1992

[7.22] P.J. Probert and J.E. Carroll, “Design features of multi-port reflectometer”, Proc. Inst. Elec. Eng., pt. H, vol. 129, pp. 245-252, Oct. 1982

[7.23] A.L. Cullen and S.P. Yeo, “Six-port reflectometer theory for symmetrical five-port junction with directional coupler”, Proc. Inst. Elec. Eng., vol 133, pt. H, pp. 277-287, Aug. 1986

[7.24] J. Juroshek, “A dual six-port network analyzer using diode detectors”, IEEE Trans. Microwave Theory Tech., vol. 32, pp. 78–82, Jan. 1984